Modelling the Neutralisation Process in Neutral Beam Injectors

N. J. Fitzgerald

Ph.D. 2009

Modelling the Neutralisation Process in Neutral Beam Injectors

A thesis for the degree of

Doctor of Philosophy

Presented to

Dublin City University

By

Niall J. Fitzgerald B.Sc.
School of Physical Sciences,
Dublin City University.

Research Supervisors

Prof. Miles M. Turner
Dr. Albert R. Ellingboe

External Examiner: Dr. Brendan Crowley
Internal Examiner: Dr. Enda McGlynn

September 2009

Thesis Declaration

I hereby certify that this material, which I now submit for assessment on the programme of study leading to the award of Ph.D. (Physics) is entirely my own work, that I have exercised reasonable care to ensure that the work is original, and does not to the best of my knowledge breach any law of copyright, and has not been taken from the work of others save and to the extent that such work has been cited and acknowledged within the text of my work.

Signed: Student ID number: 98520849

Date:

Acknowledgements

I want to thank my co-supervisors Dr. Albert Ellingboe and Prof. Miles Turner for all their help. I also want to gratefully acknowledge the help of Dr. Derek Monahan, who composed most of the MATLAB code used to plot the simulation results, as well as helping me with other computational matters. Among many others, I would particularly like to thank Dr. Deirdre Boilson for her encouragement and assistance. I take this opportunity also to thank my external examiner Dr. Brendan Crowley and internal examiner Dr. Enda McGlynn. Reflecting on more first principled grounds for acknowledgement, I'm delighted to be able to formally thank my parents, Patrick and Jean, our forefathers and foremothers, and above all, the cause of our origin and that of the universe in which we fleetingly dwell - in the eternal spirit of my Catholic faith, I thus prayerfully give thanks and praise to God our father through our lord Jesus Christ (cf. Genesis 1:1, Genesis 1:3, Wisdom 13:1, John 1:3, 1 John 3:1, Revelation 1:1).

… and from studying the works did not *acknowledge* the workmaster (Wisdom 13:1).

… the world does not *acknowledge* us because it did not *acknowledge* God (1 John 3:1).

Contents

Abstract

High power neutral beams currently play an important role in heating, fuelling and diagnosing magnetically confined thermonuclear fusion plasmas. At the Joint European Torus (JET) in Oxfordshire, England, the formation of such a beam involves passing a positive ion beam through a neutral gas target wherein beam electron-capture collisions result in a neutral beam component. The subsequent beam injection into the fusion plasma requires the sole use of this neutral component, since the charged component cannot penetrate through the large magnetic confinement fields of the tokamak. The observed failure to achieve near maximum theoretical neutralisation efficiency, has given motivation to those concerned to endeavour to understand the reason thereof. This neutralisation efficiency deficit is almost certainly due to gas target depletion, while the general consensus is that indirect heating of the neutraliser gas by the beam is its main cause [19, 30]. Paméla [31, 34] proposed a simplified analytical model of beam indirect gas heating over twenty years ago. The aim of this endeavour was to gain a more thorough understanding of the interaction between the beam and the neutraliser gas (beam plasma), via electrostatic Particle-in-Cell (PIC) computer simulations incorporating Monte Carlo collisions (MCC). Results under varying beam & gas parameters include the calculation of plasma parameters and the resultant gas heating. The simulation results are qualitatively consistent with the experimental results from the Langmuir probe investigation of Crowley et al. [36] (which includes spectroscopic measurements to estimate the gas temperature [30], and invokes the gas heating model developed by Paméla), while they predict the existence of four significant gas heating pathways not accounted for in the Paméla model i.e. direct kinetic energy transfer by H_3^+ ions, H_2^+ ions, H atoms (formed via H_3^+ formation) and electrons. However, the gas heating results do not account for the extent of the observed neutralisation inefficiency. In agreement with Surrey [40], results from a similar simulation investigation of future (ITER) negative ion neutralisers predict insignificant gas heating effects. Beam composition simulations predict the existence of a specific gas line density pertaining to maximum neutralisation efficiency, as opposed to the generally assumed increasing asymptotic behaviour, while an experiment is proposed to verify this prediction.

Chapter 1

Introduction

1.1 Thermonuclear Fusion Research

1.1.1 Background Perspective

The work presented herein relates to the field of Controlled Thermonuclear Fusion Research. More specifically, it concerns the area of Neutral Beam Injection, which serves heating and fuelling functions in magnetically confined thermonuclear fusion experiments. Academically, this project may reside in the area of beam-generated plasma physics or alternatively under the umbrella of computational plasma physics. The physics of the neutralisation process, i.e. anything that occurs inside the volume of the neutraliser and at the neutraliser walls, provides the scope for this investigation.

The field of magnetically confined thermonuclear fusion began in the 1930s, from attempts to confine a hot plasma using magnetic fields. The prospect of harnessing nuclear energy, proceeded the achievements of, *inter alios*, Einstein's [1] mass-energy equivalence relation (deduced from his theory of Special Relativity [2]), Aston's [3] mass deficit measurements, and Bethe's [4] explanation of how gravity enables fusion reactions to occur in the centre of stars (thereby supplying their sustaining energy).

It wasn't until the 1950s that Soviet physicists [5] demonstrated the now favoured tokamak-type of fusion machine, with a magnetic configuration similar to that currently used at the Joint European Torus (JET) in Oxfordshire, England [6]. A basically equivalent (plasma confining) magnetic configuration is due to be employed at the International Thermonuclear Experimental Reactor (ITER, Latin for "the way"), under construction in Cadarache, France [7]. ITER is designed to replace JET as the world's leading fusion reactor, and will bring the thermonuclear fusion community ever closer in their endeavour to make commercial fusion energy production a reality.

The official goal of ITER is "to demonstrate the scientific and technological feasibility of fusion power for peaceful purposes" [7], while the efficient, cost-effective generation of electricity is intended as its most immediate application. Realisation of this would certainly be welcomed internationally, given the present day dependence on diminishing supplies of fossil fuels, coupled with the desire for reducing carbon emissions as part of a global strategy in response to the apparently significant/detrimental effects of climate change, supposedly ("very likely" [8]) caused by such anthropogenic effects cf. [9].

1.1.2 Fusion Reaction Basics

Nuclear fusion entails the coming together of two or more nuclei/atoms to form a single more massive nucleus/atom. The new elemental species has less mass than the sum of the individual nuclei/atoms. This mass deficit is determined from their respective nuclear binding energies and is thus converted into energy, satisfying Einstein's famous $E = mc^2$ equation [1, 2]. For a fusion reaction to occur between two nuclei/atoms, sufficient energy (the phenomenon of quantum tunnelling can lessen this required energy) is needed to overcome the Coulomb barrier i.e. the mutually repulsive electromagnetic force due to the positive charge of a nucleus' constituent protons. This energy enables the particles to come close enough together for the short-range attractive strong nuclear force to become dominant, which causes the particles to fuse.

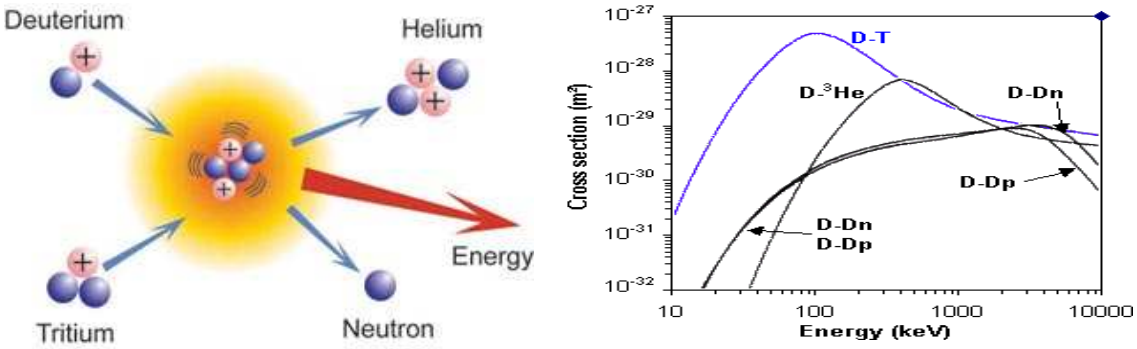

Figure 1: (a) Schematic of the D-T fusion reaction [7]. (b) Comparison of the D-T fusion reaction with various other less favourable options [6].

Among perspective candidates for anthropogenic fusion, hydrogen isotopes, each with only one positive 'elementary' charge, provide the least repulsive electrical force to overcome, and thus require the least fusion activation energy. The main function of a tokamak is to create a high temperature environment conducive to such fusion reactions, hence the prospect of generating more energy than that required to cause and sustain such thermonuclear fusion plasmas (*Section 1.2.1*). Due partly to these high temperature constraints (*Section 1.2.2*), deuterium-tritium (D-T) is presently the favoured fusion fuel choice, given its relatively favourable cross section (*Figure 1 (b)*), and its desirable, highly energetic products {3.5MeV alpha particle (helium nucleus), and 14.1MeV neutron, *Figure 1 (a)*}. The magnetic bottle type confinement (*Section 1.2.1*) of such a high-density, high-temperature plasma, for an adequate period of time, (cf. Lawson criteria [10]) continues to be one of the greatest challenges in tokamak design.

1.1.3 Electrical Power via Fusion

In a possible D-T fusion reactor operating scenario (*Figure 2*), the alpha particles stay magnetically confined in the plasma and therefore also contribute to the plasma heating, while the fast neutrons escape to the lithium blanket at the walls and cause the breeding (via *fission*) of the tritium fuel (deuterium can be extracted from sea water, and lithium, a relatively abundant metal in the earth's crust, can be mined) [7]. Basically, the fast neutrons carry the majority of the energy (*Section 1.1.2*), and a fusion power plant could utilise such fast particles to boil water and drive an electricity generator i.e. a conventional steam turbine with a different fuel and furnace. For example, 1kg of D + T could produce (via a fusion power station) the same electrical energy as ~ 10,000 tonnes of coal (the daily consumption in a 1GW coal power station) [11], while it has the potential to be financially competitive with other carbon free electricity sources.

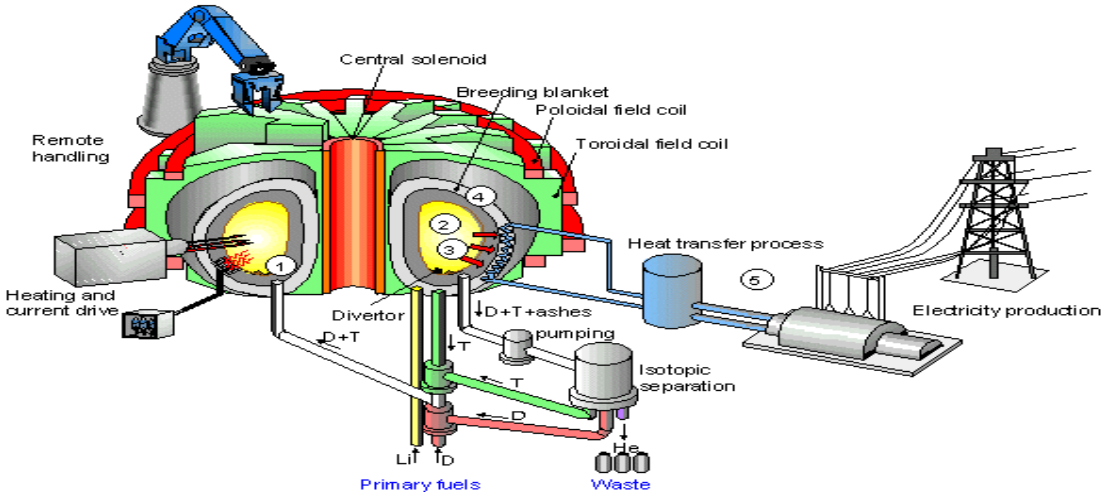

Figure 2: Schematic of a possible electricity producing fusion power plant [6].

1.1.4 Fusion versus Fission

The production of electricity via nuclear fission is a reality and has been since the 1950s. Fission power stations exist in most 'developed countries' (Ireland being an example of a 'nuclear-free, advanced economy country') and produce ~ 14% of the world's electricity [12]. Per total kilowatt-hours of electricity consumption; France is the leading producer/consumer (~ 80%), while other countries such as Japan (~ 30%), the US (~ 20%) and the UK (~ 20%) also use substantial amounts of fission energy.

Regarding possible future nuclear fusion power production, JET has demonstrated that this will certainly be within our scientific/technological capabilities. The construction of ITER commenced in 2008, with a new target of 2018 for its debut operation [7]. While ITER promises to be a major step forward in the path to fusion power, the actualisation of reliable, economically viable power production is still many decades away. The next step after ITER is envisaged to be the construction of a prototype power plant ('DEMO'). *Figure 3* compares a probable commercial reactor with ITER ('Next Step') and two European reactors, JET and Tore Supra (located in Cadarache, France).

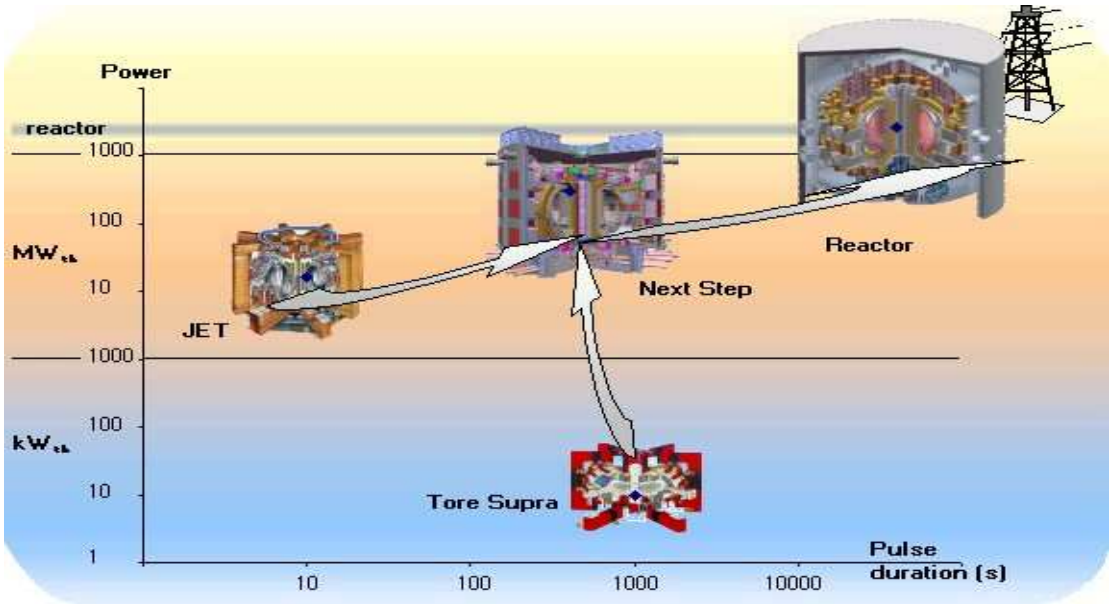

Figure 3: A comparison of present day reactors (drawn to scale), JET and Tore Supra with the ITER ('Next Step') design and a likely commercial reactor, in terms of their maximum attainable power output and pulse duration [6].

D-T Fusion has an effectively limitless fuel supply, second to none in its net energy gain capabilities, while common fission fuels (uranium/plutonium isotopes) are less abundant, more difficult to extract, and have lower energy densities. In such fusion reactions, the percentage of matter transformed into energy is a few times greater than in such fission reactions, due to bigger differences in binding energies [10].

In common with prospective fusion power plants, fission power plants effectively produce no carbon dioxide or other greenhouse gases nor indeed any other environmentally harmful gases. However, a lot of controversy and strong disagreement still persists over issues related to the relatively long-lived dangerous (direct) high-level radioactive waste (HLW) products from fission power plants. In contrast, fusion power

plants would produce no direct nuclear waste, the main cause of concern being that some fusion reactor components become radioactive via high-energy neutron impact. The resulting (indirect) HLW from such neutron activation will require burial (deep geological disposal) for ~ 50 years before it becomes low-level nuclear waste (LLW), which will then necessitate another ~ 100 years containment (shallow land disposal) [13]. Thus, in comparison with fission waste products, which remain radioactive for thousands of years, the nuclear fusion waste has relatively short half-lives and therefore creates a more short-term waste containment responsibility [13], conducive to sustainable energy/development and nearly in keeping with the 'user pays' principle. Fusion materials research is still ongoing in its endeavour to determine the best materials that would minimise any such adverse effects caused by neutron impact and be able to withstand the high temperatures resulting from the substantial heat flux emanating from the plasma - especially pertinent to plasma facing components (PFCs).

At present, many evolving types/classifications of fission reactors are being used, not only for electricity generation, but also for various other morally questionable purposes e.g. providing certain fissile materials for nuclear weapons. All such man-made fission reactors stemmed from the discovery of fission chain reactions [10], though it has been hypothesised [14] that natural fission reactors existed in the earth ~ 2 billion years ago, supported by supposable evidence from uranium ore deposits at Oklo in Gabon [15]; consisting of measurements - conducted by the French Atomic Energy Commission (CEA) - that suggest uranium isotope (^{235}U) concentration deficits (i.e. compared to other mines) similar to that resulting from man-made fission reactors. In contrast to such disputable, circumstantial evidence, more substantial (albeit indirect) evidence exists for natural fusion reactions in stars [3, 4, 16] cf. [17], while fusion reactors would entail no potentially troublesome chain reactions. D-T fusion power plants would, by themselves, offer no danger of nuclear proliferation i.e. while they would use tritium, a radioactive gas, which can be produced *in situ* (yet the ITER plan is to initially use tritium produced from fission reactors before testing tritium breeder technology [18]), this can only be used for nuclear weapons in conjunction with enriched fissile materials.

Thus, even though it is more technologically challenging to sustain sufficient fusion power i.e. enough for a viable power plant; all the preceding comparisons suggest that fusion is the better alternative harness-able source of nuclear energy to fission.

1.2 Neutral Beam Injection at JET

1.2.1 Overview of JET

The Joint European Torus (JET) is up and running since 1983 and remains to be a valuable test bed for fusion experiments, especially for specific ITER related tests. It currently holds the record for fusion power production (16.1MW peak fusion power, with over 10MW for more than 0.5s [6]), although it has only ever nearly reached breakeven with regard to energy production. Breakeven (energy gain factor; Q = 1) represents the scenario where the power produced equals the power used to maintain the plasma in steady-state (ITER is designed to achieve a Q of ~ 10, still short of what an economically viable electricity producing fusion power plant is anticipated to require).

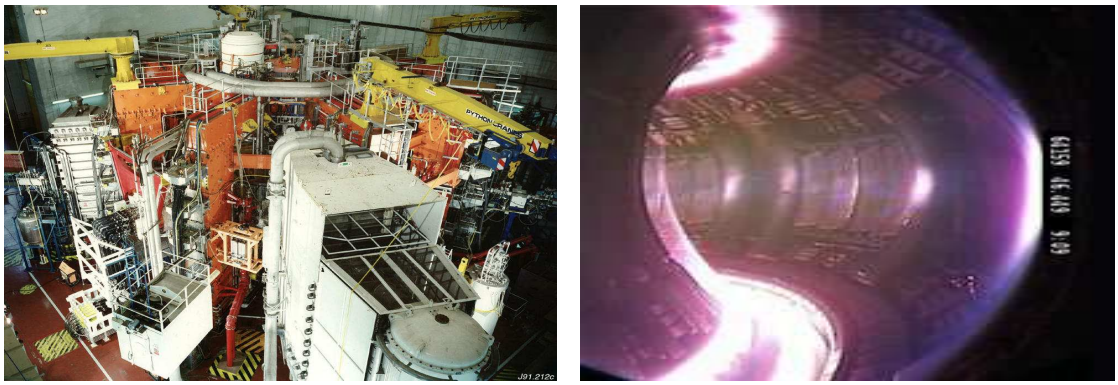

Figure 4: (a) A view of JET from the Torus hall, showing one of two neutral beam injection boxes (NIBs) [6]. (b) A photograph of an actual discharge [6].

Changing current in the tokamak's central solenoid induces ~ 5MA of current drive in the D-T plasma i.e. via a transformer technique [6]. This induced current heats the plasma up via resistive (ohmic) heating, resulting in a few MW of heating power. Toroidal and poloidal magnetic fields, produced by electromagnetic coils (the plasma current also induces a poloidal magnetic field), serve a plasma confining function, while additional coils help to position and shape the plasma. Many different plasma diagnostics (including neutral beam diagnostics [6]) are positioned at multiple access points (*Figure 4 (a)*). The bulk fusion plasma (*Figure 4 (b)*) is colourless except at its boundaries, where a lower temperature plasma exists containing some atoms, molecules and ions with bound electrons capable of producing visible light emission (Bremsstrahlung, including synchrotron radiation is also emitted from the plasma).

1.2.2 Auxiliary Heating Methods

Additional heating methods (*Figure 5 (a)*) are employed at JET, to heat the plasma up to temperatures high enough for it to yield a sufficient number of D-T fusion reactions {in excess of $1x10^8$K (~ 8.6keV, ≅ ten times as hot as the centre of the sun) - neutral beam diagnostics are used to estimated the plasma temperature [6]}. Typically, Neutral Beam Heating (neutral particles can be injected straight into the plasma i.e. un-deviated by the confining magnetic fields) supplies up to ~ 23MW (via kinetic energy transfer collisions with the fusion plasma particles), along with a potential of up to ~ 32 MW from Radio Frequency Heating (Ion Cyclotron Heating) [6]. Lower Hybrid Current Drive is another technique which, albeit inefficient in directly heating the plasma, can be used to drive a further ~ 3MA of current by exploiting other resonant frequencies of the plasma (it entails generating 3.7GHz microwaves with a power capacity of ~ 12MW to accelerate the plasma electrons, thus supplying this extra plasma current) [6].

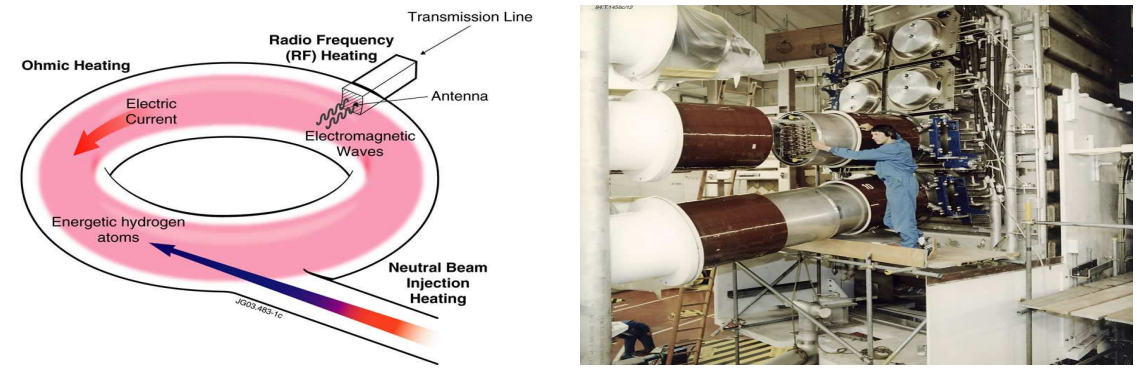

Figure 5: (a) Schematic of the various plasma heating mechanisms used at JET [6]. (b) A photograph taken during the installation of the PINIs [6].

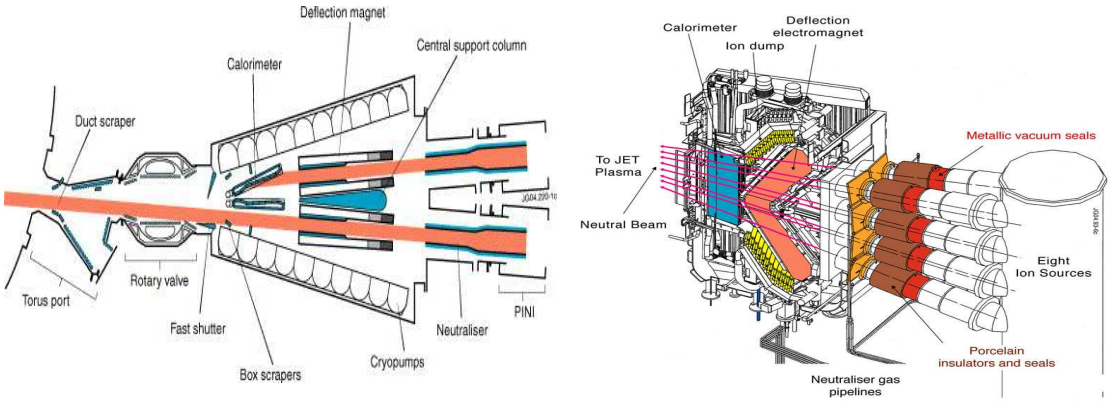

Figure 6: (a) A plan view schematic of the JET neutral injection box (NIB) with attached PINIs [19]. (b) An interior elevation view schematic of a NIB, showing the eight merging neutral beams originating from their respective PINIs [6].

1.2.3 Neutral Beam Injection

JET neutral beam injectors (NBIs) consist of two types of separate vessels (*Figure 6*); positive ion neutral injectors (PINIs), and a neutral injection box (NIB). Up to eight PINIs can be attached to each NIB (*Figures 5 (b)* & *6*). Each PINI contains; an ion source (dc arc discharge, producing positive ions), accelerating grids (including a grid to electrostatically prevent neutraliser electrons from flowing upstream) and the 1st stage of a (copper) neutraliser (~ 0.86m). The NIB houses the 2nd stage neutralisers (~ 1m), the deflection electromagnet (removes the un-neutralised beam ions) and the ion dump (receives the positively charged beam ions). Cryo-pumps are employed in the NIB to create a sufficient vacuum to minimize re-ionisation of the un-deflected, separated 'pure' neutral beam, and gas particles entering the tokamak (*Figure 6 (a)*).

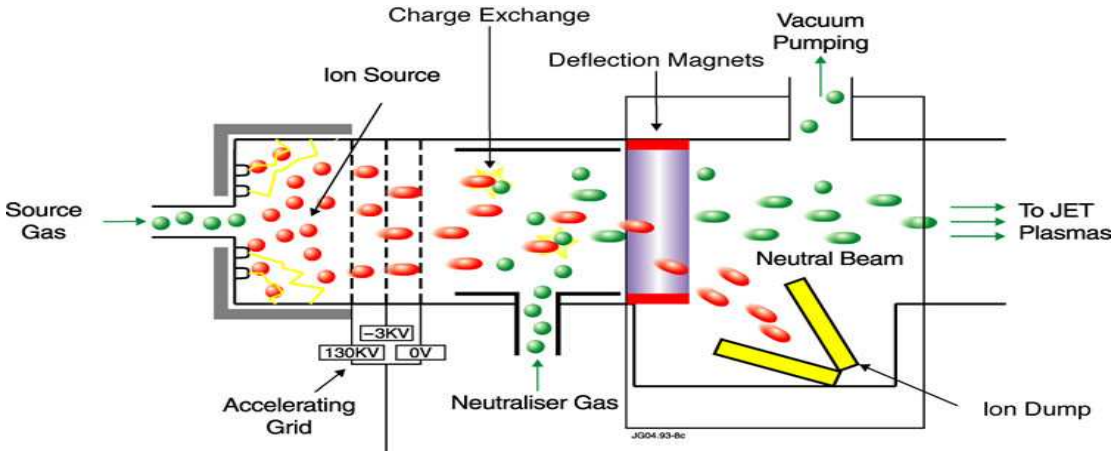

Figure 7: An elevation view schematic of a JET neutral beam injector (NBI) [6].

The JET building also contains a separate Neutral Beam Test Bed facility adjacent to the Torus hall. Its function is to provide a test bed for scientific investigations aimed at; improving the NBI heating capacity, performing tests on problematic NBIs and pre-tests before new/upgraded NBIs become commissioned to operate on the tokamak. Most of the scientific investigations involve testing upgrades to the ion source and accelerating grid systems (to produce greater beam power [20]), although improved neutralisation motivated investigations have occasionally been embarked upon (*Section 1.4.1*).

A magnetic cusp configuration is positioned around the ion source (containing either hydrogen, deuterium, tritium or helium [21] gas) to achieve the desired ion species ratios. Ion extraction/acceleration and subsequent beam dissociation &/or neutralisation produces a composite beam consisting of molecular and atomic ions/neutrals of four

different energies (1/3, 1/2, 2/3 and full energy, cf. *Sections 2.2.1* & *4.1*). The beam (initially consisting of 262 individual beamlets) emanates from the ion source through two grid plates (each containing 131 circular holes of 11mm aperture), positioned at a slight angle to one another (grid tilt), in order for the beamlets to merge correctly. For the duration of beam (neutraliser) transit, the beam envelope has a cross sectional area of ~ 0.064m^2 (0.16m x 0.40m, horizontal and vertical width, respectively). Some beam interception occurs mainly at the end of the second stage neutraliser (~ 0.088m^2; 0.20m x 0.44m), and results in beam power (transmission) losses of ~ 4% [22]. JET PINIs can produce beam currents of up to ~ 65A and beam energies of up to ~ 130keV [20].

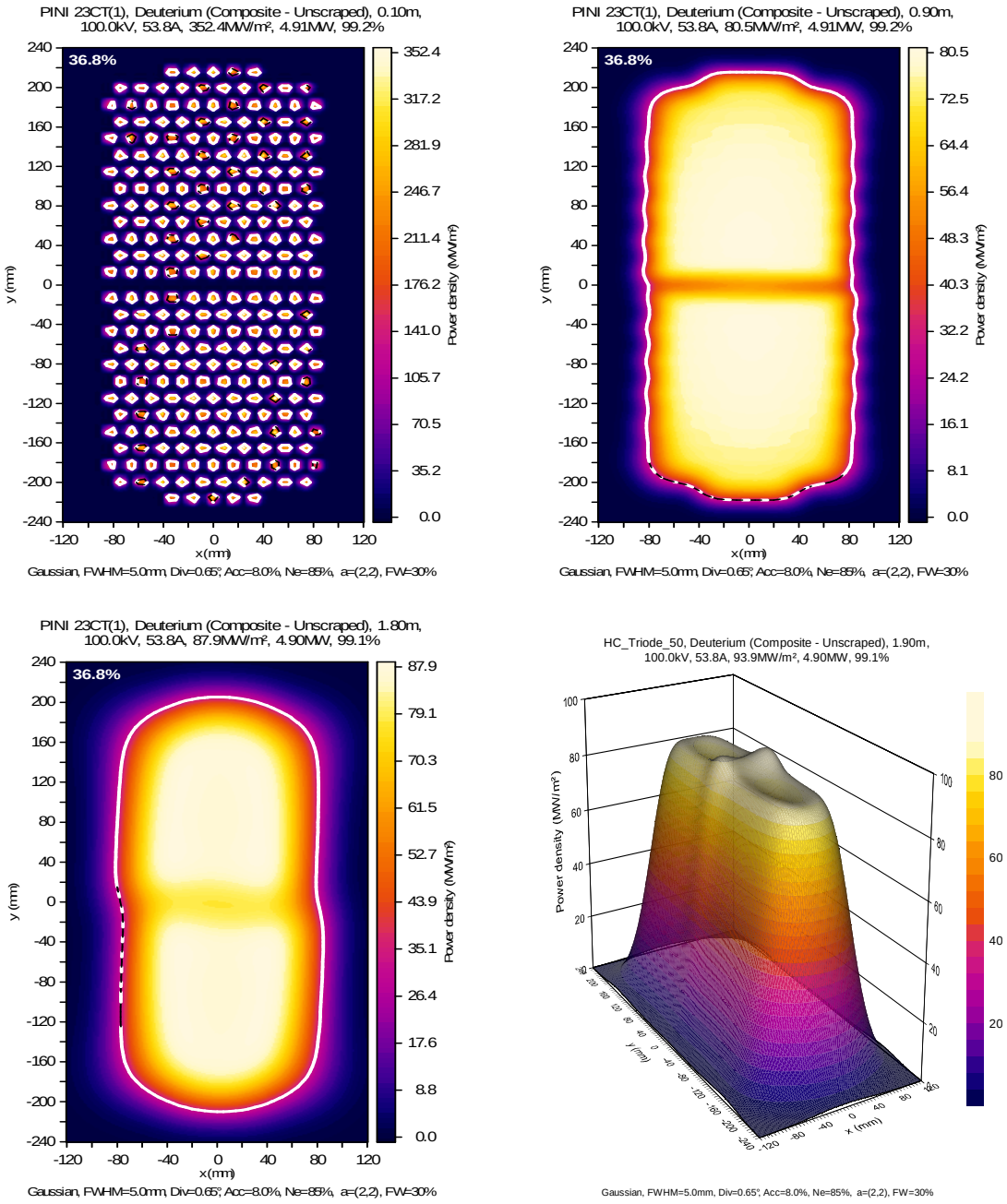

Figure 8: Beam profile simulation results at various neutraliser positions [23].

1.3 Neutralisation Efficiency of JET NBIs

1.3.1 Beam Neutralisation Theory

The theoretical maximum neutral beam component can be estimated, given the initial multiple-ion beam densities and energies (assumed to remain constant, *Section 4.2*), and the relevant beam (energy dependent) charge-changing cross sections. Beam fractions are most succinctly expressed as functions of the neutraliser gas line density [24]:

$$\frac{dF_n}{d\Pi} = \sum_{m=-1}^{z}(F_m\sigma_{mn} - F_n\sigma_{nm}), \qquad \sum_{n=-1}^{z}F_n = 1, \qquad n,m = -1,0,1...z \tag{1.1}$$

F_n = fraction of the beam with charge n

Π = neutraliser gas line density (neutraliser gas density integrated over its length)

σ_{mn} = cross section for a change of charge from m to n

A multiple-ion beam reaches dynamic charge-equilibrium after travelling a certain distance through a gas corresponding to the charge-equilibrium gas line density:

$$\frac{dF_n}{d\Pi} = 0 \quad \Rightarrow \quad \sum_{m=-1}^{z}(F_m^{\infty}\sigma_{mn} - F_n^{\infty}\sigma_{nm}) = 0, \qquad F^{\infty} = \text{equilibrium fraction}$$

$e\sum_{n=1}^{z} n(F_n^{\infty} - F_{-n}^{\infty})$: beam net charge magnitude, e = 'elementary' charge

Consider the elementary case of an atomic hydrogen beam {assuming only beam species H^+ & H exist (no H^-) and that $F_1 = 1$ & $F_0 = 0$ at $\prod = 0$, i.e. the pre-injected beam consists solely of protons} injected into a neutraliser containing any stable gas:

$$\begin{aligned}\frac{dF_1}{d\Pi} &= F_0\sigma_{01} - F_1\sigma_{10} \\ \frac{dF_0}{d\Pi} &= F_1\sigma_{10} - F_0\sigma_{01}\end{aligned} \quad \equiv \quad \frac{dF}{d\Pi} = \begin{pmatrix} -\sigma_{10} & \sigma_{01} \\ \sigma_{10} & -\sigma_{01}\end{pmatrix}F = AF, \qquad F = \begin{pmatrix} F_1 \\ F_0\end{pmatrix} \tag{1.2}$$

Solution of the form: $F = x_1 e^{\lambda_1\Pi} + x_2 e^{\lambda_2\Pi}$, where λ_1, λ_2 and

$x_1 = \begin{pmatrix} x_{11} \\ x_{12}\end{pmatrix}$, $x_2 = \begin{pmatrix} x_{21} \\ x_{22}\end{pmatrix}$ are the eigenvalues and eigenvectors of A, respectively.

The characteristic equation {det(A-λI)=0, *Appendix A*} gives the two eigenvalues:

$$\lambda_1 = -(\sigma_{01} + \sigma_{10}), \qquad \lambda_2 = 0$$

Substitution into the eigenvector equation {Ax=λx, *Appendix A*} yields the two eigenvectors x_1, x_2 and hence expressions for the two beam charge fractions F_1, F_0:

$$x_1 = \begin{pmatrix} \frac{\sigma_{10}}{\sigma_{01}+\sigma_{10}} \\ \frac{-\sigma_{10}}{\sigma_{01}+\sigma_{10}} \end{pmatrix}, \qquad x_2 = \begin{pmatrix} \frac{\sigma_{01}}{\sigma_{01}+\sigma_{10}} \\ \frac{\sigma_{10}}{\sigma_{01}+\sigma_{10}} \end{pmatrix}$$

$$F_1 = \frac{\sigma_{10}}{\sigma_{01}+\sigma_{10}} e^{-(\sigma_{01}+\sigma_{10})\Pi} + \frac{\sigma_{01}}{\sigma_{01}+\sigma_{10}},$$

$$F_0 = \frac{-\sigma_{10}}{\sigma_{01}+\sigma_{10}} e^{-(\sigma_{01}+\sigma_{10})\Pi} + \frac{\sigma_{10}}{\sigma_{01}+\sigma_{10}}$$

F_1 & F_0 can be further expressed in terms of their equilibrium fractions:

$$\begin{matrix} \lim_{\Pi\to\infty}(F_1) = F_1^{\infty} \\ \lim_{\Pi\to\infty}(F_0) = F_0^{\infty} \end{matrix} \quad \Rightarrow \quad \begin{matrix} F_1^{\infty} = \frac{\sigma_{01}}{\sigma_{01}+\sigma_{10}} \\ F_0^{\infty} = \frac{\sigma_{10}}{\sigma_{01}+\sigma_{10}} \end{matrix} \quad \Rightarrow \quad \begin{matrix} F_1 = F_1^{\infty}(1 + \frac{\sigma_{10}}{\sigma_{01}} e^{-(\sigma_{01}+\sigma_{10})\Pi}) \\ F_0 = F_0^{\infty}(1 - e^{-(\sigma_{01}+\sigma_{10})\Pi}) \end{matrix} \qquad (1.3)$$

The function of the close-coupled neutralisers used in JET NBIs [6] is to enable a positive multiple-ion beam attain a maximum neutral beam *power* (density, if and only if all beam components have the same energy). This is achieved by supplying a minimally sufficient gas line density (thus minimising gas pumping requirements and re-ionisation of the un-deflected 'pure' neutral beam). Since, in this simplified analysis, the beam charge-changing process is asymptotic (*Figure 9*), it is useful [25] to define the 'optimum' (*Section 4.1*) gas target as that which yields 3 beam attenuations, corresponding to the beam reaching ~ 95% of its maximum neutral density (*power*).

80keV hydrogen beam {density; $6.725x10^{14} m^{-3}$ (27A)} traversing a H_2 neutraliser

3 beam attenuations: $F_0 = F_0^{\infty}(1 - e^{-3}) \approx \frac{\sigma_{10}}{\sigma_{01}+\sigma_{10}}(0.95) \approx 0.3$

requires a neutraliser gas target of: $\Pi = \frac{3}{(\sigma_{01}+\sigma_{10})} \approx 1.67x10^{20}\, m^{-2}$

yielding a neutral beam density of: $n_{bH} = 0.3(6.725x10^{14}\, m^{-3}) \approx 2.026x10^{14}\, m^{-3}$

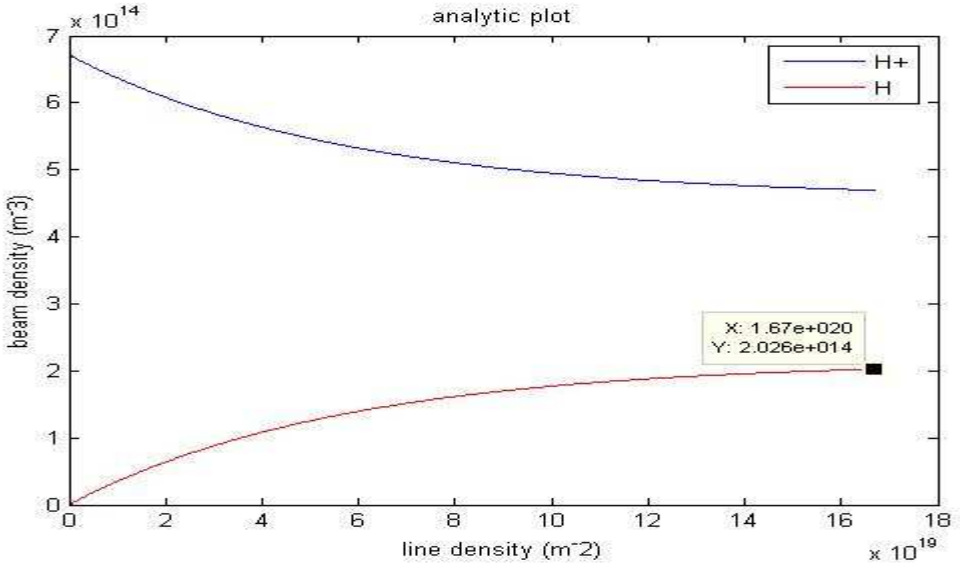

Figure 9: 80keV/27A H^+/H densities as a function of the H_2 neutraliser gas target.

1.3.2 *Expected Neutralisation Efficiency*

The neutraliser gas target is directly controlled by the neutraliser gas flow rate (gas from the ion source also reaches the neutraliser). A moving ion gauge has previously been used to estimate the longitudinal neutraliser gas pressure profile, in the absence of beam injection (*beam on* measurements are unfeasible) [26, 19]. The neutraliser pressure (and hence the density, assuming a constant temperature) has a near constant value along its 1st stage and then drops off nearly linearly (in the 2nd stage neutraliser) to ~ 15% of this value (*Figure 10*). From the outset of neutral beam injection at JET, the gas target has consistently been overestimated [27, 28]. This stemmed from an underestimation of the neutraliser conductance, by assuming it operated in the molecular flow regime. In fact, typical neutraliser pressures correspond to the transitional flow regime, which predicts a higher conductance, via an additional term, directly proportional to the pressure [28].

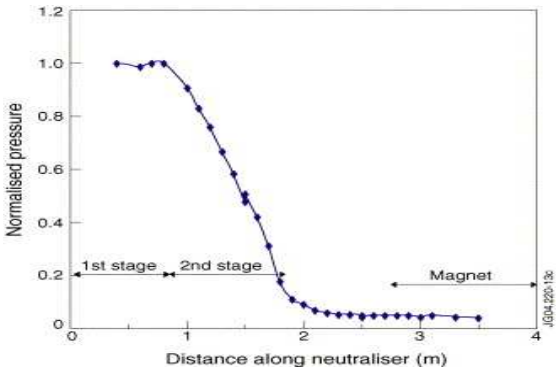

Figure 10: The measured normalised pressure distribution along the neutraliser [19], cf. [26].

For both molecular and transition gas flow regimes, the gas line density is inversely proportional to the conductance, while the conductance is proportional to the square root of the temperature [29]. It therefore implies that the gas line density is inversely proportional to the square root of the temperature. The exact scaling of the JET NBI neutraliser gas line density with temperature is in fact unknown, yet results from Surrey et al. [19] suggest a linear scaling. Either way, a substantial increase in temperature [30], during beam (neutraliser) transit, will cause a significant reduction in the gas target. However, the neutralisation efficiency is not as sensitive to changes in the gas target (*Figure 9*, *Section 1.3.1* cf. *Section 5.1.5*), especially for excessive gas targets.

Given a value for the effective (hot and therefore depleted cf. *Chapter 5*) gas target, the expected neutralisation efficiency can be calculated via a beam charge-changing analytical model (*Section 1.3.1*), or more accurately via *beam composition* simulations that can kinetically model all possible charge-changing collisions (*Section 4.1*).

1.3.3 *Actual Neutralisation Efficiency*

The actual *neutraliser* neutralisation efficiency can loosely be defined as the ratio of the neutral beam power (at the neutraliser exit) to the extracted beam power, and can be indirectly measured [19] by comparing beam impact calorimetric data (downstream) with/without the deflecting electromagnet turned on {taking into account re-ionisation of the separated neutral beam (due to the presence of residual gas - mainly coming from the neutraliser and arising from recombined beam ions) and beam transmission losses (dependant on beam & gas parameters in addition to the beamline setup, *Section 3.1*) [27]}. Another method reported in [19] uses measurements of the tokamak response to neutral beam injection to ascertain the neutralisation efficiency. This method is based on a comparative approach, whereby measurements of the power supplied by neutral beam injection of known neutralisation efficiency (reference beam) are used to calculate the power supplied by a NBI of unknown neutralisation efficiency. Yet another method involves the comparison of the "rate of highest energy protons resulting from *D(d,p)T* reactions with and without ion deflection by the magnet" [31] cf. [32].

1.3.4 Neutralisation Efficiency Deficit

Figure 11 (a) shows the discrepancy between the measured neutral beam power (from two different techniques; calorimetry and plasma response [19]), and that expected from either a cold or hot (Paméla model) neutraliser gas target {the decreasing slopes of both curves is due to the decrease in neutralisation efficiency with increasing beam energy, evidenced by the cross section data shown in *Figure 11 (b)*} - taking into account beam transmission & re-ionisation losses [19]. This so called neutralisation efficiency deficit is almost certainly due to a depletion of the neutraliser gas target in the presence of the beam, and is thought to be mostly caused by gas heating [19, 30] cf. *Section 1.4.1*.

(a) (b)

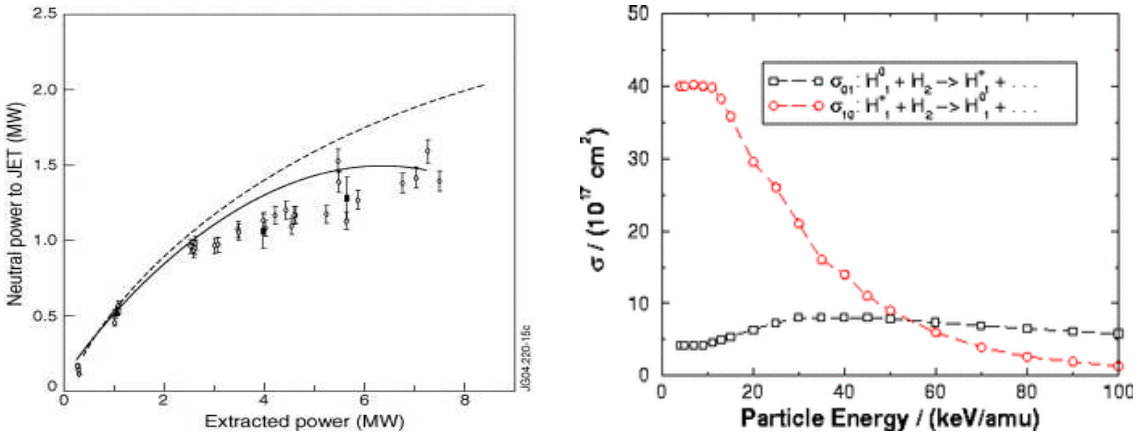

Figure 11: (a) Neutral beam power (as a function of the extracted power) transmitted to the JET fusion plasma as measured by; calorimetry (diamond), plasma response (box), and calculated using; a cold gas target (gaped line) and a hot depleted gas target (continuous line) [19]. (b) Electron stripping (beam re-ionisation) & electron capture (beam neutralisation) cross sections as a function of particle (beam) energy per nucleon, for a Hydrogen beam in transit through a H_2 gas cell (neutraliser) [25].

Although the data displayed in *Figure 11 (a)* suggests that gas heating may account for all of the neutralisation deficit {e.g. at 7MW, a ~ 27% (±4%) shortfall in neutral beam power is inferred from the calorimetric measurements, while the Paméla model predicts a value of ~ 23%}, other factors such as gas implantation (wall pumping) & re-emission [33] could also have a significant bearing on the (beam on/off) gas target [27]. Investigating these factors is beyond the scope of this computational endeavour, which instead focuses on quantifying the neutraliser gas heating (*Chapter 5*).

1.4 Background and Goal of this Work

1.4.1 Related Investigations

In the mid 1980s Paméla [31, 34] proposed that the neutralisation efficiency deficit was due to (neutraliser gas density depleting) beam indirect gas heating via the formation of a low temperature plasma inside the neutraliser. More than 15 years elapsed before an experimental investigation into the neutraliser beam plasma commenced at the JET Neutral Beam Test Bed facility. This initially entailed the insertion of a diagnostic collar in between the first and second stage of the neutraliser, and formed part of the Improved NB Neutraliser JET Enhancement Project [35], which was completed in November 2002, cumulating in a paper by Crowley et al. [36].

Two analytical neutraliser plasma models [22] were developed by Surrey prior to this investigation (one based on a static theory of a beam plasma [37] and the other based on a more elaborate model developed by Holmes [38]). These proved useful in determining the expected range of plasma parameters encountered in the neutraliser, and so helped with the design specifications of the Langmuir probe used by Crowley et al. [36].

The diagnostic collar (*Figure 12 (b)*) thus facilitated neutraliser plasma diagnostic investigations i.e. Langmuir probe measurements (used to determine the plasma parameters) and spectroscopic measurements (used to calculate the gas temperature), as well as various pressure sensor measurements (can also be used at additional positions along the neutraliser to estimate the axial pressure profile [26, 19]). The electron density, electron temperature and plasma potential as a function of; neutraliser gas pressure, beam power and time, were determined from the Langmuir probe traces [36]. These results were used as empirical inputs in Paméla's gas heating model to estimate the gas temperature rise, and were found to be in good agreement with the measurements of Surrey & Crowley [30] {who used spectroscopic measurements of rotational vibrational emission bands in diatomic molecules (Fulcher α Spectrum) together with the de Graaf (corona) model [39] to estimate the translational gas temperature}. Resultant temperatures were inferred to be up to and in excess of 1000 K.

More recent measurements of the depleted neutraliser gas target (*Figure 11 (a), Section 1.3.4*) were published (online) in August 2005 [19], again supporting the gas heating

hypothesis. In May 2006, Surrey also published a paper attempting to predict gas heating effects in the neutralisers of ITER injectors [40]. Here she adapted her beam plasma model for positive beams into a model for the ITER heating (HNB) and diagnostic (DNB) negative ion neutral beam injectors. She concluded by saying that gas heating is unlikely to be severe in either of the injectors, and as a result, the neutralisation target is expected to remain close enough to the design value (*Chapter 6*).

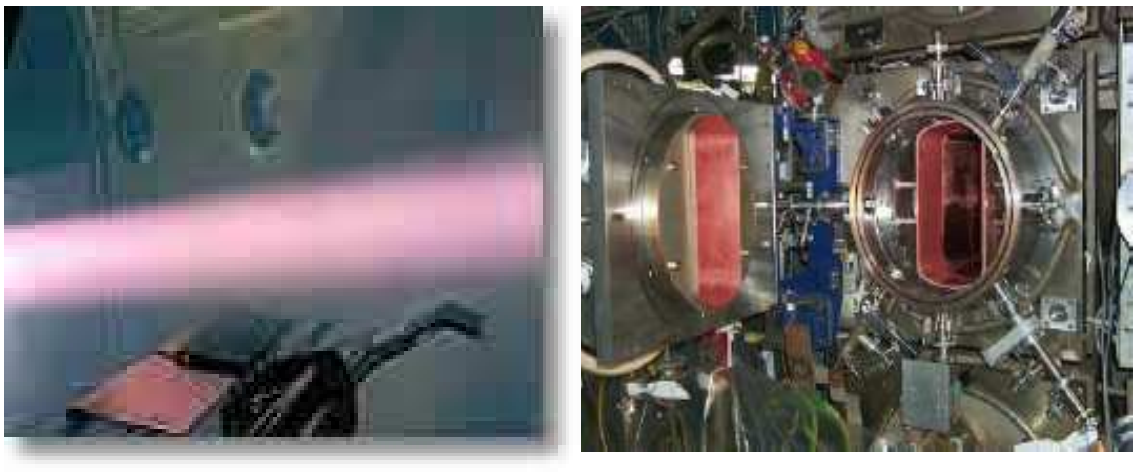

Figure 12: (a) Photograph of a Hydrogen beam [6]. (b) Photograph of the diagnostic collar positioned in between the first and second stage of the neutraliser [35].

1.4.2 Motivation and Aim

Surrey's two beam plasma models [22] are deficient due to their inaccurate assumptions e.g. assuming an ion temperature of one-tenth the electron temperature [37], and assuming the beam to be isolated from the neutraliser walls [38]. Paméla's gas heating model is also deficient for similar reasons e.g. it involves a "naïve" [34] zero-dimensional plasma model and omits important gas heating pathways (*Section 5.2*).

A further Improved Neutralisation JET Enhancement Project was started in 2003 [41], acknowledging the need to further develop Surrey's neutraliser plasma models and Pamela's gas heating model. It was also foreseen that these models could be "combined to give a complete description of the neutraliser physics system" [41], hence the motivation of this work, which to this end, employs electrostatic beam plasma Particle-in-Cell (PIC) computer simulations incorporating Monte Carlo collisions (MCC).

The simulation directly calculates various plasma parameters (resolved in either the transverse or longitudinal beam spatial dimensions), with such results providing data for the calculation of the power transferred indirectly by the beam to the neutraliser gas. The PIC MCC technique (*Chapter 2*) incorporates a kinetic model, which assumes little in comparison with Surrey's and Paméla's aforementioned beam plasma models, and is capable of simulating many of the vast array of possible collision events in a reasonable time on a modern PC. The overall merit of this approach is therefore due to its more thorough treatment of the relevant physics while invoking fewer assumptions.

In common with Paméla's beam indirect gas heating model [31, 34], a neutraliser gas steady-state scenario is assumed in order to calculate the gas temperature rise i.e. where the gas power gained indirectly from the beam equals the gas power lost at the walls (*Section 5.1*). However, in contrast to Paméla's zero-dimensional model [31, 34] (requires some empirically determined quantities cf. [36]), the gas power gained indirectly from the beam is obtained via neutraliser beam plasma one-dimensional simulations. The 1D3v PIC MCC *Transverse* (*Section 2.2.1*, *2.2.4*) simulation approach assumes the neutraliser beam plasma as being vertically and axially uniform. Hence, strictly speaking (cf. *Figure 10, Section 1.3.2*), this simulation approach only yields a valid model of the 1st stage neutraliser beam plasma system cf. *Section 2.2.3*.

The effective neutraliser gas target, resulting from gas density depletion, is directly dependent on the gas temperature rise, while the exact correlation between these parameters is again still unknown. Effective neutraliser gas line density results are thus presented for; a standard hot gas density-temperature relationship i.e. assuming that the gas target is inversely proportional to the square root of the gas temperature (from molecular/transitional gas flow theory [29]), and an ideal gas law density-temperature relationship i.e. the gas target being inversely proportional to the gas temperature [19].

Overall, the goal of this work is to elucidate the physics of neutraliser gas cell positive/negative ion beam neutralisation, and thus acquire knowledge that would help to improve the neutralisation efficiency (and therefore the overall energy efficiency) of present JET neutralisers, and future negative ion neutralisers such as those designed for ITER's heating (HNB) and diagnostic (DNB) neutral beams.

1.5 Elementary Plasma Physics

1.5.1 The Prevalence of Plasmas

The plasma state is often categorised as the fourth state of matter, coming after solid, liquid and gas in order of increasing constituent particle (thermal) energy, and is presently thought to prevail in ~ 99.99% of the universe. Common examples include the sun and other stars, the interstellar medium (ISM) being a lesser-known example. Closer to earth, we find plasmas such as the magnetosphere and the ionosphere, along with visible and more spectacular examples like an aurora {partly caused by proton-gas (solar wind–earth's atmosphere) 'positive ion neutraliser occurring' radiative collisions} and lightning (*Figure 13*). From our earthly perspective, these natural plasmas are relatively remote, which helps explain why this complex state of matter remains elusive to common knowledge. Despite this lack of public awareness, the occurrence of application driven man-made plasmas has increased greatly over the last few decades.

Figure 13: (a) An image of the galaxy NGC 1512 taken by the Hubble Space Telescope, which includes light from the infrared, visible, and ultraviolet regions of the spectrum [42]. (b) An aurora pictured over houses in Ramfjordmoen, Norway, on March 4th 2002, during the suns active (sunspot) phase (the bright red colour indicates the presence of atomic oxygen) [42]. (c) Lightning striking a tree. Note the positive streamer rising from a pole near a house in the front left of the photograph [42].

Familiar man-made plasmas include lighting sources such as; the widespread sodium street lamp, neon signs, florescent lights, and even candle flames. More elaborate plasmas are used for many other applications including; thermonuclear fusion (arguably the most favourable potential new energy source available to mankind, and the field most relevant to this work), etching and deposition (extremely important processes in

the multi-billion dollar microelectronics industry), surface modifications (causing material changes in hardness, wettability etc.), gas lasers, welding arcs, waste treatments and such medical applications as sterilisation. These useful applications obviously provide motivation for the study of plasma physics, although it could be argued that even without such applications, an investigation into the fundamentals of plasma physics is still a worthwhile endeavour in its own right, as part of the ongoing pursuit in trying to understand nature more comprehensively, in all its forms.

1.5.2 Qualitative Plasma Characterisation

Basically speaking, a plasma consists of a gas containing significant numbers of charged particles with an overall (macroscopic) near neutral (quasineutral) charge. It may contain many different species of particles e.g. neutral atoms/molecules, electrons, positive ions, negative ions, radicals, dust particles. Hence, due to the presence of more 'free' charges, one of the main differences between the physics of plasmas and that of normal gases (both gaseous fluids) is in their responsiveness to electromagnetic fields.

The charged particles in a plasma interact with each other via electromagnetic forces. As a result of the relatively long-ranged Coulomb force, the various electric fields produced by the charged particles, have an effect on other constituent charged particles and not just on their nearest neighbours. This phenomenon is known as collective behaviour and is partly what makes plasma physics more complex than normal gaseous physics where nearest neighbour interactions (e.g. collisions) are of most importance. In addition to these self-generated electromagnetic fields, external electromagnetic fields are frequently applied in man-made plasma tools, and therefore also partly determine the motion of the constituent particles. Like all plasma particles, charged particles also move due to diffusive behaviour and particle-particle/particle-wall collisions. The plasma state of matter is also a superb medium for producing many types of electrostatic and electromagnetic wave phenomena (hence its use as a radiation source).

Some collisions in a plasma (e.g. inelastic collisions i.e. where the kinetic energy is not conserved) are more complicated than the billiard-ball-like (elastic) collisions predominant in relatively cold, ordinary gases. Moreover, charged particles can undergo other elastic scattering processes such as Coulomb collisions and polarization scattering

collisions. Coulomb collisions arise when charged particles closely approach each other, electromagnetic forces causing their trajectories to become curved (the energy exchanged depends on the mass of both particles and the deflection angle). Since the majority of neutraliser beam plasma electrons are of relatively high energy, neutral particles have relatively little time to polarize in their vicinity. Hence, polarization scattering is not deemed significant enough to warrant inclusion in the limited set of allowable collision pathways modelled in this simulation investigation.

In all plasmas, the crucial collisions are the ones that cause and sustain its existence. These inelastic collisions occur between sufficiently energetic particles and the source gas. In the majority of man-made plasma devices, electrons have the fastest particle velocities, due to the 'preferential' nature of the heating mechanisms employed, and the relatively small momentum transfer between light electrons and heavier particles. Electron impact ionisation therefore tends to be the dominant source of ionisation, and requires electrons of energy equal to, or exceeding, that of the relevant gas ionisation threshold energy {as the particle species in a plasma usually have a relatively large spread of velocities, these electrons reside in the high-energy tail of the electron energy distribution function (eedf). Moreover, large numbers of electrons together with high electron-electron momentum transfer collision rates often yield a thermal distribution of speeds well described by the Maxwell-Boltzmann speed distribution}.

For example, during the etching of silicon wafers in the microelectronics industry (one of the many material processing applications involving non-thermal plasmas), electrons respond best to externally applied radio frequency fields (their relatively small mass inertia causes their relatively high mobility), and consequently attain much higher velocities than the heavier particles. Plasmas can thus provide relatively high temperature (particular species) chemistry at relatively low physical temperatures, which is generally why they are so prevalent in many industrial applications. Even in the case of thermal plasmas i.e. where electrons are in thermal equilibrium with the heavy particles (e.g. ions), the electron velocities are higher due to their lower mass. Electrons therefore become the main workhorses in nearly all man-made plasmas.

Other important plasma collisions include; dissociation collisions (an especially important step leading to gas heating in neutraliser beam plasmas), association collisions, excitations (electronic excitations leading to radiative emissions, and

vibrational and/or rotational excitations in molecular species), charge transfer collisions and recombinations. For material processing plasmas, such plasma chemistry is of vital importance, whereas in noble gas plasmas, much less chemistry occurs.

1.5.3 Plasma Defining Criteria

For an ionised gas to be classified as a plasma, three criteria need to be satisfied:

Although most stable plasmas are quasineutral, a local break from charge neutrality pertains over small distances, quantified by the Debye length (λ_D) cf. [43]. This phenomenon of Debye shielding (charge screening), where for example a positive ion attracts a sphere of electrons around it, causes the self-generated electric fields to be damped out over distances greater than λ_D. To remain quasineutral, a plasma must satisfy the conditions that its dimensions (L) are much greater than its Debye length:

$$L >> \lambda_D \tag{1.4}$$

In order for this phenomenon to prevail, there must also be a sufficiently large number of electrons (N_D) within a sphere of radius equal to the Debye length (Debye sphere). This quantity is often referred to as the plasma parameter:

$$N_D >> 1 \tag{1.5}$$

A third defining criteria for plasmas involves the so-called plasma frequency (ω_p) cf. [43], which quantifies the plasmas' collective response time to 'quiver motion' caused by externally applied forces (e.g. electromagnetic fields) and/or internally originating electromagnetic fields (involving fleeting spatial perturbations of charge). The plasma frequency is required to be greater than the collision frequency (f_c). This criterion implies that electromagnetic interactions play a major part in the overall motion of the plasma, and that nearest-neighbour, ordinary gas interactions (e.g. collisions) don't dominate. Typically the electron plasma frequency lies in the gigahertz range, while the corresponding ion plasma frequency is usually only in the low megahertz range:

$$\omega_p > 2\pi f_c \tag{1.6}$$

A plasma is usually broadly characterised by two parameters; the plasma (number) density {number of like charged particles per unit volume} and the electron temperature {a measure of the mean thermal energy of an equivalent electron population in thermodynamic equilibrium, represented by a Maxwellian distribution}. Other distinct plasma parameters (not mentioned thus far) include; the plasma potential and skin depth, as well as the thermal velocity and mean free paths of each particle species.

1.5.4 The Plasma Sheath

A plasma sheath (also known as a Debye or electrostatic sheath) forms at any plasma-material interface. The physics of the plasma sheath plays a crucial role in the overall behaviour of the plasma system. A net charge (a break from the bulk plasma quasineutrality) develops in a plasma sheath due to the inequality of escaping negative and positive species. As explained in *Section 1.5.2*, in a typical plasma, electrons are faster than any positive species and are therefore quickest to escape. This causes a net positive charge to reside in the sheath, and leads to the formation of an electric field, which confines electrons within the plasma and accelerates positive ions out of the plasma; thus preserving bulk plasma quasineutrality by maintaining an equality between positively and negatively charged outward fluxes.

As a result of Debye shielding, most of the spatial variation in electric potential occurs only locally in the sheath region. Even in the case of a plasma in the presence of an external electric field e.g. a capacitive discharge [43], the voltage is dropped mainly over the sheaths, leaving the quasineutral bulk plasma at a ‘constant’ plasma potential (the steady-state plasma potential may oscillate depending on the nature of the dynamic equilibrium between plasma particle formation & loss, and the presence of plasma waves). Consequently, most plasmas have sheath widths of the order of their Debye length. Negative sheath potentials can also exist e.g. when positive ions are faster than negative ions and/or electrons. More commonly they occur when excess negative charge is produced e.g. in negative ion neutralisers cf. *Chapter 6*, cf. *Section 2.2.4*.

For a more thorough introduction to Plasma Physics see *Bibliography* [43, 44, 45].

Chapter 2

Neutraliser Beam Plasma Model

2.1 Particle-in-Cell Simulations with Monte Carlo Collisions

2.1.1 Electrostatic PIC Technique

PIC simulations are a popular tool for modelling low temperature plasma behaviour, as they invoke relatively few assumptions, and incorporate a thorough kinetic model of plasma dynamics. Unlike fluid models, which assume certain particle energy distributions e.g. Maxwellian distributions, PIC models are capable of computing the energy distribution functions of each particle species. Even though one simulated particle (*super-particle*) can represent ~ 10^{10} real particles (3D simulation), PIC MCC simulations have proven to be physically accurate [46], and thus continue to provide an important test bed for computer experiments in plasma science and technology.

The standard (non-relativistic) plasma kinetic description involves the Boltzmann equation for each particle species, coupled with Maxwell's equations, including charge density and current density relationships, along with the continuity equation. cf. [43]:

$$\frac{\partial f_i}{\partial t} + v \cdot \nabla_r f_i + \frac{q_i}{m_i}(E + v \times B) \cdot \nabla_v f_i = \left(\frac{\partial f_i}{\partial t}\right)_c$$: Boltzmann equation

$$\nabla \cdot E = \frac{\rho}{\varepsilon_0} \qquad \nabla \times E = -\frac{\partial B}{\partial t}$$

$$\nabla \cdot B = 0 \qquad \nabla \times B = \varepsilon_0 \mu_0 \frac{\partial E}{\partial t} + \mu_0 i$$: Maxwell's equations

$$\rho = \sum_i q_i \int d^3 v f_i \qquad J = \sum_i q_i \int d^3 v f_i v$$: charge & current density relationships

$$\frac{\partial \rho}{\partial t} + \nabla \cdot J = 0$$: continuity equation

Obtaining the exact analytic solution to these equations is not practically feasible, although PIC MCC simulations can yield reasonably accurate approximations. Here the continuous distribution functions (f_i) are replaced by discrete particles, and the integrals with summations over all particles [45]. The PIC model divides the spatial dimension up into a number of discrete cells, which are populated by the super-particles. Partial differential equations (PDEs) for f_i reduce to ordinary differential equations (ODEs) for the particles' position and velocity. These ODEs are used in their discretised form, thus allowing the computer to solve them by a finite difference technique (the explicit

Leapfrog scheme [47] is used in this work) at each particle position and discrete time-step (index, n). However, the motion causing electrostatic fields (magnetic effects are assumed to be negligible) are solved only at the cell-nodes (also called grid or mesh points), rather than at each particle position. An interpolation technique (*Gather*) is used (via a shape function, S) to ascribe the charge density (ρ) to each cell-node (index, i), i.e. from the charged particle positions (index, j) within the cells. The electrostatic interactions of the charged particles are then modelled using Poisson's equation to find the electric potential (φ) and its spatial gradient i.e. the electric field (E), at every cell-node. The electric field at each cell-node is then interpolated back (*Scatter*) to the actual particle positions, where the equations of motion are numerically integrated to find their new velocities and positions. In contrast to kinetic simulations involving fixed-field equations, the electrostatic field equations are thus solved self-consistently i.e. the cell-node charge distributions and resulting electric fields are continuously updated in accordance with the charged particles' ever changing positions. The full cell-node particle weighting procedure is then repeated at each successive time-step. cf. [47]:

Gather: $\rho = \sum_i q_i \int d^3 v f_i \quad \rightarrow \quad \rho_i = \partial\rho \sum_j S(x_i, x_j)$

$(\rho_i, \varphi_i, \varphi_{i-1}) \rightarrow (E_i, \varphi_{i+1})$:

$$\frac{d^2\varphi}{dx^2} = -\frac{\rho}{\varepsilon_0} \quad \rightarrow \quad \frac{\varphi_{i+1} - 2\phi_i + \varphi_{i-1}}{\Delta x^2} = -\frac{\rho_i}{\varepsilon_0}, \qquad E = -\frac{d\phi}{dx} \quad \rightarrow \quad E_i = \frac{\varphi_{i+1} - \varphi_{i-1}}{2\Delta x}$$

Scatter: $E_j = \sum_i E_i S(x_i, x_j)$

$(E_n, x_n, v_{n-\frac{1}{2}}) \rightarrow (x_{n+1}, v_{n+\frac{1}{2}})$:

$$\frac{dv}{dt} = \frac{qE}{m} \quad \rightarrow \quad \frac{v_{n+\frac{1}{2}} - v_{n-\frac{1}{2}}}{\Delta t} = \frac{qE(x_n)}{m}, \qquad \frac{dx}{dt} = v \quad \rightarrow \quad \frac{x_{n+1} - x_n}{\Delta t} = v_{n+\frac{1}{2}}$$

2.1.2 Basic MCC Model

When a super-particle is moved (after the integration of the equations of motion and before the particle's charge is distributed to the nearby cell-nodes, cf. *Figure 14*, *Section 2.1.3*) it has a certain probability of making a binary collision with another super-particle. This collision probability is determined from the cross sections of the possible collisions, and a Monte Carlo technique governs whether or not an actual collision takes

place. The cross sections (as functions of energy) are initially inputted into the code as a data table, which is interpolated to find cross sections at energies in between those quoted. The so-called null-collision method is used so that the super-particle collision frequency (ν, calculated from the cross section data) is independent of energy, hence causing the probability of a collision to be also independent of energy:

$P = 1 - e^{-\nu \Delta t}$ and $\nu_{total}(E) = \sum_i \nu_i(E)$ (P and ν_{max} are independent of energy)

Choose $\nu_{null}(E)$ such that $\nu_{total}(E) + \nu_{null}(E) = \nu_{max}$

$0 \le R_1 < 1$: computer generated pseudorandom number

If $R_1 < P_{max}$ => collision

Else if $R_1 \ge P_{max}$ => no collision

$P_i = \frac{1}{\nu_{max}} \sum_{j \le i} \nu_j(E)$: formula for calculating the collision probability

If null collision => no collision
Else if real collision => solve (momentum & energy conservation) collision equations

In the collision algorithm, the scattering formula is taken from Takizuka & Abe [48].

2.1.3 PIC MCC Computational Cycle

The PIC MCC computational cycle (*Figure 14*) can be summarised by five distinct steps; (I) The MCC technique determines which particles undergo collisions. The collision algorithm then solves the collision kinematic equations while implementing the results thereof. (II) Each individual particle charge is ascribed to the nearby cell-nodes (*Gather*). (III) The electric field is computed at each cell-node (via the solution of Poisson's equation). (IV) The electric field at each cell-node is used to assign a specific field value to each charged particle (*Scatter*). (V) These field values are then used to determine the motion of the charged particles (by solving the equations of motion). This cycle continues for all time-steps. Generally, the super-particle electrons are the only species moved every time-step, since it is sufficient to move (subcycle) the heavier

particles (e.g. ions) every ~ 5 time-steps (depending on their velocities) because of their slower motion. This has the highly desired effect of reducing the computational time.

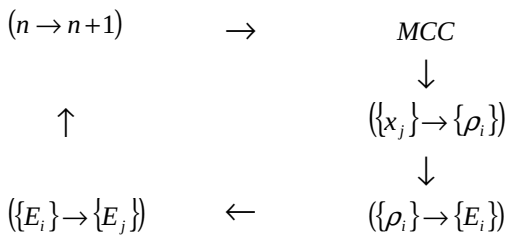

Figure 14: Flowchart of the PIC MCC computational cycle.

For a more detailed introduction to PIC MCC simulations see *Bibliography* [45, 47, 49].

2.1.4 Simulation Accuracy Constraints

One of the three basic computational constraints to ensure physical relevance and accuracy involves an upper limit on the cell size, in proportion to the Debye length (λ_D). λ_D is inversely proportional to the square root of the electron density, since charge screening occurs over a smaller distance when the plasma is denser i.e. when there are more charges in closer vicinity to screen each other. Higher plasma densities therefore imply shorter Debye lengths and hence require smaller cell sizes, which entails using more computational cells to divide up the resolved length. This provides the spatial resolution whereby the electrostatic field equations are solved over distances less than the Debye length, rather than over longer distances where charge screening pertains. The electron temperature also has a significant bearing on the required cell size. λ_D is proportional to the square root of the electron temperature, due to the fact that lower electron temperatures are more conducive to charge screening. Lower electron temperatures therefore produce smaller Debye lengths and thus require more cells per unit length. Quantitatively, all this can be summed up by one inequality, which states that the cell size (Δx) needs to be less than ~ half the Debye length:

$$\Delta x <\sim \frac{\lambda_D}{2} \tag{2.1}$$

Time-steps of the order of picoseconds are needed to simulate the fastest physical phenomena occurring in typical plasmas e.g. (electron) plasma oscillations. The second

constraint provides such sufficient temporal resolution, and requires the time-step (Δt) to be less than ~ a fifth of the reciprocal of the plasma frequency (ω_p):

$$\Delta t \omega_p <\sim 0.2 \tag{2.2}$$

One representative weight is chosen in each simulation to define the 'super-particle assumption' e.g. a weight of $1x10^{10}$ suggests that one simulated super-particle (3D simulation) adequately represents the physics of this number of real particles. The third computational constraint relates to the number of these super-particles per cell. This constraint ensures a realistic simulation of a plasma, which must have a sufficient number of particles within a Debye sphere (*Section 1.5.3*) i.e. a sufficient number of super-particles per cell (*N)* to adequately model charge screening phenomena:

$$N >> 10 \tag{2.3}$$

While the three aforementioned simulation accuracy constraints are not rigid numerical stability requirements, in the event of a cell size, time-step, or super-particle number constraint being violated, non-physical effects may arise in the simulations e.g. non-physical heating of electrons when the cell size is too large [47]. Ideally, when Δx & Δt and N are decreased and increased respectively, beyond the above simulation accuracy constraints, no significant change should result in the simulation results. Although in practice, obtaining such strictly converged simulation results is sometimes unfeasible due to time constraints imposed by limited computational speed and number of computers (these restrictions certainly compromised the quality of this investigation). Furthermore, the inclusion of Monte Carlo collisions has been found to tighten these constraints [50]. Hence a compromise is usually made between physical fidelity and computational expense i.e. achieving an adequate solution within a reasonable time.

A further constraint (usually covered by the time-step accuracy constraint specified above) is required for numerical stability. It demands that even the fastest particle (velocity, v_{max}) must not travel a distance greater than the cell size in one time step. This is called the Courant-Fredrichs-Lewy (CFL) condition [45]:

$$v_{\max} \Delta t \leq \Delta x \tag{2.4}$$

2.2 Beam Plasma 1D3v PIC MCC Simulations

2.2.1 Description of the Beam Plasma Model

The simulation code (containing strictly conforming C and trivial C++ computer programming languages, cf. attached CD) is an adapted version of the "en" electrostatic plasma 1D3v PIC MCC simulation code composed by Miles Turner. A comparison of this code with other similar plasma simulation codes has been published [51]. Herein PIC and MCC computational techniques are used in unison to simulate the continuous propagation of a hydrogen beam through a H_2 gas neutraliser. The beam is assumed to have a top-hat density & velocity spatial profile with a rectangular beam head area of $0.064m^2$ (0.16m x 0.40m), centred in a neutraliser cell of dimensions: 0.20m, 0.44m, 1.86m (0.86m 1^{st} stage neutraliser, 1m 2^{nd} stage), horizontal/transverse (x), vertical (y), axial/longitudinal (z), neutraliser/beam dimensions, respectively. The neutraliser gas is assumed to have a uniform temperature (300K) & (horizontal) pressure/density profile, and an axial pressure/density profile similar to *Figure 10, Section 1.3.2*.

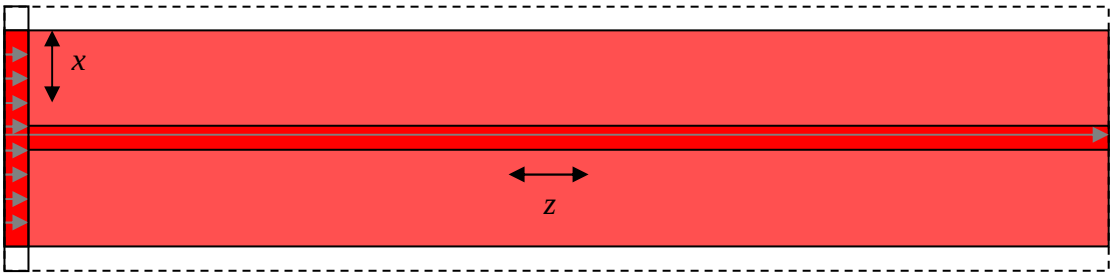

*Figure 15: A plan view schematic of the first stage neutraliser (to scale), showing the Longitudinal and Transverse simulation model approaches (the grey arrows indicate the beam direction within the **dark** red space showing the **respective 1D** beam region**s**).*

The 3D physics of the neutraliser can be reduced to a 2D problem (*Figure 15*), since the vertical dimension (y) is effectively 'redundant' due to symmetry. While the development of a full 2D simulation is beyond the scope of this investigation, *Longitudinal* and *Transverse* electrostatic 1D3v PIC MCC simulations are employed to provide a quasi-2D beam (& beam plasma) characterisation i.e. along (z) and perpendicular (x) to the beam direction, respectively. Both 1D3v simulations namely entail only one spatial degree of freedom for each super-particle, although their full 3D velocity vectors are consistently calculated at each time step, cf. *Section 2.1*.

In *Longitudinal* simulations (*Figure 15*), the beam is constantly injected at one end of the 1D resolved length (neutraliser axial dimension) towards the other (grounded wall). The only sink for beam plasma particles is at either end, which means that unless a sufficiently accurate particle loss mechanism is implemented to mimic the (transverse) loss of particles at the neutraliser walls, this method is not capable of accurately quantifying the beam plasma behaviour. However, it can be used to characterise any beam plasma changes in the beam direction, along the centre of the 1st stage neutraliser (full neutraliser length simulations are not performed due to their excessive computational expense and the difficulty in modelling the varying 2nd stage neutraliser gas pressure). *Section 2.2.3* shows how this *Longitudinal* simulation approach can provide a beam (& beam plasma) characterisation as a function of the 1st stage neutraliser axial position. Unlike *Longitudinal* simulations, *Transverse* simulations (*Section 2.2.4*) are capable of resolving the beam plasma sheath, and are henceforth employed to quantitatively model the neutraliser beam plasma system.

In *Transverse* simulations an adaptation to the "en" code is necessary in order to simulate a spatially-fixed beam travelling in a direction perpendicular to the resolved length (*Figure 15*). This beam-neutraliser simulation model thus consists of a constant density (while allowing for beam compositional changes via beam collisions with the neutraliser gas) & velocity top-hat beam spatial profile (beam width of 0.16m) centred in the 1D resolved length (neutraliser horizontal width of 0.2m), with grounded boundaries at each end (representing the neutraliser walls). *Section 2.2.4* describes how this *Transverse* simulation approach can be used to investigate the beam (& beam plasma) behaviour as a function of time and 2D space (x, z).

In *both* simulation approaches, the 1D resolved length is divided into thousands of cells (depending on the expected beam plasma Debye length), while the other key defining simulation parameters i.e. the time-step and the super-particle number/weight are also chosen to satisfy the accuracy constraints (*Section 2.1.4*). The neutraliser gas (density of the order of thousands times that of the plasma) is modelled as a fixed, uniform density & temperature background gas, while its empirical axial pressure profile (*Figure 10, Section 1.3.2*) is taken into account in all volume-averaged calculations (*Section 5.1.3*).

Simulation diagnostics (e.g. particle densities) are calculated at interval time-steps (e.g. every 10000 time-steps) with cellular resolution (no. spatial data points = no. cells + 1),

and saved to the relevant data file . The MATLAB mathematical software package is used to plot and analyse these results e.g. the electron temperature is calculated from the electron thermal-energy-density diagnostic [49] assuming the equipartition of energy.

To separately track certain particles of the same species, they are labelled differently e.g. *beam* hydrogen atoms (bH) and *plasma* hydrogen atoms (fH, f5H, aH). In order to simulate the fast H/H^+ particles formed by dissociation collisions with kinetic energies: 2.2, 5, 10 eV [43, 34], a two-step model is used e.g. first step: e + H2 -> e + H2*****d with a certain positive threshold energy, second step: H2*****d -> fH + fH with a negative threshold energy, each fH receiving half this energy (*Section 2.2.2*). A similar two-step technique is employed to simulate any beam collision that produces more than two collision products (since the existing *Inelastic Forward* collision algorithm is limited to collisions comprising of two reactants and two products, *Section 2.2.2*).

The gas heating caused by the fast particles is calculated from power density transfer calculations, using additional computational procedures (composed in MATLAB) to integrate the kinetic energy transferred (from fast particle elastic collisions with the neutraliser gas) and the corresponding rate coefficients $\{\sigma(E)v(E)\}$ over the particle energy distributions (*Section 5.1*). The gas heating contribution of all tracked particles can thus be determined. For example, the (direct) electron contribution (overlooked by Pamela) is found to be significant, as a result of their relatively high density and kinetic energy, despite their relatively low percentage energy transfer (due to their mass being much less than that of the neutraliser gas molecules).

The Hydrogen beams in the JET NBIs initially consist of H^+, H_2^+, and H_3^+ full energy (E) ions. H_3^+ (E) beam ions can dissociate into H_2^+ (2E/3), H_2 (2E/3), H^+ (E/3), and H (E/3) beam particles, while H_2^+ (E) {2E/3} beam ions can dissociate into H^+ (E/2) {E/3} and H (E/2) {E/3} beam particles. Complete cross section data for high energy (of the order of hundreds of keV) H_2^+ and H_3^+ collisions with the neutraliser gas (e.g. important plasma forming collisions) is not presently available (to the best of our knowledge). Hence, the *beam plasma* simulations do not account for the plasma forming collisions of the full ensemble of beam component species. Instead, *beam plasma* simulations are run with a beam initially consisting of 100% protons, with charge-changing collisions only allowing one other possible beam species to exist, namely that of neutral hydrogen atoms (as in the two-component beam model, *Section 1.3.1*). Although, results from

beam composition simulations involving 11 distinct beam components, encompassing 5 different beam species (H_3^+, H_2^+, H_2, H^+, H) are also presented (*Section 4.1*), wherein only beam composition-changing collisions are simulated.

2.2.2 List of particles and their collisions

label	description	mass (kg x 10^{-27})
H2	*background gas H_2 molecule*	*3.34706*
bH+	beam proton	1.67262
bH	beam hydrogen atom	1.67353
bH*****es	intermediate bH prior to electron stripping	1.67353
e	electron	0.00091
f5H+	H^+ ion formed with kinetic energy of 5eV	1.67262
f10H+	H^+ ion formed with kinetic energy of 10eV	1.67262
H2+	H_2^+ ion	3.34615
H2+*****d	intermediate H_2^+ prior to dissociation	3.34615
H3+	H_3^+ ion	5.01968
aH	hydrogen atom formed via H_3^+ formation	1.67353
fH	hydrogen atom formed with kinetic energy of 2.2eV	1.67353
f5H	hydrogen atom formed with kinetic energy of 5eV	1.67353
xH2	H_2 molecule formed from H_2^+ charge exchange	3.34706
rxH2	H_2 molecule formed by xH2 reflection at either wall	3.34706
rnH2	H_2 molecule formed by H_2^+ recombination & reflection	3.34706
H2*****d	intermediate H_2 prior to dissociation	3.34706
H2*****i	intermediate H_2 prior to ionisation	3.34706
H2*****di	intermediate H_2 prior to dissociative ionisation	3.34706
H2*****ddi	intermediate H_2 prior to dissociative double ionisation	3.34706

Collision threshold energies are in brackets (eV), cross sections are on attached CD:

(I) Beam Collisions

*proton beam collisions (IF) **

bH+	elastic	bH+ + H2 -> bH+ + H2	[52, 53]
bH+ (8.900)	dissociation	bH+ + H2 -> bH+ + H2*****d	[34]
bH+ (23.100)	ionisation	bH+ + H2 -> bH+ + H2*****i	[52, 54]
bH+ (52.500)	dissociative ionisation	bH+ + H2 -> bH+ + H2*****di	[52, 53]
bH+ (75.600)	dissociative double ionisation	bH+ + H2 -> bH+ + H2*****ddi	[54]
bH+ (2.745)	electron capture	bH+ + H2 -> bH + H2+	[52, 53]
bH+ (11.645)	dissociative electron capture	bH+ + H2 -> bH + H2+*****d	[34]

*neutral hydrogen beam collisions (IF) **

bH	elastic	bH + H2 -> bH + H2	[52, 53]
bH (8.900)	dissociation	bH + H2 -> bH + H2*****d	[34]
bH (23.100)	ionisation	bH + H2 -> bH + H2*****i	[52, 54]
bH (52.500)	dissociative ionisation	bH + H2 -> bH + H2*****di	[54]
bH (75.600)	dissociative double ionisation	bH + H2 -> bH + H2*****ddi	[54]
bH (13.600)	electron stripping	bH + H2 -> bH*****es + H2	[54]
bH (66.100)	electron stripping with dissociative ionisation	bH + H2 -> bH*****es + H2*****di	[54]
bH (89.200)	electron stripping with dissociative double ionisation	bH + H2 -> bH*****es + H2*****ddi	[54]

(II) Plasma Collisions

electron collisions (I) *

e	elastic *(E)* *	e + H2 -> e + H2	[52]
e (8.900)	dissociation	e + H2 -> e + H2*****d	[53]
e (15.400)	ionisation	e + H2 -> e + H2+ + e	[52]
e (18.000)	dissociative ionisation	e + H2 -> e + H2*****di	[53]

H_2^+ collisions (I) *

H2+	elastic *(E)* *	H2+ + H2 -> H2+ + H2	[53]
H2+ (0.000)	charge exchange	H2+ + H2 -> xH2 + H2+	[52]
H2+ (-3.420)	association	H2+ + H2 -> H3+ + aH	[53, 52]

H_3^+ collisions (E) *

H3+	elastic	H3+ + H2 -> H3+ + H2	[52]

H^+ collisions (E) *

f5H+	elastic	f5H+ + H2 -> f5H+ + H2	[52]
f10H+	elastic	f10H+ + H2 -> f10H+ + H2	[52]

H collisions (E) *

aH	elastic	aH + H2 -> aH + H2	[52]
fH	elastic	fH + H2 -> fH + H2	[52]
f5H	elastic	f5H + H2 -> f5H + H2	[52]

H_2 collisions (E) *

rnH2	elastic	rnH2 + H2 -> rnH2 + H2	[53]
xH2	elastic	xH2 + H2 -> xH2 + H2	[53]
rxH2	elastic	rxH2 + H2 -> rxH2 + H2	[53]

(III) Second Step 'Collisions' *(D)* *

"bH*****es -> bH+ + e"	(0.000)
"H2+*****d -> f5H + f5H+"	(-10.000)
"H2*****d -> fH + fH"	(-4.400)
"H2*****i -> H2+ + e"	(0.000)
"H2*****di -> f5H + f5H+ + e"	(-10.000)
"H2*****ddi -> f10H+ + f10H+ + e + e"	(-20.000)

*: The simulation uses the following four set types of 'collision' handlers:
Elastic (E), Inelastic (I), Inelastic Forward (IF), and *Decay (D).*

The conservation of energy and momentum apply to all collisions, while in elastic collisions the kinetic energy is also conserved.

Elastic and *Inelastic* collision handlers entail isotropic scattering distributions, and are the choice collision handler for all electron and other plasma particle collisions.

The *Inelastic Forward* collision handler is chosen for all beam collisions, and entails no beam scattering i.e. all beam particles continue in the same direction after the collision. This collision treatment is deemed to be of sufficient physical fidelity to real beam collisions; where beam particles undergo only slight scattering of the order of milli-radians [55], with other product particles exhibiting various anisotropic scattering distributions cf. experimentally determined electron scattering distributions [56, 57].

Decay 'collisions' differ from all the other collision types in that they are defined by a fixed decay frequency, rather than by (energy dependent) cross sections. This 'collision' type is adopted as the second step in all two-step collisions, i.e. by choosing a maximum allowable decay frequency (determined by the simulation time-step), the second step occurs virtually simultaneously with the first step, thereby adequately mimicing what any ideal one-step collision treatment would produce.

The adapted "en" code is also capable of simulating Coulomb collisions among charged particles of same/different species. In addition to simulating the collision phenomena occurring in the neutraliser volume, the process whereby H_2^+ ions (H2+) are both neutralised and reflected as H_2 molecules (rnH2) at the neutraliser walls are also

simulated, and similarly whereby charge-exchanged H_2^+ ions (xH2) get reflected as rxH2 particles (both subsequently contribute to gas heating). The Implementation of these processes entails assuming a fixed neutralisation &/or reflection coefficient of 0.6, along with a common energy loss coefficient of 0.5. Both coefficients are assumed to be independent of the energy of the impacting H2+/xH2 particle. The values of 0.6 and 0.5 are in agreement with the composite coefficient of 0.3 (0.6 x 0.5) assumed by Paméla [31, 34] to account for neutralisation, reflection, and energy loss [58, 59].

The main beam plasma characterisation *Transverse* simulations (*Chapter 4*) investigate 3 different neutraliser H_2 gas densities ($3x10^{19}m^{-3}$, $6x10^{19}m^{-3}$, $9x10^{19}m^{-3}$) and 3 different proton beam energies/currents (80keV/27A, 120keV/50A, 134keV/60A, corresponding to specific current-voltage optimum beam perveances cf. *Section 3.1*), and thus 3 different beam powers (2.16MW, 6.00MW, 8.04MW, respectively). The simulation input file (sample on attached CD) requires that beam energies/currents are translated into beam velocities and densities. For example, the 80keV/27A proton beam has a velocity of $3.915x10^6 ms^{-1}$ $\{m_p v_p^2/2 = 80keV\}$, a flux of $2.633x10^{21}m^{-2}s^{-1}$ $\{|e|f_p(0.16m)(0.4m) = 27A\}$, and thus a beam density of $6.725x10^{14}m^{-3}$ $\{f_p = n_p v_p\}$, where m_p is the proton mass (~ $1.67262x10^{-27}$kg), $|e|$ is the absolute value of the 'elementary' charge (~ $1.6022x10^{-19}$C) , f_p is the proton beam flux, and v_p is the proton beam velocity (the latter two parameters being vector quantities in the beam direction).

2.2.3 Longitudinal Simulation Approach

As derived in the two-component hydrogen beam model {Equation (1.3), *Section 1.3.1*} ; the neutral beam fraction is usually expressed as: $F_0 = F_0^\infty (1 - e^{-(\sigma_{01}+\sigma_{10})\Pi})$

It can also be expressed as a function of the neutraliser axial position (z), for a constant neutraliser H_2 gas density (n_{H2} represents the average density i.e. the integral of the real neutraliser density versus position profile over the first 1.86m divided by 1.86m):

$\Pi = n_{H_2} z \Rightarrow$ $\quad F_0 = F_0^\infty (1 - e^{-[(\sigma_{01}+\sigma_{10})n_{H_2}]z})$ (2.5)

3 beam (80keV/27A) attenuations: $F_0 = F_0^\infty (1 - e^{-3}) \approx \frac{\sigma_{10}}{\sigma_{01}+\sigma_{10}}(0.95) \approx 0.3$

resulting in a neutral beam density of: $n_{bH} = 0.3(6.725x10^{14} m^{-3}) \approx 2.026x10^{14} m^{-3}$

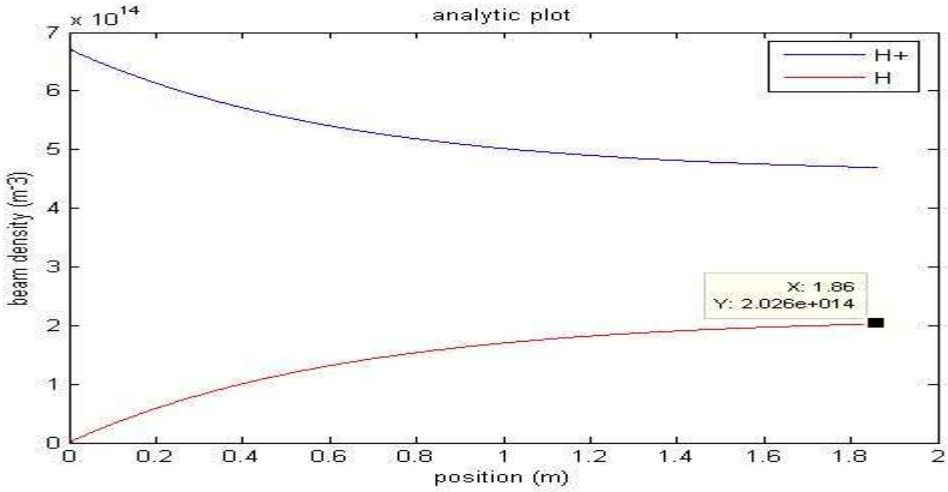

Figure 16: 80keV/27A H^+/H densities as a function of the H_2 neutraliser axial position.

The *beam* species fractions from a 1D3v *Longitudinal* simulation {at 'optimum' H_2 gas density, $9x10^{19}m^{-3}$ cf. Equation (2.7), *Section 2.2.4*} over a distance of 0.86m (length of the first stage neutraliser) are shown in *Figure 17*. Despite the noisy results (unphysical noise caused by having relatively few super-particles per cell), the simulated beam density as a function of position, closely follows the analytical solution.

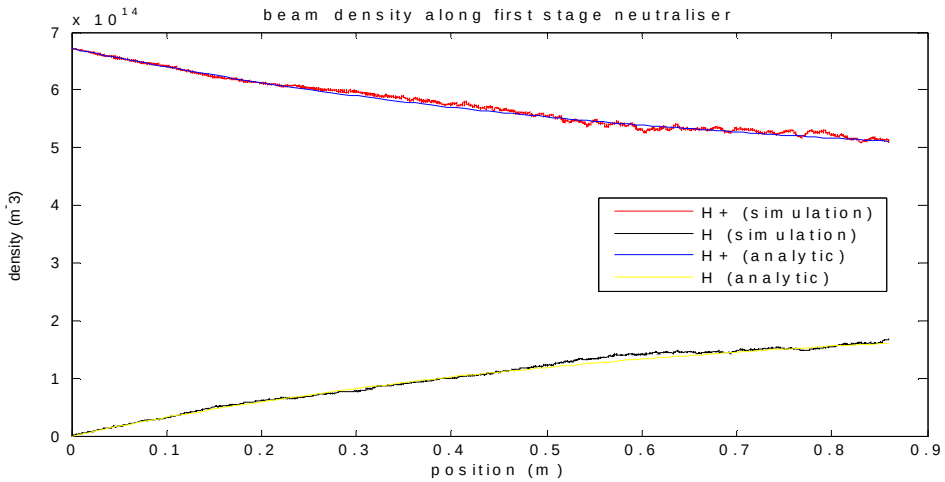

Figure 17: Simulation & analytic results comprising 80keV/27A Hydrogen beam component densities as a function of the H_2 (1^{st} stage) neutraliser axial position.

The same *Longitudinal* simulation (*Figure 17*) can also characterise the *beam plasma* behaviour. The charged particle density (longitudinal) spatial results shown in *Figure 18* {the (blue) total positive charge density overlaps the (red) electron density, due to plasma quasineutrality} imply that the character of the beam plasma, along the 1^{st} stage neutraliser, does not change significantly enough to warrant a full 2D characterisation.

The grounded wall boundary conditions seem reasonable electrostatically {neutral grid at start of 1st stage neutraliser (*Figure 7, Section 1.2.3*) and quasineutral plasma at end}. The slightly increasing electron and H_2^+ density profiles are due to the fact that the plasma particles formed via beam collisions are not formed isotropically in space, but rather with a forward scattering bias. The neutralisation of the beam along this axial length has a negligible bearing on such profiles, as can be seen from *Figure 19*. Recalling the full neutraliser pressure profile (*Figure 10, Section 1.3.2*); the linear decreasing pressure profile in the 2nd stage is kept relatively constant by the vacuum pumping, and is not thought to lead to any significant axial plasma flow.

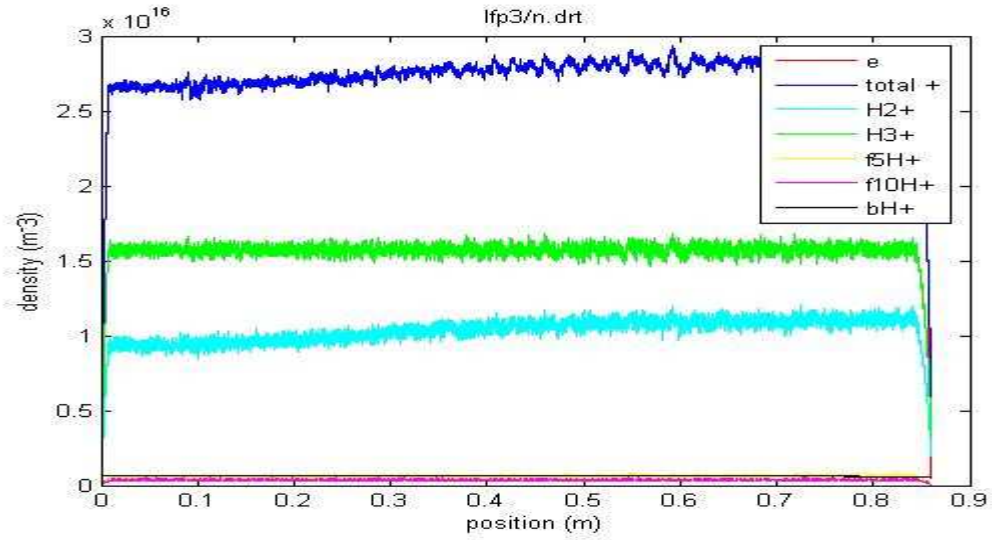

Figure 18: Longitudinal profile of the charged particle densities.

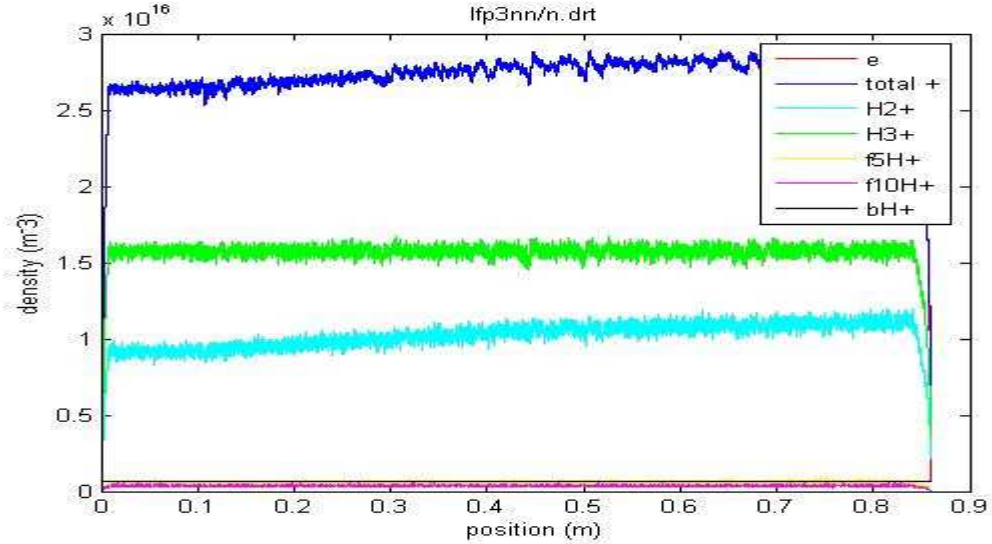

Figure 19: Longitudinal profile of the charged particle densities {no beam charge-changing collisions}.

2.2.4 Transverse Simulation Approach

Similarly to *Section 2.2.3*, the neutral beam fraction can furthermore be expressed as a function of time, assuming a constant neutraliser H_2 gas density (n_{H2}):

$z = v_b t$, Equation (2.5) $\Rightarrow$ $\quad F_0 = F_0^{\infty}(1 - e^{-[(\sigma_{01}+\sigma_{10})n_{H_2} v_b]t})$ (2.6)

$v_b = 3.915e6 ms^{-1}, L = 1.86m \Rightarrow$ $\quad t = \frac{L}{v_b} \approx 0.475 \mu s$

3 beam (80keV/27A) attenuations: $\quad F_0 = F_0^{\infty}(1 - e^{-3}) \approx \frac{\sigma_{10}}{\sigma_{01}+\sigma_{10}}(0.95) \approx 0.3$

resulting in a neutral beam density of: $\quad n_{bH} = 0.3(6.725x10^{14} m^{-3}) \approx 2.027x10^{14} m^{-3}$

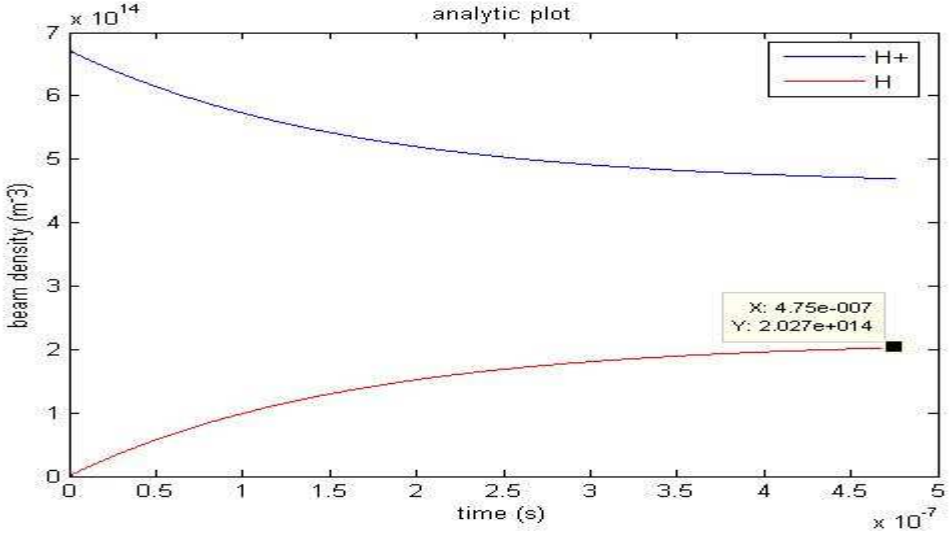

Figure 20: 80keV/27A H^+/H densities as a function of time.

As in *Section 2.2.3*, the constant (average) neutraliser H_2 gas density represents the integral of the real neutraliser density versus position profile over the first 1.86m divided by 1.86m, and its 'optimum' value {i.e. that which causes 3 beam attenuations (~ 95% maximum neutralisation) within the 475ns it takes for a 80keV proton to traverse the full neutraliser length of 1.86m} is chosen as the (fixed) neutraliser H_2 gas density in the following 1D3v *Transverse* simulations:

Equation (2.6) $\Rightarrow$ an 'optimum' density of: $\quad n_{H_2} = \frac{3}{(\sigma_{01}+\sigma_{10})v_b t} \approx 9x10^{19} m^{-3}$ (2.7)

{$\sigma_{01} \cong 0.56x10^{-20}m^{-2}$ and $\sigma_{10} \cong 1.20x10^{-20}m^{-2}$ for a 80keV Hydrogen beam [60]}

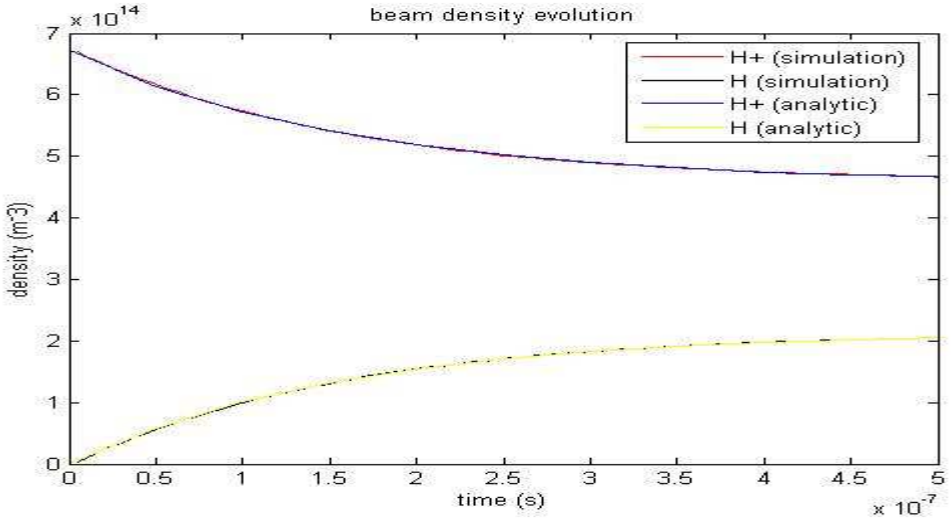

Figure 21: Simulation & analytic results comprising 80keV/27A H^+/H densities as a function of time {initial H^+ injection into a H_2 neutraliser gas of density $9x10^{19}m^{-3}$}.

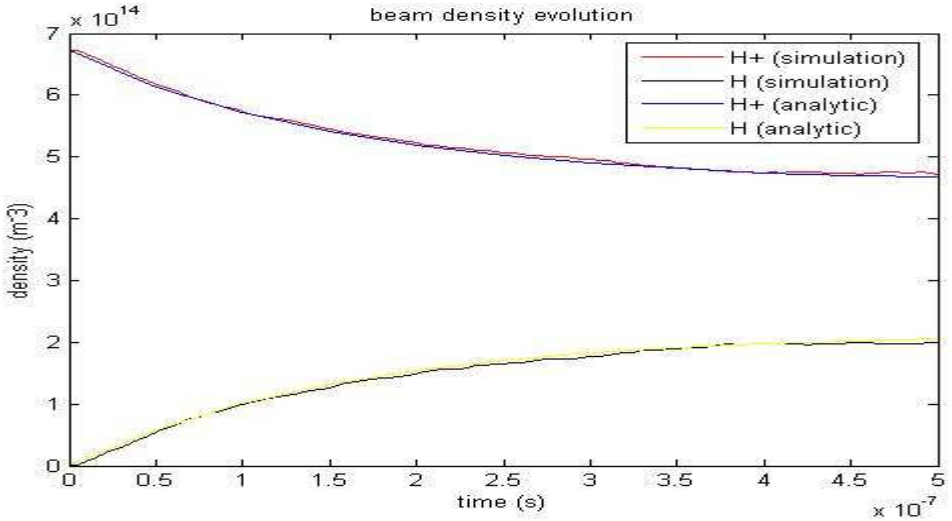

Figure 22: Simulation & analytic results comprising 80keV/27A H^+/H densities as a function of time (neutraliser axial position, gas target) {H^+ re-injection into a steady-state Hydrogen neutraliser beam plasma, initial gas density of $9x10^{19}m^{-3}$}.

Note that in *Figure 21*, the beam plasma is in the early stages of formation, yet since the beam species fractions depend only on the beam & gas parameters, the situation remains the same at steady-state (*Figure 22*). The beam species fractions as a function of time (*Figure 21*), exhibit the same behaviour as a function of neutraliser axial position in similar *Longitudinal* simulations (*Figure 17, Section 2.2.3*), consistent with the accuracy of their common analytic solutions (*Section 1.3.1*). Hence, in regards to the *beam* behaviour, this shows that the time dimension in *Transverse* simulations can represent the neutraliser axial position and the neutraliser gas target. Here for example

(*Figure 21*); 475ns corresponds to 1.86m and $1.674 \times 10^{20} m^{-2}$ (the 'optimum' gas target i.e. $9 \times 10^{19} m^{-3}$ x 1.86m). This *interchangeable variables* technique is employed in *Sections 4.1, 4.2, 5.1.5, 6.1.2* & *6.1.3*.

Furthermore, the same *Transverse* simulation (*Figure 21*) can somewhat help to elucidate the *beam* '*plasma*' behaviour as a function of time (*Appendix B* contains more early evolution beam 'plasma' parameter plots) and the neutraliser *axial* position:

(a)

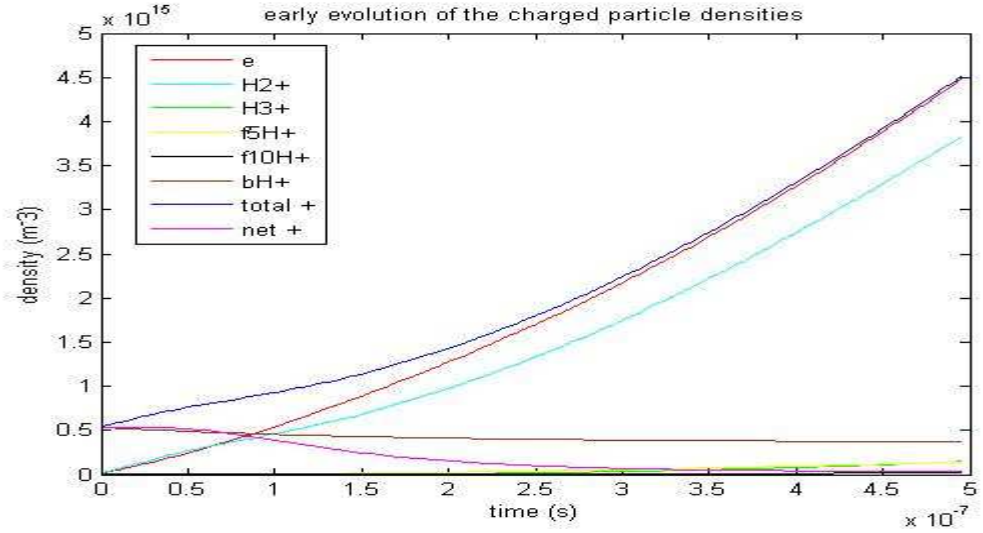

(b)

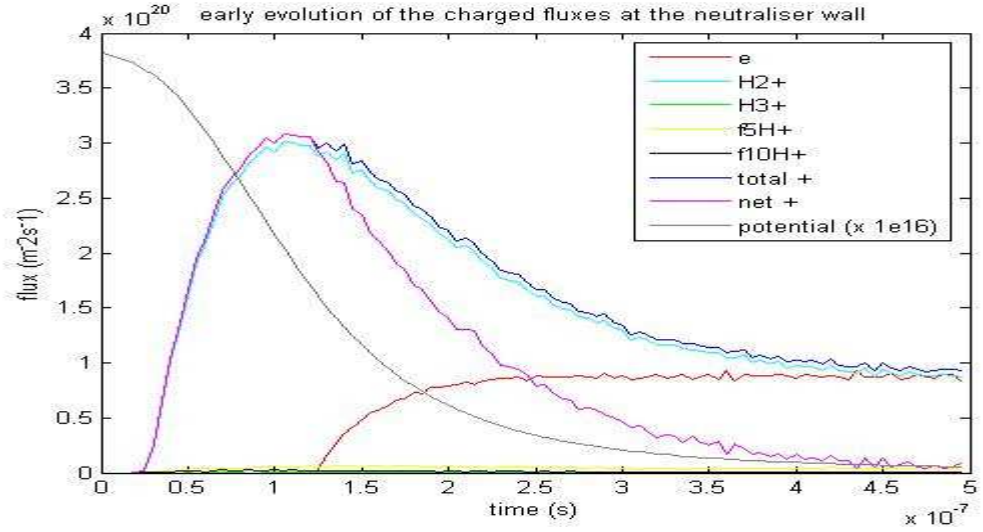

Figure 23: (a) Spatially averaged charged particle density evolution, (b) charged particle flux evolution at the neutraliser walls, and the (scaled up) plasma potential.

Initially, proton beam (positive ion) injection into the (neutral gas) neutraliser obviously provides a net positive charge density therein. The beam (bH+) neutralisation (electron capture) process produces a further (localised) net positive charge density in the

neutraliser, in the form of H_2^+ ions, since the captured electrons move off with the beam velocity. This is evident in *Figure 23 (a)*, where the net+ density is greater than the bH+ density for the first ~ 70ns, while a relatively quick plasma response leads to the ejection of the excess H_2^+ ($/H_3^+/H^+$) ions (*Figure 23 (b)*), eventually resulting in ~ zero net+ density (and flux) after ~ 475ns. This localised excess positive charge decreases also via the 'simultaneous' production of a localised net negative charge from beam (bH) re-ionisation (electron stripping) collisions, albeit a relatively small effect due to the greater bH+ density (*Figure 21*), despite the more favourable cross sections for bH re-ionisation at this (80keV) energy (*Figure 11 (b)*, *Section 1.3.4*).

Along with an ejection of excess positive charge (initially consisting of H_2^+ ions originating either from beam neutralisation collisions or from beam/electron impact ionisations i.e. prior to significant H_3^+/H^+ plasma particle formation), the large plasma potential (mainly provided by the beam space-charge) also causes an initial confinement of electrons (*Figure 23 (b)*). After ~ 125ns, some electrons (in the tail of the electron energy distribution function) have enough kinetic energy to overcome the (decreasing) plasma potential, and can thus escape to the neutraliser walls. Soon afterwards, at ~ 475ns (1.86m), the beam reaches dynamic charge-equilibrium (cf. *Figure 21*) i.e. when electron capture by bH+'s balances electron stripping of bH's, resulting in an orthodox quasineutral plasma situation (no localised excess charge), where the negative flux at either wall equals the positive flux (*Figure 23 (b)*).

Figure 23 (b) can also shed some light on the net+ flux behaviour (net current profile) at either wall as a function of the neutraliser *axial* position. Although *Figure 23 (b)* certainly wouldn't accurately resemble the steady-state charged particle fluxes versus neutraliser axial position {e.g. the initial zero electron flux at both walls (always nonzero at steady-state), and the continuing positive flux compositional changes (constant at steady-state)}, the net+ flux versus time profile from the ~ 125–(600) ns, is indicative of the real net+ flux versus neutraliser axial position profile during dynamic steady-state. This is because the amount of net excess charge (from electron capture/stripping collisions - Surrey's beam plasma models didn't include the latter collisions [22]) dumped to the neutraliser walls, depends only on the beam & gas parameters (i.e. not on the plasma parameters, even though the plasma potential and other plasma parameters change with time up to a dynamic steady-state). Moreover, in the presence of no significant axial electric fields (significant axial plasma flow has

already been ruled out by the simulation results outlined in *Section 2.2.3*), it is reasonable to assume that the net+ (plasma) charge responds only to transverse electric fields, hence resulting in plasma fluxes entirely perpendicular to the beam.

Transverse simulations can more accurately quantify the neutraliser *beam plasma* behaviour as a function of the neutraliser *horizontal* position e.g. *Figures 24* & *25* show some plasma particle densities versus time and position, for 80keV/27A proton beam injection into a H_2 gas of density $9x10^{19}m^{-3}$. The top-hat beam profile (*Sections 2.2.1*) obviously results in no beam collisions in the 2cm regions either side of the beam, hence the substantial decrease in plasma densities therein (*Figures 24 & 25 (b)*), despite electron impact ionisation (*Tables 1* & *3*, *Section 4.4*), plasma diffusion and drift.

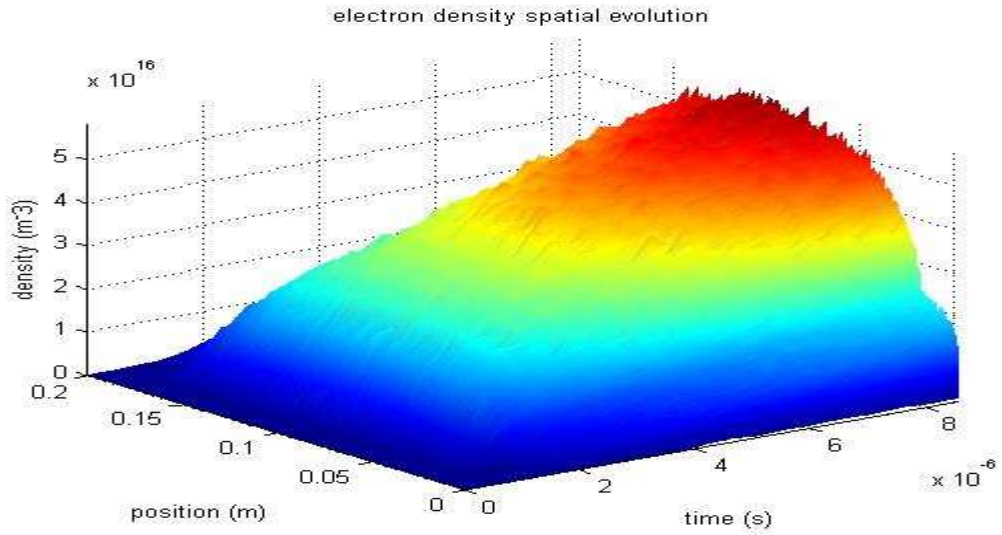

Figure 24: Early spatial evolution of the electron density.

(a) (b)

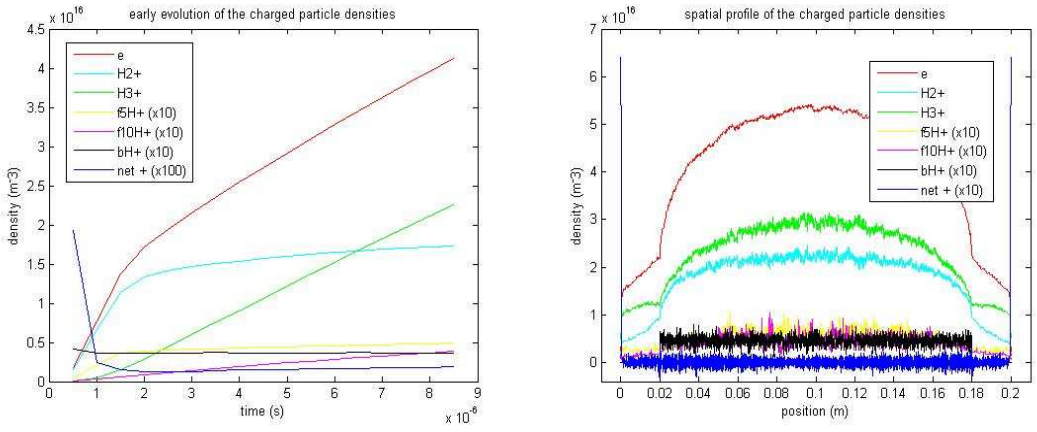

Figure 25: (a) Early evolution of the spatially averaged charged particle densities, and (b) their respective spatial profiles @ t = 8.0 μs.

Chapter 3

Proton Beam Space-Charge Effects

3.1 Chapter Overview

JET NBIs operate at specific I-V values pertaining to minimum beam (transverse) divergence (optimum beam perveance) at a given background gas pressure, which limits the total (longitudinal) beam current extraction from the ion source, at any given accelerating voltage. The Child-Langmuir law for non-relativistic charged particles [43, 61] quantifies such space-charge limited beam extraction, while these matters reside in the field of ion beam optics, involving important considerations such as beam steering, which can include the use of electrostatic fields to provide a divergent lenses effect [25].

Accurate beam neutralisation efficiency measurements rely upon accurate knowledge of beam transmission losses (due to nonzero beam temperature, beam aberrations & alignment/steering issues and beam space-charge effects) [27]. In this chapter, beam longitudinal and transverse space-charge effects are investigated via *Longitudinal* and *Transverse* (with unconstrained beam particle densities & velocities) proton *beam propagation in vacuum* simulations, respectively cf. *Chapter 2*. The *Longitudinal* and *Transverse* results consist of plots of the beam density & velocity as a function of position i.e. along and perpendicular to the beam axis, respectively.

In the *Longitudinal* simulations (*Section 3.2*), space-charge limited beam propagation effects are observed along this spatial dimension i.e. the beam protons slow down from their initial injection velocity and accumulate in-between the grounded boundaries, due to their mutual electric repulsion, resulting in a build-up of beam particles (positive charge) and a subsequent repelling of oncoming beam particles. This phenomenon is known as virtual anode behaviour, in a similar analogous fashion to the more commonly known virtual cathode (space-charge limiting beam propagation) effects associated with electron beam generation/propagation. In the *Transverse* simulations (*Section 3.3*), beam space-charge expansion (divergence) is observed. As in *Section 3.2*, the pure vacuum simulation conditions don't prevail in any real ion beam injectors since space-charge compensation {via primary (beam-gas) ionisation and secondary (e.g. electron-gas) ionisation} is a prerequisite for achieving reasonably good (relatively low emittance [61]) beam propagation. Moreover, the simulated beams have zero temperature. Hence the limitations in any experimental comparisons.

A similar overall analysis would equally apply to negatively charged beams [62].

3.2 Longitudinal Space-Charge Limiting Beam Propagation

3.2.1 Results under varying beam density

The effect of beam density on the beam (longitudinal) propagation is investigated, by performing simulations at three different (initial) beam densities (currents), at constant (initial) beam velocity. Where the beam density is high (in regions of space-charge accumulation), the corresponding velocity is low and visa-versa (*Figure 26*). The space-charge effects increase as the beam density increases, due to the greater Coulombic (mutual) repulsion between closer charges {In *Figures 26 – 28*, the beam propagation has reached a (dynamic) steady-state, whereby an ideal non self-interacting (space-charge neutral) beam would have a constant value density & velocity spatial profile}.

(a)

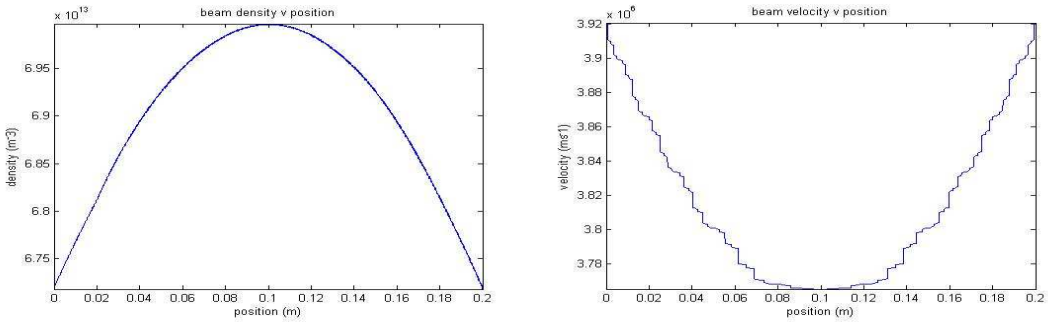

(b)

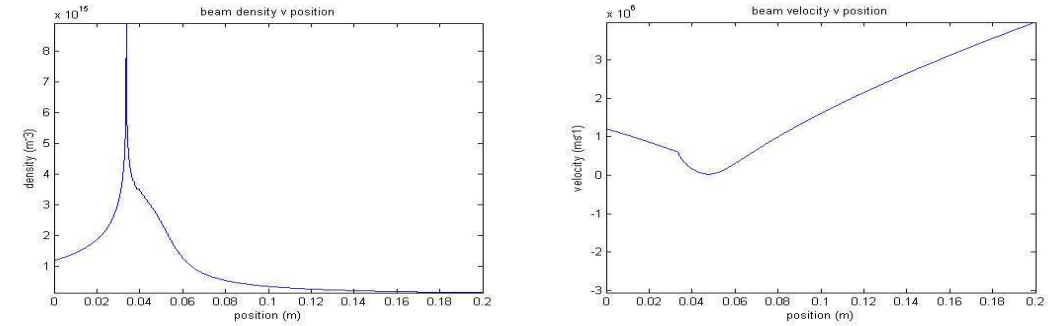

(c)

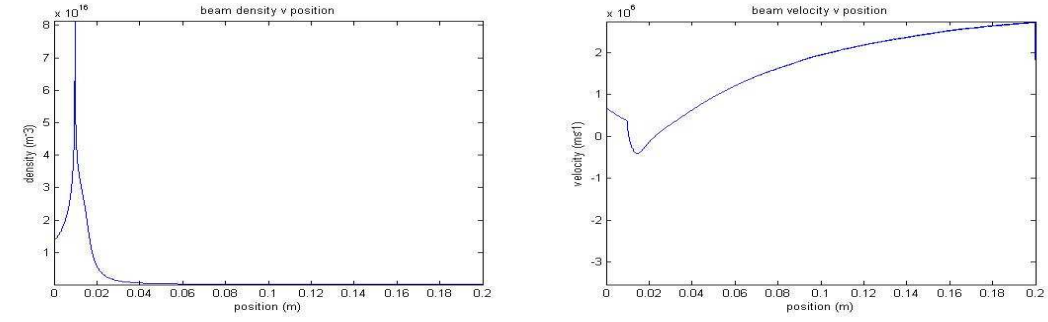

Figure 26: Beam density & velocity spatial profiles at beam densities; (a) 6.722x10^{13}m^{-3} (80keV/2.7A), (b) 6.722x10^{14}m^{-3} (80keV/27A), (c) 6.722x10^{15}m^{-3} (80keV/270A).

3.2.2 Results under varying beam velocity

For constant (initial) beam density, the (initial) beam velocity is varied (therefore also varying the initial beam current). The resulting beam propagation is more ideal at higher currents (*Figure 27*), which is opposite to the trend in *Section 3.2.1*. This is due to the fact that the beam space-charge effects are less at higher beam velocities, e.g. in the 800keV/270A case (*Figure 27 (c)*), the beam propagation is virtually unhindered.

(a)

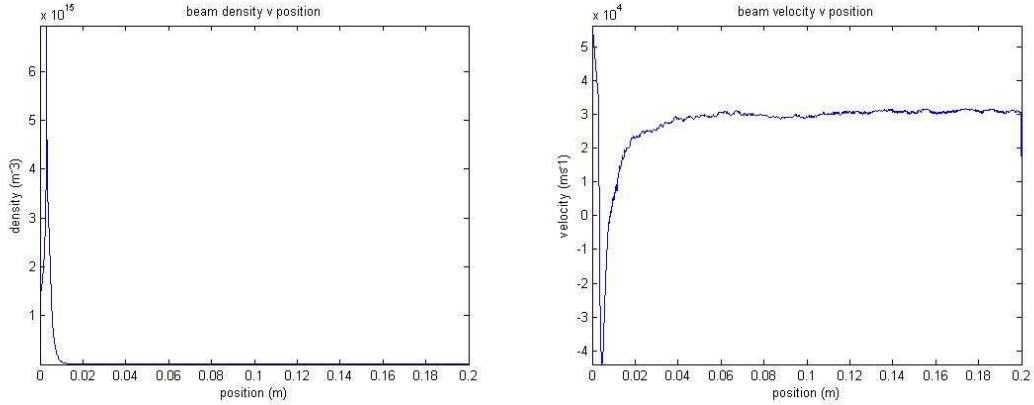

(b)

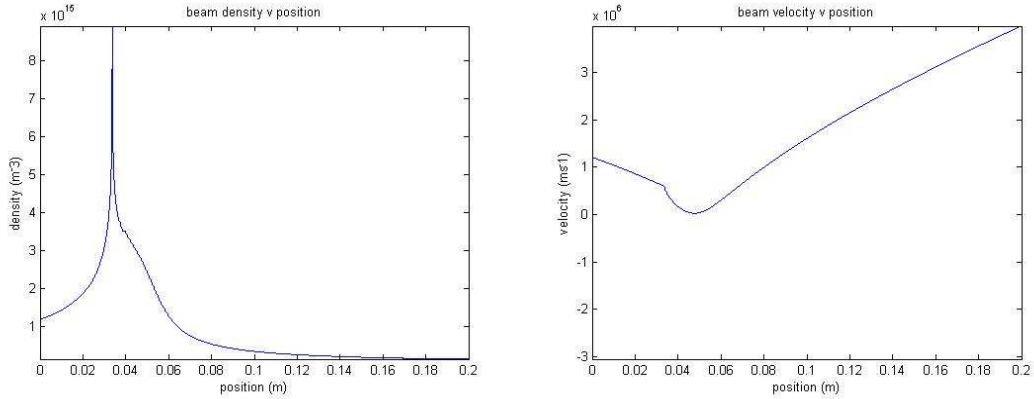

(c)

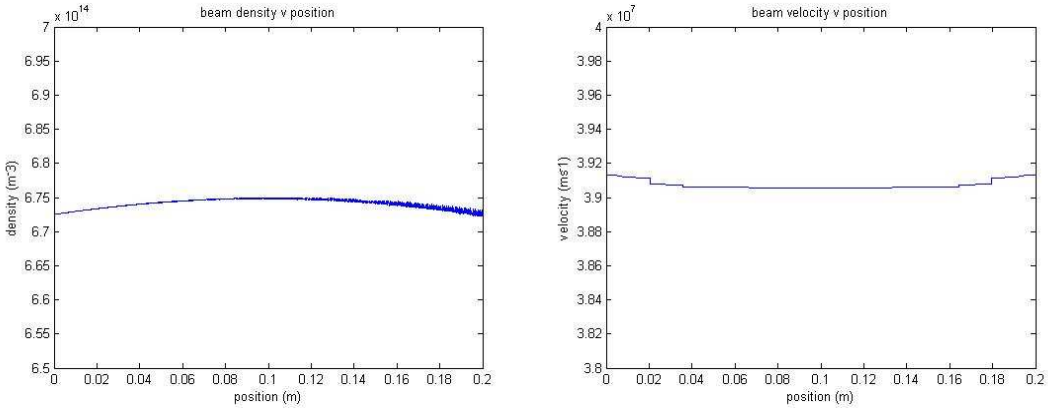

Figure 27: Beam density & velocity spatial profiles at beam velocities; (a) 3.918x10^5 ms^{-1} (8keV/2.7A), (b) 3.918x10^{6}ms^{-1} (80keV/27A), (c) 3.918x10^{7}ms^{-1} (800keV/270A).

3.2.3 Results for a constant beam current

At constant (initial) beam current, the space-charge effects decrease as the (initial) beam density decreases (*Figure 28*) due to the coupled behaviour of this decrease in (initial) beam density and the simultaneous increase in (initial) beam velocity (both effects are independently investigated in *Sections 3.2.1 & 3.2.2*, respectively). In the 800keV case (*Figure 28 (c)*), beam space-charge limiting effects are effectively non-existent.

(a)

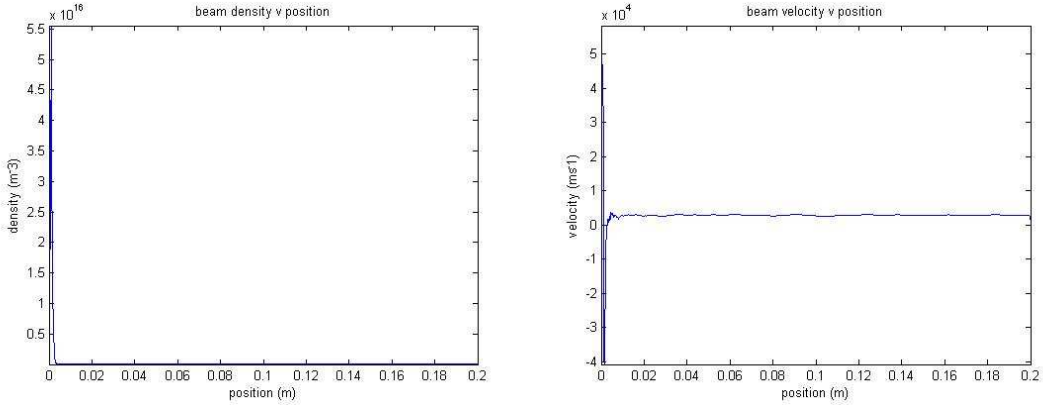

(b)

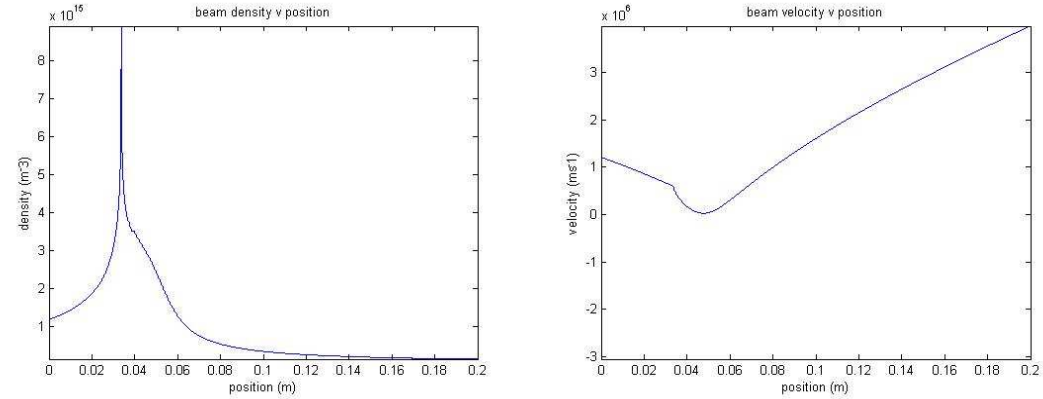

(c)

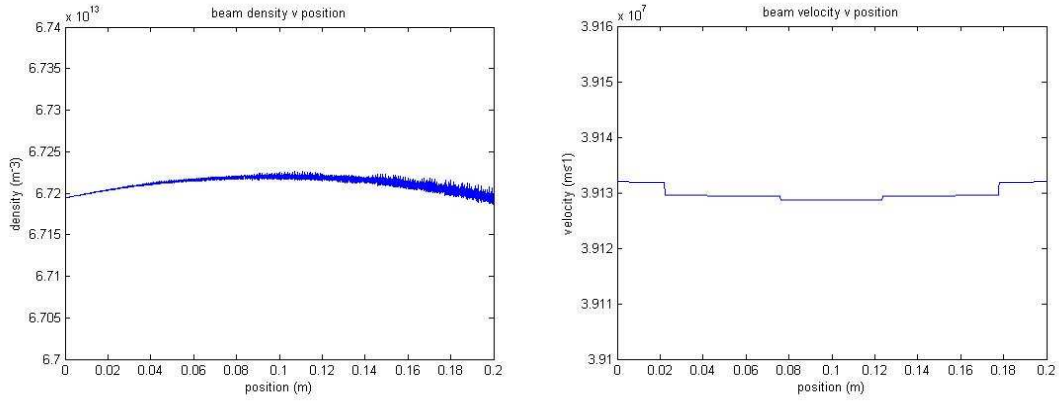

Figure 28: Beam density & velocity spatial profiles at beam densities; (a) 6.722x10^{15}m^{-3} (8keV/27A), (b) 6.722x10^{14}m^{-3} (80keV/27A), (c) 6.722x10^{13}m^{-3} (800keV/27A).

3.2.4 Conclusions and General Remarks

Knowledge of beam current alone is insufficient to predict the scale of (longitudinal) space-charge limited beam propagation effects (*Sections 3.2.1 - 3.2.3*). Typical particle beam textbooks [61] state that the beam current is the defining parameter that determines the degree of space-charge limited beam propagation, mentioning two crucial current limits. The first limit (in order of increasing beam current) concerns electrostatic effects, where, above this value, space-charge neutralisation is required. This occurs when the electrostatic potential energy exceeds the beam kinetic energy (i.e. at relatively high beam densities and/or relatively low beam velocities, as evidenced in *Sections 3.2.1 - 3.2.3*) and the beam propagation thus becomes space-charge limited. The magnitude of this effect is reduced in the presence of oppositely charged particles, which provide the space-charge neutralisation. The second limit is due to self-magnetic effects, where, above this limit, the self-magnetic field energy exceeds the beam kinetic energy. Current neutralisation is then also required for maximum beam flow, while it would be necessary to know both the beam density and velocity (i.e. not just the current density), in order to predict the extent of any self-magnetic limiting beam propagation.

The self-magnetic field (B) due to a 27A (I) proton beam, at transverse positions equal to the beam radius of 8cm (r), is ~ 0.68G {$B(2\pi r) = \mu_0 I$ (Ampere's law cf. [61]), where μ_0 is the permeability of free space}, which is sufficiently small to have a negligible effect on the beam (and plasma). Hence, the beam currents encountered in JET NBIs are small enough to rule out significant self-magnetic effects {the phenomenon of beam pinching (convergence) is often seen in many electron beam sources i.e. a given accelerating voltage produces a relatively high velocity, due to their relatively low mass, which is also the reason for their relatively better response to the resulting (self-focusing) self-magnetic fields - in such cases, both space-charge neutralisation and current neutralisation are required for unhindered electron beam propagation [61]}.

Space-charge limited beam propagation effects can cause undesirable beam optics (again, the magnitude of which depends on both the beam density and velocity), and are very sensitive to the background gas pressure (source of space-charge neutralising electrons). Thankfully these effects are minimal in the JET NBIs due to the high accelerating electric fields set up by the large voltage biases on the accelerating grids, and the sufficiently high gas pressures in these regions.

3.3 Beam Transverse Space-Charge Expansion

This section investigates beam space-charge effects in the beam transverse dimension. The following *Transverse* simulation results quantify the resultant beam divergence:

3.3.1 Results under varying beam density

(a)

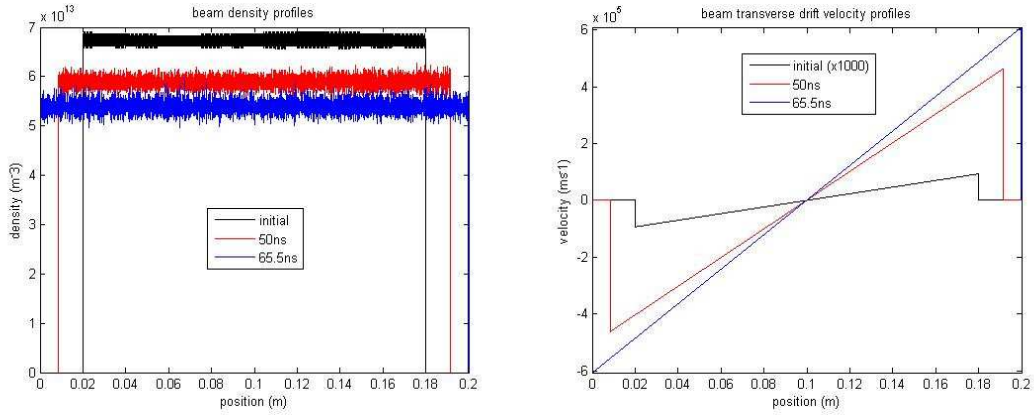

(b)

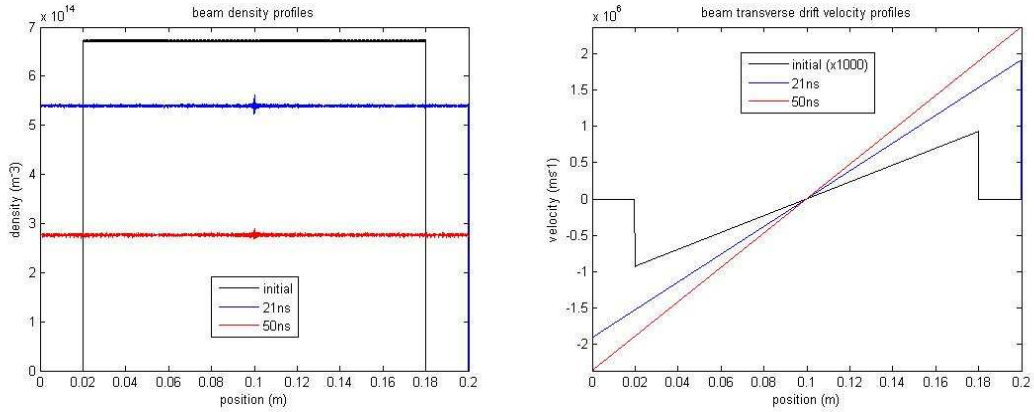

(c)

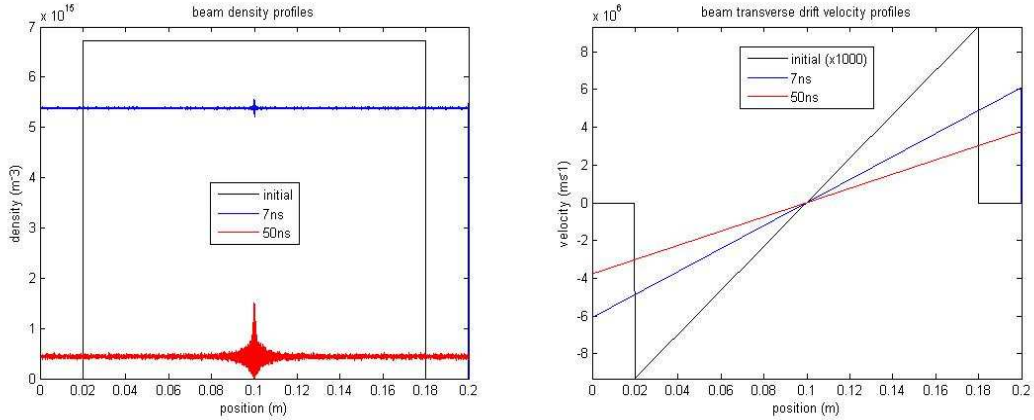

Figure 29: Beam density & velocity spatial profiles at beam densities; (a) 6.722x10^{13}m^{-3} (80keV/2.7A), (b) 6.722x10^{14}m^{-3} (80keV/27A), (c) 6.722x10^{15}m^{-3} (80keV/270A).

For a constant (initial) beam (longitudinal) velocity, the beam (transverse) expansion depends on the (initial) beam density (*Figure 29*). As the (initial) beam density is increased by a factor of 10; the beam (transverse) drift velocity increases by a factor of ~ 10 initially, and by a factor of ~ 3 for the first beam particle to reach the wall, hence the time it takes for the beam envelope to touch the wall decreases by a factor of ~ 3.

3.3.2 Results under varying beam velocity

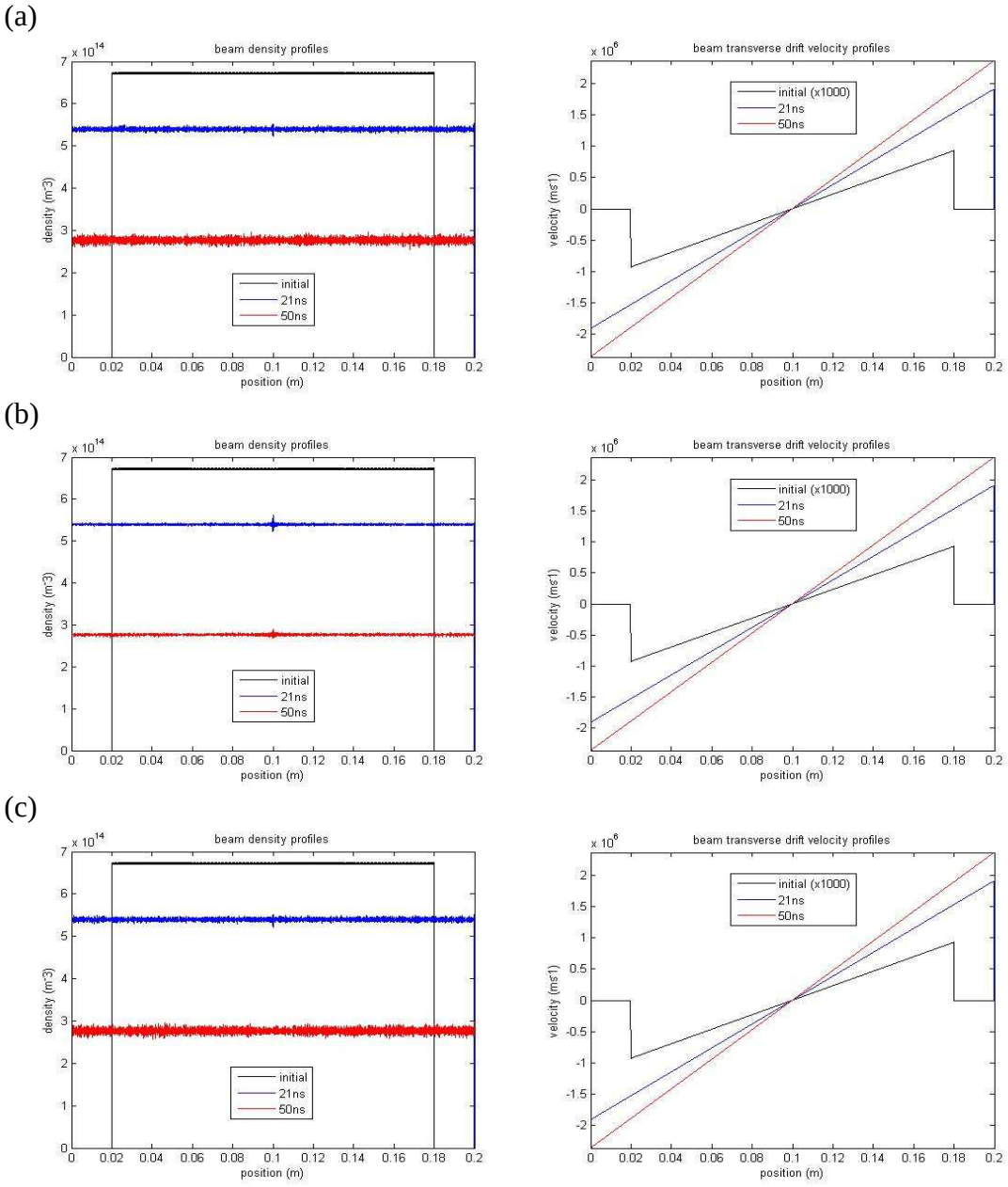

Figure 30: Beam density & velocity spatial profiles at beam velocities; (a) 3.918x10^{5} ms^{-1} (8keV/2.7A), (b) 3.918x10^{6}ms^{-1} (80keV/27A), (c) 3.918x10^{7}ms^{-1} (800keV/270A).

The results shown in *Figure 30* suggest that the (transverse) beam space-charge expansion is independent of the beam (longitudinal) velocity. Even though the (initial) beam current increases by a factor of ten from one simulation to the next, the beam divergence remains the same and is solely determined by the (initial) beam density.

3.3.3 Results for a constant beam current

(a)

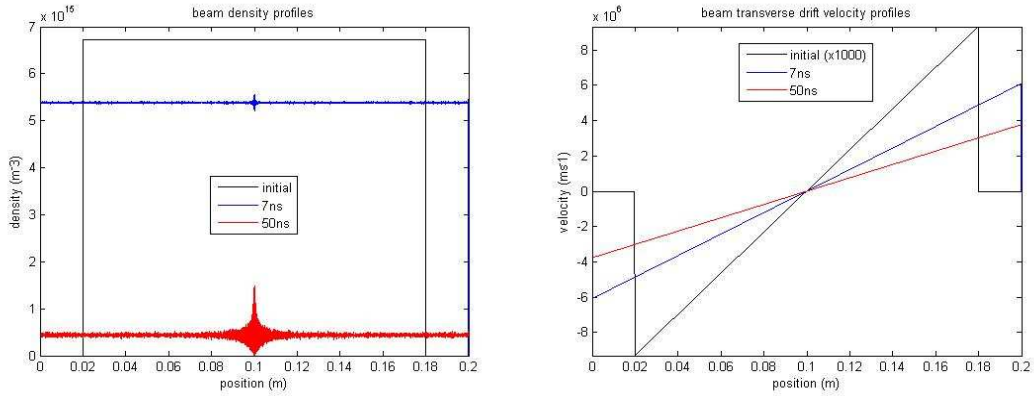

(b)

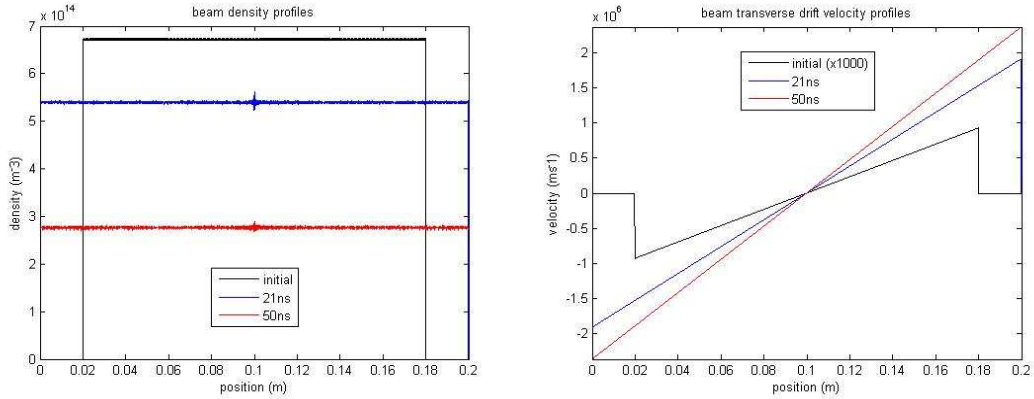

(c)

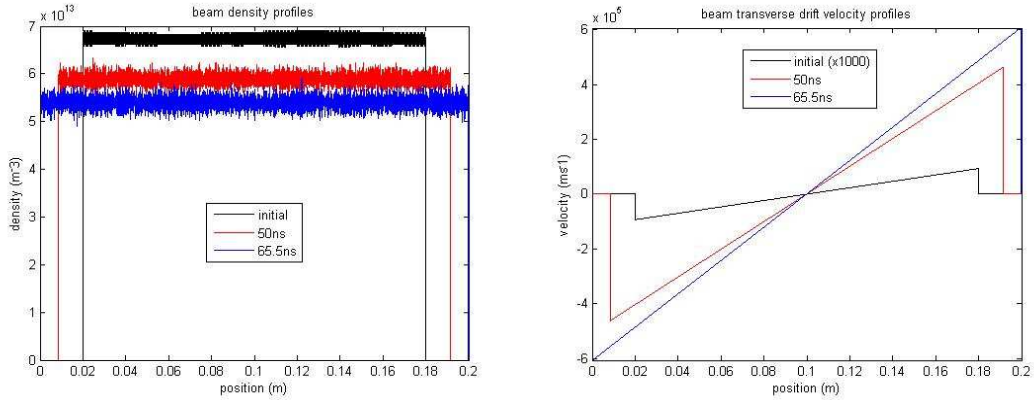

Figure 31: Beam density & velocity spatial profiles at beam densities; (a) 6.722x10^{15}m^{-3} (8keV/27A), (b) 6.722x10^{14}m^{-3} (80keV/27A), (c) 6.722x10^{13}m^{-3} (800keV/27A).

The results in *Figure 31* show that (same species) charged particle beams of equal (initial) current can produce different degrees of space-charge expansion. Again the (initial) beam charge density is shown to be the sole determinant of such effects. In reverse order to similar results shown in *Figure 29*, as the (initial) beam density is decreased by a factor of 10, the time it takes for the beam envelope to touch the wall increases by a factor of ~ 3, i.e. the beam divergence is slower for less dense beams due to less (mutual) Columbic repulsion between charges further away from one another.

3.3.4 Conclusions and General Remarks

The observed beam divergence (*Sections 3.3.1 - 3.3.3*) is solely caused by beam space-charge repulsion (like in *Section 3.2*, turning off Coulomb collisions between the beam particles made no significant difference to the results). The beam density determines the amount of space-charge repulsion {this (transverse) expansion is not a function of the beam (longitudinal) velocity (*Section 3.3.2*)}; causing a change in the beam transverse drift velocity (in proportion to the resulting transverse electric field) leading to the actual divergence of the beam {Holmes [38] concluded from his theoretical/experimental beam space-charge investigation that the beam divergence & plasma potential is less for larger diameter beams, although in these *beam propagation in vacuum* simulations the divergence is directly proportional to the beam width}.

Beam scraping (interception) at the neutraliser walls has been observed in the Neutral Beam Test Bed, resulting in beam power losses [22]. Notwithstanding the fact that these beams propagate in non-vacuum conditions, these (*beam propagation in vacuum*) simulation results suggest that; the real (*beam propagation in gas*) beam transmission losses due to beam space-charge blow-up will be more severe for higher beam densities. A *beam propagation in gas* simulation investigation (i.e. accounting for space-charge compensation) would better elucidate such issues, including those occurring in the extraction/acceleration regions of NBIs (ideally involving accurate beamlet profiles). The positive ion beam analytical models of Holmes [38] and Gabovich et al. [63] {and the negative ion numerical model of Gorshkov et al. [62]} imply that beam-electron Coulomb collisions have a significant effect on the neutralisation of the beam's space-charge (*Chapter 7*), and hence also on its divergence {the space-charge of negative beams can become overcompensated leading to beam convergence (gas focusing) [62]}.

Chapter 4

Neutraliser Beam Plasma Characterisation

4.1 Hydrogen Beam Composition Results

Two sets of hydrogen *beam composition* simulation results are presented; 80keV & 120keV, both consisting of an initial beam composition ratio of 8:1:1 for H^+, H_2^+, H_3^+ beam species, respectively (see empirical values for deuterium shown in *Figure 32*). The charge-changing cross sections (12 collisions) are taken from Kim & Haselton [60].

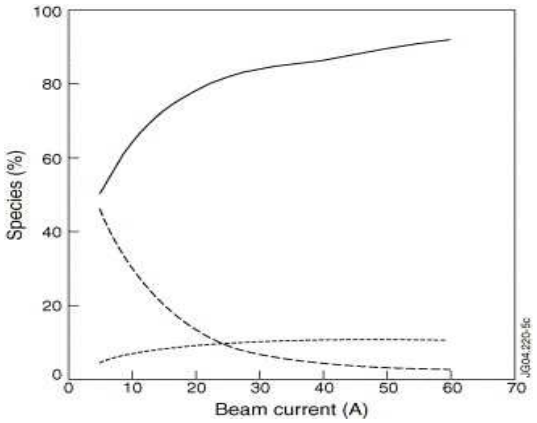

Figure 32: Ion species ratios in the PINI source as a function of beam current; D^+ (continuous line), D_2^+ (dotted line), D_3^+ (gaped line), measured by Doppler shift spectroscopy [19, 64].

In these *Transverse* simulations (*Section 2.2.1*), the *interchangeable variables* technique (time ≡ neutraliser gas target, *Section 2.2.4*), is used to calculate the optimum neutraliser H_2 gas target, and the resulting theoretical maximum neutralisation efficiency:

80keV (27A) hydrogen beam composition results

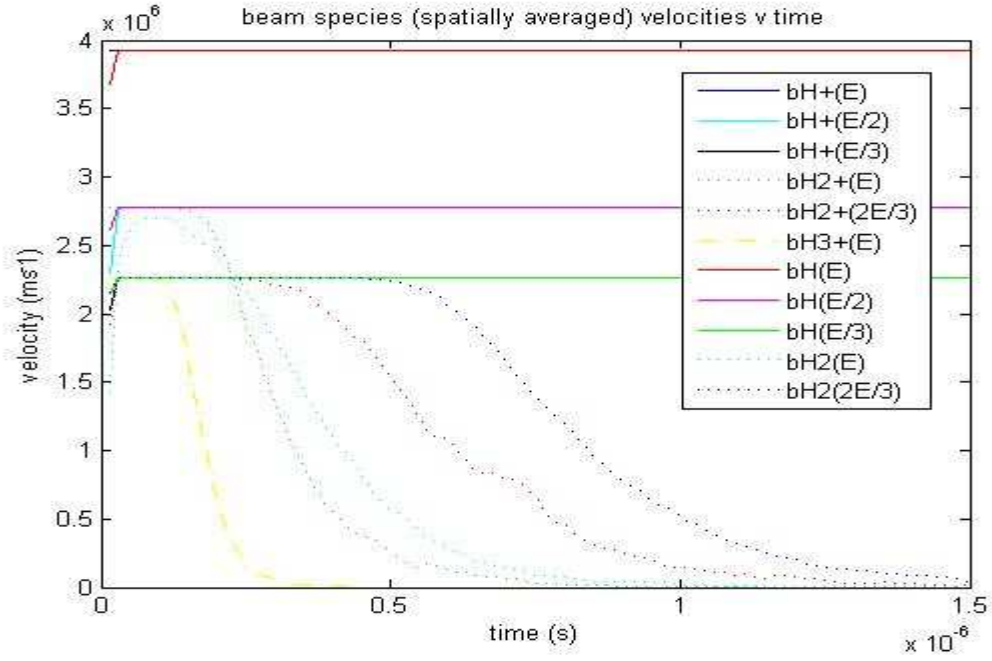

Figure 33: Evolution of beam species mean velocities (2 values overlap at 3 velocities).

All the beam species velocities remain fixed, in accordance with the *Transverse* simulation approach (*Section 2.2.1*), thereby neglecting all beam energy-sapping collision effects (relatively negligible with respect to the beam energy cf. *Section 4.2*), although the *spatially averaged* velocities (over the beam width of 16cm) for the beam particles; bH2+(E), bH2+(2E/3), bH3+(E), bH2(E), and bH2(2E/3) decay to zero (*Figure 33*), as these non-monatomic particles eventually breakdown into monatomic beam species (*Figure 34*) - beam negative ion formation is assumed negligible [60].

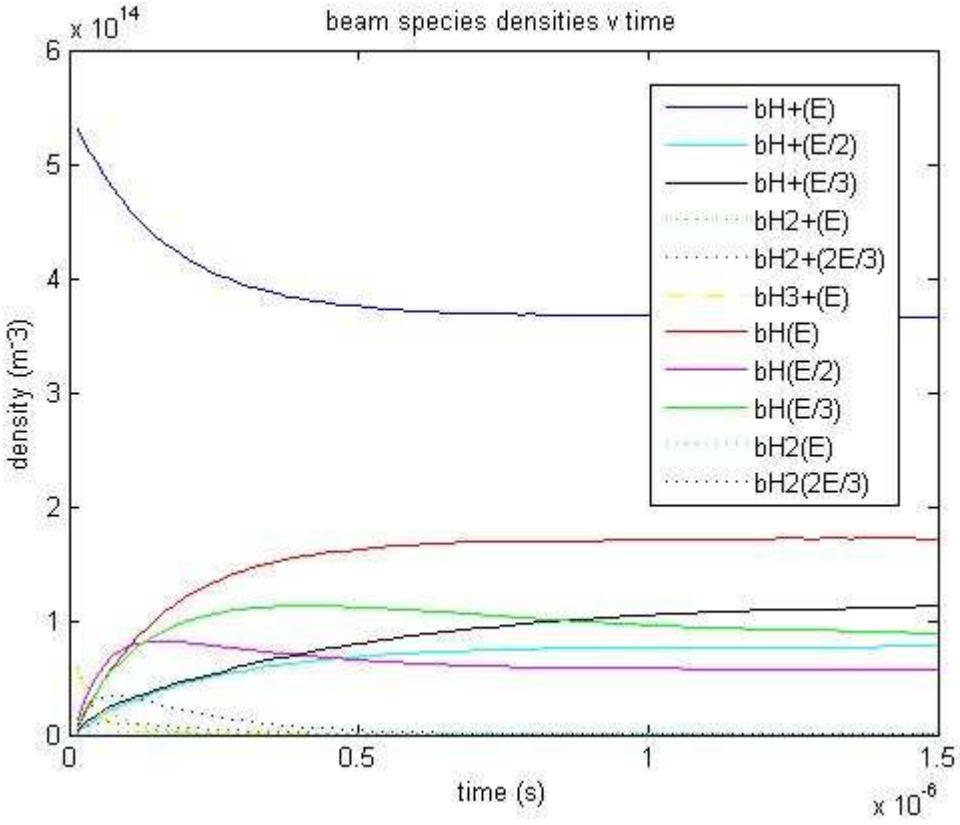

Figure 34: Evolution of beam species densities.

The total beam number density is ~ $6.725 \times 10^{14} m^{-3}$, which initially consists of ~ $5.38 \times 10^{14} m^{-3}$ for H^+ and ~ $6.725 \times 10^{13} m^{-3}$ each for H_2^+ and H_3^+ beam species (8:1:1). Since all the H_2^+ and H_3^+ beam species eventually get broken down into H^+ or H beam species, the bH+(E/2) plus bH(E/2) beam species densities amount to a density of ~ $1.345 \times 10^{14} m^{-3}$ i.e. $6.725 \times 10^{13} m^{-3}$ multiplied by two, while the bH+(E/3) plus bH(E/3) beam species densities total ~ $2.0175 \times 10^{14} m^{-3}$ i.e. $6.725 \times 10^{13} m^{-3}$ multiplied by three, all of which are consistent with the simulation results plotted in *Figure 34*.

At first glace the fixed simulated neutraliser average H_2 gas density of $9 \times 10^{19} m^{-3}$ {the two-component hydrogen 80keV beam model 'optimum' neutraliser (average) H_2 gas

density, Equation (2.7), *Section 2.2.4*} seems too low, since the 80keV beam takes ~ 1.5μs to reach charge-equilibrium (*Figure 34*) i.e. the optimum neutraliser gas target should be achieved within the neutraliser length of 1.86m, corresponding to 475ns ($1.86m/3.915x10^{6}ms^{-1}$). Although, *Figure 35* implies that a definite *maximum* neutral beam fraction can be achieved within 375ns {The *minimum* positive beam fraction occurs at a slightly earlier time because, unlike the beam mean energy densities (*Figures 36* & *38*), their sum is not conserved e.g. a density of 1 H_2 particle can change, via a dissociation collision, into a density of 2 H particles}. This contrasts to the basic *increasing* asymptotic behaviour predicted by Kim & Haselton's analytic calculations [60]*, and suggests that the simulated H_2 gas density ($9x10^{19}m^{-3}$) is excessive.

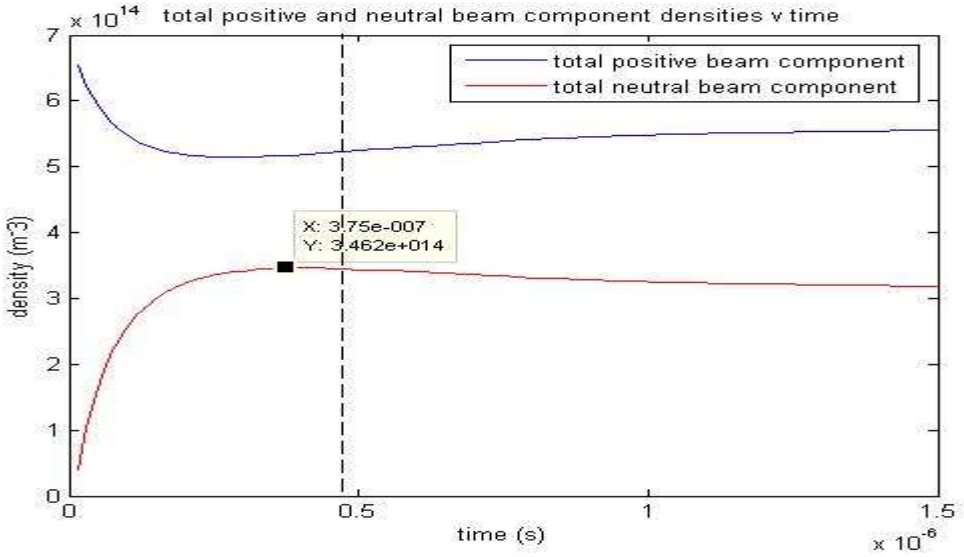

Figure 35: Evolution of beam (total) positive/neutral component densities.

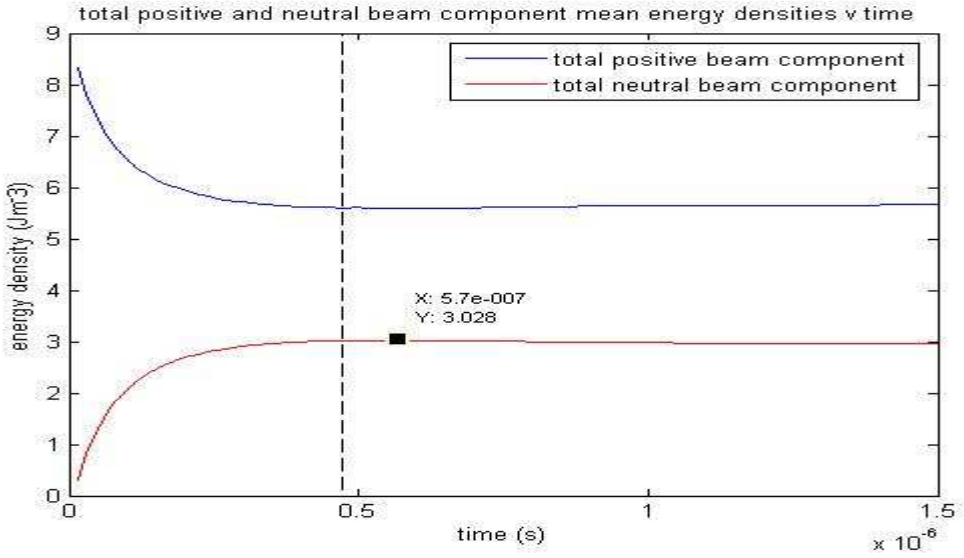

Figure 36: Evolution of beam (total) positive/neutral component mean energy densities.

However, the maximum neutral beam power (mean energy density, *Figure 36*), pertaining to maximum neutralisation efficiency, occurs at the later time of 570ns, due to the still increasing bH(E) density (*Figure 34*) via bH+(E) electron capture collisions. The neutral beam power then *decreases* asymptotically, due to opposing electron capture and stripping collisions (80keV stripping cross sections are ~ twice that for capture [60]) of the 6 remaining hydrogen monatomic beam components (*Figure 34*). Thus, the optimum gas target can be defined as that which is required for the beam to reach a maximum neutral component mean energy density, within the neutraliser length.

A corollary to this is that, too high a neutraliser gas line density produces a less than maximum neutralisation efficiency (gradual decrease as the beam approaches charge-equilibrium, *Figure 36*). This previously unpublished possible source of neutralisation inefficiency should be a significant issue in cases where gas heating density depletion does not rectify an excessive gas target (*Chapter 5*) i.e. the effective gas target remains higher than that required for maximum neutralisation. It is therefore not desirable for such positive ion beams to reach charge-equilibrium.

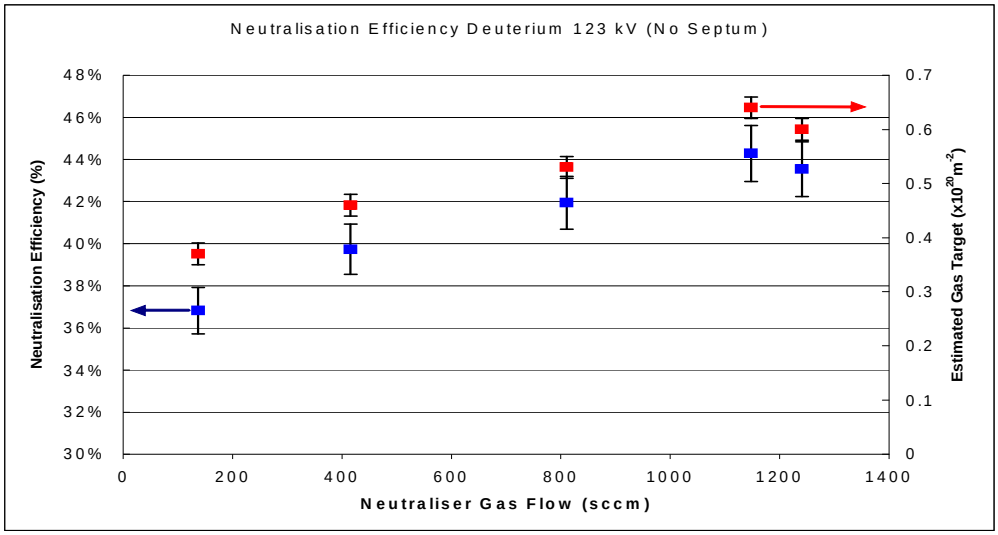

Figure 37: Neutralisation Efficiency (blue, left axis) and estimated gas target (red, right axis) as a function of neutraliser gas flow [65].

Possible evidence of this prediction is shown in *Figure 37* [65] i.e. an apparent maximum in neutralisation efficiency versus gas flow. The estimated gas target (last data point) was deduced from the neutralisation efficiency measurement, although the gas target should be proportional to the gas flow (assuming gas heating - 'saturates' with gas flow cf. *Figure 58*, *Section 4.4.3* [36] - and cryo-pumping effects don't change drastically between the last two data points). Moreover, *Figure 36* shows that two

possible (pre beam ion deflection) gas target values can provide the same neutralisation efficiency. The reduced neutralisation efficiency value (*Figure 37*) was thought to be due to beam re-ionisation [65] i.e. due to the *post neutraliser* (magnet path [19]) gas target (the *separated* 'pure' neutral beam is sure to acquire an ionic component unless a perfect vacuum is established for the remainder of its path). The simulation results (*Figure 36*) predict that another factor might be due to a reduction in the *pre-separated* beam neutralisation efficiency as a result of an excessive *neutraliser* (cf. *Section 1.3.3*) gas target. Accurate knowledge of how the *post neutraliser* gas target varies with gas flow (dependant upon the cryo-pumping) would be required to resolve the matter. However, a change from a decreasing to an increasing trend in positive ion beam power versus gas flow (i.e. a minimum, opposite to that of *Figure 37*) at the *ion dump* would verify the existence of a maximum in neutralisation efficiency versus gas target.

*: Kim & Haselton [60] used an analytical approach similar to *Section 1.3.1*, accounting for all 12 beam component changing collisions common with this simulation approach plus 4 more involving the $H^-(E)$ beam component. As previously mentioned, this cumbersome mathematical procedure predicted a basic *increasing* asymptotic neutralisation efficiency (cf. *Figure 44* [66]), contrary to the simulation results, which predict a distinct neutralisation efficiency maximum (*Figure 36*), followed by an asymptotically *decreasing* approach to charge-equilibrium cf. *Figure 35*.

The theoretical maximum neutralisation efficiency can be obtained from *Figure 36* i.e. $3.028 Jm^{-3}/8.612 \times 10^{14} Jm^{-3}$ ~ 35% {the two-component beam model (initial beam composition of 100% protons) yields a value of ~ 32%}. This maximum neutral beam mean energy density is reached at a time of ~ 570ns (*Figure 36*), which implies that the optimum neutraliser H_2 gas (average) density is ~ $1.08 \times 10^{20} m^{-3}$ (570ns/475ns x $9 \times 10^{19} m^{-3}$), giving an optimum neutraliser gas target of ~ $2.01 \times 10^{20} m^{-2}$ (*Section 5.1.5*). The accuracy of these results is determined by the accuracy of the beam charge-changing cross sections [60] and the simulation collision models (*Section 2.1.2*). This simulation procedure can therefore calculate the optimum neutraliser gas target, which ideally should be achieved during any NBI operation. In practice this is certainly not straightforward, as *beam on* gas pressure measurements are not yet possible on the present Neutral Beam Test Bed facility. Instead *beam off* gas pressure measurements and quantitative knowledge of gas target depletion (e.g. due to gas heating) would need to be combined in order to estimate the effective *beam on* neutraliser gas target.

More results from this 80keV *beam composition* simulation are presented below, namely; beam species mean energy densities (*Figure 38*), and beam species fluxes with a separate total positive/neutral component breakdown (*Figures 39 & 40*). Note that the maximum neutral beam flux (*Figure 40*) does not occur at the same time (gas target) as the maximum neutral beam density (*Figure 35*) or mean energy density (*Figure 36*).

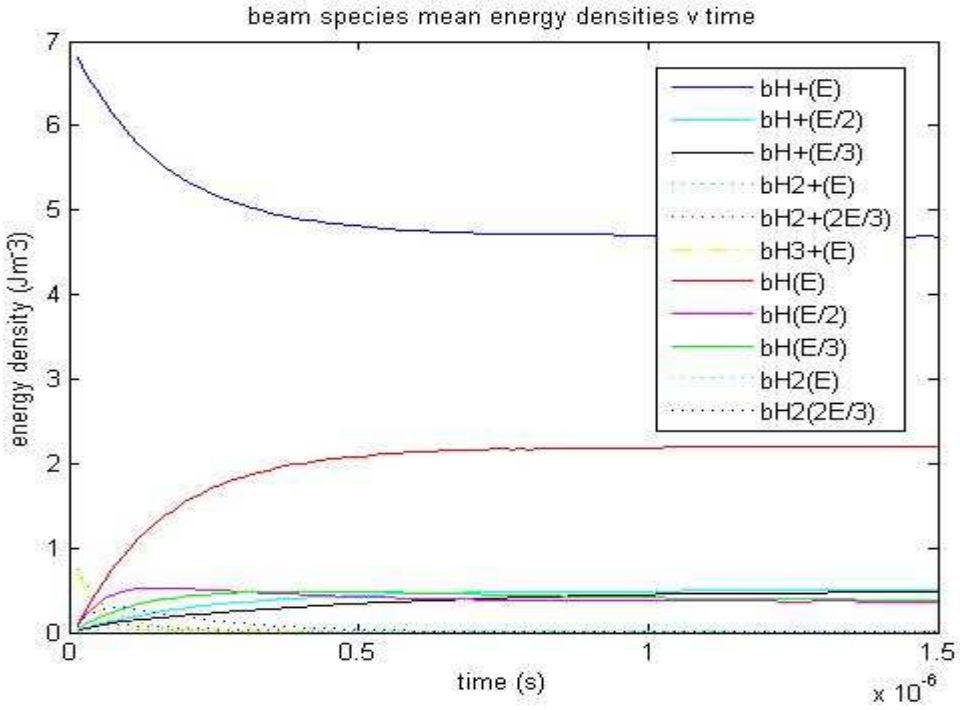

Figure 38: Evolution of beam species mean energy densities.

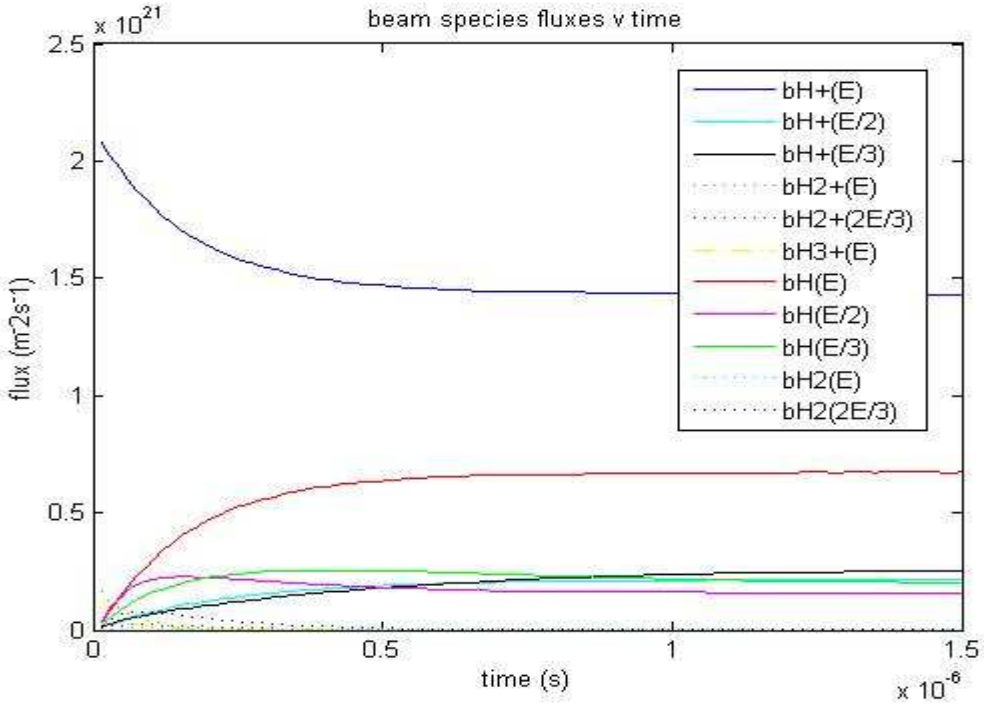

Figure 39: Evolution of beam species mean fluxes.

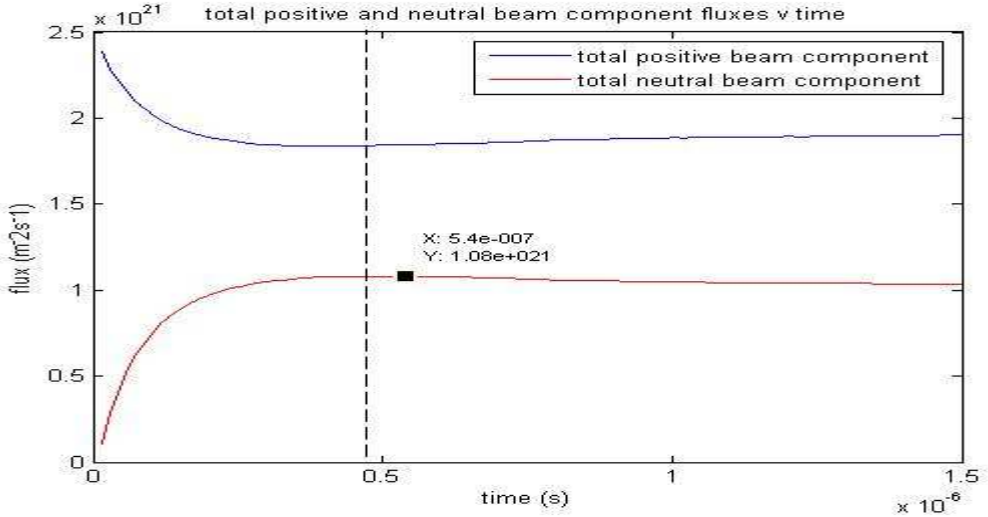

Figure 40: Evolution of beam (total) positive and neutral component fluxes.

120keV (50A) hydrogen beam composition results

Similarly, Equation (2.7) yields an 'optimum' (average) neutraliser fixed H_2 gas density of ~ $1.4 \times 10^{20} m^{-3}$ for a 120keV hydrogen beam (*Section 2.2.4*). The maximum neutral beam component should ideally be achieved within ~ 387ns i.e. the beam (neutraliser) transit time for a 120keV proton beam particle ($1.86m/4.794 \times 10^6 ms^{-1}$).

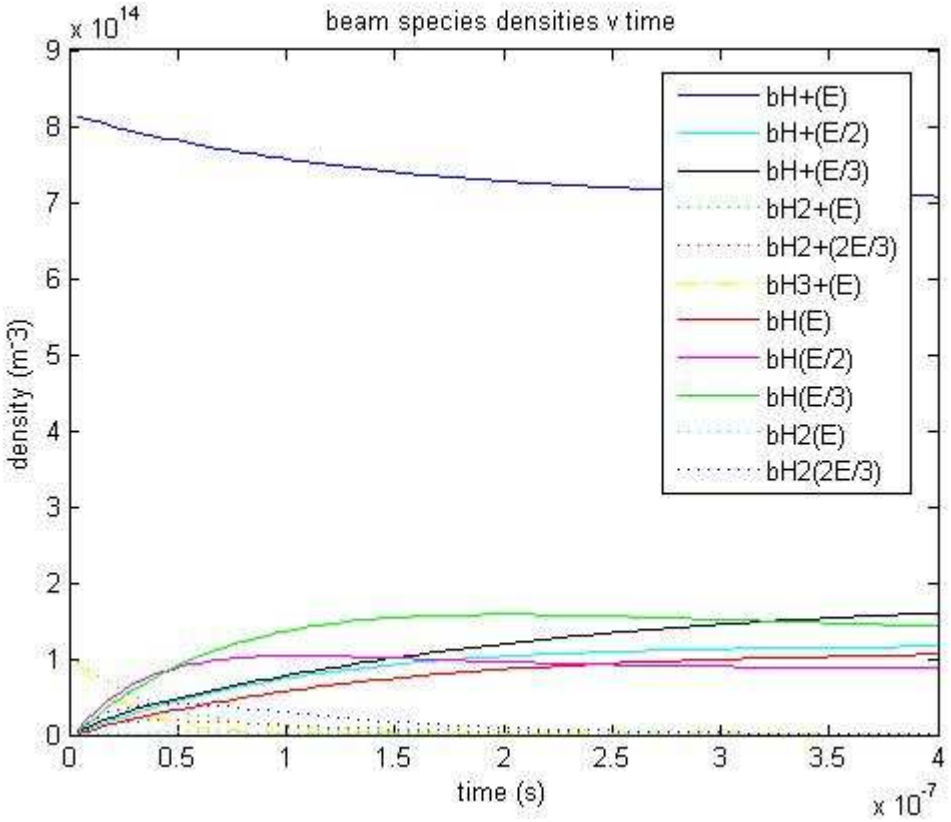

Figure 41: Evolution of beam species densities.

Unlike the 80keV hydrogen beam case, the bH(E/3) particles are the highest neutral component (*Figure 41*), due to the more favourable electron capture cross sections at lower beam velocities (*Figure 11 (b), Section 1.3.4*).

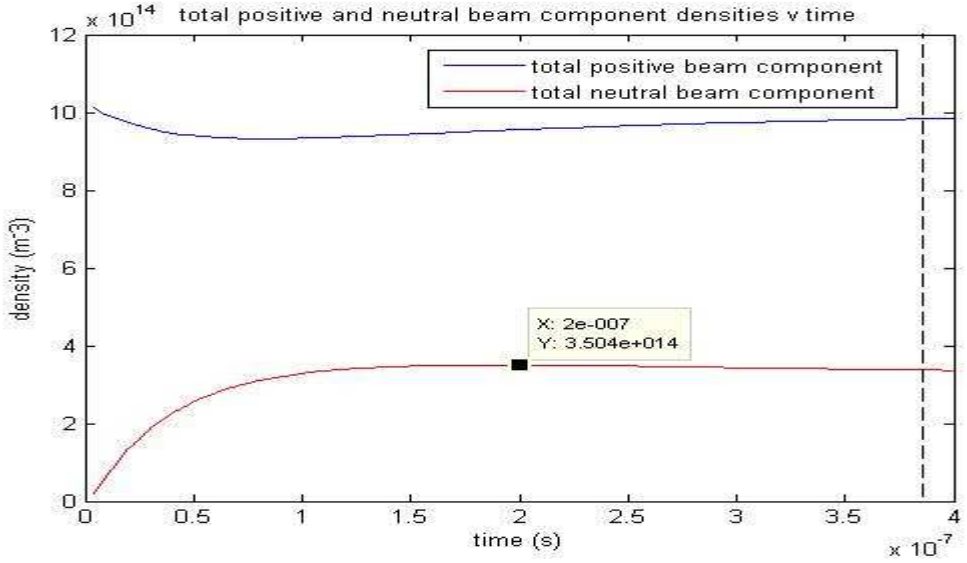

Figure 42: Evolution of beam (total) positive/neutral component densities.

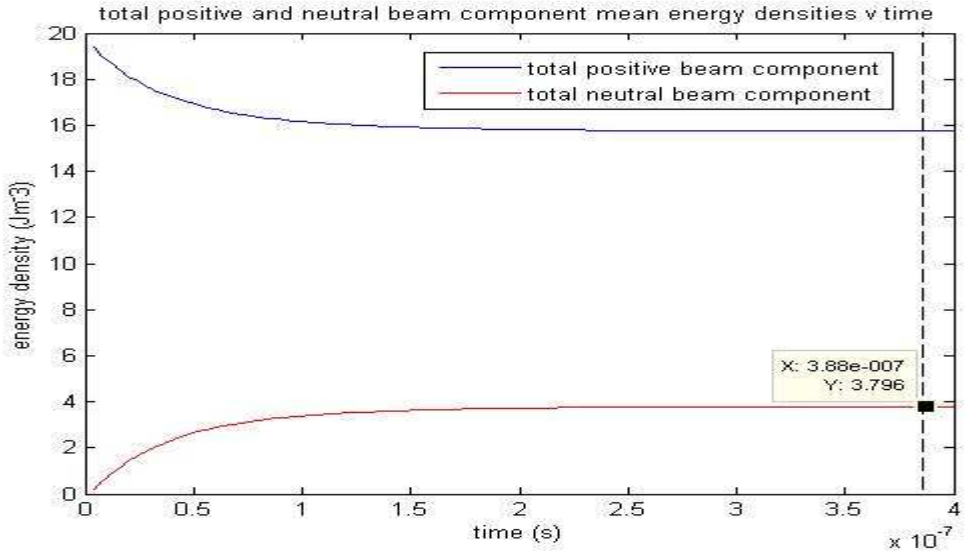

Figure 43: Evolution of beam (total) positive/neutral component mean energy densities.

Maximum neutralisation efficiency occurs at a time of ~ 388ns (*Figure 43*), which implies that the optimum H_2 gas density is ~ $1.4 \times 10^{20} m^{-3}$ (388ns/387ns x $1.4 \times 10^{20} m^{-3}$), a gas target of ~ $2.61 \times 10^{20} m^{-2}$ (~ $2.01 \times 10^{20} m^{-2}$ at 80keV) cf. *Section 5.1.5*. The two-component hydrogen beam model suggests that the optimum neutraliser gas target should be inversely proportional to the sum of the charge-changing cross sections (*Section 1.3.1*). These cross sections decrease with increasing energy (80 – 120 keV),

thus correctly predicting that the optimum gas target should increase for the 120keV case. This is consistent with the analytical calculations (similar to [60]) shown in *Figure 44* [66]. The optimum neutraliser H_2 gas target thus depends on the beam energy.

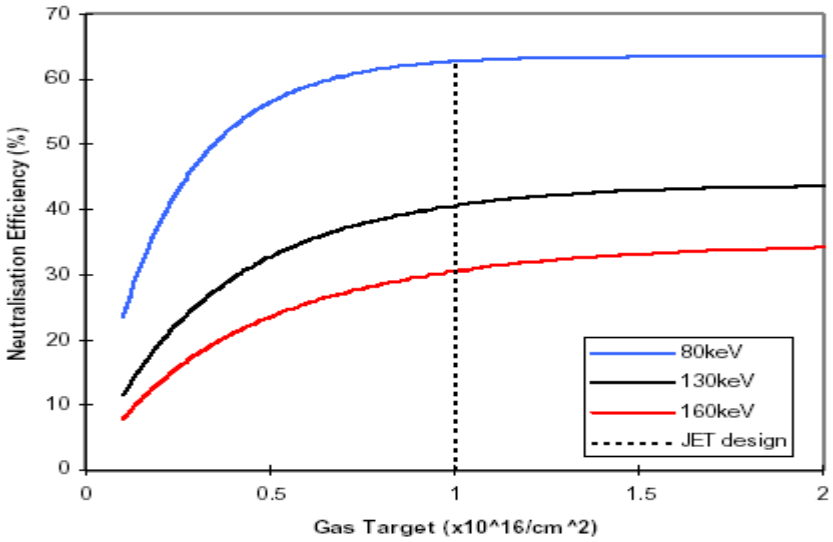

Figure 44: Neutralisation efficiency versus gas target (deuterium model) [66].

The theoretical maximum neutralisation efficiency; $3.796 Jm^{-3}/19.553 Jm^{-3}$ (*Figure 43*) is ~ 19% {compared to ~ 14% for the two-component beam model (initial beam composition of 100% protons)}. In the 80keV case, the theoretical maximum neutralisation efficiency was much higher (~ 35%), which is to be expected given the more favourable electron capture cross sections at lower beam energies (*Figure 11 (b)*, *Section 1.3.4*) cf. *Figure 44* [66]. The fact that the positive ion beam neutralisation efficiency is inversely proportional to the beam energy, has led to the development of negative ion beams, in order to achieve adequate beam neutralisation at the high beam energies required for heating tokamaks significantly larger than JET. Despite the shift in focus towards negative ion beam neutral injector research (*Section 6.1.1*), positive ion neutral injectors are still operational on tokamaks other than JET e.g. at the superconducting KSTAR (Korea Superconducting Tokamak Advanced Resesearch) facility {where a recent paper [67] on positive multiple-ion hydrogen beam neutralisation implicitly assumes that beam charge-equilibrium is desirable i.e. it speaks of attaining "95% equilibrium neutralisation" (citing [60]) rather than of a distinct maximum (this multiple ion-gas collision physics issue may already be resolved)}.

All of the above results could have alternatively been obtained from *Longitudinal* simulations, although this would be considerably more computationally expensive.

4.2 Beam Power Loss during Neutraliser Transit

The following beam mean energy density (& beam energy) results as a function of time (gas target) are from *Transverse* simulations of a *charge-equilibrated* hydrogen beam in transit through a (neutraliser) H_2 gas. By allowing the beam (longitudinal) velocity to change (unlike the normal *Transverse* simulation approach, *Section 2.2.1*) i.e. decrease via inelastic collisions with the H_2 gas, the beam energy loss can be determined.

4.2.1 Results as a function of neutraliser gas density

(a)

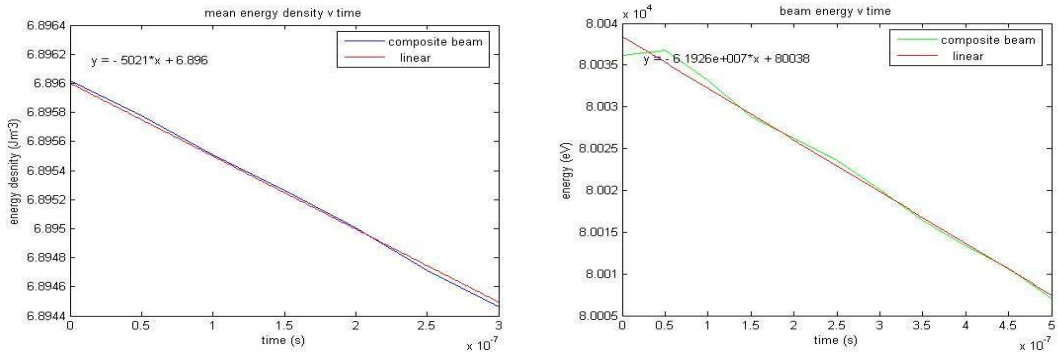

(b)

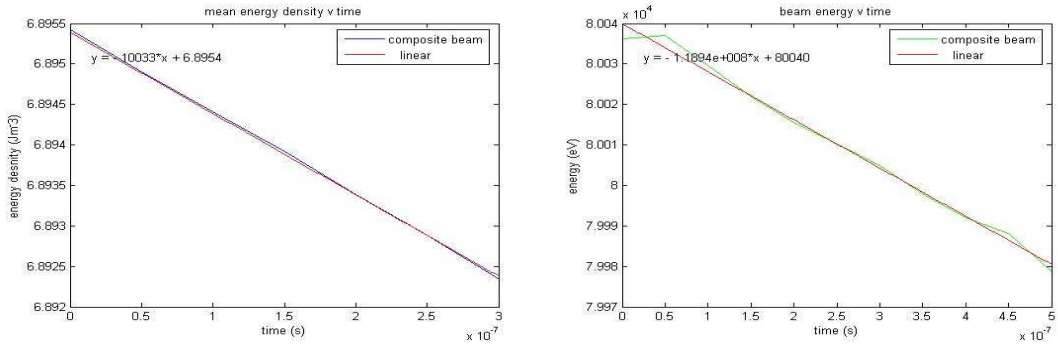

(c)

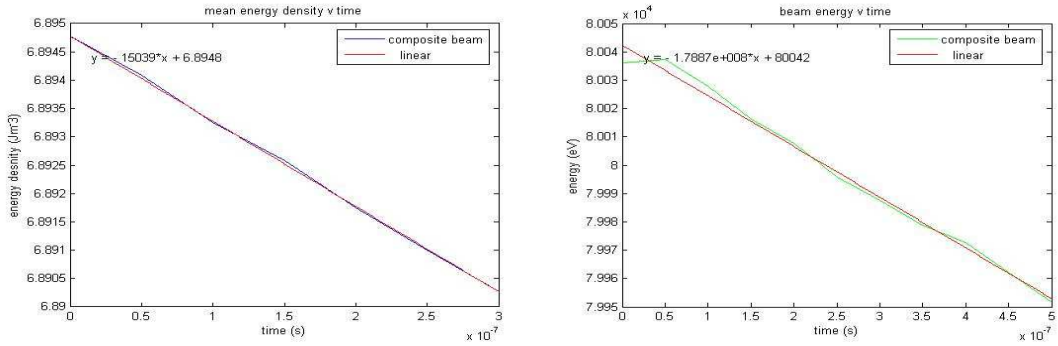

Figure 45: Beam mean energy densities (& beam energies, initial increase due to computational inaccuracies) as a function of time for 80keV/27A hydrogen beam transit through three neutraliser H_2 gas densities; (a) $3x10^{19}m^{-3}$, (b) $6x10^{19}m^{-3}$, (c) $9x10^{19}m^{-3}$.

From inspection of the beam energy versus time plots (*Figure 45*, right hand column), we see that for the ~ 475ns it takes the initial 80keV proton beam to travel the full neutraliser length (~ 1.86m); ~ 28eV, ~ 56eV and ~ 84eV of energy (corresponding to ~ 0.035%, ~ 0.07% and ~ 0.105% of the total beam energy) is lost on average by each beam particle during neutraliser transit in (a), (b) and (c), respectively.

Alternatively, these values can be calculated from the beam mean energy density versus time plots (*Figure 45*, left hand column), by multiplying the best-fit slope (beam power density loss to the neutraliser gas) by the total constant density equivalent neutraliser volume (gives the total beam power loss) and by the beam (neutraliser) transit time (gives the total beam energy loss) and finally dividing the result by the number of beam particles that reside in the constant density equivalent neutraliser volume at any given instant. The total volume of the neutraliser is $0.16368m^3$ (0.2m x 0.44m x 1.86m). Since the neutraliser gas density has a non-constant axial profile (*Figure 10, Section 1.3.2*), its total volume is multiplied by 0.772 to get the constant density equivalent neutraliser volume, $0.126m^3$. The number of beam particles that reside in the constant density equivalent neutraliser volume at any given instant is equal to the spatially averaged beam density ($6.725x10^{14}m^{-3}$ x 0.16m/0.20m) multiplied by the constant density equivalent neutraliser volume, which gives a value of $6.779x10^{13}$ beam particles.

Hence, the total beam energy lost in the neutraliser of density $3x10^{19}m^{-3}$ (*Figure 45 (a)*) is $5021Wm^{-3}$ x $0.126m^3$ x 475ns, which yields $3.005x10^{-4}$J ($1.876x10^{15}$eV). In terms of energy loss per beam particle, $1.876x10^{15}$eV corresponds to ~ 28eV ($1.876x10^{15}eV/6.779x10^{13}$) of energy lost on average by each beam particle i.e. the same value as mentioned above from simple inspection of the beam energy versus time plot. Similarly, for the case of the neutraliser of density $6x10^{19}m^{-3}$ (*Figure 45 (b)*), the beam energy lost is $6.005x10^{-4}$J ($3.748x10^{15}$eV), an average energy loss per beam particle of ~ 56eV. For the $9x10^{19}m^{-3}$ case (*Figure 45 (c)*), the beam energy lost is $9.001x10^{-4}$J ($5.619x10^{15}$eV), an average energy lost by each beam particle of ~ 84eV. The accuracy of these results depends upon the accuracy of the beam inelastic collision simulation models and the cross sections and threshold energies used therein (*Section 2.2.2*). These average % beam energy losses are consistent with the stopping power measurements (which entail the use of a Cockcroft-Walton ion accelerator [68], gas cells, magnets, and a electrostatic deflector energy analyser) of Allison et al. [69]; energy loss of less than 0.1% for one beam attenuation cf. [70], [56].

The plots shown in *Figure 45* imply that the beam energy density (and hence the beam energy, since the total beam density remains constant) decreases linearly with time for any neutraliser gas density. The slopes of the beam mean energy density versus time plots (*Figure 45*, left hand column) give the respective values for the beam power density loss, which is thus constant for a given beam transit through a gas. These beam power density loss values are plotted as a function of the neutraliser gas density in *Figure 46*. The resulting straight line graph shows that the beam power (power density) loss is directly proportional to the neutraliser gas density. This conclusion is consistent with basic physical sense i.e. more energy-sapping collisions at higher gas densities.

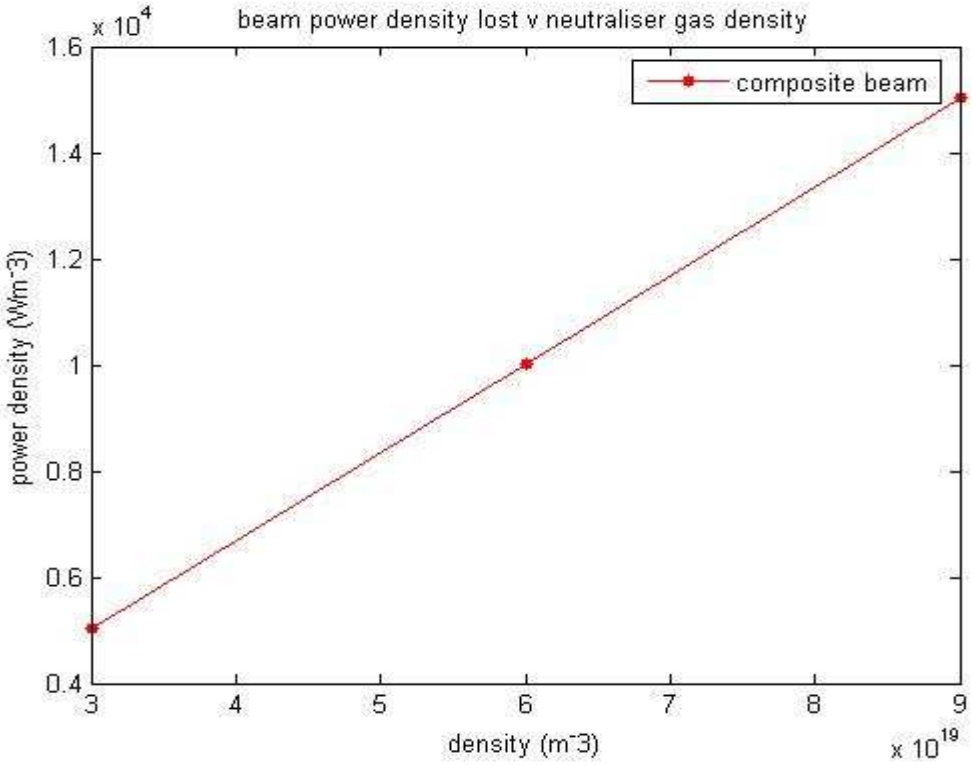

Figure 46: beam power density loss as a function of the neutraliser gas density.

4.2.2 Results as a function of beam energy

(a)

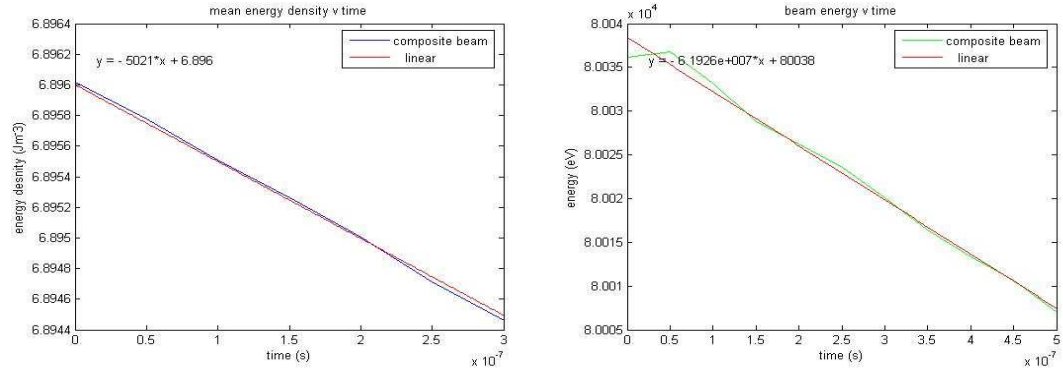

(b)

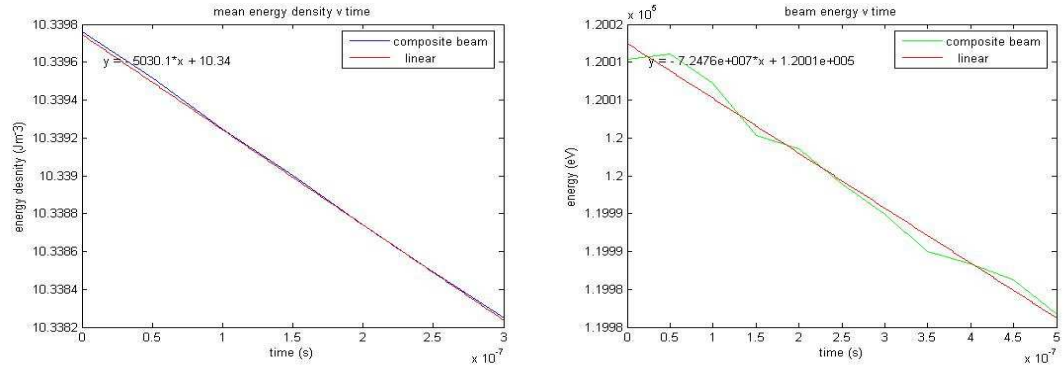

(c)

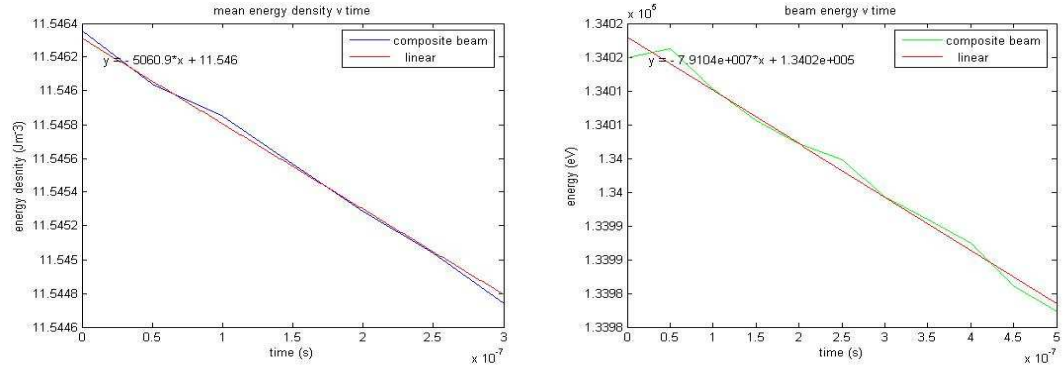

Figure 47: Beam mean energy densities (& beam energies) as a function of time for 27A hydrogen beam transit through a neutraliser H_2 gas (density, $3x10^{19}m^{-3}$), for three beam energies; (a) 80keV, (b) 120keV, (c) 134keV.

The best-fit slopes shown in *Figure 47* indicate that the beam power loss increases only relatively slightly with beam energy. The beam energy loss in inelastic collisions (beam elastic collisions are negligible, *Section 5.1.1*) is proportional to its kinetic energy i.e. at higher beam energies there is more beam energy loss per collision. Although this effect is counterbalanced by the fact that the cross sections decrease for increasing beam energy (over this range of beam energies) i.e. less collisions at higher beam energies.

4.2.3 Results as a function of beam current

The (initial) beam density is varied, while the (initial) beam velocity remains constant:

(a)

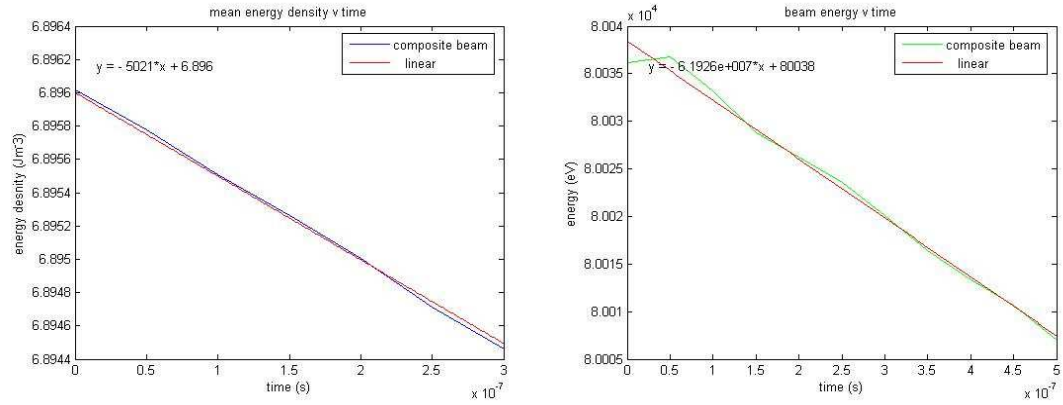

(b)

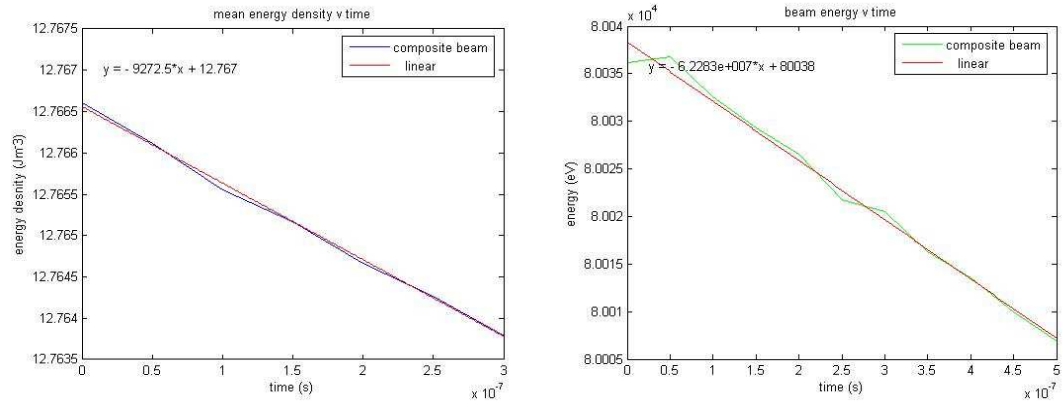

(c)

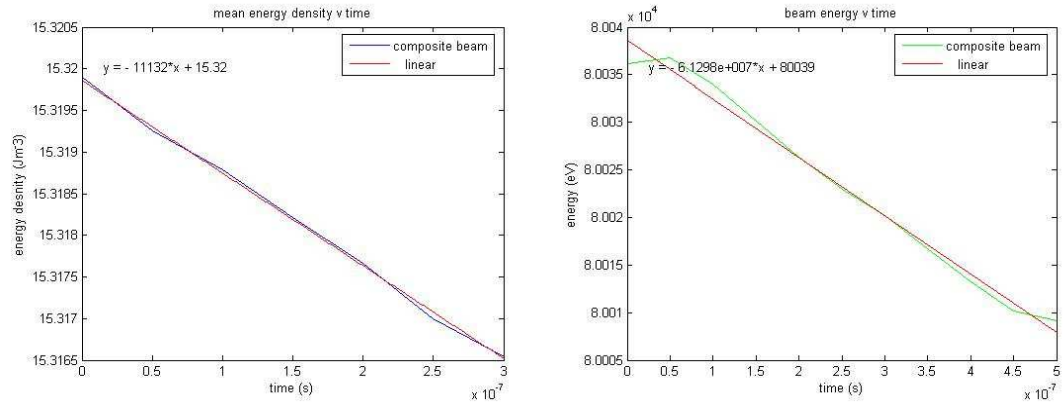

Figure 48: Beam mean energy densities (& beam energies) as a function of time for 80keV hydrogen beam transit through a neutraliser H_2 gas (density, $3x10^{19}m^{-3}$), for three beam currents; (a) 27A, (b) 50A, (c) 60A.

Like in the case of *Section 4.2.1* (results for varying neutraliser gas density), the beam power (density) loss is directly proportional to the beam current (*Figure 49*). Again this is consistent with basic physical sense i.e. more beam current in this case means more beam particles, which leads to more energy-sapping beam inelastic collisions with the neutraliser gas {while the average energy loss by each beam particle remains constant for the three cases, ~ 28eV (*Figure 48*, right hand column) cf. *Section 4.2.1*}, and therefore results in proportionately greater beam power loss.

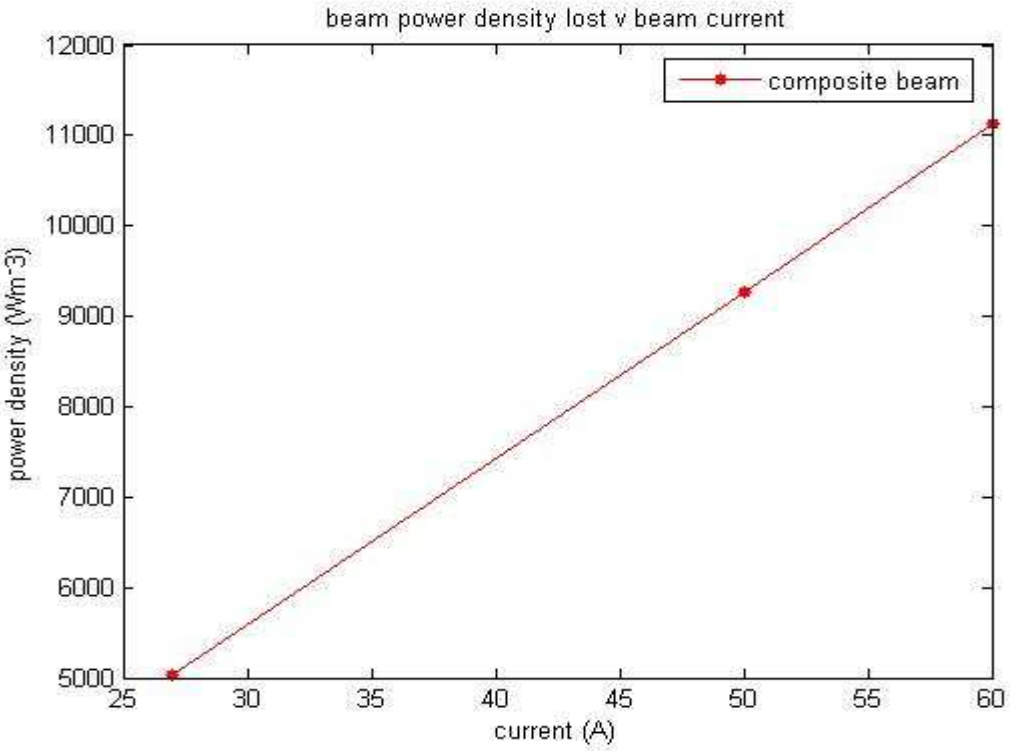

Figure 49: beam power density loss as a function of the beam current.

4.2.4 Results as a function of beam power

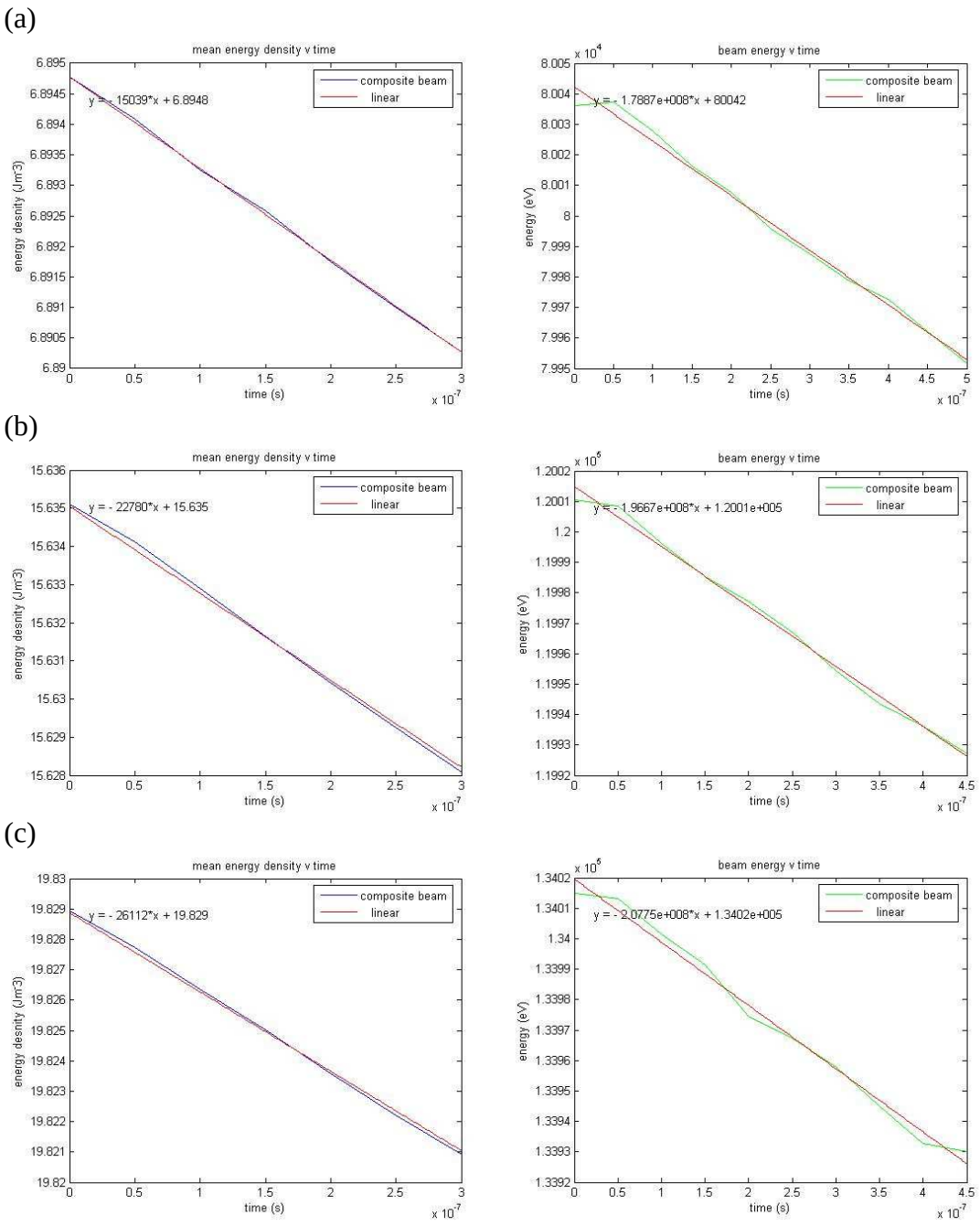

Figure 50: Beam mean energy densities (& beam energies) as a function of time for hydrogen beam transit through a neutraliser H_2 gas (density, $9x10^{19}m^{-3}$), for three beam powers; (a) 2.16MW (80keV/27A), (b) 6MW (120keV/50A), (c) 8.04MW (134keV/60A) i.e. at optimum (JET PINI) beam perveance.

The results of *Figures 50 & 51* follow on from the independent results of *Sections 4.2.2 & 4.2.3*. A similar plot to *Figure 51* would be linear if the beam velocity was constant. The degree to which it deviates from linearity depends on the deviance of beam energy among the 3 data points (each corresponding to the results of a particular simulation).

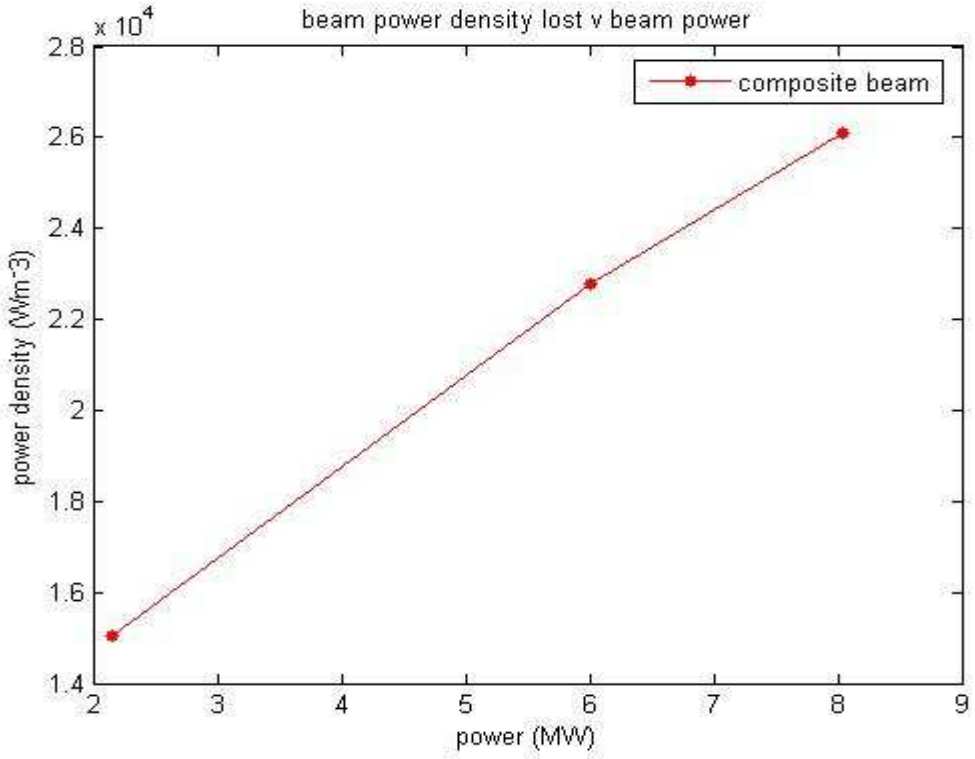

Figure 51: beam power density loss as a function of the beam power.

4.3 Beam Plasma Evolution towards Steady-State

The initial (0-415 ns) beam 'plasma' evolution, resulting from 80keV/27A proton beam injection into a neutraliser H_2 gas of density $3x10^{19}m^{-3}$, is shown in *Appendix B*, while its evolution towards steady-state (0–51.5 μs) is shown in *Figure 52*:

(a)

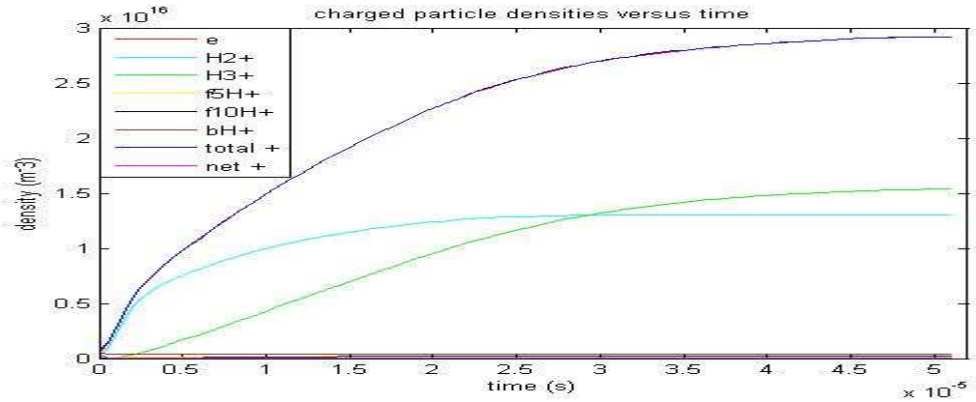

(b)

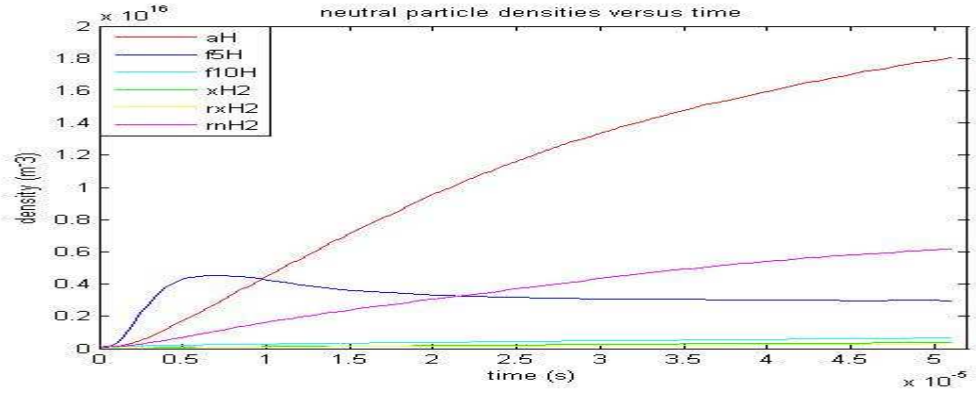

(c)

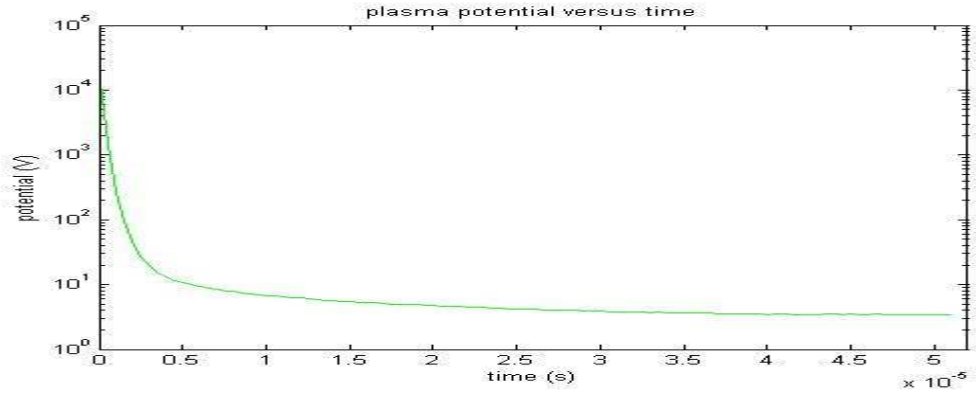

Figure 52: Early evolution of the spatially averaged (a) charged particle densities, (b) neutral particle densities and (c) plasma potential {$3x10^{19}m^{-3}$, 2.16MW}.

As described in *Section 2.2.2*, five beam plasma *Transverse* simulations* are conducted, investigating three neutraliser H_2 gas densities {$3x10^{19}m^{-3}$, $6x10^{19}m^{-3}$, $9x10^{19}m^{-3}$} at

constant H^+ beam power {2.16MW (80keV/27A)}, and three H^+ beam powers {2.16MW (80keV/27A), 6.00MW (120keV/50A), 8.04MW (134keV/60A)} at constant neutraliser H_2 gas density {$9x10^{19}m^{-3}$}. *: The five simulations commenced (*Figure 53*, values at time zero are continuations from restored simulations) from initial guesses (overestimated densities; *Figure 53 (a)*) of the steady-state plasma parameters (inputted with constant top-hat/flat-top spatial profiles cf. attached CD). The simulation running times (~ 15 months) were found to be even longer than if the simulations had been started from scratch. Of the five simulations, only the $3x10^{19}m^{-3}$ and $6x10^{19}m^{-3}$ simulations (*Figure 53 (b)*) reached a definite steady-state. Spatially resolved plasma parameters at the next diagnostic time steps (data points shown in *Figure 53 (a)*) are presented in *Appendix C*, while *Section 4.4* presents some of these (spatially averaged) plasma parameters as a function of neutraliser H_2 gas density and H^+ beam power, and includes a comparison with the experimental results of Crowley et al. [36].

(a)

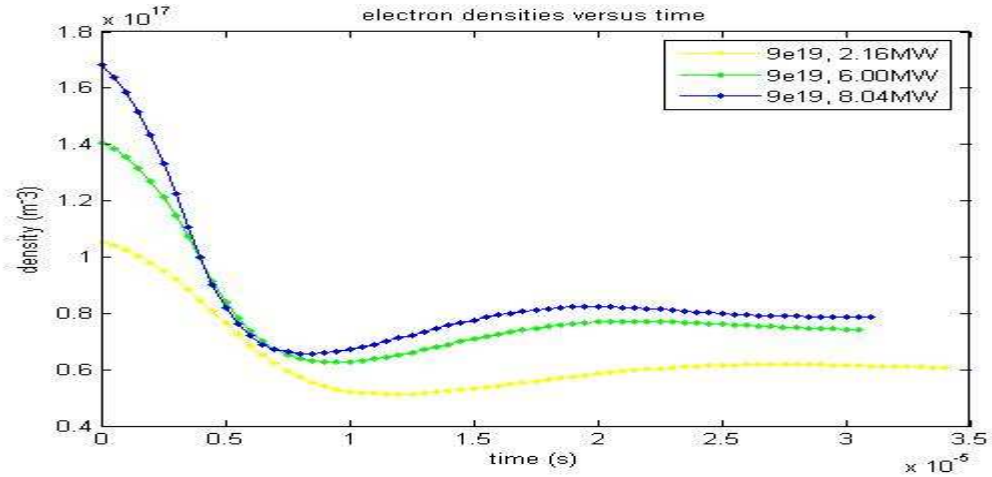

(b)

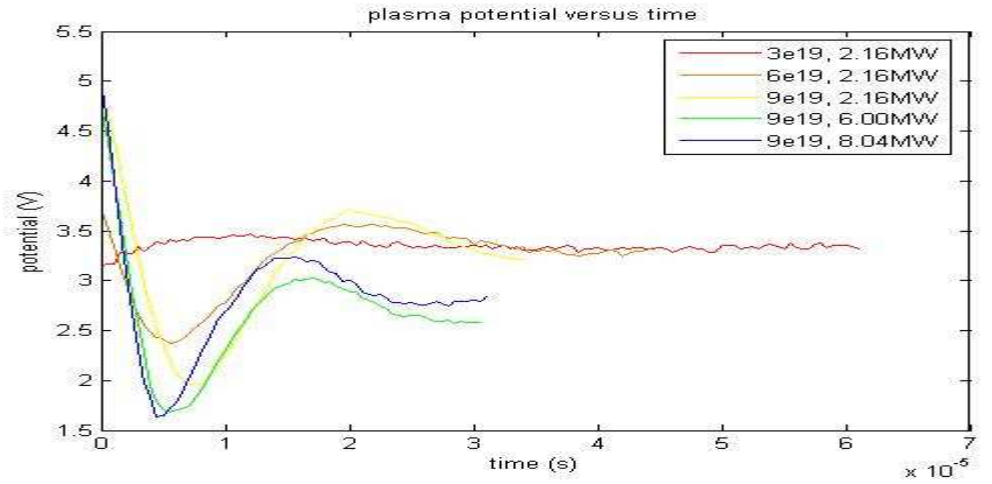

Figure 53: Spatially averaged (a) electron density (‘*3e19*’ *and* ‘*6e19*’ *were unable to be plotted due to insufficient computer memory) and (b) plasma potential evolution.*

4.4 Steady-State Plasma Parameter Results

Approximate steady-state beam plasma simulation results are presented cf. *Section 4.3*:

4.4.1 Results versus neutraliser gas density

(a)

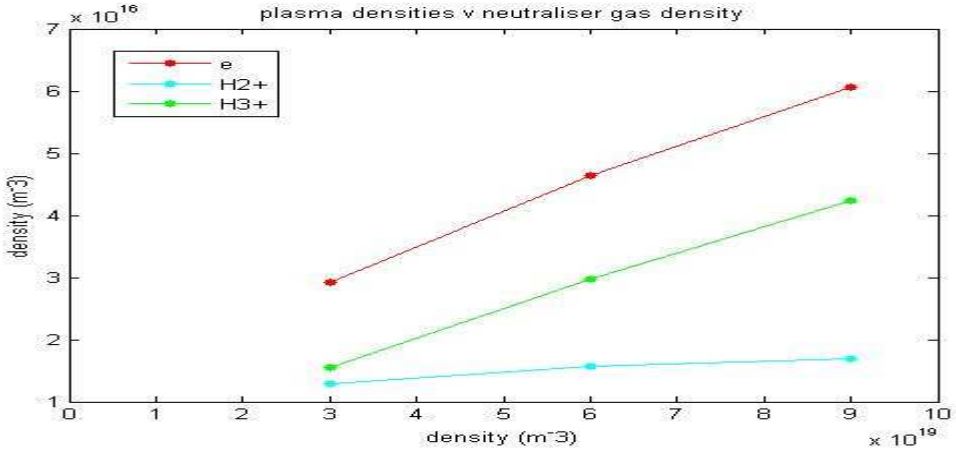

(b)

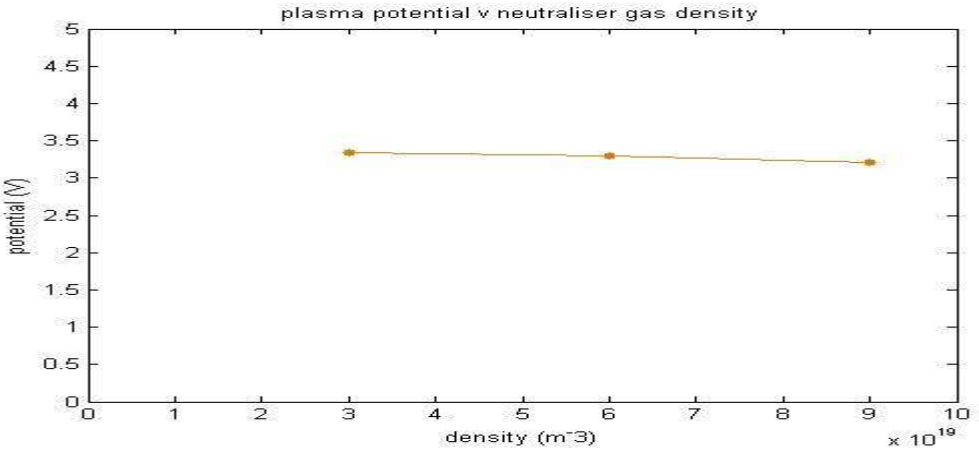

(c)

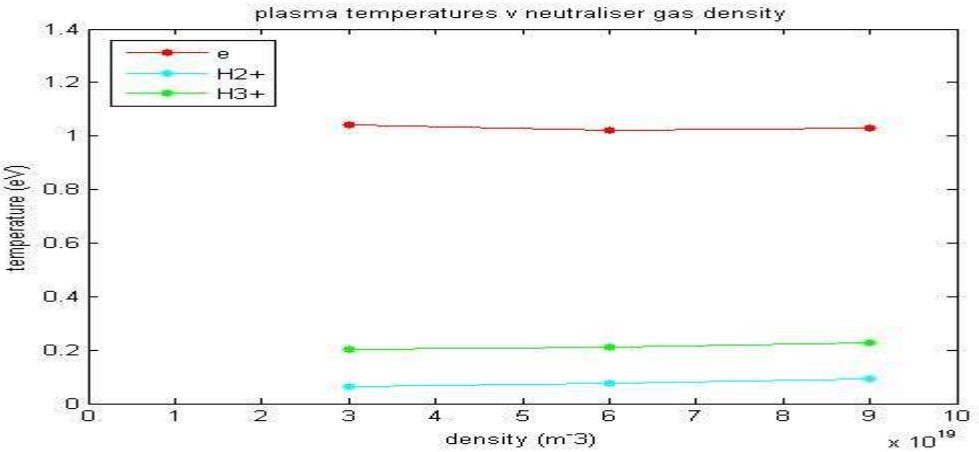

Figure 54: Steady-state plasma (a) densities, (b) potentials and (c) temperatures, as a function of the neutraliser H_2 gas density (hydrogen beam power, 2.16MW).

The (slightly less than) linear increase in electron density with increasing neutraliser gas density (*Figure 54 (a)*) is due to the greater number of beam & electron impact ionisations at higher gas densities. *Table 1* shows the percentage direct (impact) ionisation contributions from the three ionisation source particles (*Section 2.2.2*).

	bH+	bH	e
(a)	70.4%	17.0%	12.6%
(b)	69.2%	17.6%	13.2%
(c)	68.5%	18.1%	13.4%

Table 1: Steady-state bH^+, bH and electron percentage ionisation contributions, at the three neutraliser H_2 gas densities; (a) $3x10^{19}m^{-3}$, (b) $6x10^{19}m^{-3}$, (c) $9x10^{19}m^{-3}$.

The results displayed in *Table 1* show that primary ionisation (from the two beam species) is dominant, although secondary ionisation (from electrons) does play a significant role in the overall plasma formation & maintenance, becoming slightly more important at higher neutraliser gas densities ('electron avalanche' [43]) cf. *Figure 55*.

The plasma potential is determined mainly by (proportional to the square root of [43]) the electron temperature, from which the initial loss rate of electrons to the neutraliser walls depends (the plasma potential is also proportional to the natural logarithm of the square root of the; positive ion mass divided by the electron mass [43]).

The electron temperature decreases slightly with increasing neutraliser gas density. The results in *Figure 54 (c)* actually show a decrease followed by an increase, although the third data point is not a definite steady-state value (*Figure 53*, *Section 4.3*) i.e. the electron temperature - third data point, *Figure 54 (c)* - would be expected to decrease, as the plasma potential continues to decrease (*Figure 53 (b)*, *Section 4.3*).

Despite the slight increase in electron temperature between the last two data points, the plasma potentials show a strictly decreasing trend (*Figure 54 (b)*). Moreover, despite such indefinite trends in electron temperature (*Figure 54 (c)*) with neutraliser gas density (conclusive trends cannot be drawn from such slight variations), the electron impact ionisation (process whereby electrons lose most energy) reaction rates (*Figure 55*) are directly proportional to the neutraliser gas density cf. *Table 1*.

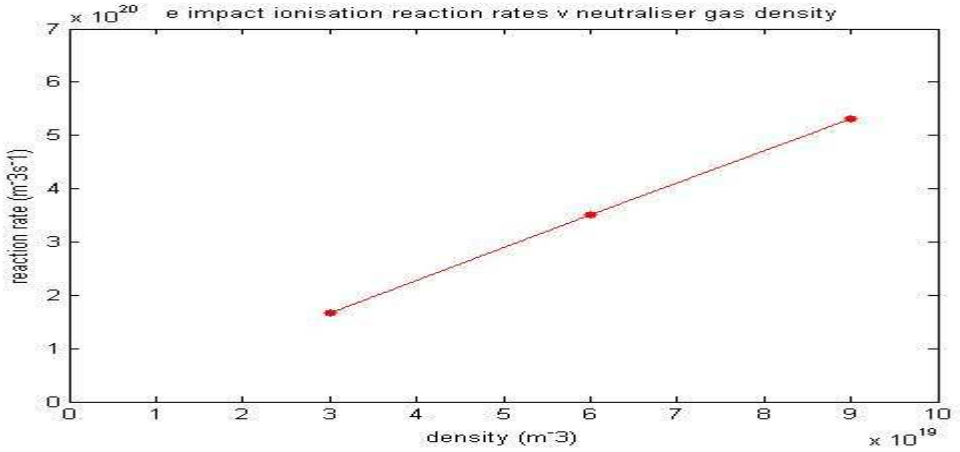

Figure 55: Steady-state electron impact ionisation reaction rates as a function of the neutraliser H_2 gas density.

The H_3^+ ion becomes the main positive ion in all neutraliser beam plasma simulations. The H_3^+:H_2^+ ratio increases with neutraliser H_2 gas density (*Figure 54 (a)*) - the H_2^+ density only increasing slightly. This is partly due to the greater number of H_2 gas molecules available for H_2^+ association (H_3^+ forming) collisions, cf. *Section 2.2.2*.

The H_3^+ & H_2^+ ion temperatures (calculated assuming their energy is confined to three translational degrees of freedom i.e. no rotational or vibrational degrees of freedom) increase with neutraliser gas density (*Figure 54 (c)*), while they are considerably lower than the electron temperatures (due mainly to their greater mass cf. *Section 1.5.2*).

% ionisation:	(a) 0.098%,	(b) 0.077%,	(c) 0.067%.
% dissociation:	(a) 0.120%,	(b) 0.155%,	(c) 0.169%.

Table 2: Neutraliser H_2 gas percentage ionisation & dissociation for neutraliser H_2 gas densities; (a) $3x10^{19}m^{-3}$, (b) $6x10^{19}m^{-3}$, (c) $9x10^{19}m^{-3}$.

The ionisation fractions (*Table 2*) decrease with neutraliser gas density (cf. *Figure 54 (a)*), and are all less than 0.1%, which limits the number of plasma-gas collisions and hence the potential plasma particle contribution to gas heating (*Sections 5.1* & *5.2*). The dissociation fractions (*Table 2*) increase with neutraliser gas density, and are likewise relatively small, thus also limiting the potential gas heating contribution from fast dissociated H^+/H plasma particles - which account for two out of the three gas heating pathways in the Paméla gas heating model (*Appendix D*) [31, 34] cf. *Sections 5.1* & *5.2*.

4.4.2 Results versus beam power

(a)

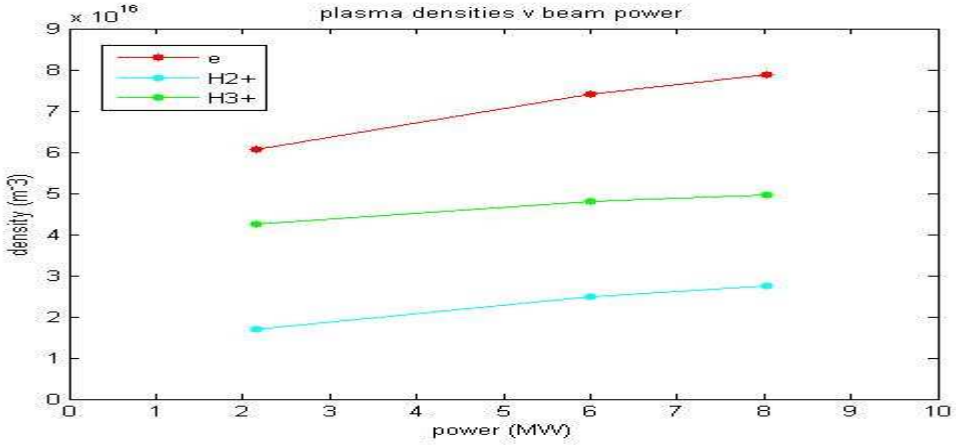

(b)

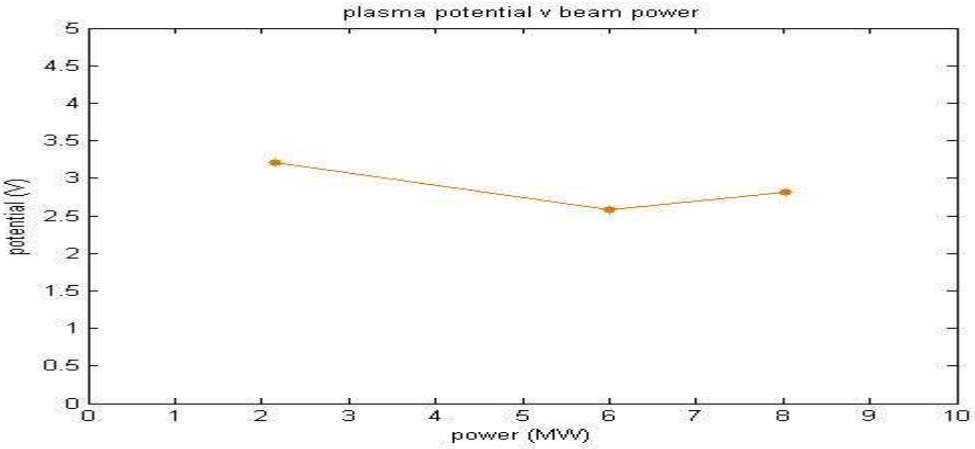

(c)

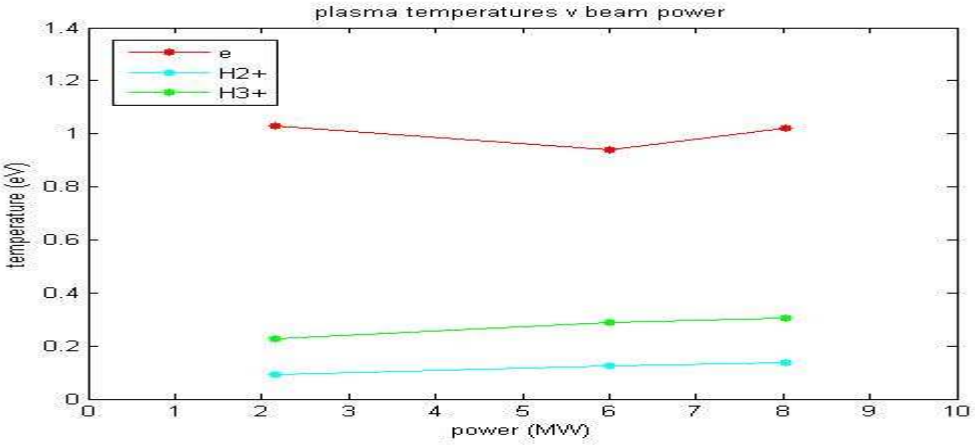

Figure 56: Steady-state (a) plasma densities, (b) potentials and (c) temperatures, as a function of the proton beam power (neutraliser H_2 gas density, $9x10^{19}m^{-3}$).

In contrast to the positive ion trend with neutraliser H_2 gas density (*Figure 54 (a), Section 4.4.1*), the H_3^+ ion becomes less dominant at higher beam powers (*Figure 56 (a)*). As mentioned in *Section 4.4.1* such conclusions could be misleading due to the

lack of exact like-with-like comparison criteria e.g. differing evolution time and simulation parameters. The 2.16MW simulation - first data points, *Figure 56* - used less computational cells (8000) than the other two (10000), while all three have differing particle weights (one beam particle per cell in each). Moreover, due to computational resource limitations, the number of particles per cell in each simulation was less than ideal, leaving unanswered questions regarding convergence (cf. *Section 2.1.4*) e.g. how much would the results vary with more particles per cell ?

Displayed below (*Table 3*) are the percentage direct neutraliser gas ionisation contributions from the three ionisation source particles.

	bH+	bH	e
2.16 MW	68.5%	18.1%	13.4%
6.00 MW	79.9%	9.8%	10.3%
8.04 MW	80.5%	9.2%	10.3%

Table 3: Steady-state bH^+, bH and electron percentage ionisation contributions, at the three hydrogen beam powers: (a) 2.16 MW, (b) 6.00 MW, (c) 8.04 MW.

The (less than linear) increase in electron density with beam power (*Figure 56 (a)*) is due to the greater number of beam particles at the higher beam powers (cf. *Table 4*) and hence the greater number of beam (and electron) impact ionisations i.e. due to the increase in the beam density rather than the increase in beam energy.

Increasing the beam energy above 60keV actually lessens the beam impact ionisation (cf. *Section 4.2.2*), since the beam H^+ impact ionisation cross sections (cf. attached CD) peak at ~ 60keV (that for beam H peak at ~ 28keV, and decrease more sharply over the 80-134 keV energy range, causing their % ionisation contribution to decrease with beam power, *Table 3*). This effect is further compensated by electron impact ionisation (cross sections increase up to ~ 70eV), since the electron temperature increases with beam power (*Figure 56 (c)*; the second and third data points together provide a more reliable trend - better like-with-like comparison criteria - than any trend encompassing the first data point, which may be relatively overestimated as explained in *Section 4.4.1*).

Simulations at constant beam energy and density would be required to obtain separate plasma parameter correlations with beam density and energy, respectively.

The trend in plasma potential versus beam power (*Figure 56 (b)*) follows the trend in electron temperature versus beam power (*Figure 56 (c)*), as would be expected. The H_3^+ & H_2^+ ion temperatures are considerably lower than the electron temperatures, and are shown to increase with beam power (*Figure 56 (c)*).

The (greater than linear) rise in electron impact ionisation (process whereby electrons lose most energy) reaction rates with beam power (*Figure 57*) - bearing in mind the less than linear relationship between electron density and beam power (*Figure 56 (a)*) – 'implies' more electron energy loss (per electron) at higher beam powers. However, the increasing trend in electron temperatures with beam power can be explained by the fact that the electrons receive more energy (in electron 'forming' beam-H_2 collisions) at higher beam energies [56] cf. [69, 70], which is consistent with *Figure 57*.

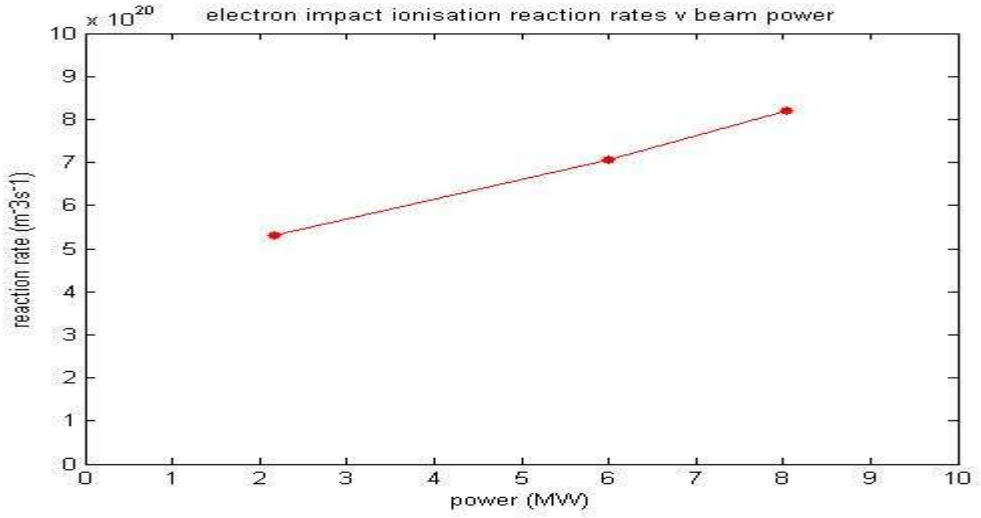

Figure 57: Steady-state electron impact ionisation reaction rates as a function of the proton beam power.

The dissociation fractions (*Table 4*) increase significantly at higher beam powers. Coupled with the higher plasma particle temperatures at higher beam powers (*Figure 56 (c)*), these results predict a larger plasma particle gas heating contribution at higher beam powers, which is consistent with the gas heating calculations (*Section 5.3*).

% ionisation:	(a) 0.067%,	(b) 0.082%,	(c) 0.087%.
% dissociation:	(a) 0.169%,	(b) 0.232%,	(c) 0.270%.

Table 4: Neutraliser H_2 gas percentage ionisation & dissociation for hydrogen beam powers; (a) 2.16 MW, (b) 6.00 MW, (c) 8.04 MW.

4.4.3 Comparison with Experimental Data

For varying neutraliser gas density

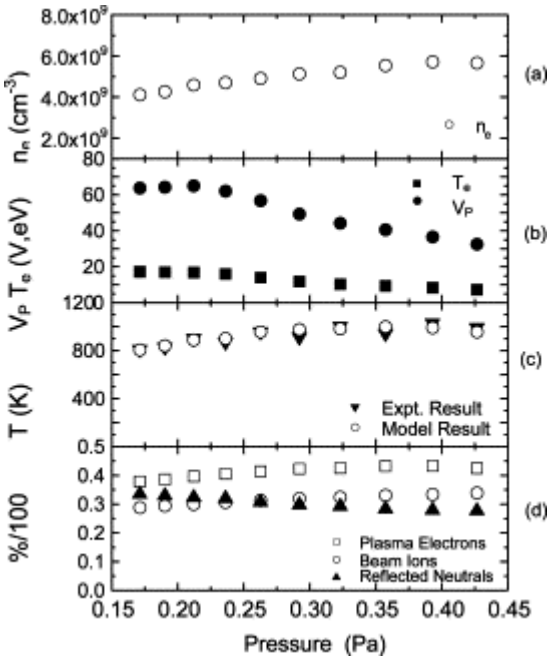

Figure 58: Plasma parameters (electron density, electron temperature, plasma potential), neutraliser H_2 gas temperature and percentage contributions from the three gas heating mechanisms considered in the Pamela model, as a function of (beam off) neutraliser H_2 gas pressure (80keV/32A multiple ion hydrogen beam injection) [36].

The neutraliser H_2 gas densities investigated in the simulations; $3x10^{19}m^{-3}$, $6x10^{19}m^{-3}$, $9x10^{19}m^{-3}$ (effectively *beam on* gas densities as opposed to the *beam off* gas pressures in *Figure 58*) equate to ~ 0.125Pa, 0.248Pa, 0.372Pa, respectively, assuming the validity of the ideal gas equation, and a H_2 gas temperature of 300K. Although in reality the neutraliser gas temperature increases [30] (cf. *Section 5.2*) causing a depletion in gas density. Since the simulated neutraliser gas density is kept fixed (undepleted), the simulations thus overestimate the plasma densities (*Figure 54 (a), Section 4.4.1*).

An overestimation of plasma densities results in an underestimation of electron temperatures and plasma potentials (*Figure 54, Section 4.4.1*). Moreover, since the simulated beam has reached charge-equilibrium, the plasma potentials, which decrease along the neutraliser as less excess positive charge is produced cf. *Section 2.2.4*, effectively represent values at the end of a correspondingly thick neutraliser.

Another reason for the discrepancy between the simulation and experimental results is due to the fact that the simulations are run with a 80keV/27A two-component (H^+, H) beam, as opposed to the 80keV/32A multiple ion hydrogen beam (consisting of H^+, H_2^+, H_3^+ beam species in proportions similar to those shown in *Figure 32, Section 4.1*) used in the experimental diagnostic investigation (*Figure 58*).

Notwithstanding the aforementioned quantitative comparison limitations, the trends in electron density, plasma potential and electron temperature with neutraliser gas density (*Figure 58*) seem consistent with the simulation results (*Figure 54, Section 4.4.1*).

The *Deuterium* results shown in *Figure 59* (beam power, 1.15MW) correspond to an electron density of $2.9 \times 10^{15} m^{-3}$ and an electron temperature of 6.31eV [36]. Such beam & plasma parameter magnitudes differ significantly to those of the beam plasma simulations, although a comparison is a still worthwhile.

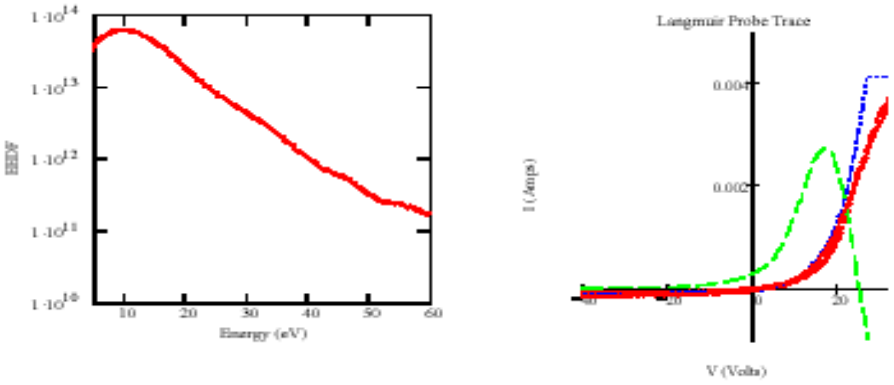

Figure 59: Electron energy distribution function and Langmuir probe I/V trace [36].

The logarithmic electron energy distribution function was obtained by interpreting the Langmuir Probe Trace - I/V characteristic - (*Figure 59*) [36]. A slight trough (15-60 eV) could be interpreted from the curve (*Figure 59*). This may be caused by a depopulation of electrons over this energy range due to electron inelastic collisions. At ~ 50eV the slope of the eedf curve increases significantly. In the simulations, the electron energies are significantly less, although a similar change in slope is evident in the tail of the eedf (*Figure 90, Appendix C*), signalling the presence of more high energy electrons than what would be the case with a Maxwellian-like distribution. The simulation results confirm that beam electron-stripping collisions are the supply source of these high-energy electrons. A similar larger than expected presence of high-energy H_2^+ ions,

evident from their energy distribution functions (*Figure 92, Appendix C*), might also be due to the relatively high-energy H_2^+ forming beam collisions (i.e. ionisation and electron capture cf. *Section 2.2.2*). In contrast, the H_3^+ particles are not directly formed in beam collisions, and subsequently their energy distribution functions (*Figure 94, Appendix C*) show no such high-energy tails.

For varying beam power

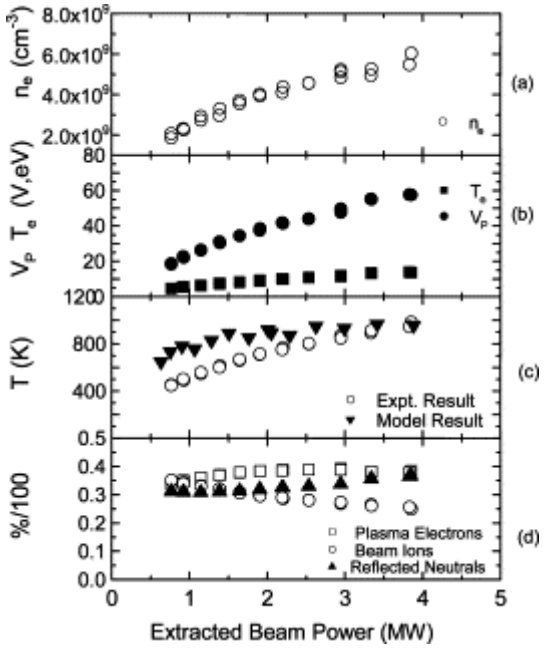

Figure 60: Plasma parameters (electron density, electron temperature, plasma potential), neutraliser H_2 gas temperature and percentage contribution from the three gas heating mechanisms considered in the Pamela model, as a function of beam power (at constant initial neutraliser H_2 gas pressure) [36].

The beam power range investigated in the simulations is 2.16-8.04 MW, while the experimental results from Crowley et al. [36] are at beam powers of ~ 0.7-3.8 MW (*Figure 60*). As in the trends with neutraliser gas density; the trends in electron density, plasma potential and electron temperature as a function of beam power (*Figure 60*) are similar to the simulation results (*Figure 56, Section 4.4.2*), although their respective magnitudes are different partly due to the comparison limitations previously mentioned.

For varying time

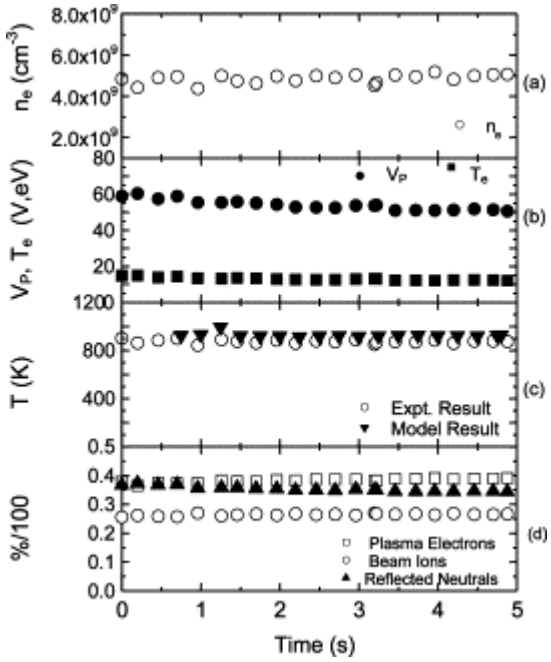

Figure 61: Plasma parameters (electron density, electron temperature, plasma potential), neutraliser H_2 gas temperature and percentage contribution from the three gas heating mechanisms considered in the Pamela model, as a function of time [36].

The experimental results (*Figure 61*) are for a 5 second 80keV/32A composite hydrogen beam pulse, in contrast to the 80keV/27A two-component (H^+, H) beam injection modelled in the simulations, over a much shorter time (*Figure 53*, *Section 4.3*).

The slight variations in time (*Figure 61*) were concluded to be due to fluctuations in the neutraliser gas flow [36]. In the simulation results (*Figure 53*, *Section 4.3*), slight variations in the steady-state plasma potentials (which cannot be due to variations in gas density since the simulation background gas has a constant density) maybe due to the prevalence of beam plasma waves. However, simulation inaccuracies (e.g. caused by using too few particles per cell) cannot be ruled out as their main cause.

See *Concluding Remarks - Chapter 7* - regarding general simulation limitations.

Chapter 5

Neutraliser Gas Heating

5.1 Gas Heating Calculations

5.1.1 Introduction & Calculation Approach

Paméla assumed that beam energy losses from elastic collisions with the neutraliser gas are negligible [31, 34]. This claim might not seem intuitively obvious, although the cross section [53] for H_2 ionisation by a 100keV proton is ~ 100,000 times greater than the cross section [54] for a 100keV proton-H_2 elastic collision cf. [69]. The results of this work further support Paméla's assumption, since only a few beam elastic collisions occurred in the simulations. Hence, the neutraliser gas can only get significantly heated *indirectly* by the beam i.e. the beam breaks down the neutraliser gas to form fast particles, which (themselves or by forming other particles through further breakdown of the gas via their impact e.g. electrons) are either formed with or subsequently acquire sufficient energy (e.g. via acceleration across sheath regions or via Coulomb collisions with the beam), and are sufficiently numerous and massive enough, to transfer significant kinetic energy to the neutraliser gas molecules (via elastic collisions).

In addition to the gas heating mechanisms accounted for by Paméla (*Appendix D*), the (*Transverse*) simulation results enable other possible gas heating mechanisms to be quantified, thereby providing a more complete picture of the gas heating process. A steady-state situation is assumed in the calculations, whereby the gas power gained indirectly from the beam equals the gas power lost at the neutraliser walls (assuming the gas has reached a constant increased temperature). Like Paméla, we assume a composite coefficient of 0.3 (*Section 2.2.2*) to account for reflected H_2 molecules (recombination and/or reflection probability multiplied by the reflected energy fraction), and a (neutraliser wall) thermal accommodation coefficient of 0.5 for the H_2 molecules [31].

The calculation procedure to find the resultant decrease in neutralisation efficiency due to gas heating consists of four interconnected calculation steps. *Step 1* (*Section 5.1.2*) entails computing the beam indirect power density transfer to the neutraliser gas and is obtained from *Transverse* simulation results, using (MATLAB) computational procedures to integrate the kinetic energy transferred (from fast particle elastic collisions with the neutraliser gas) and the corresponding rate coefficients $\{\sigma(E)v_f(E)\}$ over the particle energy distributions. *Step 2* (*Section 5.1.3*) calculates the neutraliser gas temperature rise via inputting the results from the first step into the steady-state

neutraliser gas power balance equation, Equation (5.6). *Step 3* (*Section 5.1.4*) uses the neutraliser gas temperature rise results of the previous step to estimate the neutraliser gas line density depletion. Two probable density-temperature models are investigated; one based on a standard density-temperature relationship (from molecular/transitional gas flow theory [29]) i.e. assuming that the neutraliser gas line density is inversely proportional to the square root of the gas temperature, and the other based on the ideal gas law density-temperature relationship [19] i.e. the gas target being inversely proportional to the gas temperature. Finally, *Step 4* (*Section 5.1.5*) translates the gas target depletion results of the previous step into resultant neutralisation efficiencies.

5.1.2 Power Transfer to the Neutraliser Gas

This calculation technique is based on computing the beam indirect power density transfer to the H_2 gas, in elastic collisions of fast particles (x_f) with the H_2 gas:

$$x_f + H_2 \rightarrow x_f + H_2$$

The contribution from all simulated particles is obtained (whether they be deemed relatively fast or not) via the following power density transfer (p_{den}) formula:

$$p_{den} = n_f n_{H_2} \int_0^{E_{max}} \sigma(E) v_f(E) \xi E_f f(E) dE \qquad (5.1)$$

n_f = fast particle density
n_{H2} = H_2 density
σ = fast particle-H_2 elastic cross section
v_f = fast particle velocity
E_f = fast particle K.E.
E_{max} = fast particle max K.E.
f = energy distribution function
ξ = K.E. transfer fraction
m_f = fast particle mass
m_{H2} = H_2 mass
θ = elastic (post) collision angle

$$\xi = \frac{4 m_f m_{H_2}}{(m_f + m_{H_2})^2} (\cos^2 \theta) * \qquad [43] \qquad (5.2)$$

$$v_f = \sqrt{\frac{2E_f}{m_f}} \qquad (5.3)$$

{*: $\cos^2\theta$ is approximated as 0.5 (its integral from 0 to 2π) in all calculations}

An algorithm composed in the programming language available in MATLAB is used to perform the above integration (using Simpson's Rule [71]). The required data for this calculation is obtained from the 1D3v PIC MCC *Transverse* simulation results (along with simulation input data i.e. cross sections and particle masses).

5.1.3 Neutraliser Gas Temperature Rise

Considering the neutraliser as a closed system, the first law of thermodynamics implies:

$$\frac{dE_{den}}{dt} = p_{den} - \nabla q \tag{5.4}$$

Increase in energy stored within = heat generated within - net heat conducted out

{where E_{den} (Jm^{-3}) is the internal energy density of the neutraliser gas, p_{den} (Wm^{-3}) is the power density transferred to the neutraliser gas, and q (Wm^{-2}) is the heat flux}

The neutraliser system is assumed to evolve into a steady-state situation when the gas reaches a constant (increased) temperature i.e. when:

$$\frac{dE_{den}}{dt} = 0$$

Equation (5.4) $\Rightarrow$

$$\nabla q = p_{den} \tag{5.5}$$

power density loss in gas-wall collisions = power density transferred to neutraliser gas

{assuming no other significant energy sinks for the (volume-averaged) neutraliser}

Energy loss from gas-wall collisions: $\frac{5}{2}k(T - T_r) = \frac{5}{2}k\alpha(T - T_w)$

Definition of the accommodation coefficient, α: $\alpha = (T - T_r)/(T - T_w)$

{assuming 5 degrees of freedom for the H_2 molecule i.e. 3 translational and 2 rotational, where k is Boltzmann's constant, T the (increased) neutraliser gas temperature, T_r the 'temperature' of the reflected particle, and T_w the neutraliser wall temperature}

Equation (5.5) can also be expressed as a power balance equation:

$$(\tfrac{n_{H_2} v}{4}) S_w \tfrac{5}{2} k\alpha (T - T_w) = V_{cde} \sum p_{den} \qquad \{\text{cf. Paméla formula (D.1), } \textit{Appendix D}\} \qquad (5.6)$$

(*gas thermal flux to neutraliser walls*)(*total sidewall area*)(*energy loss from gas-wall collisions*) = (*neutraliser volume*)(*total power density transferred to neutraliser gas*)

Being the only unknown in the steady-state neutraliser gas power balance equation, Equation (5.5), the increased neutraliser H_2 gas temperature (T) can thus be computed.

The following neutraliser parameters are assumed to be sufficiently accurate: Volume of the neutraliser, V = 0.2m x 0.44m x 1.86m = 0.16368m^3. Constant density equivalent neutraliser volume, V_{cde} = 0.772(V) = 0.126 m^3 (accounts for the linear decrease in neutraliser gas density in the second stage of the neutraliser, *Figure 10, Section 1.3.2*). Total neutraliser sidewall area, S_w = 2(0.44m x 1.86m) + 2(0.2m x 1.86m) = 2.3808m^2. Accommodation coefficient, α = 0.5 [31, 34]. Neutraliser wall temperature, T_w = 375K (averaged over both neutraliser stages [30]). Neutraliser gas thermal velocity, $v = (8kT/\pi m)^{1/2}$ [43] (k, Boltzmann constant. m, mass of the H_2 molecule).

5.1.4 Neutraliser Gas Target Depletion

Standard density-temperature relationship:

Here the neutraliser gas target is assumed to be inversely proportional to the square root of the gas temperature as follows from molecular/transitional gas flow theory [29]:

$$< nL > \propto \frac{1}{\sqrt{T}} \qquad (5.7)$$

Ideal Gas Law density-temperature relationship:

Alternatively the neutraliser gas target may be assumed to be inversely proportional to the gas temperature [19]:

$$< nL > \propto \frac{1}{T} \qquad (5.8)$$

5.1.5 Resultant Decrease in Neutralisation Efficiency

The neutraliser H_2 gas line density can be substituted (cf. the *interchangeable variables* technique, *Section 2.2.4*) for the time parameter along the x-axis of *Figure 36, Section 4.1* (80keV beam), as shown in *Figure 62*. Given the reduced gas line density (*Section 5.1.4*), the reduced beam total neutral component mean energy density (and hence the reduced neutralisation efficiency) can thus be read/interpolated from *Figure 62*. Due to the exponential nature of the beam mean energy density components as a function of the gas target (*Figure 62*), a 50% reduction in optimum gas target, for example, only results in a reduction in neutralisation efficiency of < 10% {the two-component 80keV hydrogen beam model (initial beam composition of 100% protons) predicts a slightly higher reduction in neutralisation efficiency (*Figure 9, Section 1.3.1*)}, even less for higher beam energies (*Figure 63*) cf. *Figure 43, Section 4.1* (120keV beam).

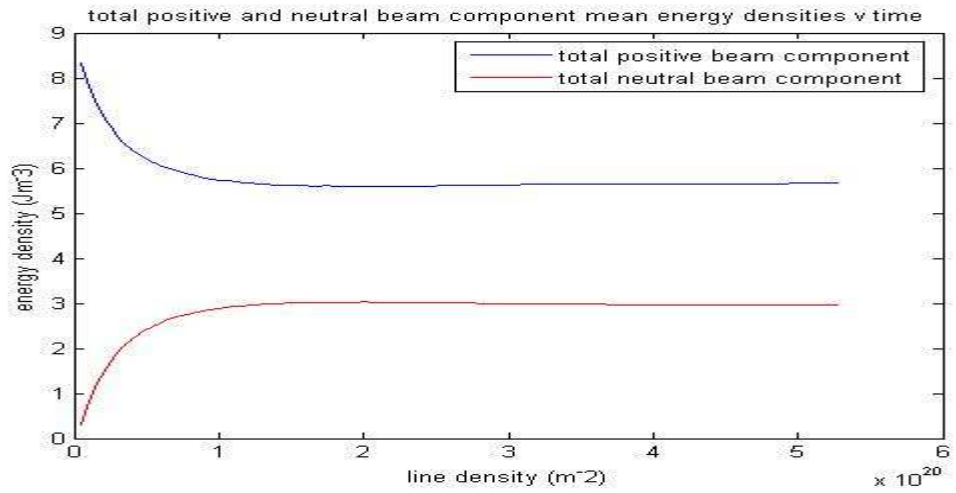

Figure 62: positive/neutral beam component mean energy densities versus gas target.

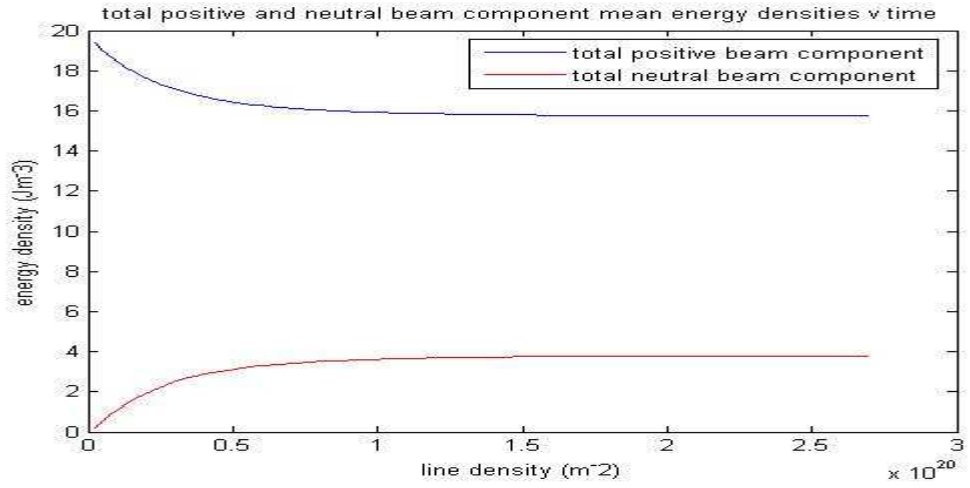

Figure 63: positive/neutral beam component mean energy densities versus gas target.

5.2 Results for varying Neutraliser Gas Density

	e	H2+	H3+	f5H+	f10H+	aH	fH	f5H	xH2	rxH2	rnH2
(a)	8.7	11.2	27.5	0.9	0.5	32.3	8.4	0.5	0.1	0.1	9.8
(b)	7.0	8.0	37.4	0.8	0.5	31.9	8.1	0.4	0.1	0.2	5.6
(c)	5.7	6.9	46.8	0.6	0.5	28.1	7.4	0.4	0.2	0.2	3.2

Table 5: Percentage power density transfer contribution from each simulated particle for neutraliser H_2 gas densities; (a) $3x10^{19}m^{-3}$, (b) $6x10^{19}m^{-3}$, (c) $9x10^{19}m^{-3}$.

	total p_{den} transfer	total beam p_{den} loss	% of total p_{den} loss	increased temperature	% decrease in gas target
(a)	$138.2Wm^{-3}$	$5021Wm^{-3}$	2.8%	402K	14%, 25%
(b)	$570.5Wm^{-3}$	$10033Wm^{-3}$	5.7%	429K	16%, 30%
(c)	$1424.3Wm^{-3}$	$15039Wm^{-3}$	9.5%	463K	20%, 35%

Table 6: Total power density transfer, total beam power density loss (Section 4.2.1), percentage of total beam power density loss, increased temperature, and percentage decrease in neutraliser gas target (two models, Section 5.1.4) for neutraliser H_2 gas densities; (a) $3x10^{19}m^{-3}$, (b) $6x10^{19}m^{-3}$, (c) $9x10^{19}m^{-3}$ (2.16MW hydrogen beam).

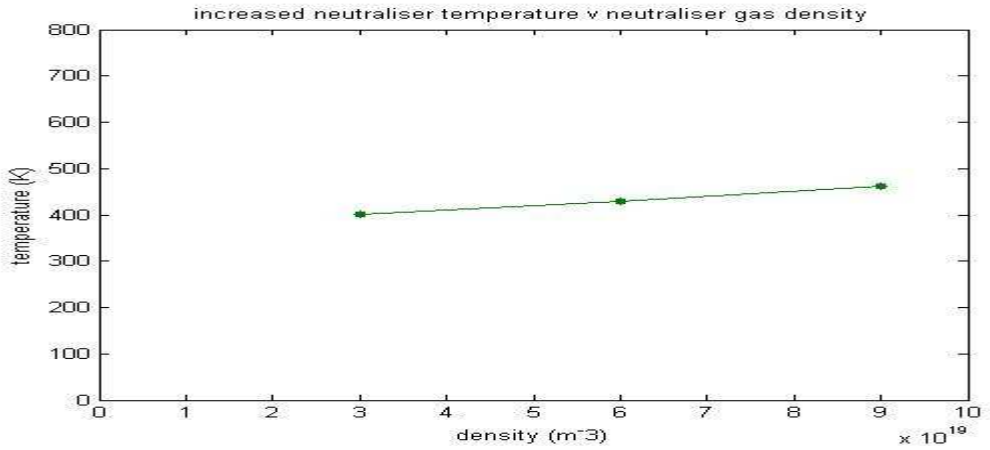

Figure 64: Increased neutraliser temperature as a function of neutraliser gas density.

Results of Crowley et al. [36] show a 'saturation' of the neutraliser gas temperature (~ 1100K, *Figure 58*, *Section 4.4.3*) for an equivalent neutraliser H_2 gas density of ~ $9x10^{19}m^{-3}$. The neutraliser gas temperature results (*Figure 64*) show a linear rise in temperature with density, while 'saturation' is not evident. Further simulations at higher gas densities would be required to establish whether temperature 'saturation' occurs.

The relative contributions from Paméla's three gas heating mechanisms (*Figure 58, Section 4.4.3*) differ to that of the simulation results (*Table 5*), which indicate that H_3^+ ions, H atoms (formed via H_3^+ formation i.e. H_2^+ association collisions with the neutraliser gas cf. *Section 2.2.2*), H atoms (formed by dissociation of the neutraliser gas), H_2^+ ions, electrons and reflected neutralised H_2^+ ions are the six main sources of gas heating. Paméla's gas heating model (*Appendix D*) [31, 34] doesn't account for four of these gas heating pathways. Moreover, contrary to the Paméla model (and the results of Crowley et al. [36]; *Figure 58, Section 4.4.3*), the simulation results (*Table 5*) predict that particles; f5H+, f10H+, fH, f5H and rnH2 have a relatively small gas heating effect {regarding the rnH2 contribution; H_3^+ ions are the majority positive ion in the simulations (*Section 4.4*), although reflected neutralised H_3^+ ions were not simulated. Paméla inferred from his "naïve [plasma] model" [34] that the D_2^+ ion should be the dominant plasma ion for neutraliser (D_2) gas densities less than ~ 1e20m^{-3}}.

The electron direct (via electron-H_2 elastic collisions) and indirect (via H_2 ionisation and dissociation) contribution to gas heating is significant (*Table 5*). If electrons were somehow slowed-down/removed from the neutraliser gas (e.g. by the use of weak magnets, which would not significantly affect the beam propagation), the plasma density (positive ions being electrostatically coupled to the electrons) and/or the electron temperature, could be reduced, subsequently reducing the gas heating (thus also reducing gas flow requirements), resulting in an increased neutralisation efficiency. Magnets are already employed to reduce the electron density & temperature in negative ion sources [25] in order to increase the negative ion formation, while other magnets are used downstream in the extraction grids [25] to deflect electrons so as to prevent them from being accelerated along with the negative ion beam (positive ion, arc discharge sources [6] use magnets to confine electrons in order to maximise the number of electron impact ionisations – the opposite effect to that desired in the neutraliser).

These gas heating calculations yield substantially lower neutraliser gas temperatures than those calculated by Surrey & Crowley [30] cf. *Figure 58, Section 4.4.3* [36]. As explained in *Section 5.1.5*, the biggest gas density depletion of 35% (*Table 6*, assuming an inversely proportional relationship between the gas target and the gas temperature) only gives a < 5% reduction in neutralisation efficiency. This is considerably less than would be inferred from the neutral beam power measurements [19] and that predicted by the Paméla gas heating model [31, 34] (*Figure 11 (a), Section 1.3.4*).

5.3 Results for varying Beam Power

	e	H2+	H3+	f5H+	f10H+	aH	fH	f5H	xH2	rxH2	rnH2
(a)	5.7	6.9	46.8	0.6	0.5	28.1	7.4	0.4	0.2	0.2	3.2
(b)	3.4	10.3	51.7	0.4	0.3	24.3	4.9	0.2	0.3	0.5	3.7
(c)	3.4	11.3	51.4	0.3	0.2	23.6	4.8	0.2	0.4	0.6	3.8

Table 7: Percentage gas heating contribution from each simulated particle for Hydrogen beam powers; (a) 2.16 MW, (b) 6.00 MW, (c) 8.04 MW.

	total p_{den} transfer	total beam p_{den} loss	% of total p_{den} loss	increased temperature	% decrease in gas target
(a)	1424.3Wm^{-3}	15039Wm^{-3}	9.5%	463K	20%, 35%
(b)	2451.0Wm^{-3}	22780Wm^{-3}	10.8%	518K	24%, 42%
(c)	2896.8Wm^{-3}	26112Wm^{-3}	11.1%	540K	25%, 44%

Table 8: Total power density transfer, total beam power density loss (Section 4.2.4), percentage of total beam power density loss, increased temperature, and percentage decrease in neutraliser gas target (two models, Section 5.1.4) for Hydrogen beam powers; (a) 2.16 MW, (b) 6.00 MW, (c) 8.04 MW (H_2 density of 9x10^{19}m^{-3}).

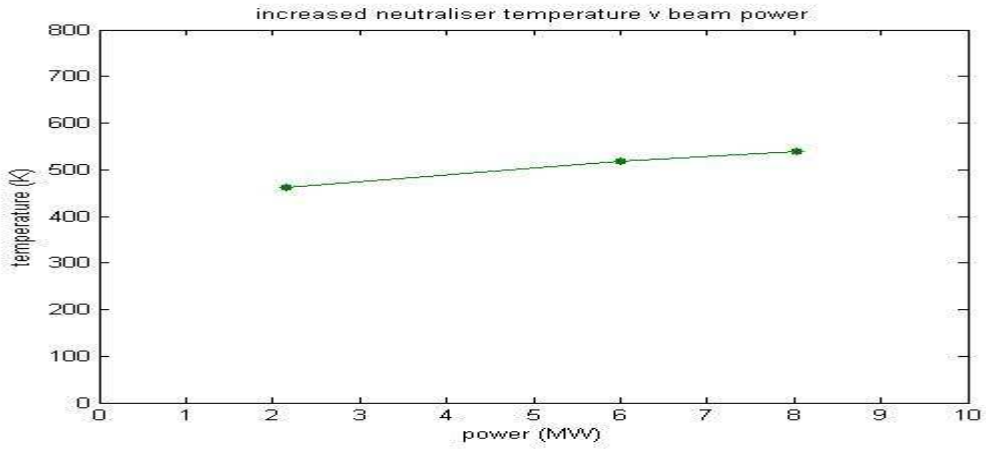

Figure 65: Increased neutraliser temperature as a function of beam power.

Similarly to *Section 5.2*, H_3^+ ions are the dominant contributors to gas heating (*Table 7*), and the increased gas temperatures (*Figure 65*) are significantly lower than those calculated by Surrey & Crowley [30] cf. *Figure 60, Section 4.4.3* [36]. The biggest gas density depletion of 44% (*Table 8*) – "70%" [19] - only gives a < 2% reduction in neutralisation efficiency (*Figure 63, Section 5.1.5*), and therefore doesn't account for the neutral beam power discrepancies shown in *Figure 11 (a), Section 1.3.4*.

Chapter 6

Negative Ion Beam Plasma Simulations

6.1 Neutralisation of Negative Ion Beams

6.1.1 ITER Neutral Beam Injectors

Neutral beam heating for the ITER tokamak requires neutral beams of energy ~ 1MeV (partly due to deposition location constraints [72]). As can be seen from *Figure 66*, positive beams would yield virtually no neutral component at such energies, although negative beams yield a relatively high (~ 60%) neutralisation fraction, due to the fact that at high energy there is more likelihood of an electron getting stripped (e.g. low electron binding energy of 0.75eV for H^-) from the beam, rather than one being captured from the neutraliser gas, evidenced by their respective cross sections [60].

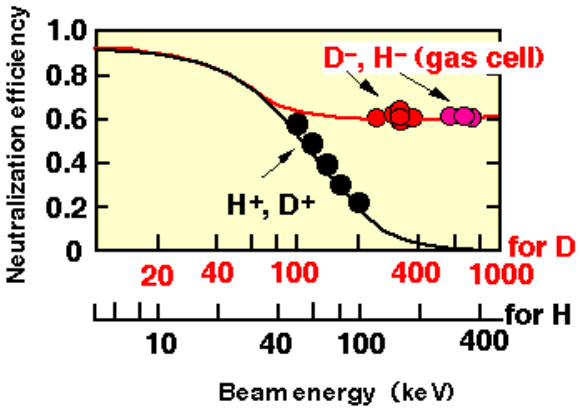

Figure 66: Plot of neutralisation efficiency versus beam energy for Hydrogen and Deuterium positive and negative ion beams (assuming their passage through their respective molecular gas neutraliser cells of optimum line density) [7].

Unlike positive beam neutralisation (*Section 4.1*), the optimum neutraliser gas line density (i.e. pertaining to maximum neutralisation efficiency) is considerably less than that required to produce beam charge-equilibrium (the positive beam component begins to dominate with denser gas targets, in agreement with *Figures 67* & *68* in *Sections 6.1.2* & *6.1.3*, respectively). Research in negative ion neutral beam injection (e.g. in ion sources, 1MeV accelerators, electrostatic beam ion deflection etc.) is still ongoing in the lead up to ITER [72]. Such smaller scale injection is operational at; the JT-60U tokamak in Naka, Japan [73, 74, 75], the DIII-D tokamak in San Diego, USA [76], and the Large Helical Device (LHD) in Toki, Japan (world's largest superconducting stellarator) [77].

Surrey [40] has adapted her beam plasma model for positive beams [22] into a model for the ITER heating (HNB) and diagnostic (DNB) negative ion neutral beam injectors. She suggests that the stripped electrons (~ 55eV, 100keV H^- beam energy multiplied by the ratio of the electron mass to the beam particle mass) produced in the DNB neutraliser (beam plasma), might become significantly thermalized, while the ~ 270eV

stripped electrons from the HNB 1MeV D^- beam are unlikely to be sufficiently thermalized (cf. *Figures 74 (c) & 78 (c)*). She concludes by saying that gas heating is unlikely to be severe in either of the injectors, and that the gas target is therefore expected to remain close enough to the design value. Again, as in the case of her similar positive beam analytical model for the JET neutraliser plasma, she states that a "much more sophisticated code" would be needed for "any detailed analysis". To this end, the PIC MCC simulation method, presented already for positive ion beams (*Chapters 1 - 5*), is thus applied in a similar way to model the ITER (DNB & HNB) neutralisers.

To the best of our knowledge, the only readily available cross section data for such (relatively high energy) negative ion beams, is for their charge-changing collisions. Surrey gets around this obstacle by setting the cross sections for negative beams as equal to that for positive beams [40]. She backs this claim up by making reference to Fogel et al. [78, 79], who apparently observed that they are similar in the case of (10-50 keV) beam impact ionisation. Conflicting data from Buckman & Phelps [52] show (10keV) H^+ impact ionisation cross sections of nearly 3 times larger magnitude than that for H^-. Despite this lack of authoritative data, DNB & HNB beam plasma simulations – the results of which are reported in the remainder of this chapter - adopt this approach of assuming an equality between positive and negative beam collision cross sections.

The DNB beam consists of a 100keV/60A (300A/m^2, 15A per channel) H^- beam [72]. As in the positive case, the DNB beam is assumed to have a top-hat density & velocity spatial profile with a narrow rectangular beam head area of 0.0966m^2 (0.07m x 1.38m), centred in a neutraliser channel of dimensions 0.10m, 1.60m, 3.00m [40, 72] (horizontal/transverse (*x*), vertical (*y*), axial/longitudinal (*z*), neutraliser/beam dimensions, respectively). The DNB neutraliser (decoupled from the accelerator to allow intervening gas pumping so as to minimise stripping losses in the accelerator [72]) is divided into four equal (vertical) channels (to reduce gas conductance [80]), separated by 5 panels, each with three 1.00m length (axial) sections (relatively short compared to the 10m neutralisers on JT-60U - to minimise space and construction cost [80]) of height 1.60m [40, 72]. It is therefore sufficient to model only one neutraliser channel, which entails simulating a 100keV/15A H^- beam. Similarly to the calculations described in *Section 2.2.2*, this translates into a beam velocity of $4.380 \times 10^6 ms^{-1}$, a beam flux of $9.693 \times 10^{20} m^{-2} s^{-1}$, and thus a beam density of $2.213 \times 10^{14} m^{-3}$.

Likewise, the 1MeV/40A (200A/m^2, 10A per channel) D^- HNB neutraliser [72] has an almost identical design (0.10m x 1.70m x 3.00m), with a beam head area of 0.0952m^2 (0.07m x 1.36m) [40]. The simulation involves a 1MeV/10A D^- beam with velocity 9.795x10^6 ms^{-1}, flux 6.556x$10^{20}m^{-2}s^{-1}$, and density 6.693x$10^{13}m^{-3}$.

In the following beam composition results (*Sections 6.1.2* & *6.1.3*) four charge-changing collisions are simulated; H^-/D^- electron stripping (detachment), H/D electron stripping, H^-/D^- double electron stripping and H^+/D^+ electron capture (cross sections are taken from the ALADDIN website [53]). Similarly to *Section 4.1*, the optimum gas targets are calculated via the *interchangeable variables* technique cf. *Section 2.2.4*.

6.1.2 DNB Beam Composition Results

The length of the DNB neutraliser is 3m, so the 100keV H^- beam (neutraliser) transit time is 684ns (3m/4.380x10^6ms^{-1}). An initial overestimated guess of 2x$10^{19}m^{-3}$ (cf. [40, 72]) is used for the fixed H_2 gas density in this DNB *beam composition* simulation.

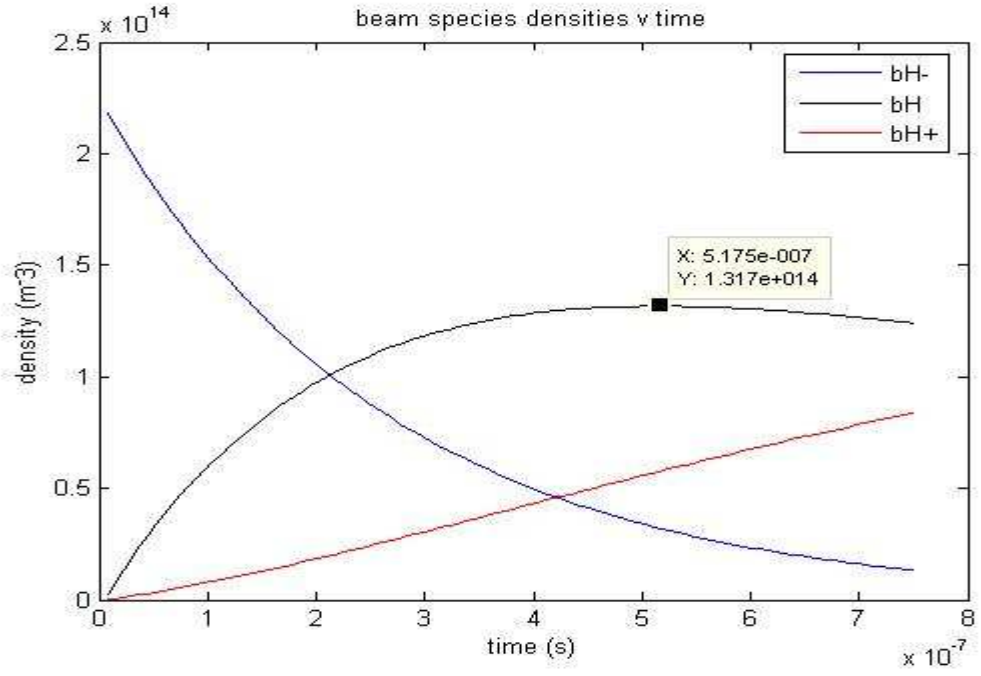

Figure 67: Evolution of the DNB beam species densities.

The theoretical maximum neutralisation efficiency is ~ 60% (1.317x$10^{14}m^{-3}$ /2.213x$10^{14}m^{-3}$, *Figure 67*). This maximum neutral beam density (mean energy density,

power) is reached at a time of ~ 517.5ns (*Figure 67*), which implies that the optimum neutraliser H_2 gas density is ~ $1.51x10^{19}m^{-3}$ {(517.5ns/684ns) x $2x10^{19}m^{-3}$}, giving an optimum gas target of ~ $4.53x10^{19}m^{-2}$ ($1.51x10^{19}m^{-3}$ x 3m). This value of $1.51x10^{19}m^{-3}$ for the DNB neutraliser optimum H_2 gas density is thus used in the DNB *beam plasma* simulations - the results of which are reported in *Sections 6.2.1*, *6.3.1* & *6.4.1*.

6.1.3 HNB Beam Composition Results

The 1MeV D^- beam transit time is 306ns ($3m/9.795x10^6ms^{-1}$). An initial overestimated guess of $8x10^{19}m^{-3}$ (cf. [40], [72]) is used for the fixed neutraliser D_2 gas density in this HNB *beam composition* simulation in order to find the optimum D_2 gas density (half energy Hydrogen cross sections are used as estimates for Deuterium cross sections).

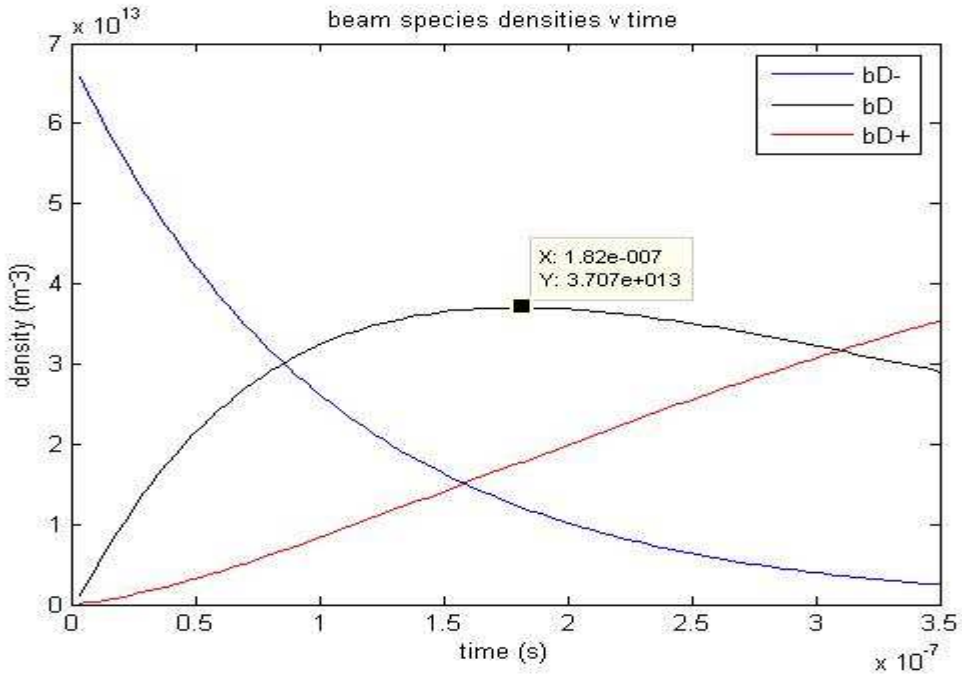

Figure 68: Evolution of the HNB beam species densities.

The theoretical maximum neutralisation efficiency is ~ 55% ($3.707x10^{13}m^{-3}$ /$6.693x10^{13}m^{-3}$, *Figure 68*). This maximum neutral beam power occurs at ~ 182ns (*Figure 68*), implying an optimum neutraliser D_2 gas density of ~ $4.76x10^{19}m^{-3}$ (182ns/306ns x $8x10^{19}m^{-3}$) i.e. an optimum gas target of ~ $1.43x10^{20}m^{-2}$ ($4.76x10^{19}m^{-3}$ x 3m) {≈$1.4x10^{20}m^{-2}$ [72]}. This value of $4.76x10^{19}m^{-3}$ for the HNB neutraliser optimum D_2 gas density is thus used in the HNB beam plasma simulations - the results thereof are reported in *Sections 6.2.2*, *6.3.2* & *6.4.2*.

6.2 Beam Power Loss during Neutraliser Transit

6.2.1 DNB Beam Power Loss Results

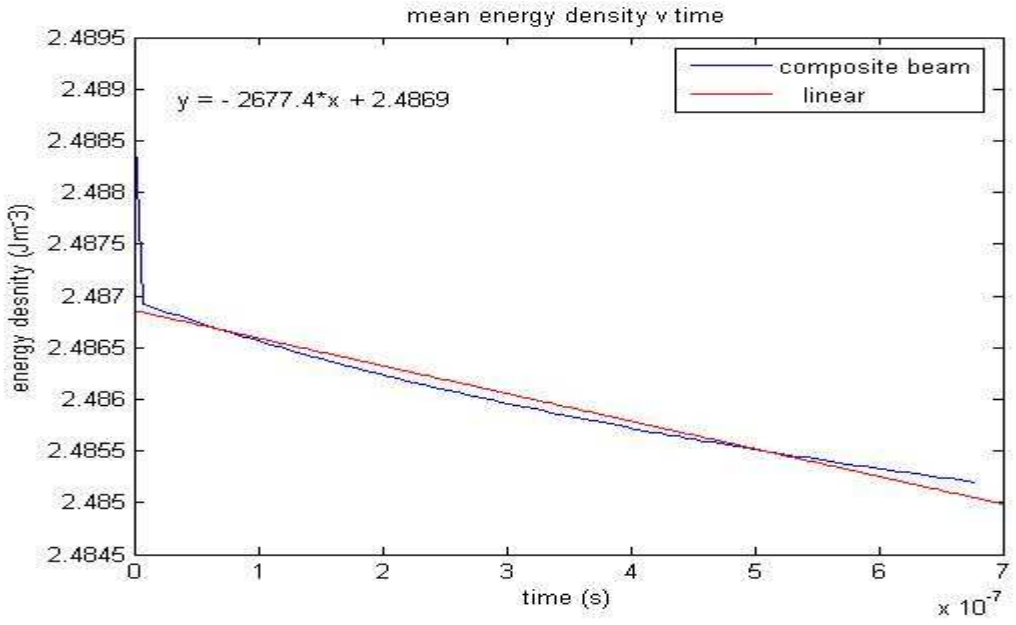

Figure 69: DNB beam mean energy density as a function of time.

Similarly to *Section 4.2*, the beam power density loss to the neutraliser gas is equal to the slope of the beam mean energy density versus time plot (*Figure 69*). Multiplying this value by the total constant density equivalent neutraliser channel volume (gives the total beam power loss) and then by the beam (neutraliser) transit time (*Section 6.1.2*), yields one quarter (4 channels) of the total beam energy lost in the neutraliser.

To calculate the average energy loss per beam particle during neutraliser transit, the total beam energy lost in each neutraliser channel is divided by the number of beam particles that reside in the constant density equivalent neutraliser channel volume at any given instant. The volume of one DNB neutraliser channel is $0.48m^3$ (0.10m x 1.60m x 3.00m), which can be taken as the constant density equivalent neutraliser channel volume, since the DNB (& HNB) neutraliser axial density profiles increase and decrease in ~ equal measures [81]. The number of beam particles that reside in the constant density equivalent neutraliser volume at any given instant is equal to the spatially averaged beam density ($2.213x10^{14}m^{-3}$ x 0.07m/0.10m, *Section 6.1.1*) multiplied by the neutraliser channel volume ($0.48m^3$); $7.436x10^{13}$ beam particles.

The total beam energy lost in each DNB neutraliser channel is therefore 2677.4Wm^{-3} x 0.48m^3 x 684ns, which works out at 8.790x10^{-4}J (5.487x10^{15}eV). This equates to ~ 0.074% {5.487x10^{15}eV/(100000eV x 7.436x10^{13}) x 100} of the total beam energy. In terms of energy loss per beam particle, 5.487x10^{15}eV corresponds to ~ 74eV (5.487x10^{15}eV/7.436x10^{13}) of energy lost on average by each beam particle.

Comparison of these DNB (& HNB) results with experimental stopping power measurements cannot be made at present, due to the lack of availability of relevant data.

6.2.2 HNB Beam Power Loss Results

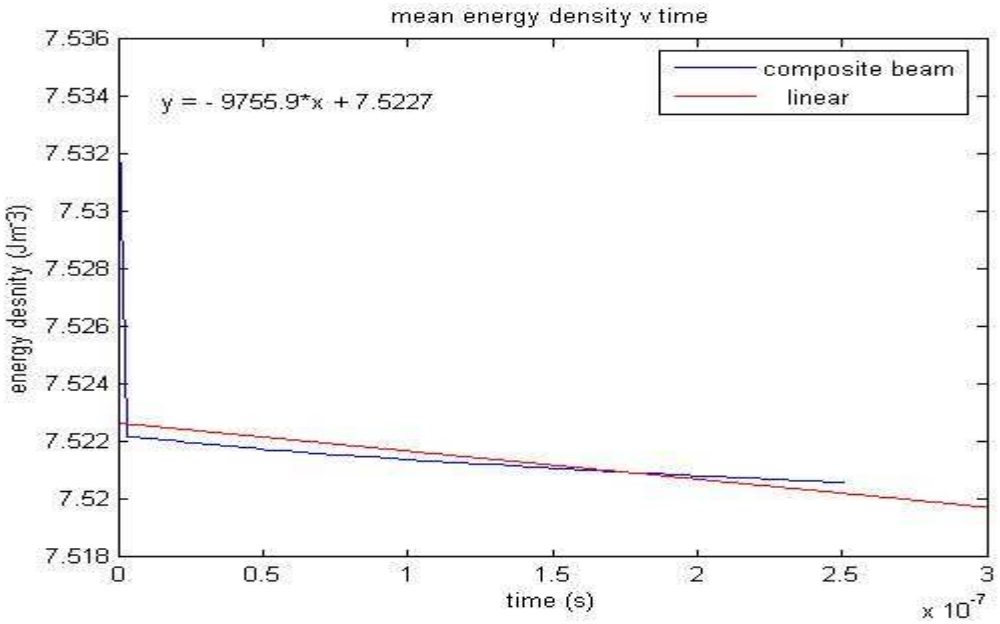

Figure 70: HNB beam mean energy density as a function of time.

The (constant) number of beam particles that reside in each HNB neutraliser channel is equal to the spatially averaged beam density (6.693x10^{13}m^{-3} x 0.07m/0.10m, *Section 6.1.1*) multiplied by the neutraliser channel volume (0.51m^3, *Section 6.1.1*), which gives a value of 2.389x10^{13} beam particles.

Similarly to *Section 6.2.1*, the total beam energy lost in each HNB neutraliser channel is 9755.9Wm^{-3} (*Figure 70*) x 0.51m^3 x 306ns (*Section 6.1.3*), which yields 1.523x10^{-3}J (9.504x10^{15}eV), and equates to ~ 0.040% {9.504x10^{15}eV/(1000000eV x 2.389x10^{13}) x 100} of the total beam energy and ~ 398eV (9.504x10^{15}eV/2.389x10^{13}) of energy lost on average by each beam particle.

6.3 Neutraliser Beam Plasma Characterisation

The ITER DNB & HNB initial beam 'plasma' evolution is shown in *Appendix E*, for the duration of their beam (neutraliser) transit times i.e. 684ns & 306ns, respectively. The DNB beam plasma simulation reached a definite steady-state (*Figure 66*), while the HNB simulation results are prior to steady-state (*Figure 70*).

6.3.1 DNB Beam Plasma Results

DNB beam plasma evolution to steady-state

(a)

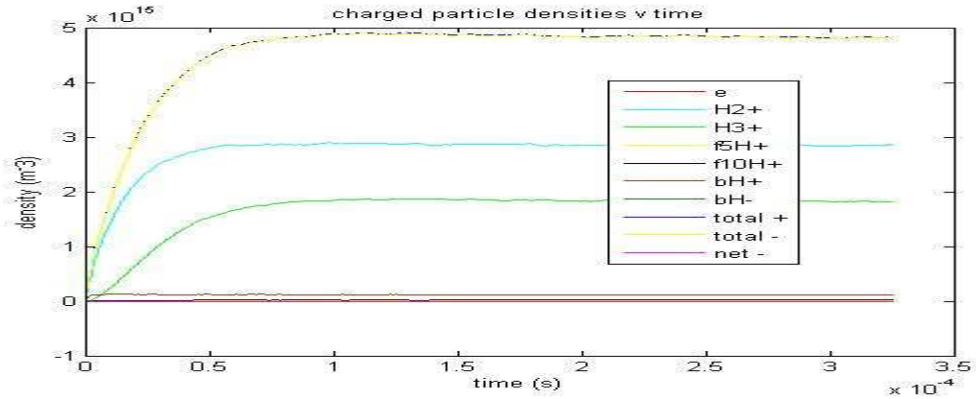

(b)

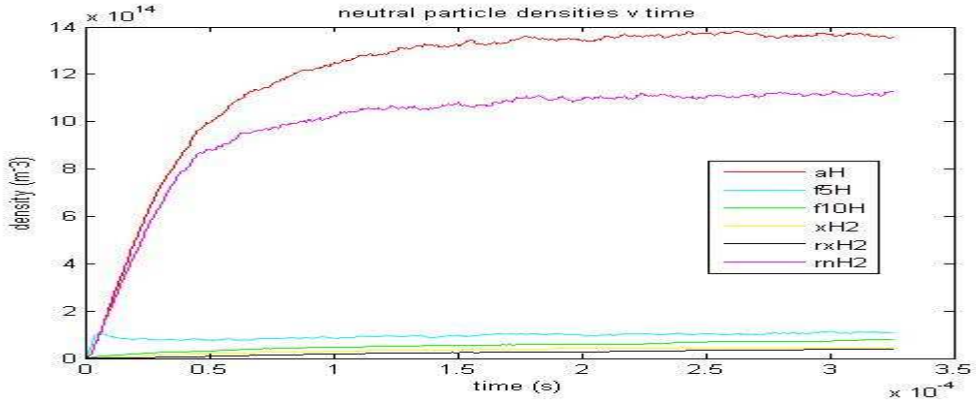

(c)

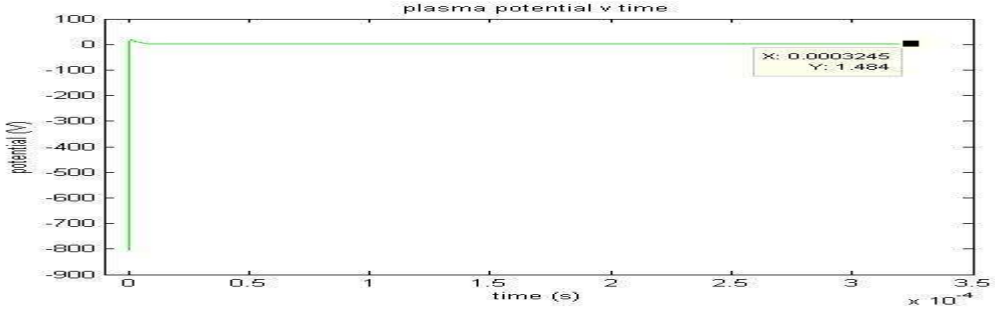

Figure 71: Evolution of the spatially averaged (a) charged & (b) neutral particle densities and (c) plasma potential.

Steady-State DNB Beam Plasma Parameters

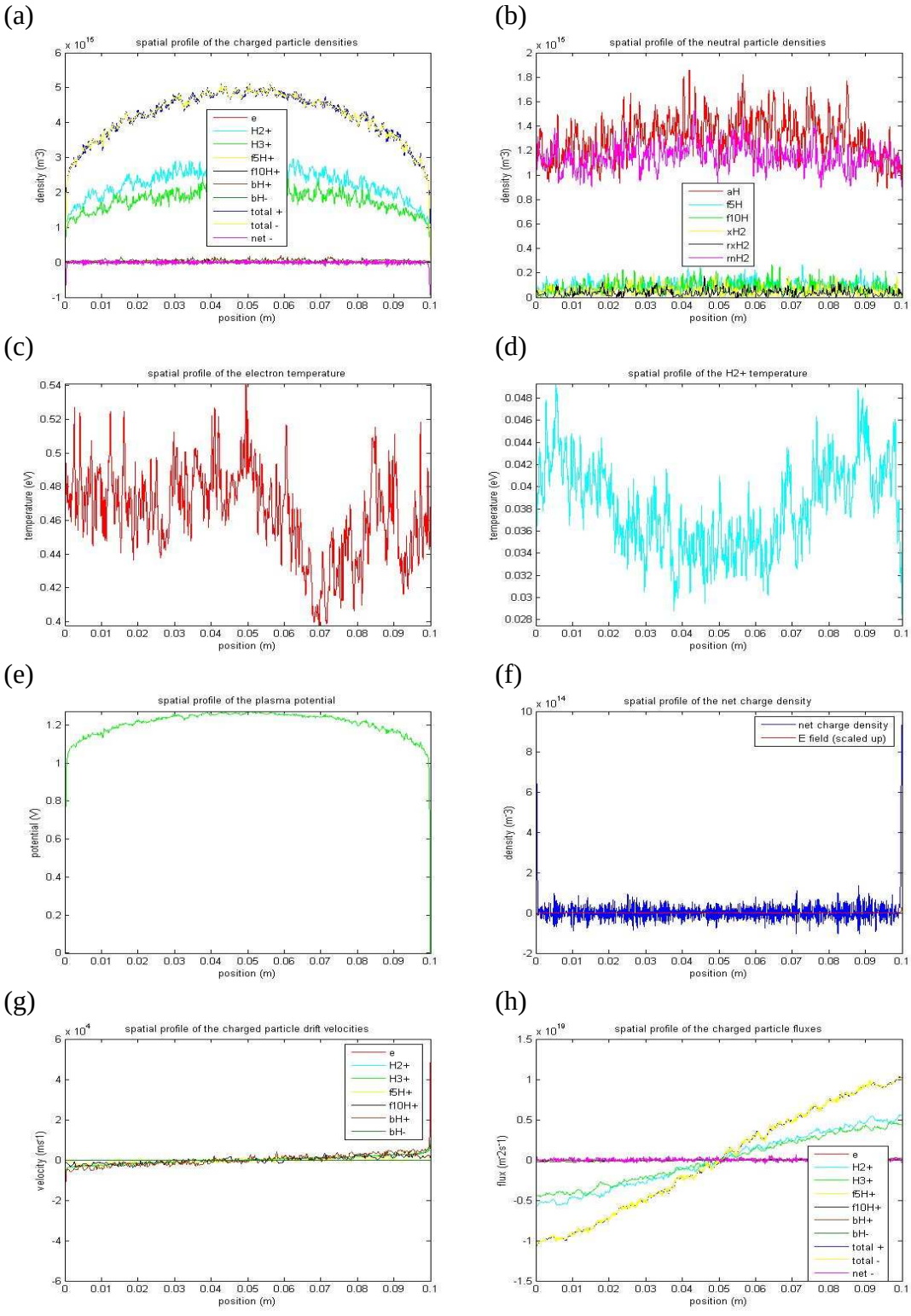

Figure 72: Spatial profiles @ steady-state; (a) charged species densities, (b) neutral species densities, (c) electron temperature, (d) H_2^+ temperature, (e) electric potential, (f) net charge density & electric field, charged particle (g) drift velocities and (h) fluxes.

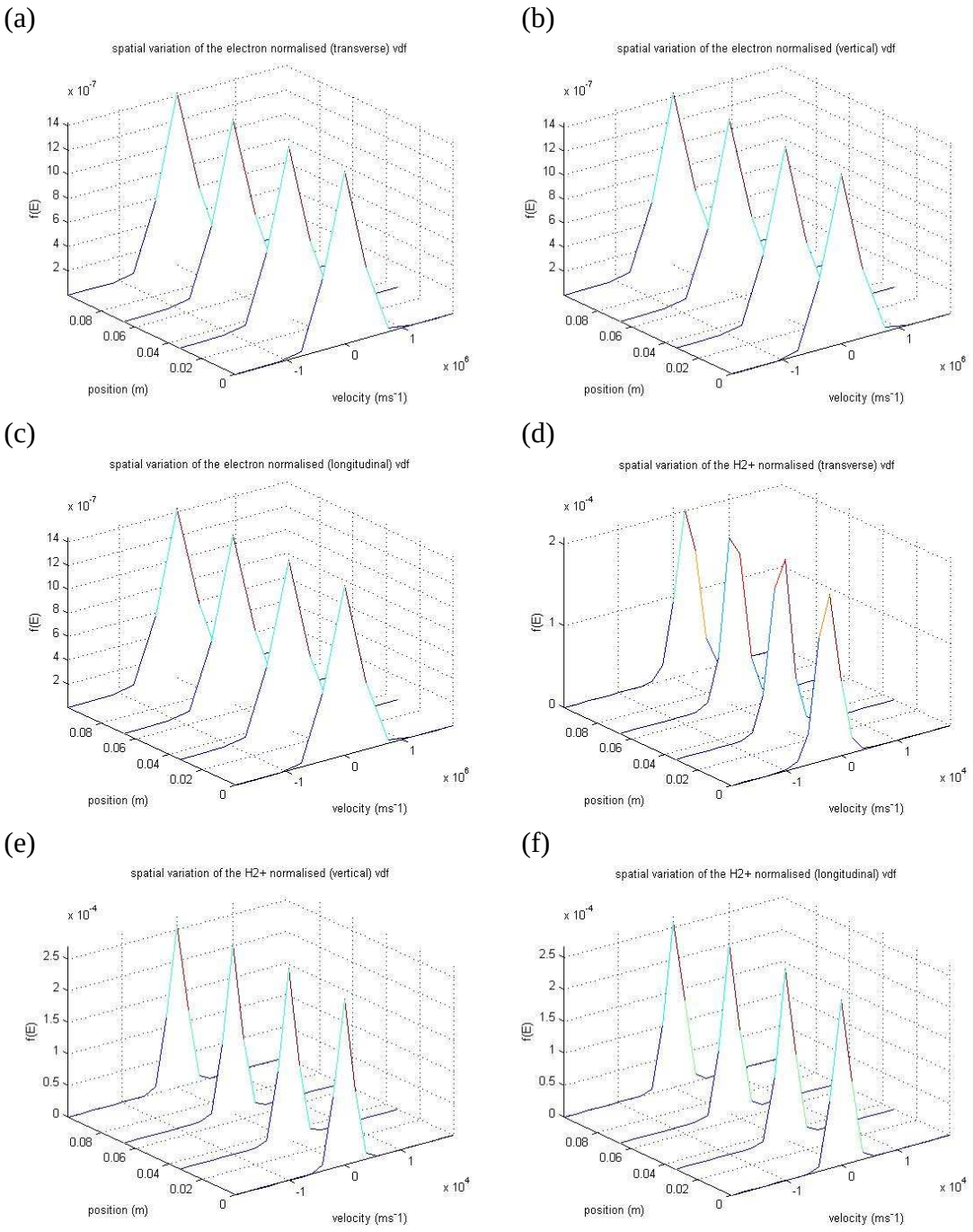

Figure 73: Electron (a) transverse, (b) vertical and (c) longitudinal velocity distribution functions. H_2^+ (d) transverse, (e) vertical and (f) longitudinal velocity distribution functions {title misprint: f(E) is not normalised}.

(a)

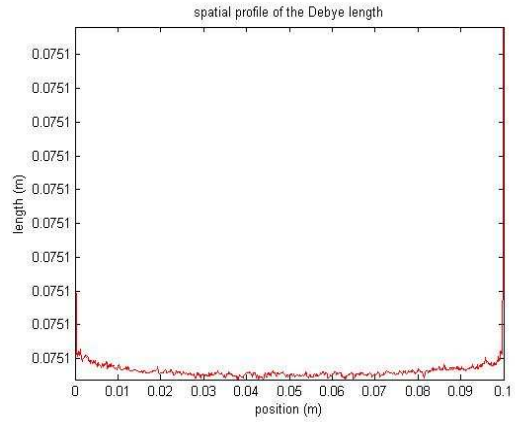

(b)

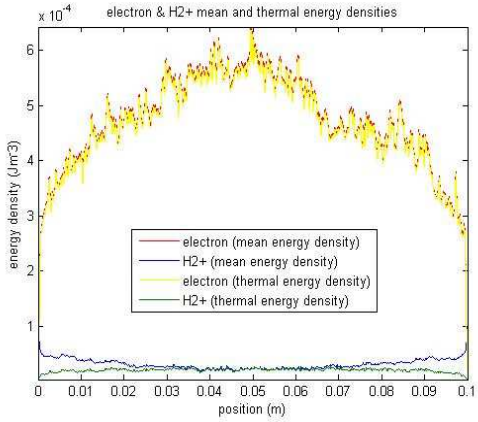

(c)

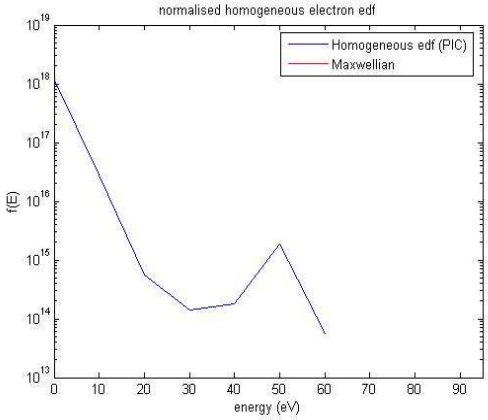

(d)

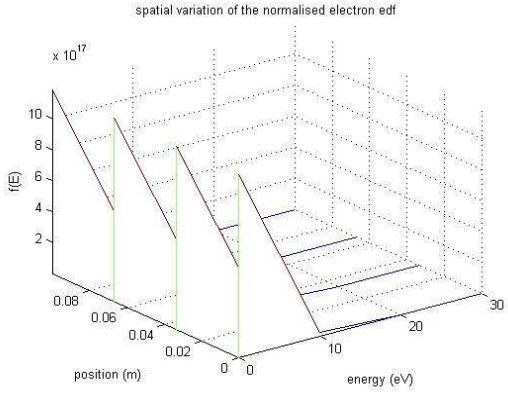

(e)

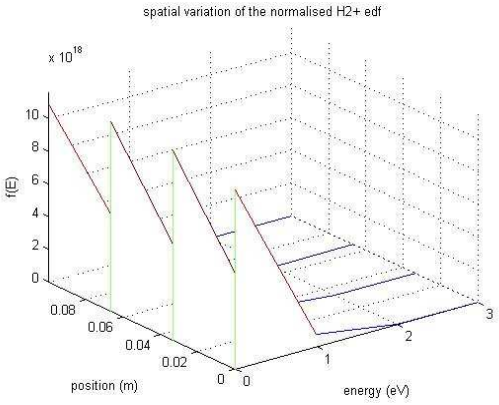

Figure 74: (a) Debye length. (b) Electron & H_2^+ mean/thermal energies. (c) Electron normalised homogenous energy distribution functions. Spatial variation of the (d) electron & (e) H_2^+ energy distribution functions {title misprint: f(E) is not normalised}.

The peak @ ~ 55eV (*Figure 74 (c)*) is due to stripped electrons cf. *Figure 111 (c)*, *Appendix E*, i.e. implying that they do not thermalise with other beam plasma electrons.

6.3.2 HNB Beam Plasma Results

HNB beam plasma evolution towards steady-state

(a)

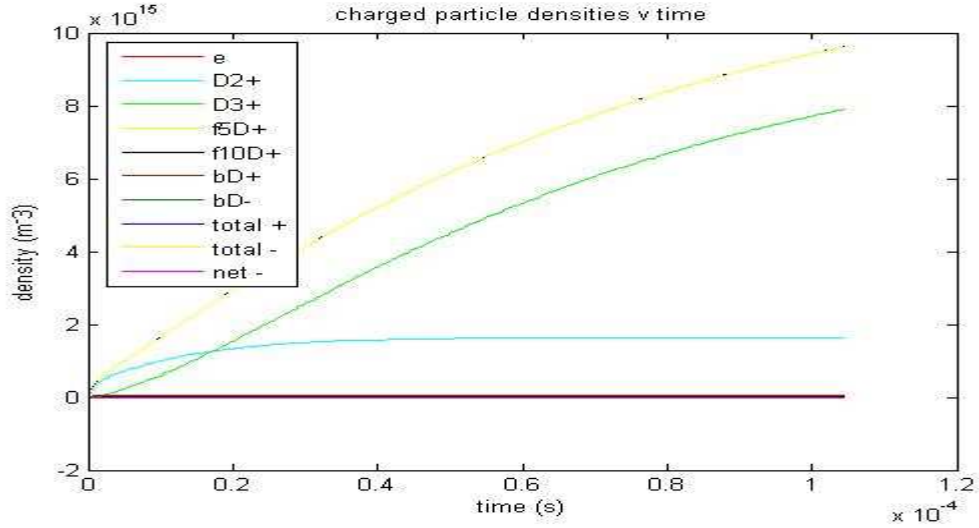

(b)

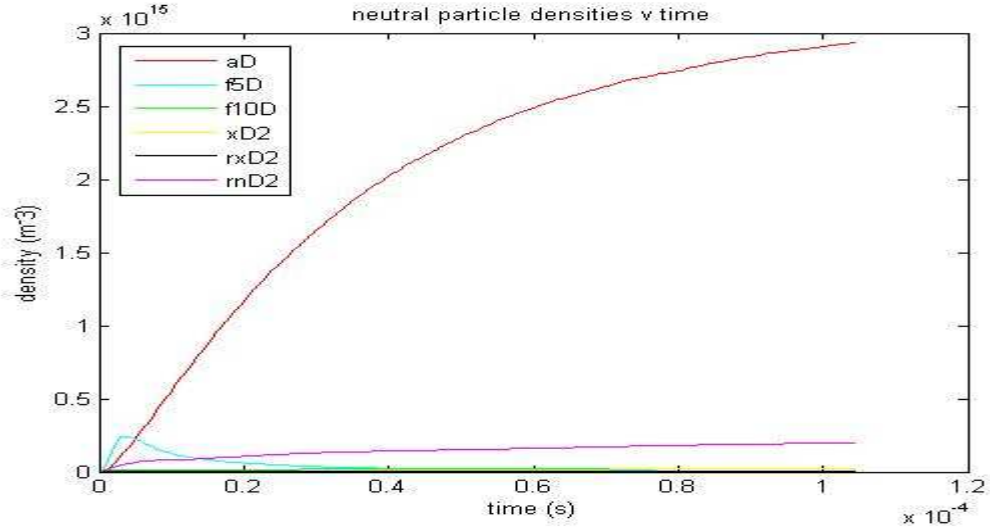

(c)

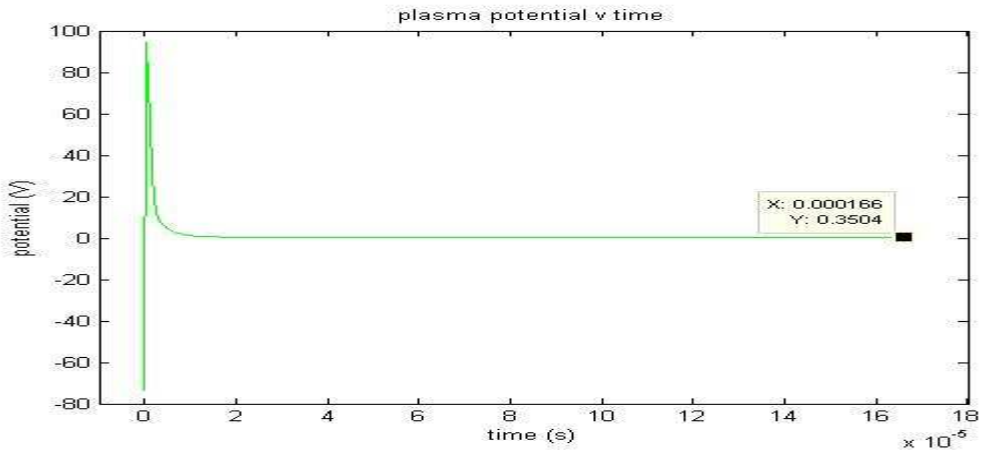

Figure 75: Evolution of the spatially averaged (a) charged & (b) neutral species densities and (c) plasma potential.

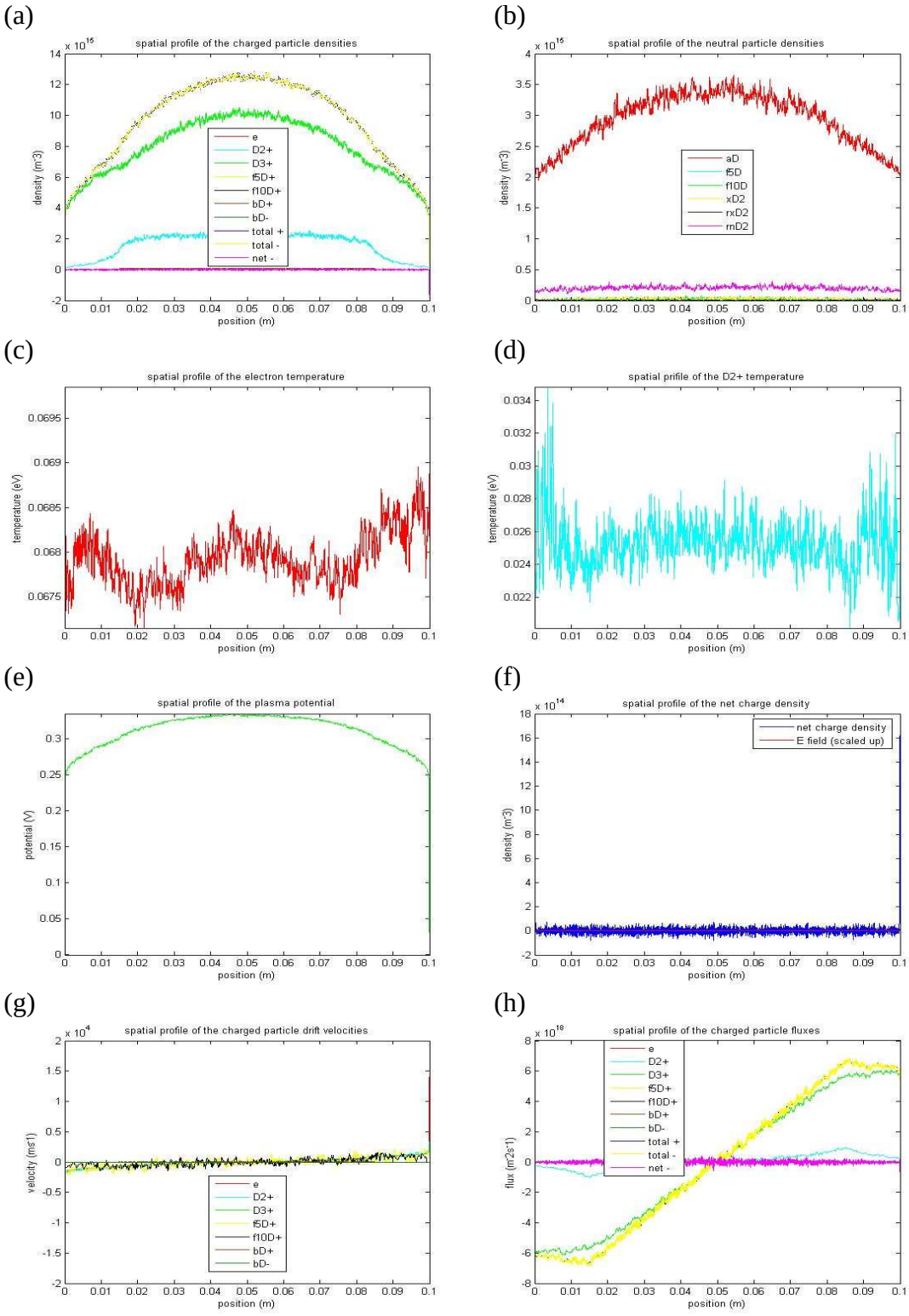

Figure 76: Spatial profiles @ steady-state; (a) charged species densities, (b) neutral species densities, (c) electron temperature, (d) D_2^+ temperature, (e) electric potential, (f) net charge density & electric field, charged particle (g) drift velocities and (h) fluxes.

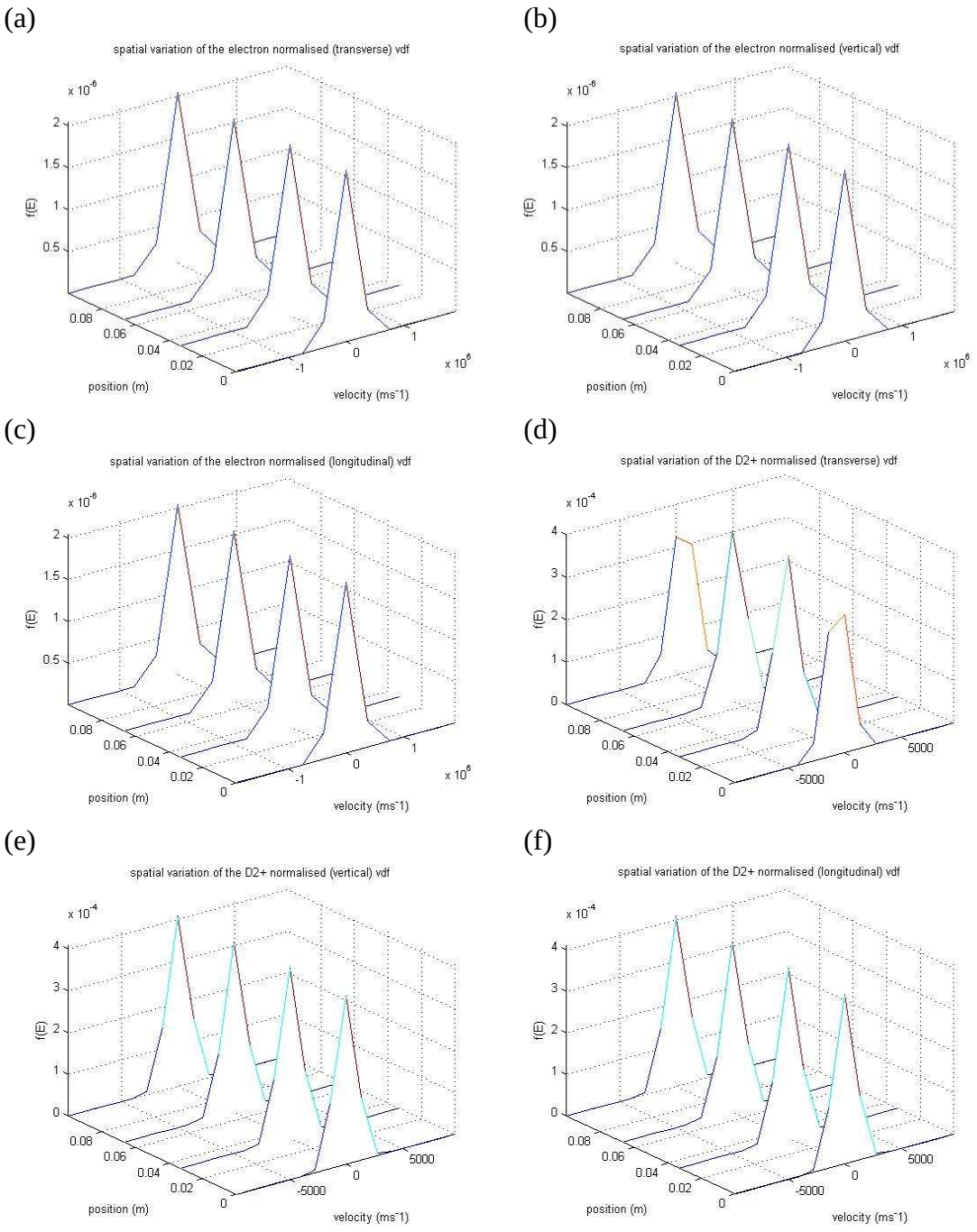

Figure 77: Electron (a) transverse, (b) vertical and (c) longitudinal velocity distribution functions. D_2^+ (d) transverse, (e) vertical and (f) longitudinal velocity distribution functions {title misprint: f(E) is not normalised}.

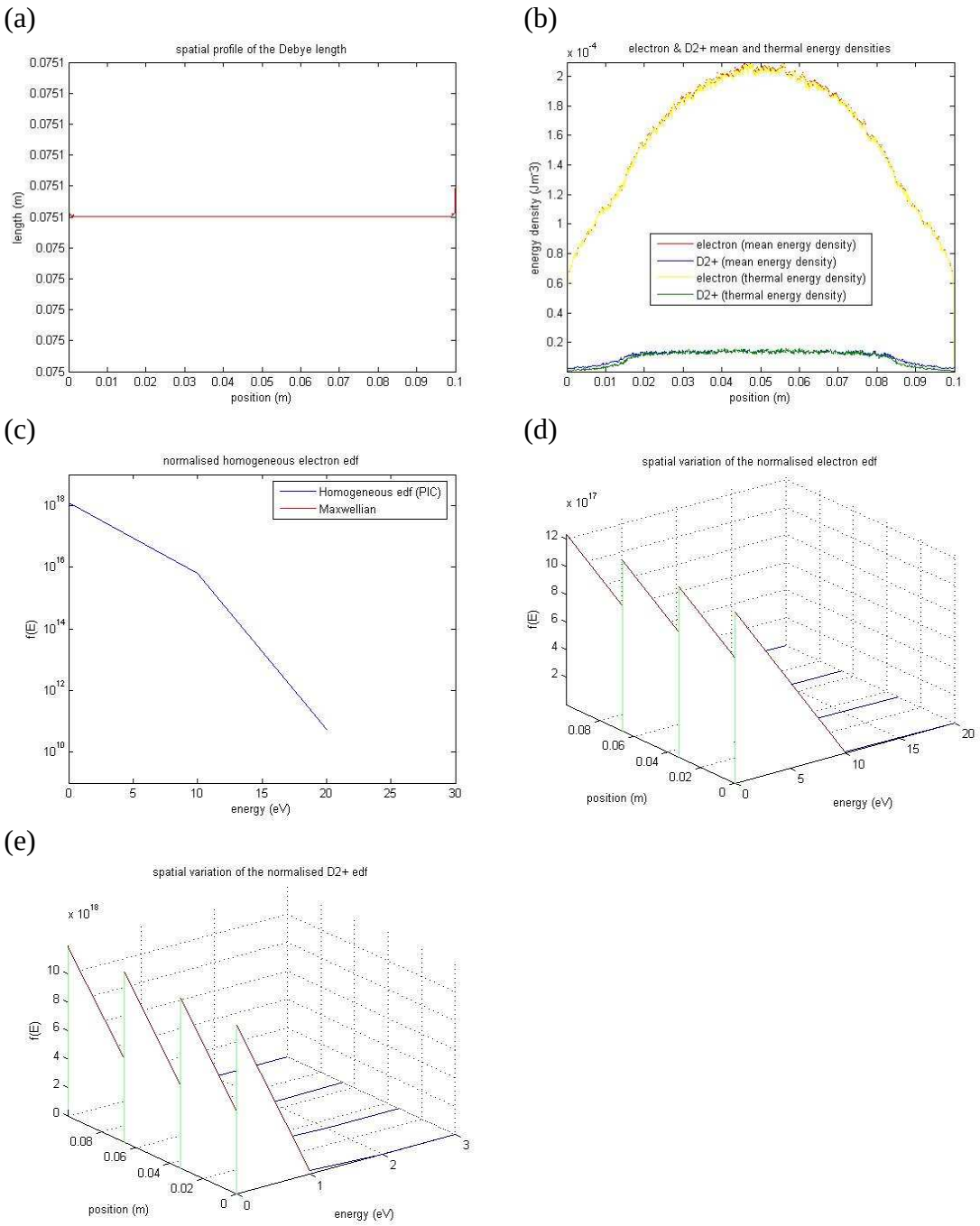

Figure 78: (a) Debye length. (b) Electron & D_2^+ mean/thermal energies. (c) Electron normalised homogenous energy distribution functions. Spatial variation of the (d) electron & (e) D_2^+ energy distribution functions {title misprint: f(E) is not normalised}.

Similarly to the DNB case, a peak in electron energy (@ ~ 270eV cf. *Figure 117 (c), Appendix E*) is expected due to stripped electrons, although *Figure 78 (c)* shows no electrons of energy greater than 20eV. This is due to the fact that beam stripping ceases altogether in this *Transverse* simulation, as the initial 1MeV D^- beam reaches a 100% D^+ composition - this would not occur in real injectors cf. *Section 6.1.1* & *Figure 68, Section 6.1.3* - (1MeV D^+ electron capture collisions were assumed to be negligible).

6.4 Gas Heating Results

6.4.1 DNB Gas Heating Results

e	H2+	H3+	f5H+	f10H+	aH	fH	f5H	xH2	rxH2	rnH2
13.1	8.9	28.4	0.1	0.1	30.0	3.6	0.1	0.1	0.1	15.5

Table 9: % power density transfer contribution from each simulated particle

total p_{den} transfer	total beam p_{den} loss	% of total p_{den} loss	increased temperature	% decrease in gas target
$4.5Wm^{-3}$	$2677.4Wm^{-3}$	0.17%	376K	11%, 20%

Table 10: Total power density transfer, total beam power density loss (Section 6.2.1), percentage of total beam power density loss, increased temperature, and percentage decrease in neutraliser gas target (two target–temperature models).

The gas heating calculations (cf. *Section 5.1*) yield a DNB neutraliser (increased) gas temperature of 376K (*Table 10*). The resulting neutraliser gas density depletion (*Table 10*) would be relatively insignificant, since it would only yield a reduction in neutralisation efficiency of < 5% cf. *Figure 67, Section 6.1.2*.

6.4.2 HNB Gas Heating Results

e	D2+	D3+	f5D+	f10D+	aD	fD	f5D	xD2	rxD2	rnD2
5.62	2.71	50.45	0.06	0.03	40.78	0.02	0.01	0.01	0.01	0.29

Table 11: % power density transfer contribution from each simulated particle

total p_{den} transfer	total beam p_{den} loss	% of total p_{den} loss	increased temperature	% decrease in gas target
$19.6Wm^{-3}$	$9755.9Wm^{-3}$	0.2%	377K	11%, 20%

Table 12: Total power density transfer, total beam power density loss (Section 6.2.2), percentage of total beam power density loss, increased temperature, and percentage decrease in neutraliser gas target (two target–temperature models).

The resulting HNB neutraliser gas temperature is 377K (*Table 12*). As in the DNB case, these results predict insignificant gas heating, in agreement with Surrey [40]. However, as in *Sections 5.2* & *5.3*, these results could be underestimating the real extent of gas heating - bearing in mind the more sensitive relationship between neutralisation efficiency and gas target for negative ion beam neutralisation (*Figure 68*, *Section 6.1.3*).

Chapter 7

Concluding Remarks

The JET NBI neutraliser beam plasma characterisation (*Chapter 4*) and gas heating (*Chapter 5*) simulation results are qualitatively consistent with the experimental results of Crowley et al. [36]. However, the simulation gas heating calculations yield very different gas heating source contributions, and predict the existence of four significant gas heating pathways not accounted for in the Paméla model [31, 34] i.e. direct kinetic energy transfer to the neutraliser gas from H_3^+ ions, H_2^+ ions, H atoms (formed via H_3^+ formation) and electrons. Moreover, as previously suggested by Falter et al. [27, 33], the simulation results (*Sections 5.2* & *5.3*) indirectly suggest that gas implantation may be a significant neutraliser gas density depletion process i.e. since the simulation gas heating results do not account for the apparent extent of the neutralisation inefficiencies (*Figure 11 (a), Section 1.3.4*). Although, given the comparison limitations between simulation and experimental results (*Section 4.4.3*), the merit of the 1D3v PIC MCC *Transverse* simulation approach, in providing a reasonably accurate model of the beam-neutraliser system, remains unestablished (in addition to the inherent limitations due to the simplified nature of the 1D3v PIC MCC model, its accuracy depends upon the accuracy of the inputted collision cross section and threshold energy data).

There is obviously scope for more improvements in the 1D3v PIC MCC simulations e.g. including volume & surface recombination, Coulomb collisions between positive beam ions and plasma electrons (purported to be the main source of electron energy [38, 63], [62]) and the formation of various H_2 (electronically, rotationally and vibrationally) excited states (providing a significant drain in electron energy). A knock-on effect of the existence of a significant population of H_2 excited states would be in their greater subsequent ionisation and dissociation (threshold energy of both processes is lower than that for the ground state H_2 molecule). Accounting for beam charge-changing events whereby the beam particles and/or the H_2 gas target molecules are in excited states could also turn out to be significant e.g. in determining the beam composition & energy and hence the neutralisation efficiency. All these omitted effects could have significant consequences especially for the electron temperature, which is a very influential plasma parameter. If the electron temperature changes then nearly everything else changes e.g.

changes in the electron energy distribution function (eedf) cause changes in the electron reaction rates, which in turn cause changes in the beam plasma composition and energy etc. Moreover, the simulation model does not account for some clearly observed effects like that of; beam interception resulting in beam density/power (transmission) losses, gas implantation (wall pumping) & re-emission [33] and the emission of various radiation from the beam plasma. Failing to simulate significant physical processes would partly explain the discrepancies between simulation and experimental results.

A 2D or 3D neutraliser beam plasma simulation, incorporating more beam-neutraliser physics, would obviously provide a greater predictive ability than the present 1D approach. Coupled with a Direct Simulation Monte Carlo (DSMC) method [82] cf. [83], the resulting hybrid neutraliser model would directly yield the neutraliser gas density depletion (by implicitly modelling gas flow changes caused by the beam plasma), thus predicting the necessary conditions pertaining to maximum beam neutralisation.

The simulation approach to modelling the neutraliser could be used to test possible design improvements i.e. proof-of-principle simulations e.g. whether a reduction in wall temperature, longer neutraliser, use of heavier neutraliser gases etc. can significantly increase the neutralisation efficiency. The idea (*Section 5.2*) of using magnetic fields to manipulate the beam plasma electrons, so as to reduce their contribution to gas heating, could also be investigated. The resulting predictions of such simulations could determine whether real proof-of-principle experiments are to be conducted. Another proof-of-principle experiment could be to run the simulations for different neutraliser widths and see how the plasma parameters vary. Paméla [31] concluded that gas heating is most significant in wider neutralisers, which makes sense from a gas-wall cooling perspective {hence the expected success of the relatively narrow channel designs for ITER DNB & HNB neutralisers (*Section 6.1.1*) i.e. in terms of limiting any significant gas heating effects cf. *Section 6.4*, [40]}, although increasing the neutraliser width might have the favourable result of reducing the electron temperature, which would then reduce the neutraliser gas heating and thus any deficits in neutralisation efficiency.

The conclusion (from the *beam composition* simulation results, *Section 4.1*) that the neutralisation efficiency has a distinct maximum with gas target (as opposed to the generally assumed increasing asymptotic behaviour [60, 66]) could be tested experimentally via calorimetric measurements at the ion dump, cf. *Section 4.1*.

Appendix A ***Beam charge-changing calculations***

Equation (1.2): $$\frac{dF}{d\Pi} = \begin{pmatrix} -\sigma_{10} & \sigma_{01} \\ \sigma_{10} & -\sigma_{01} \end{pmatrix} F = AF, \qquad F = \begin{pmatrix} F_1 \\ F_0 \end{pmatrix}$$

The eigenvalues of A are calculated via the characteristic equation {det(A-λI)=0}:

$$\det\left\{ \begin{pmatrix} -\sigma_{10} & \sigma_{01} \\ \sigma_{10} & -\sigma_{01} \end{pmatrix} - \lambda \begin{pmatrix} 1 & 0 \\ 0 & 1 \end{pmatrix} \right\} = 0$$

$$\Rightarrow \qquad \begin{vmatrix} -\sigma_{10} - \lambda & \sigma_{01} \\ \sigma_{10} & -\sigma_{01} - \lambda \end{vmatrix} = 0$$

$$\Rightarrow \qquad (-\sigma_{10} - \lambda)(-\sigma_{01} - \lambda) - \sigma_{10}\sigma_{01} = 0$$

$$\Rightarrow \qquad \sigma_{10}\sigma_{01} + \lambda(\sigma_{10} + \sigma_{01}) + \lambda^2 - \sigma_{10}\sigma_{01} = 0$$

$$\Rightarrow \qquad \lambda^2 + \lambda(\sigma_{10} + \sigma_{01}) = 0$$

$$\Rightarrow \qquad \lambda = -(\sigma_{10} + \sigma_{10}), 0$$

The eigenvectors of A are calculated via the eigenvector equation of A {Ax=λx}:

$\lambda_1 = -(\sigma_{10} + \sigma_{10})$:

$$Ax_1 = \lambda_1 x_1$$

$$\Rightarrow \quad (A - \lambda_1 I)x_1 = 0:$$

$$\begin{pmatrix} -\sigma_{10} + \sigma_{01} + \sigma_{10} & \sigma_{01} \\ \sigma_{10} & -\sigma_{01} + \sigma_{01} + \sigma_{10} \end{pmatrix} \begin{pmatrix} x_{11} \\ x_{12} \end{pmatrix} = \begin{pmatrix} 0 \\ 0 \end{pmatrix}$$

$$\Rightarrow \qquad \begin{pmatrix} \sigma_{01} & \sigma_{01} \\ \sigma_{10} & \sigma_{10} \end{pmatrix} \begin{pmatrix} x_{11} \\ x_{12} \end{pmatrix} = \begin{pmatrix} 0 \\ 0 \end{pmatrix}$$

$$\Rightarrow \qquad x_{11}\sigma_{01} + x_{12}\sigma_{01} = 0, \qquad x_{11}\sigma_{10} + x_{12}\sigma_{10} = 0$$

$$\Rightarrow \qquad x_{11} = -x_{12} \qquad \text{(A.1)}$$

$\lambda_2 = 0$:

$$Ax_2 = \lambda_2 x_2$$

$$\Rightarrow \quad (A - \lambda_2 I)x_2 = 0:$$

$$\Rightarrow \quad \begin{pmatrix} -\sigma_{10} & \sigma_{01} \\ \sigma_{10} & -\sigma_{01} \end{pmatrix} \begin{pmatrix} x_{21} \\ x_{22} \end{pmatrix} = \begin{pmatrix} 0 \\ 0 \end{pmatrix}$$

$$\Rightarrow \quad -x_{21}\sigma_{10} + x_{22}\sigma_{01} = 0, \qquad x_{21}\sigma_{10} - x_{22}\sigma_{01} = 0$$

$$\Rightarrow \quad x_{21} = x_{22}\frac{\sigma_{01}}{\sigma_{10}} \quad \text{(A.2)}$$

Beam Fraction Solution:

$F = x_1 e^{\lambda_1 \Pi} + x_2 e^{\lambda_2 \Pi}$:

$$F = \begin{pmatrix} F_1 \\ F_0 \end{pmatrix} = \begin{pmatrix} x_{11} \\ x_{12} \end{pmatrix} e^{-(\sigma_{01}+\sigma_{10})\Pi} + \begin{pmatrix} x_{21} \\ x_{22} \end{pmatrix} e^{0(\Pi)}$$

$$\Rightarrow \quad F_1 = x_{11} e^{-(\sigma_{01}+\sigma_{10})\Pi} + x_{21}, \qquad F_0 = x_{12} e^{-(\sigma_{01}+\sigma_{10})\Pi} + x_{22}$$

Initial conditions; $F_1 = 1$ & $F_0 = 0$ at $\Pi = 0$ =>

$$x_{11} + x_{21} = 1, \quad \text{(A.3)} \qquad x_{12} + x_{22} = 0 \quad \text{(A.4)}$$

(A.1), (A.3), (A.4) => $\dfrac{x_{21}}{x_{22}} + 1 = \dfrac{1}{x_{22}}$

(A.2) => $x_{22} = \dfrac{\sigma_{10}}{\sigma_{01} + \sigma_{10}}$, (A.4) => $x_{12} = -\dfrac{\sigma_{10}}{\sigma_{01} + \sigma_{10}}$

(A.2) => $x_{21} = \dfrac{\sigma_{01}}{\sigma_{01} + \sigma_{10}}$, (A.3) => $x_{11} = \dfrac{\sigma_{10}}{\sigma_{01} + \sigma_{10}}$

Appendix B Initial beam 'plasma' evolution

80keV/27A proton beam injection into a H_2 gas of density $3x10^{19}m^{-3}$:

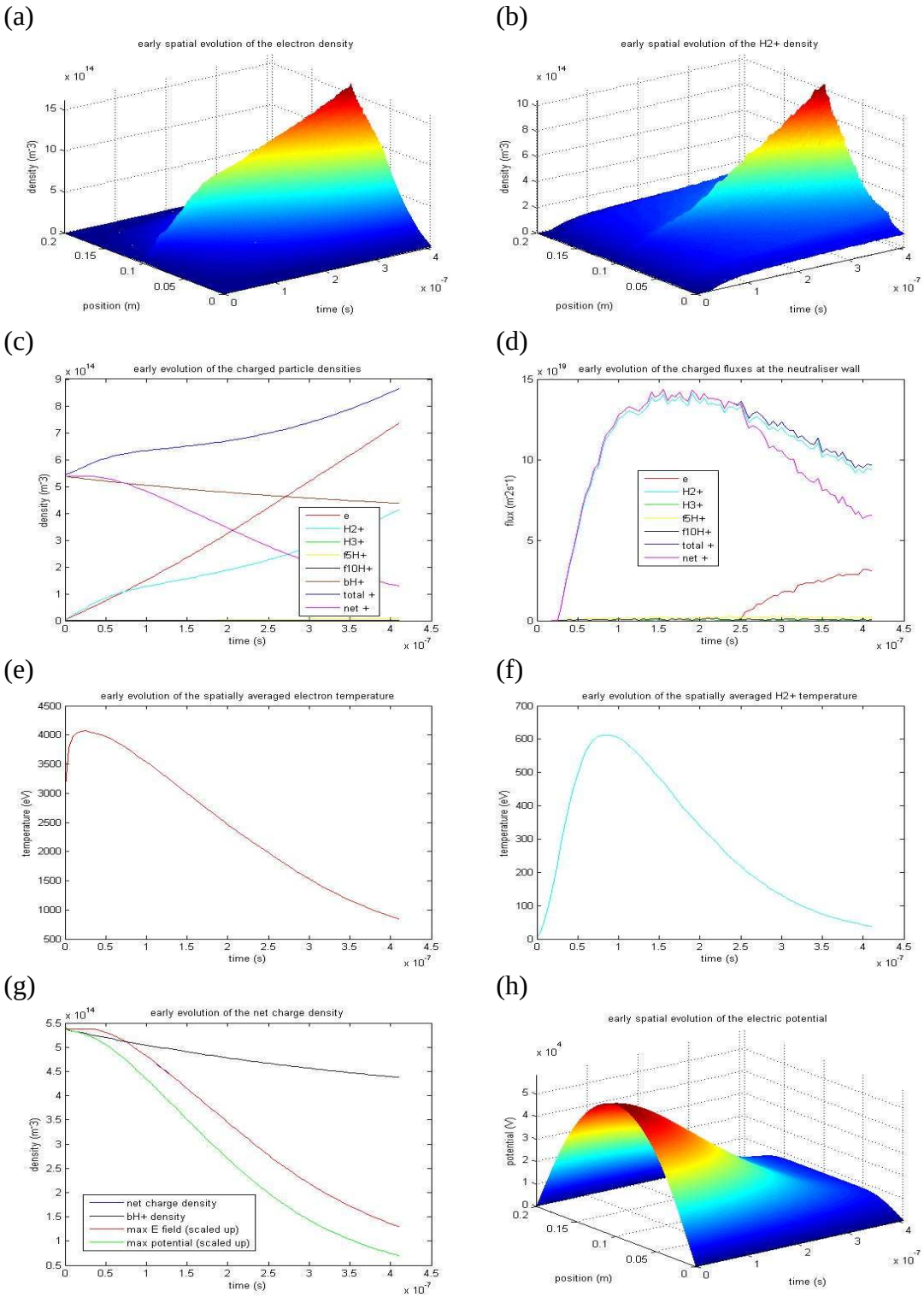

Figure 79: (a) electron density, (b) H_2^+ density, (c) charged particles densities, (d) charged particle fluxes at neutraliser wall, (e) electron temperature, (f) H_2^+ temperature, (g) net charge density ... and (h) electric potential.

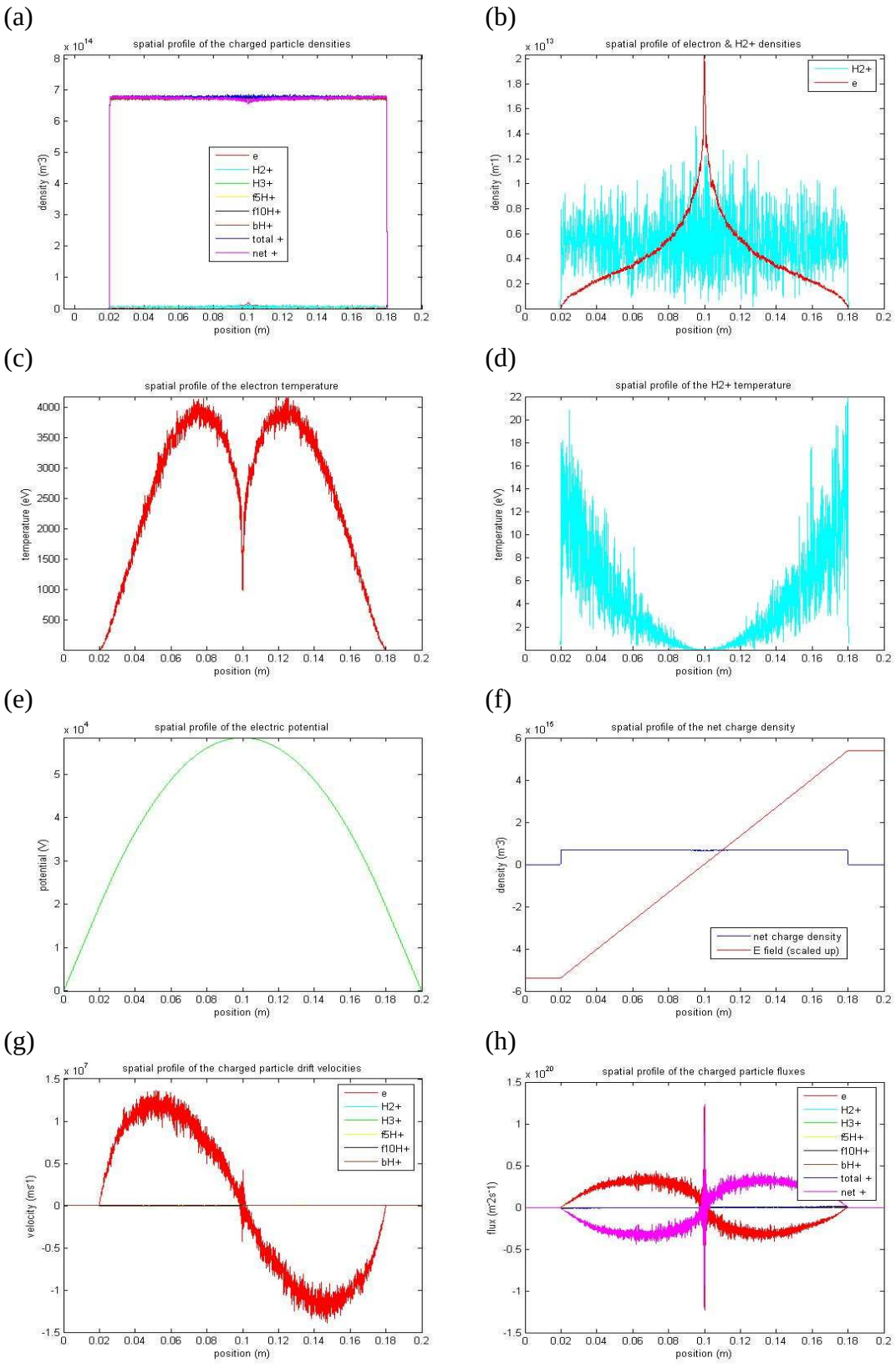

Figure 80: Spatial profiles @ t = 5ns; (a) charged particle densities (b) electron & H_2^+ density, (c) electron temperature, (d) H_2^+ temperature, (e) electric potential, (f) net charge density & electric field, charged particle (g) drift velocities and (h) fluxes.

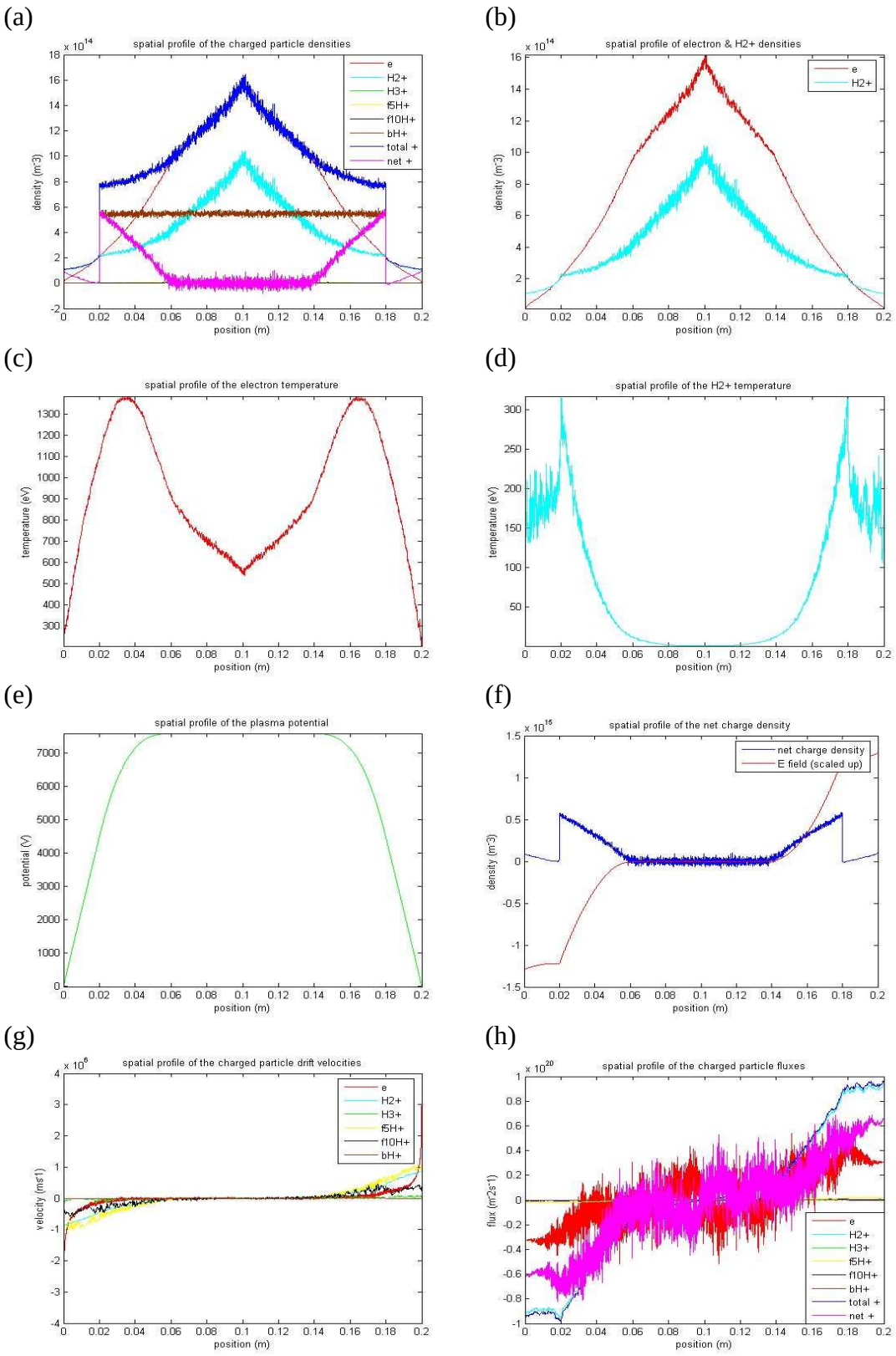

Figure 81: Spatial profiles @ t = 415ns; (a) charged particle densities (b) electron & H_2^+ density, (c) electron temperature, (d) H_2^+ temperature, (e) electric potential, (f) net charge density & electric field, charged particle (g) drift velocities and (h) fluxes.

Evidence of (fleeting) double layer formation at each side of the beam (*Figure 81 (f)*).

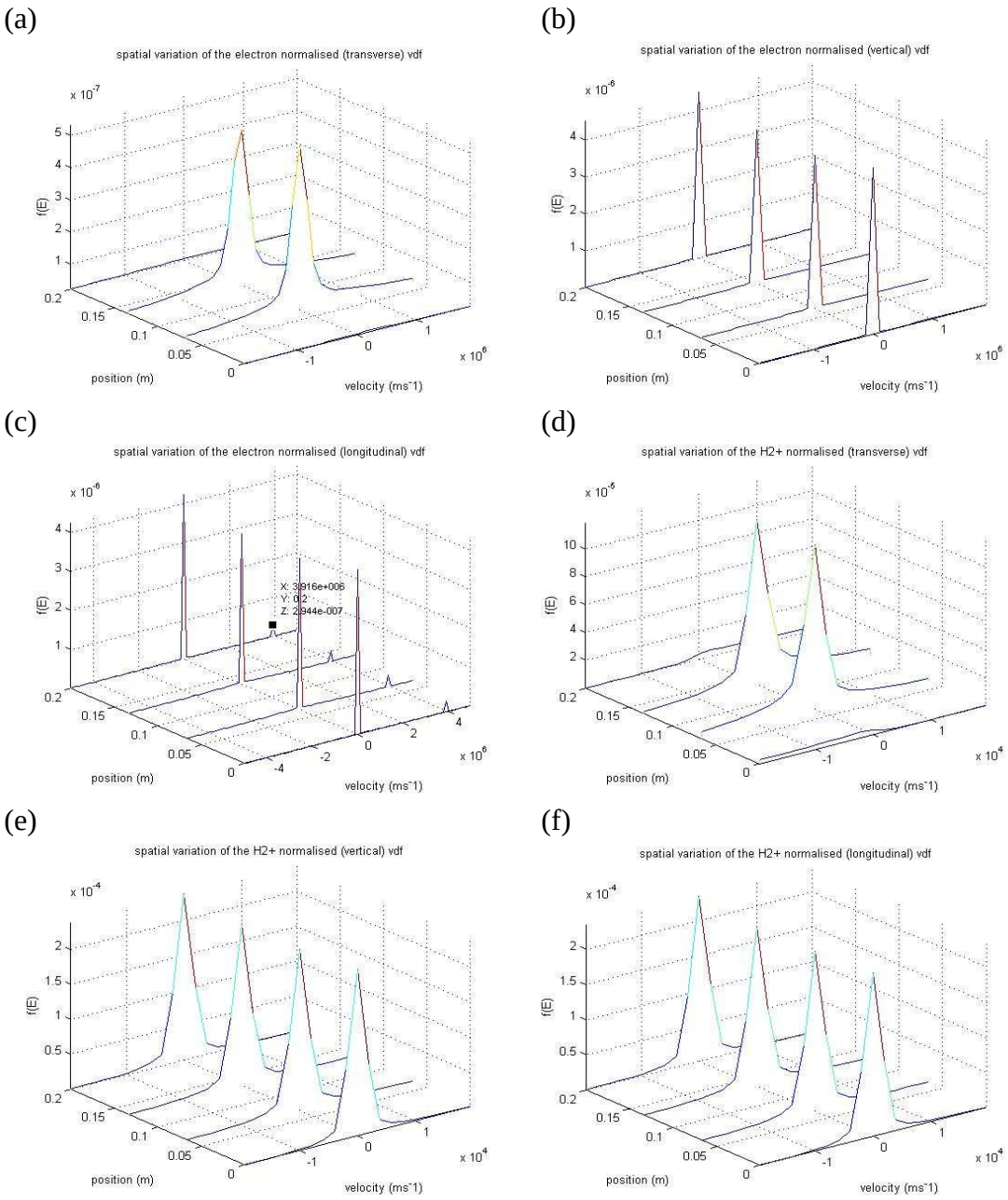

Figure 82: Electron (a) transverse, (b) vertical and (c) longitudinal velocity distribution functions. H_2^+ (d) transverse, (e) vertical and (f) longitudinal velocity distribution functions. All plots @ t = 415ns {title misprint: f(E) is not normalised}.

The (electron& H_2^+) velocity distribution functions are very similar in the vertical and longitudinal planes (*Figure 82 (b) & (c), (e) & (f)*) {beam stripped electrons only have a velocity (same as the 80keV beam) component in the longitudinal beam direction, *Figure 82 (c)*}. The differences in the electron & H_2^+ velocity distribution functions at the neutraliser walls (*Figure 82 (a)* & *(d)*) are due to the plasma sheath, where for example the H_2^+ ions have a preferential direction towards the walls (opposite direction for electrons), hence the difference in their mean and thermal energies (*Figure 83 (b)*).

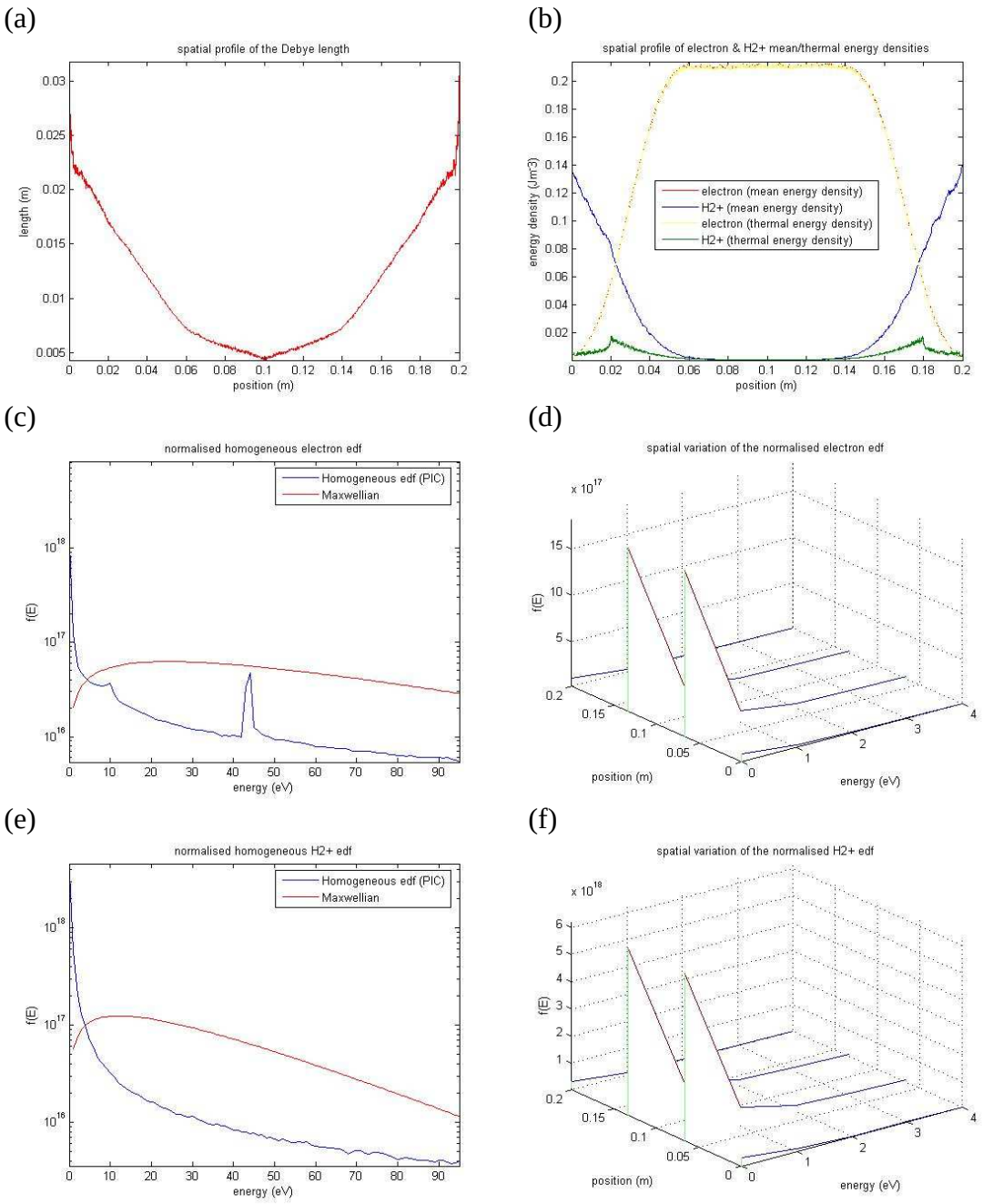

Figure 83: (a) Debye length. (b) Electron & H_2^+ mean/thermal energies. (c) Electron & (e) H_2^+ energy distribution functions. Spatial variation of the (d) electron & (f) H_2^+ edfs. All plots @ t = 415ns {title misprint: f(E) is not normalised}.

The prominent peak in the normalised homogenous electron edf @ ~ 44eV (*Figure 83 (c)*), evidences the presence of beam stripped electrons, since their initial velocity of $3.916 \times 10^6 ms^{-1}$ (*Figure 83 (c)*) corresponds to an energy of ~ 44eV. The less prominent peak @ ~ 10eV doesn't feature at steady-state (*Figure 90 (a), Appendix C*).

Appendix C Steady-state plasma parameters

Spatially resolved plasma parameters versus neutraliser gas density

80keV/27A H^+ beam, H_2 gas densities; (a) $3x10^{19}m^{-3}$, (b) $6x10^{19}m^{-3}$, (c) $9x10^{19}m^{-3}$:

(a)

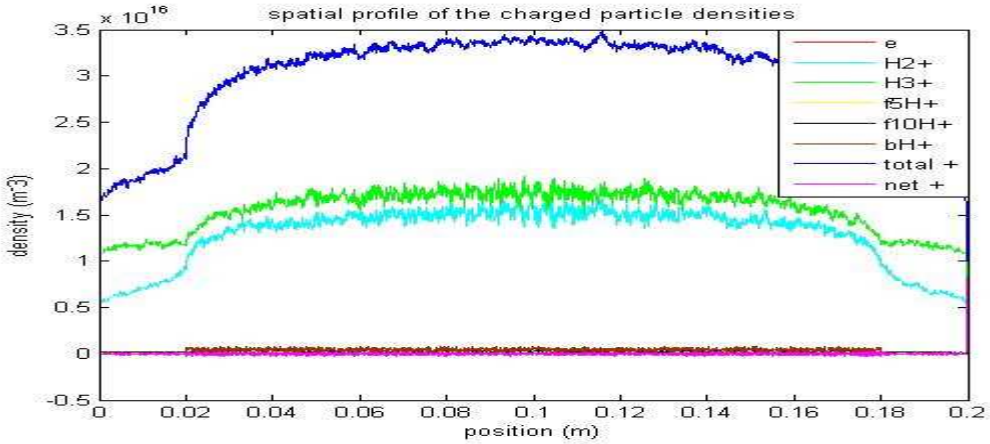

(b)

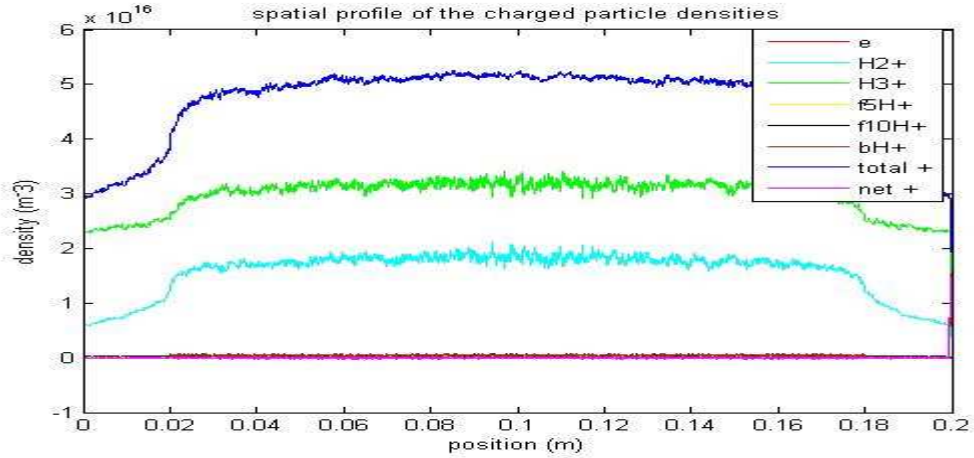

(c)

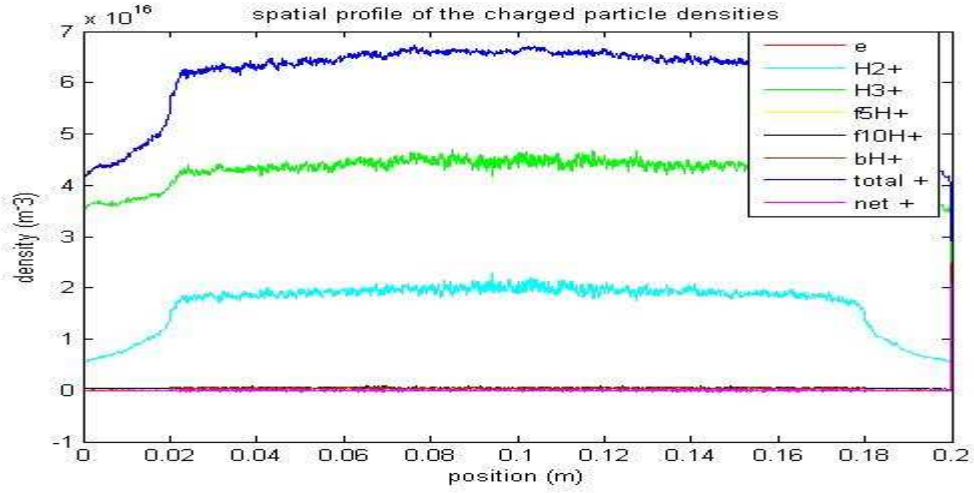

Figure 84: Spatial profiles of the charged particle densities for neutraliser H_2 gas densities; (a) $3x10^{19}m^{-3}$, (b) $6x10^{19}m^{-3}$, (c) $9x10^{19}m^{-3}$.

(a)

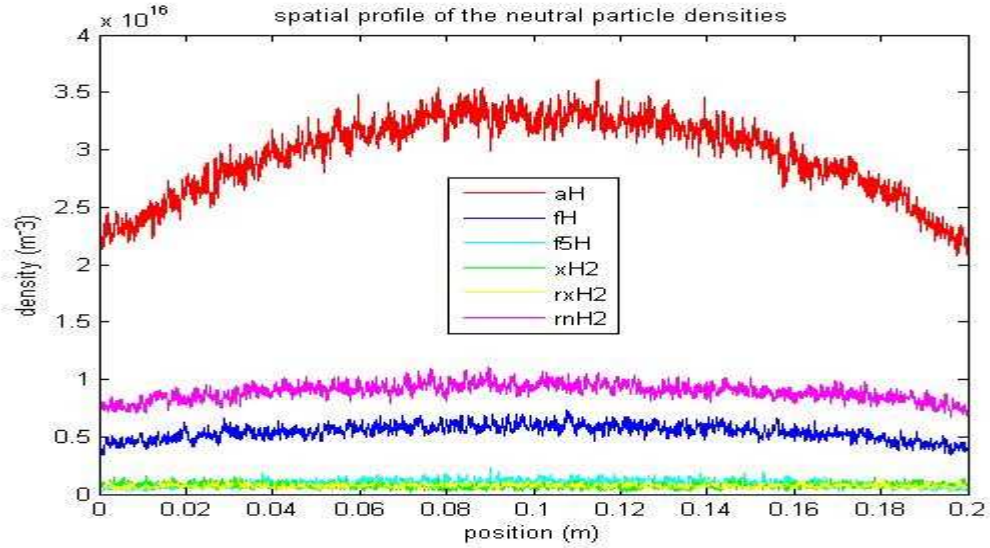

(b)

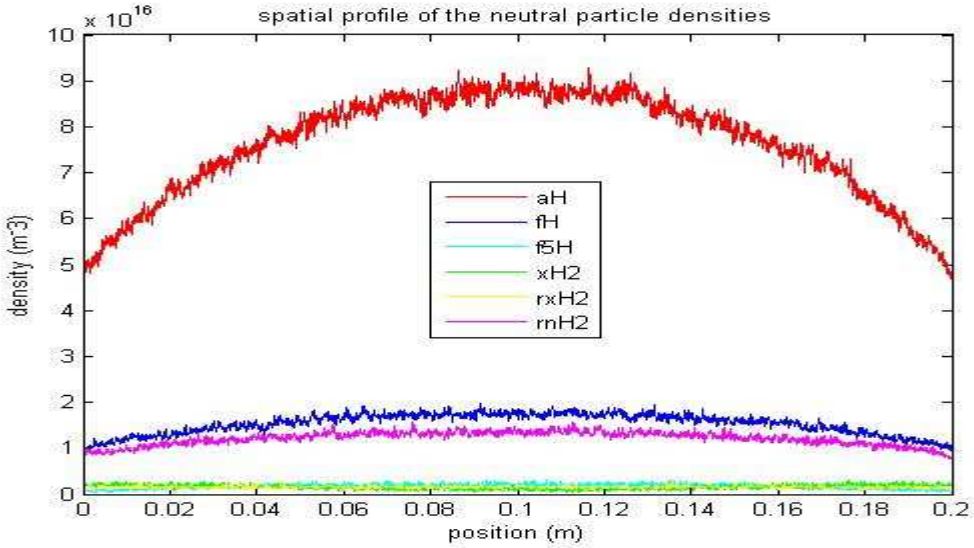

(c)

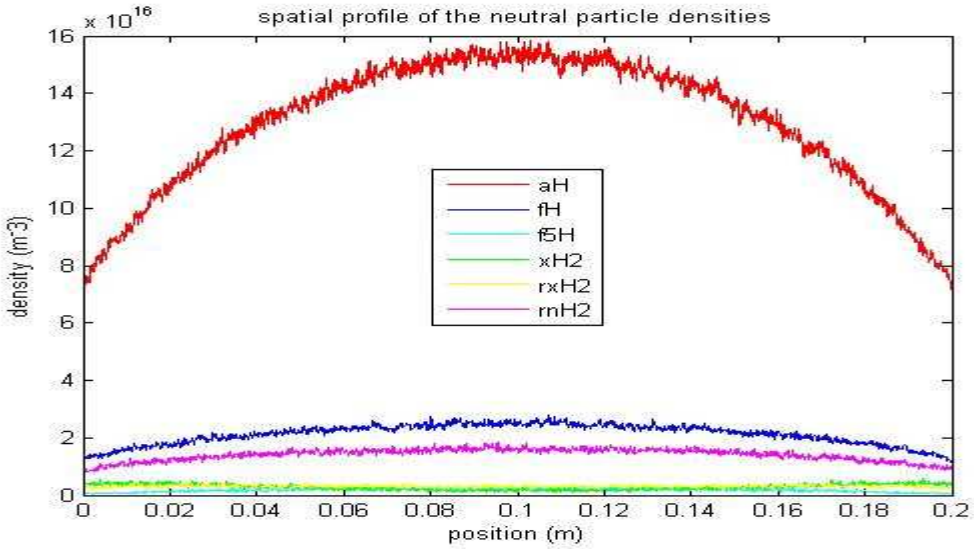

Figure 85: Spatial profiles of the neutral particle densities for neutraliser H_2 gas densities; (a) $3x10^{19}m^{-3}$, (b) $6x10^{19}m^{-3}$, (c) $9x10^{19}m^{-3}$.

(a)

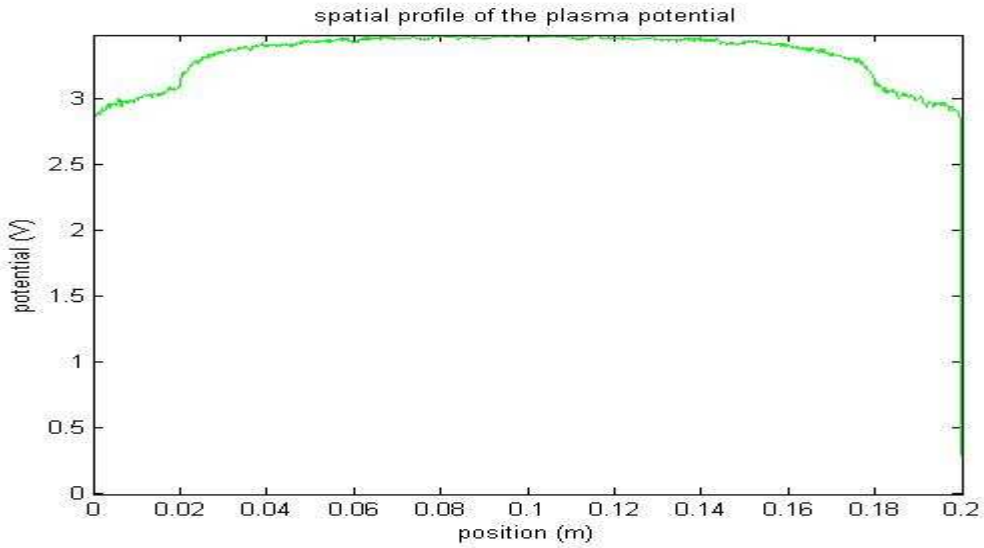

(b)

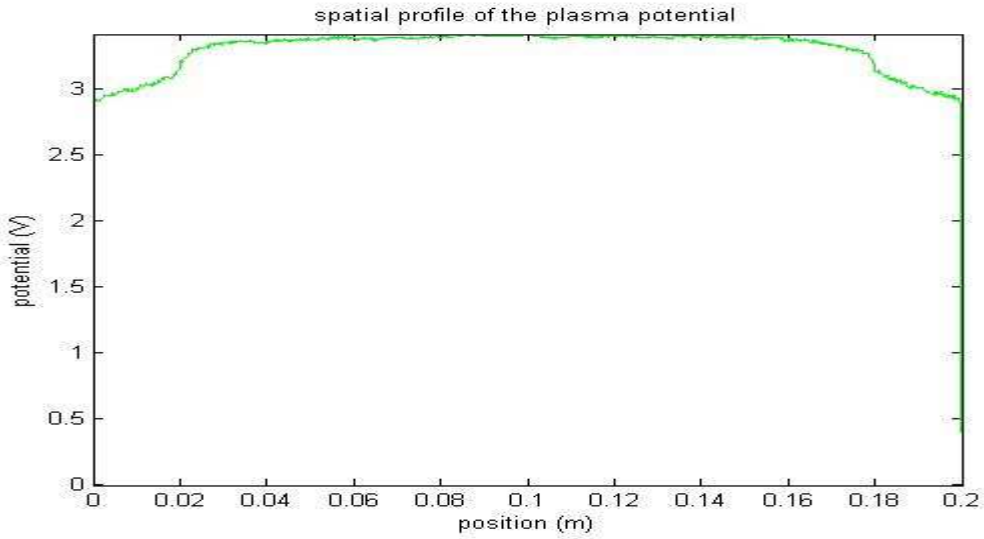

(c)

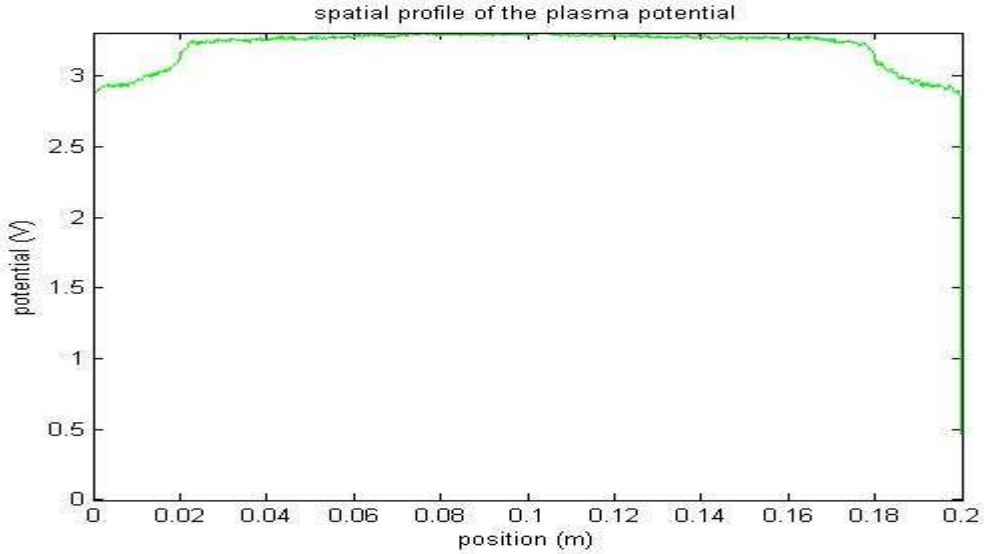

Figure 86: Spatial profiles of the plasma potentials for neutraliser H_2 gas densities; (a) $3x10^{19}m^{-3}$, (b) $6x10^{19}m^{-3}$, (c) $9x10^{19}m^{-3}$.

(a)

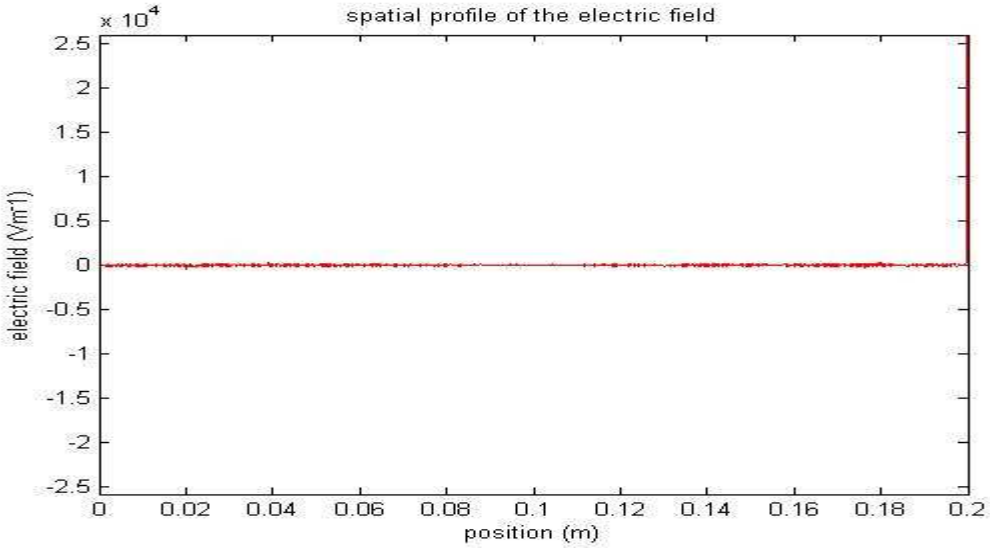

(b)

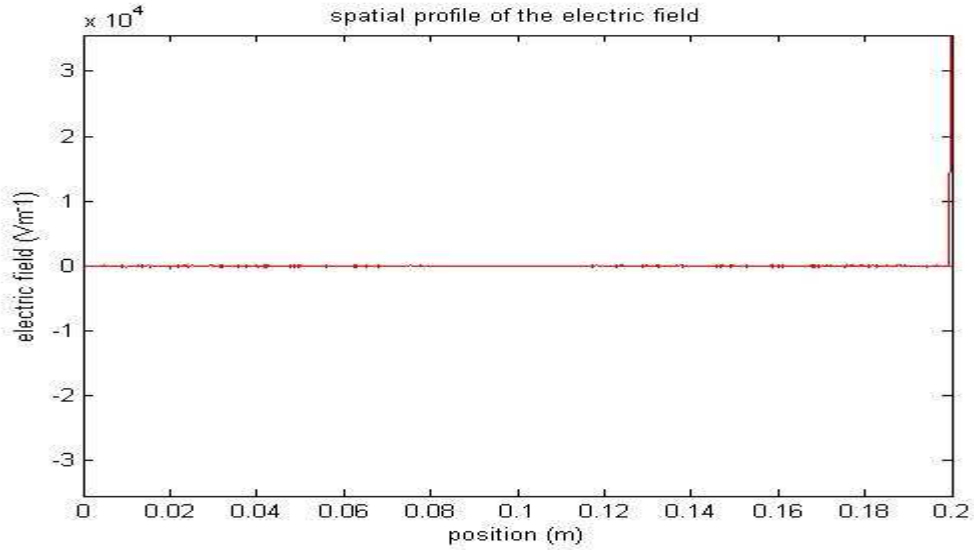

(c)

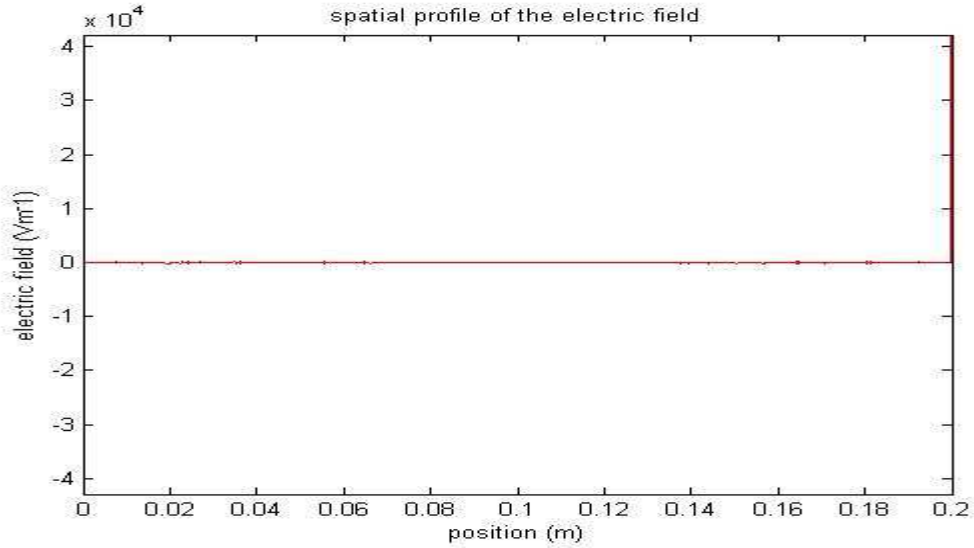

Figure 87: Spatial profiles of the electric fields for neutraliser H_2 gas densities; (a) $3x10^{19}m^{-3}$, (b) $6x10^{19}m^{-3}$, (c) $9x10^{19}m^{-3}$.

(a)

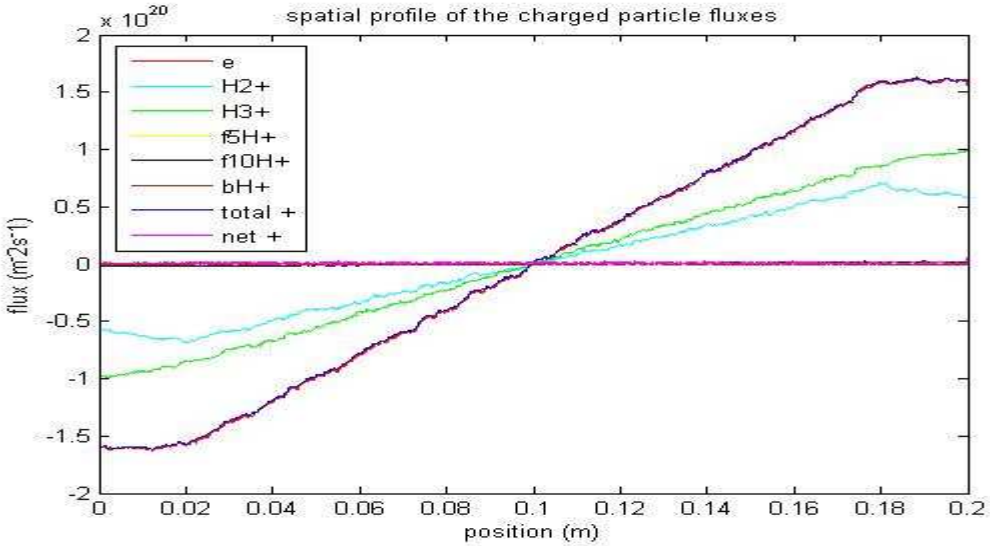

(b)

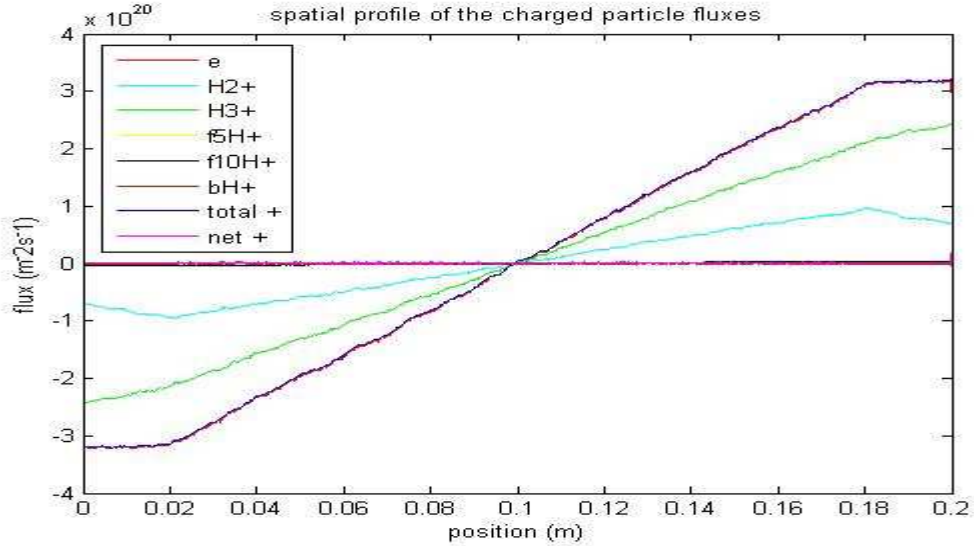

(c)

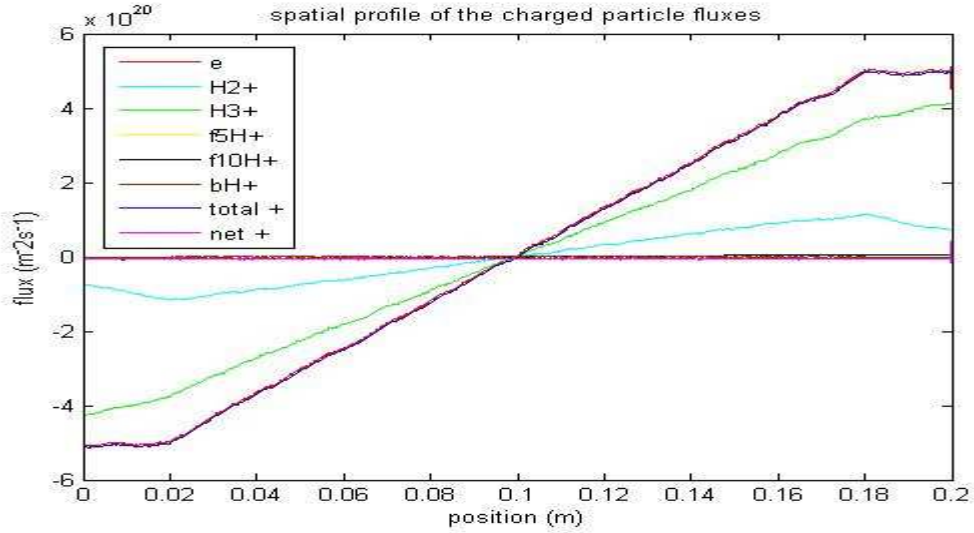

Figure 88: Spatial profiles of the charged particle fluxes for neutraliser H_2 gas densities; (a) $3x10^{19}m^{-3}$, (b) $6x10^{19}m^{-3}$, (c) $9x10^{19}m^{-3}$.

(a)

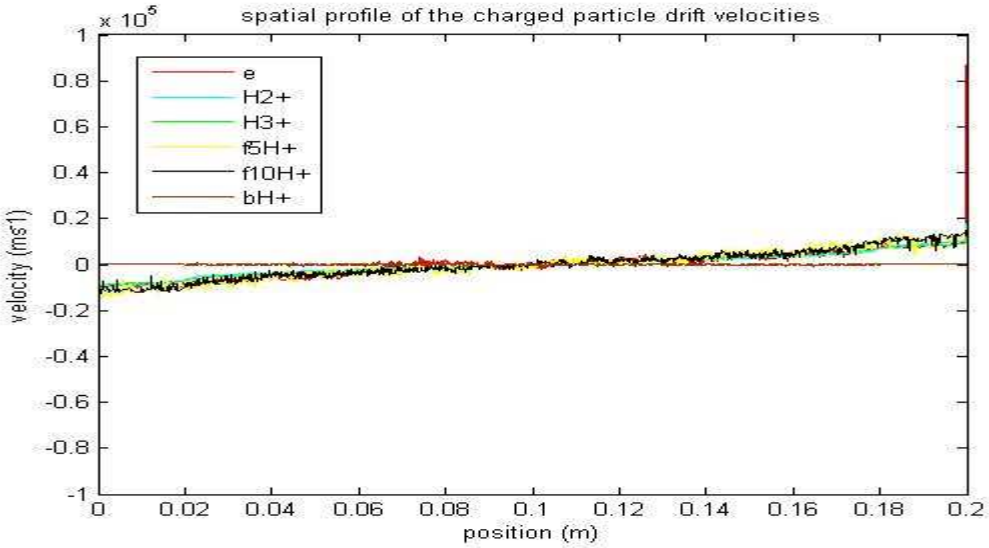

(b)

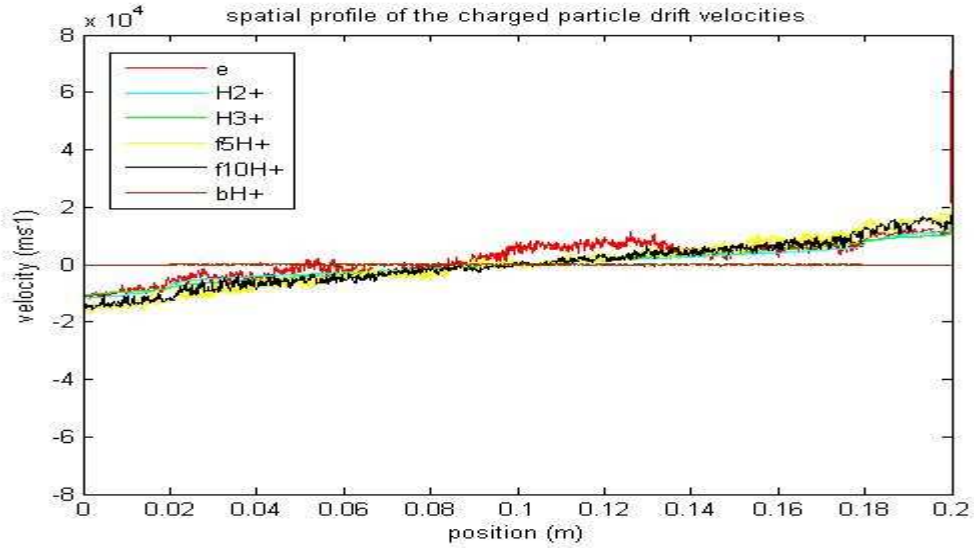

(c)

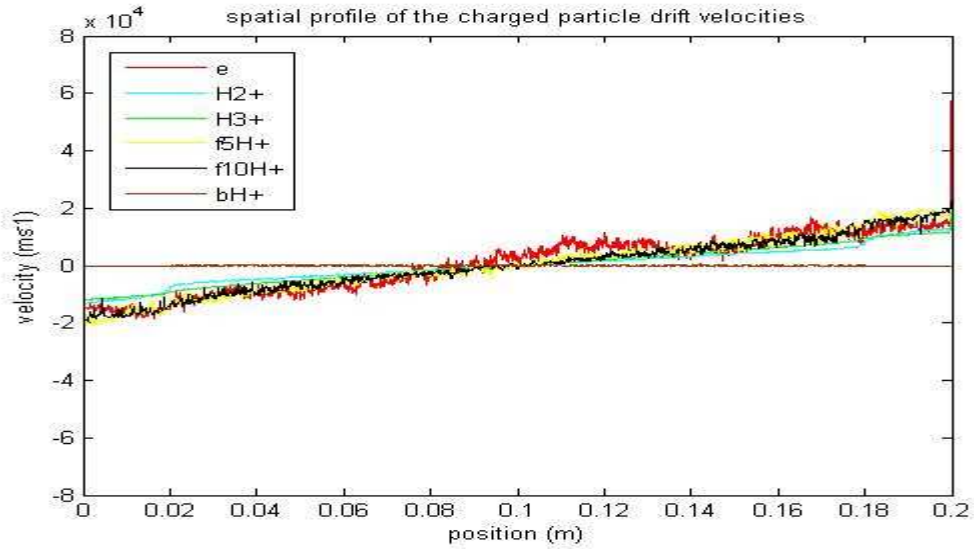

Figure 89: Spatial profiles of the charged particle drift velocities for neutraliser H_2 gas densities; (a) $3x10^{19}m^{-3}$, (b) $6x10^{19}m^{-3}$, (c) $9x10^{19}m^{-3}$.

(a)

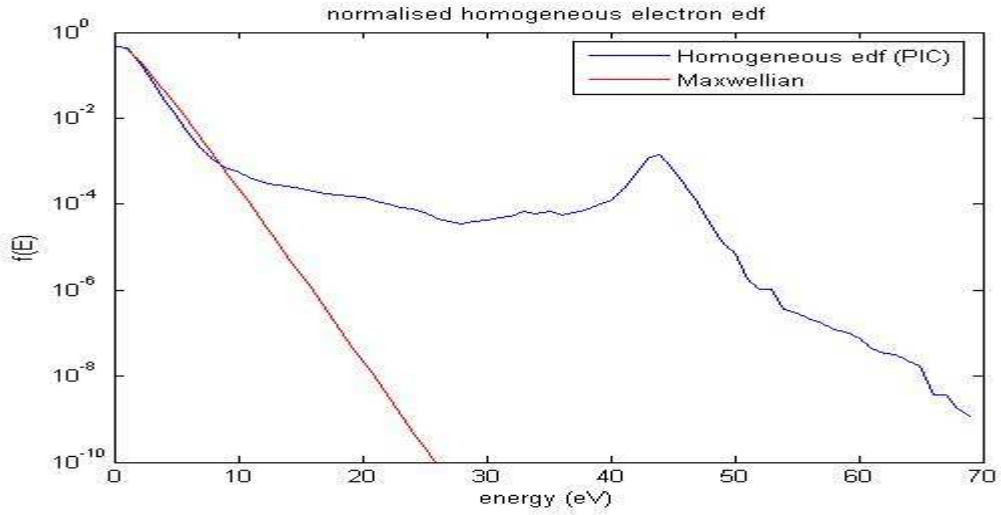

(b)

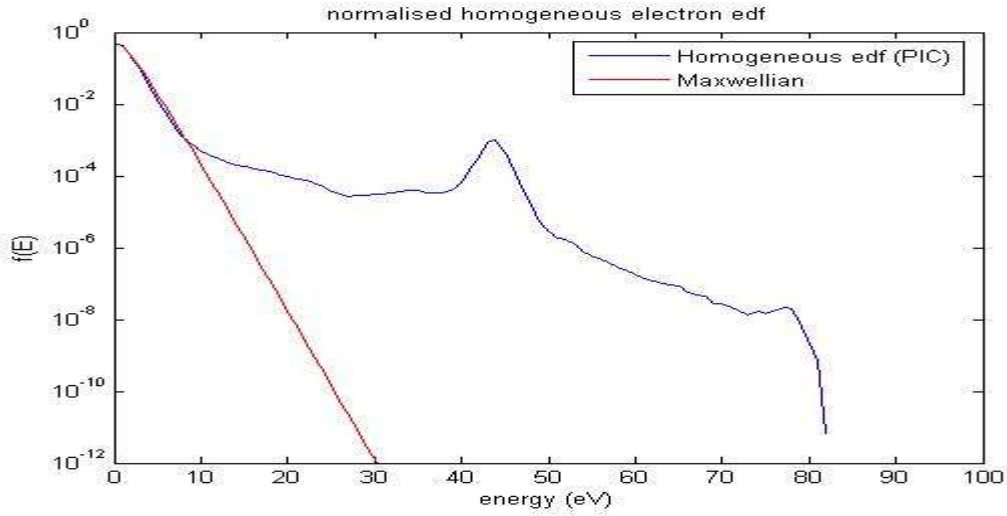

(c)

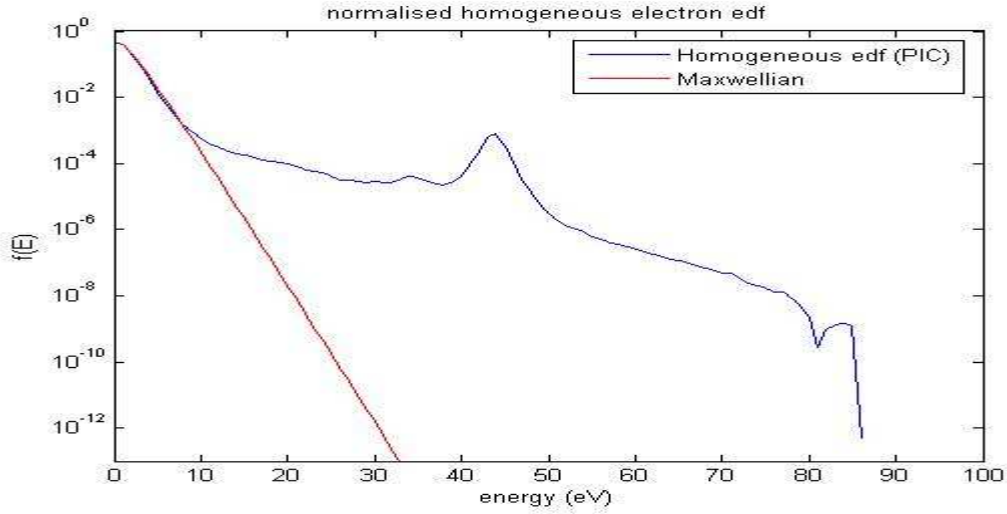

Figure 90: Normalised electron energy distribution functions for neutraliser H_2 gas densities; (a) $3x10^{19}m^{-3}$, (b) $6x10^{19}m^{-3}$, (c) $9x10^{19}m^{-3}$.

The peaks @ ~ 44eV are due to stripped electrons cf. *Figure 83 (c), Appendix B.*

(a)

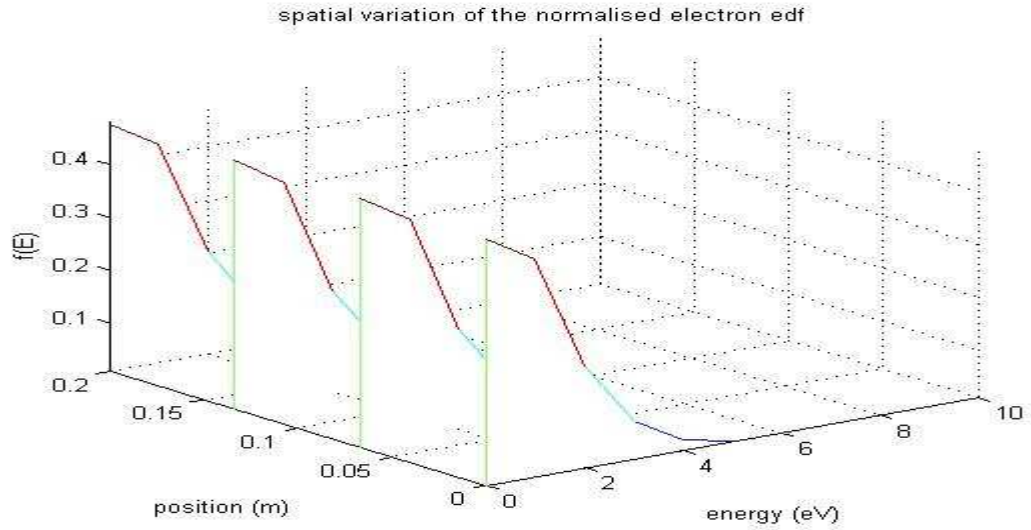

(b)

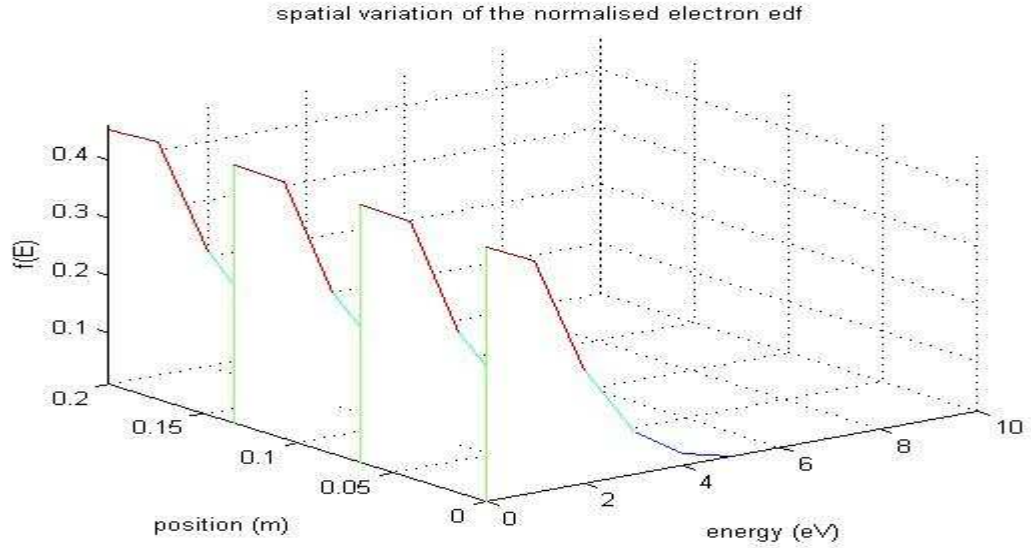

(c)

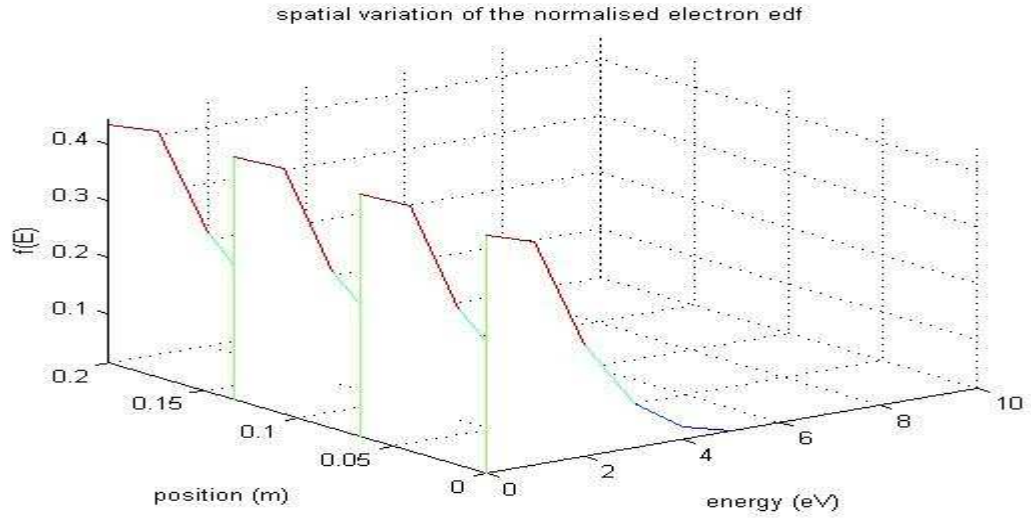

Figure 91: Spatial variation of the normalised electron energy distribution functions for neutraliser H_2 gas densities; (a) $3x10^{19}m^{-3}$, (b) $6x10^{19}m^{-3}$, (c) $9x10^{19}m^{-3}$.

(a)

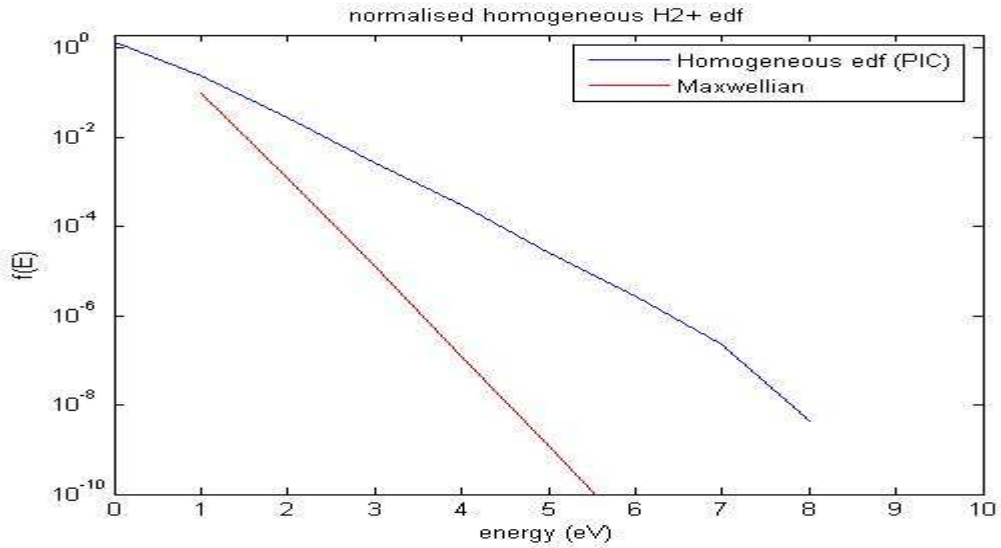

(b)

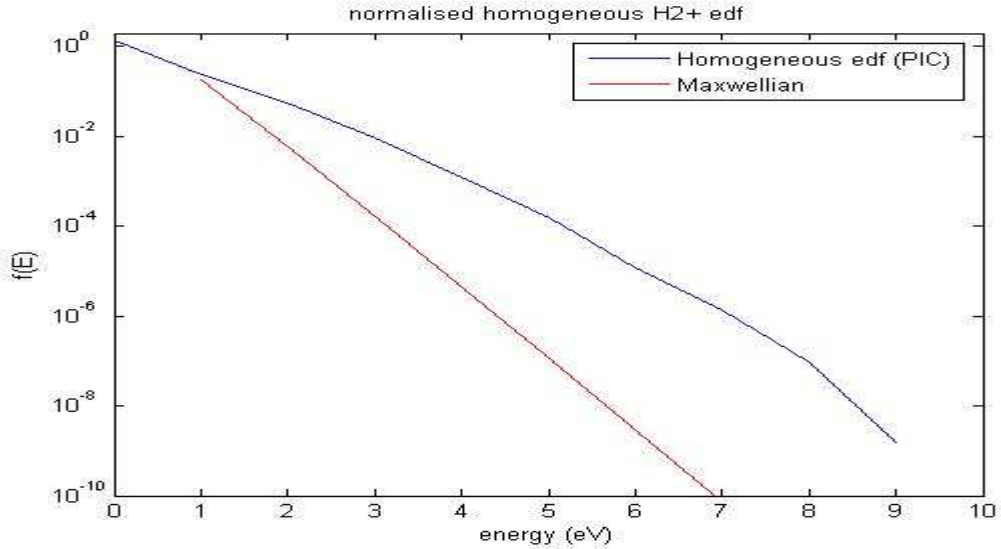

(c)

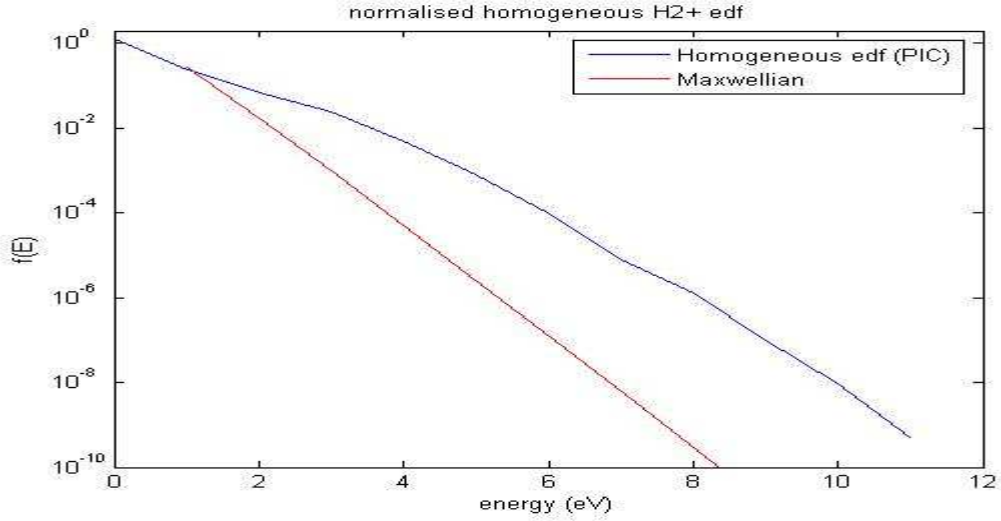

Figure 92: Normalised H_2^+ energy distribution functions for neutraliser H_2 gas densities; (a) $3x10^{19}m^{-3}$, (b) $6x10^{19}m^{-3}$, (c) $9x10^{19}m^{-3}$.

(a)

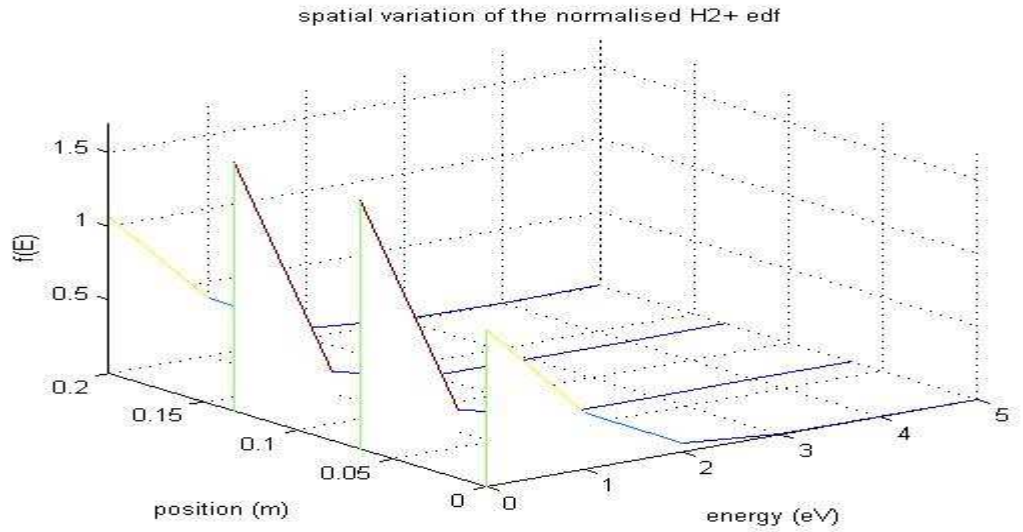

(b)

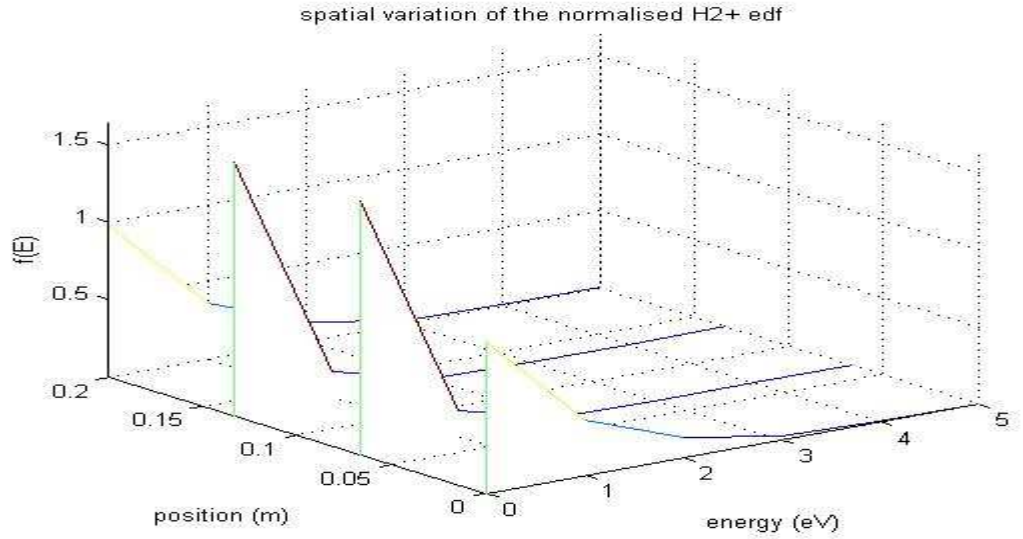

(c)

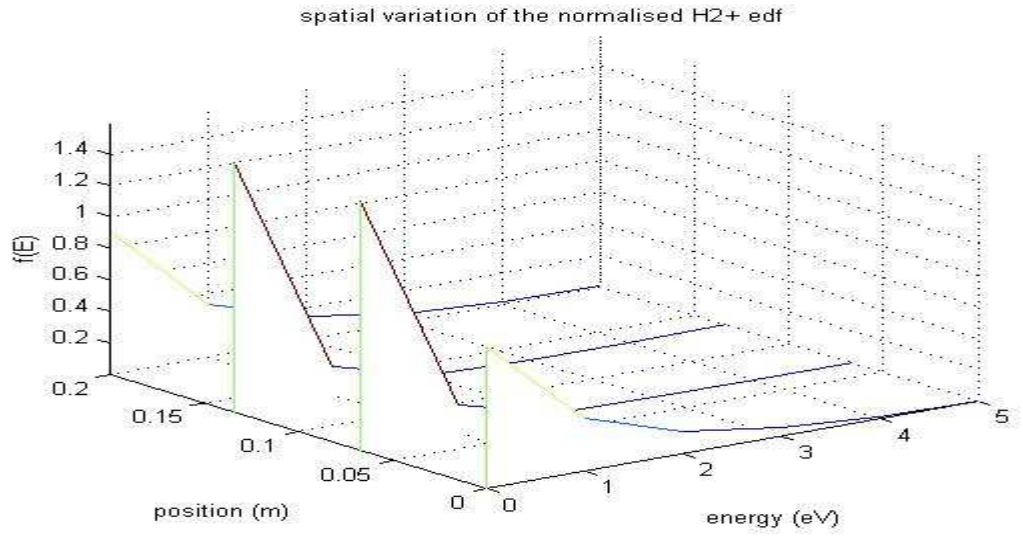

Figure 93: Spatial variation of the normalised H_2^+ energy distribution functions for neutraliser H_2 gas densities; (a) $3x10^{19}m^{-3}$, (b) $6x10^{19}m^{-3}$, (c) $9x10^{19}m^{-3}$.

(a)

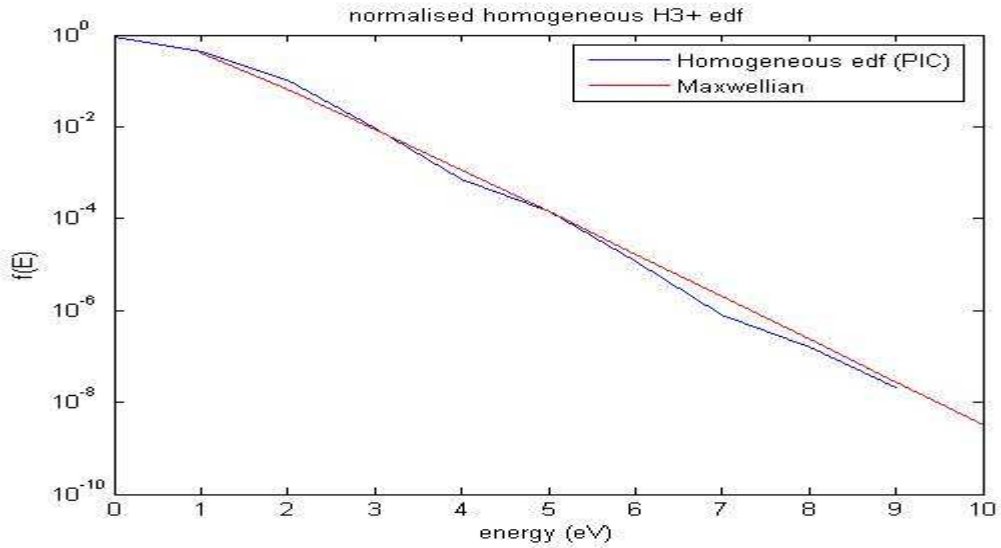

(b)

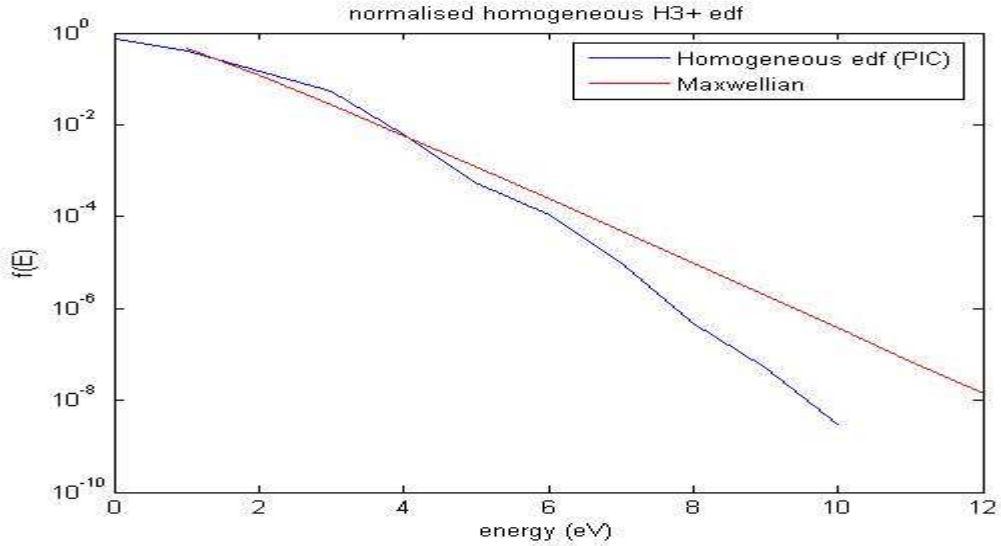

(c)

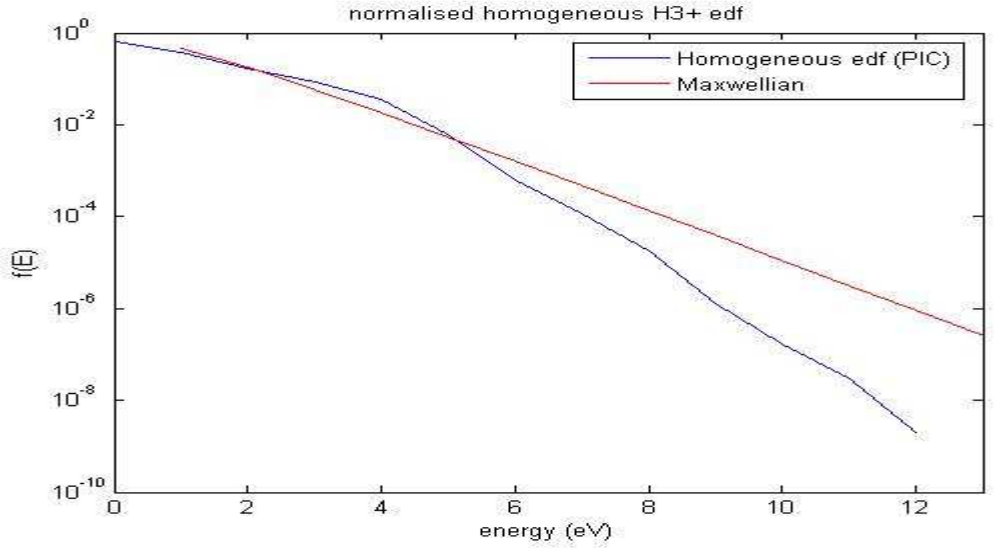

Figure 94: Normalised H_3^+ energy distribution functions for neutraliser H_2 gas densities; (a) $3x10^{19}m^{-3}$, (b) $6x10^{19}m^{-3}$, (c) $9x10^{19}m^{-3}$.

(a)

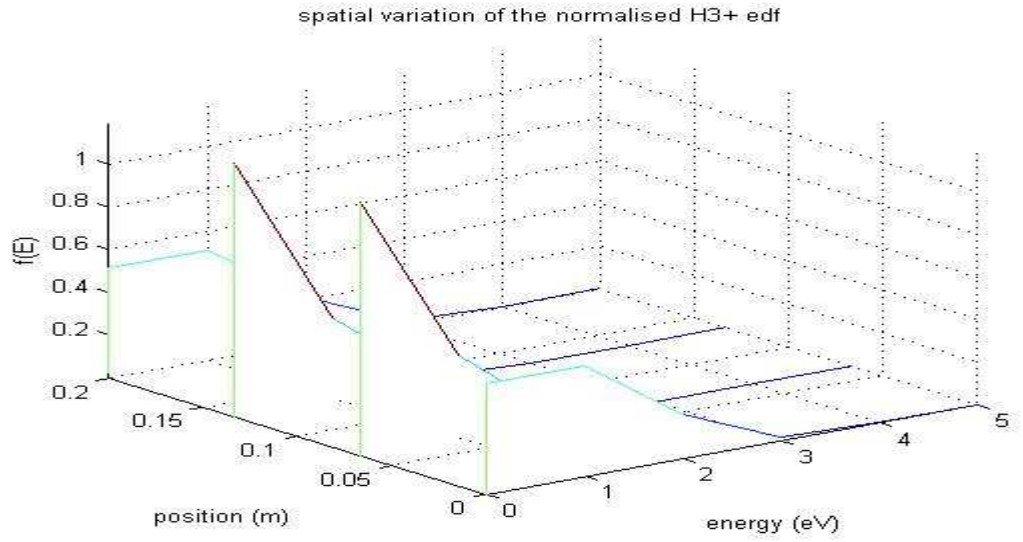

(b)

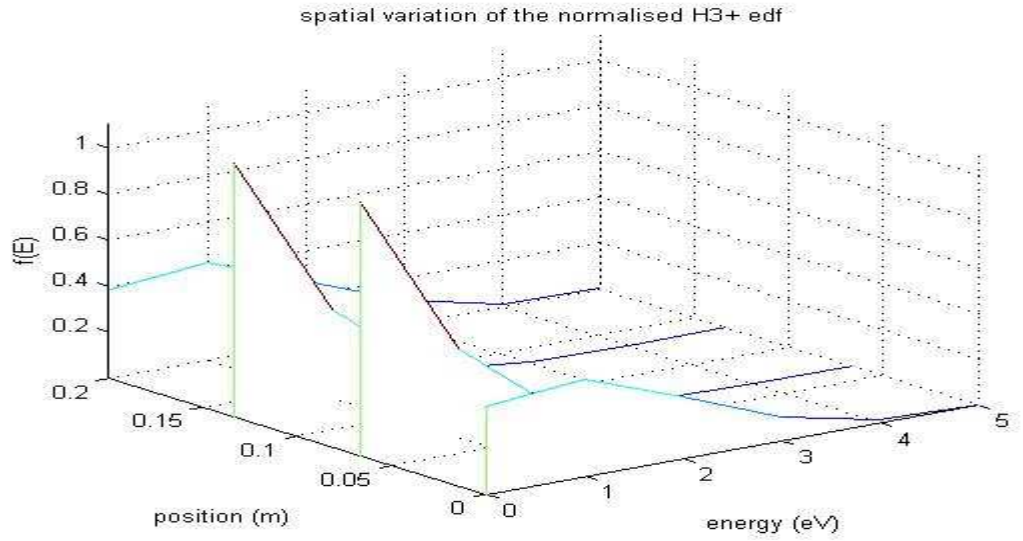

(c)

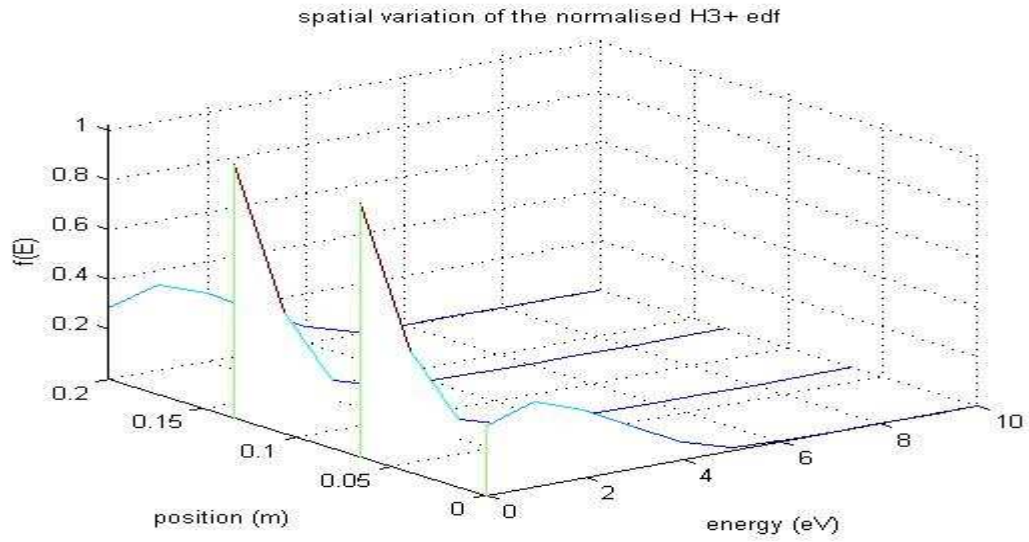

Figure 95: Spatial variation of the normalised H_3^+ energy distribution functions for neutraliser H_2 gas densities; (a) $3x10^{19}m^{-3}$, (b) $6x10^{19}m^{-3}$, (c) $9x10^{19}m^{-3}$.

Spatially resolved plasma parameters versus beam power

H_2 gas density, $9x10^{19}m^{-3}$. H^+ beam powers; (a) 2.16 MW, (b) 6.00 MW, (c) 8.04 MW:

(a)

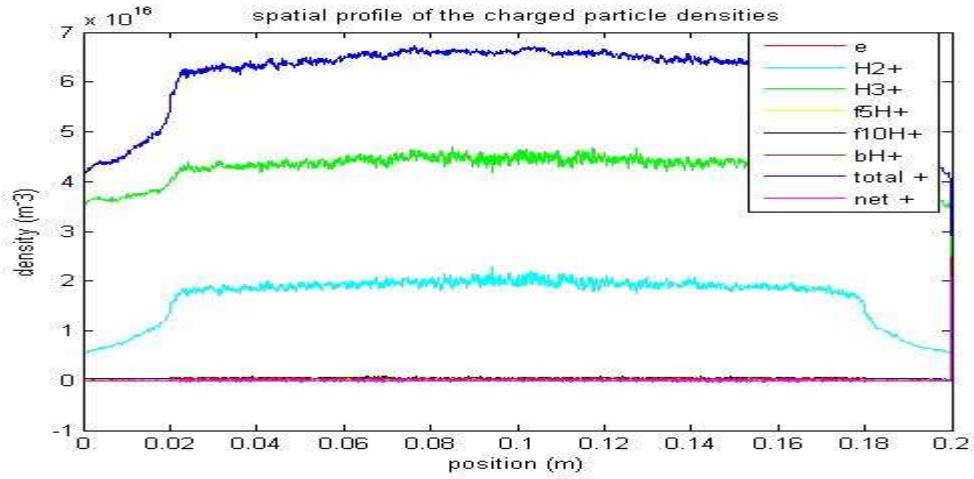

(b)

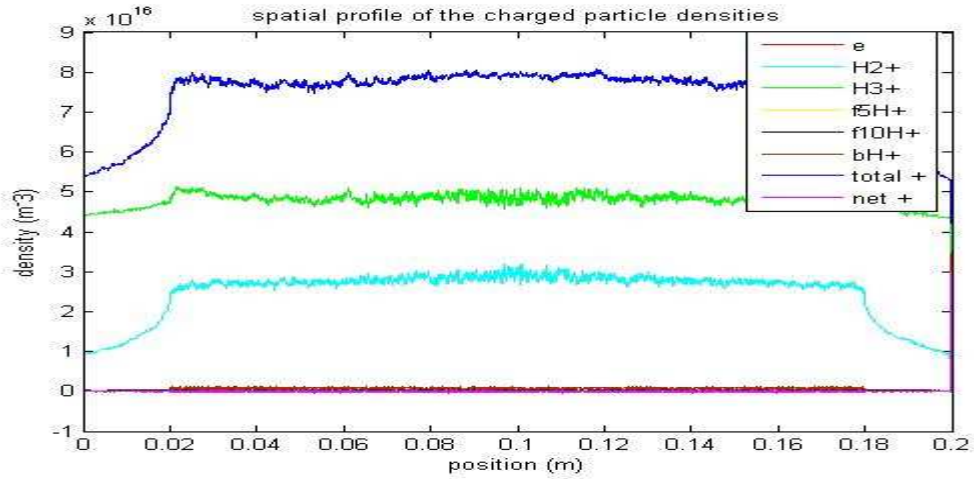

(c)

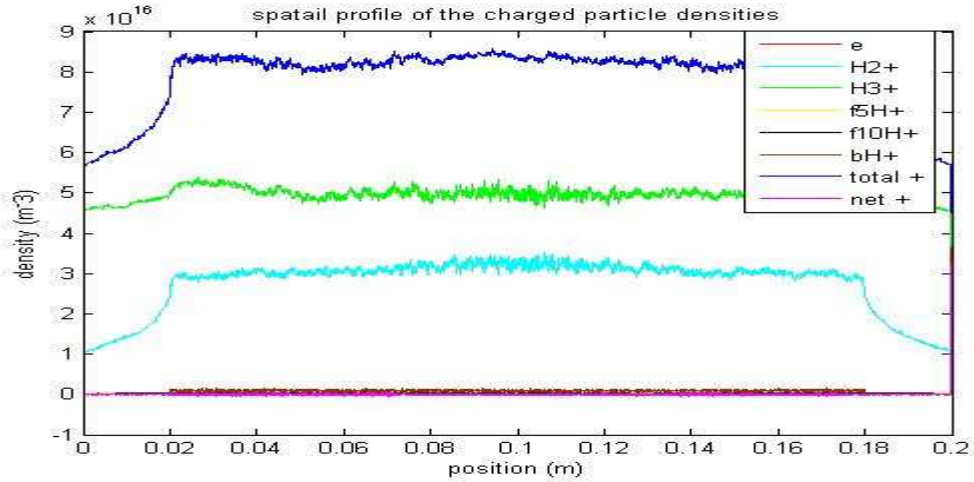

Figure 96: Spatial profiles of the charged particle densities for hydrogen beam powers; (a) 2.16 MW, (b) 6.00 MW, (c) 8.04 MW.

(a)

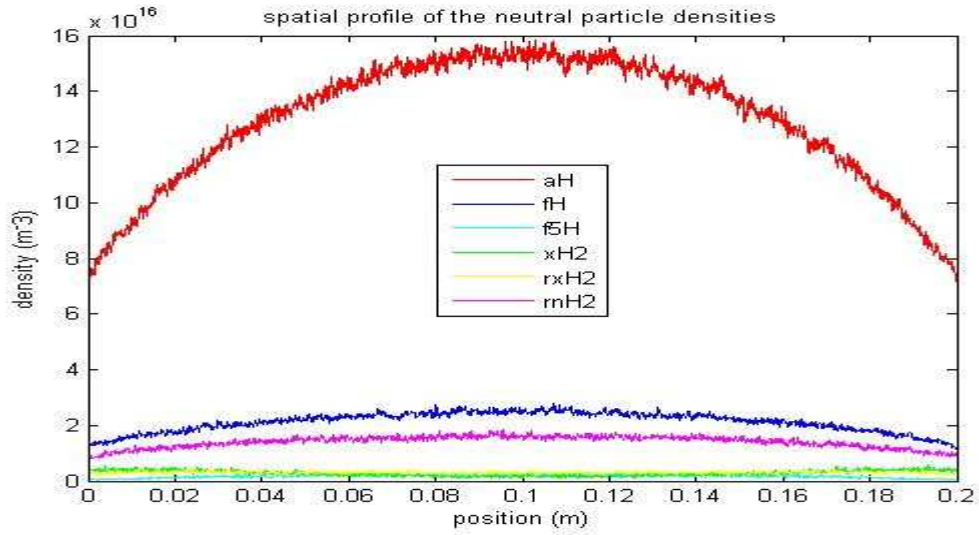

(b)

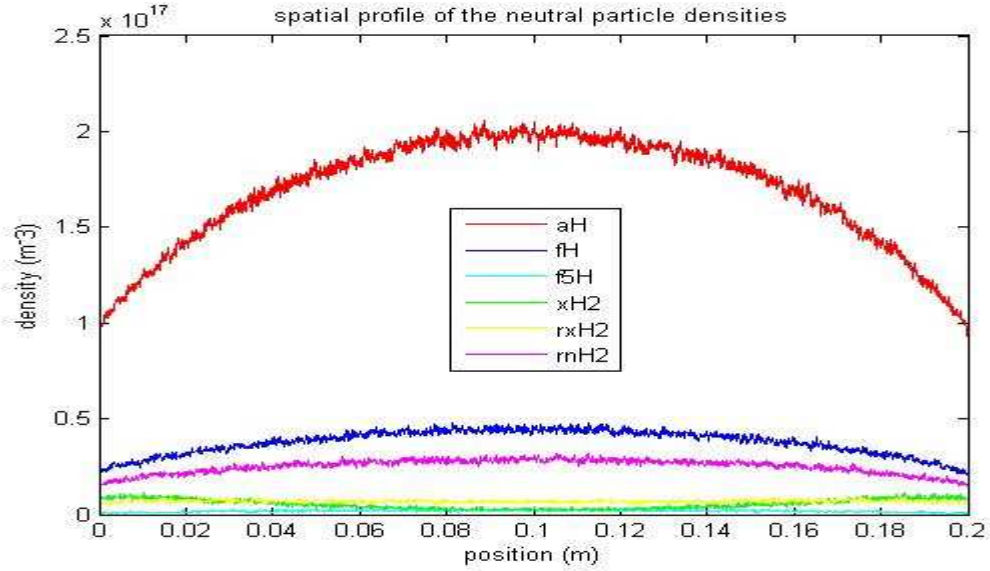

(c)

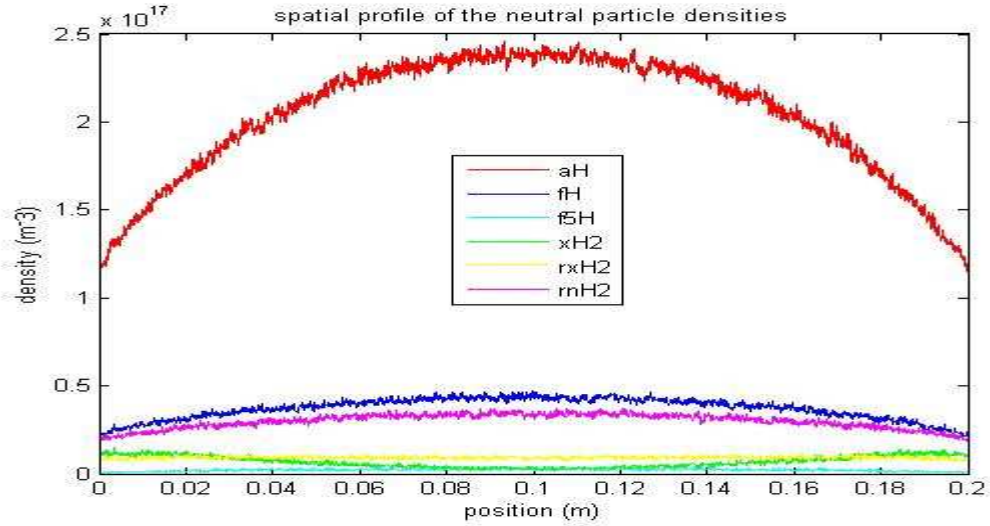

Figure 97: Spatial profiles of the neutral particle densities for hydrogen beam powers; (a) 2.16 MW, (b) 6.00 MW, (c) 8.04 MW.

(a)

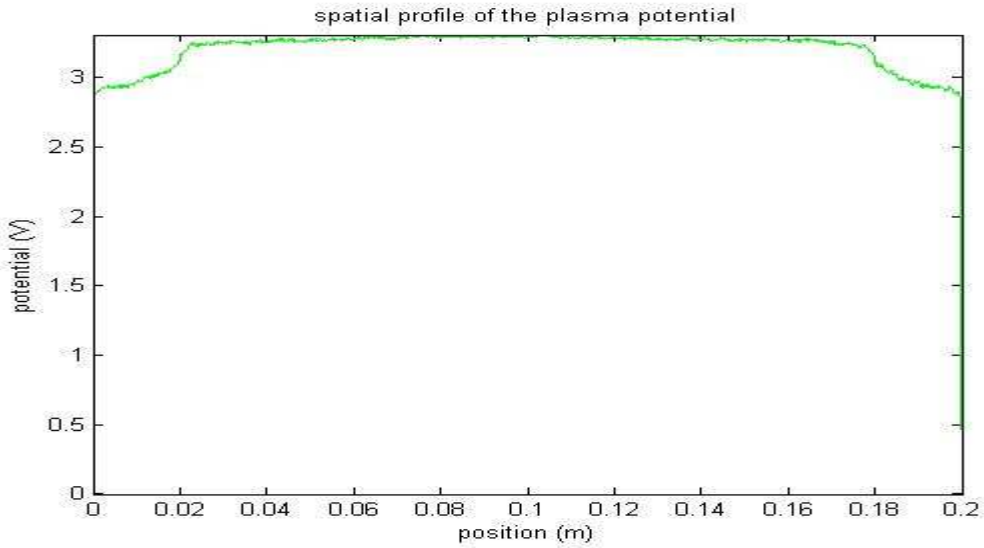

(b)

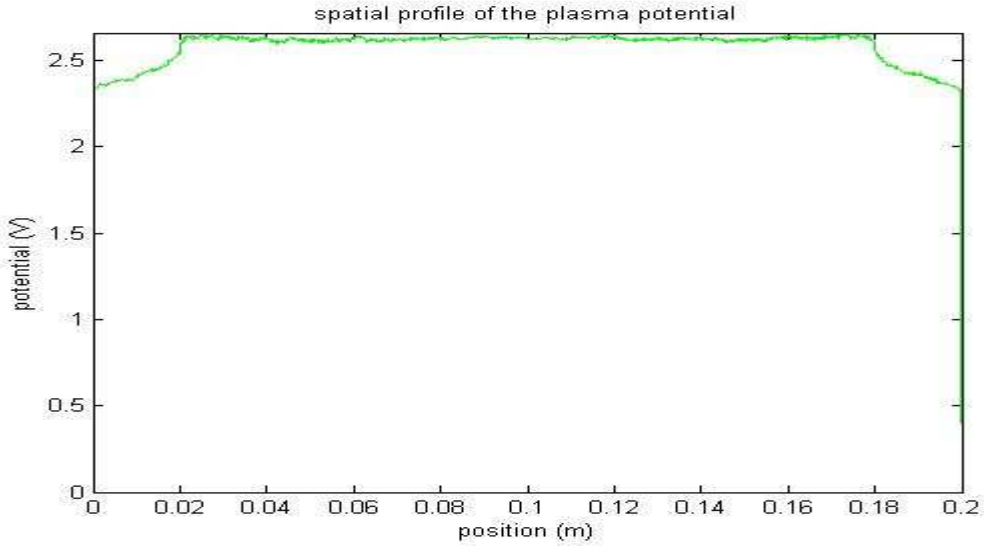

(c)

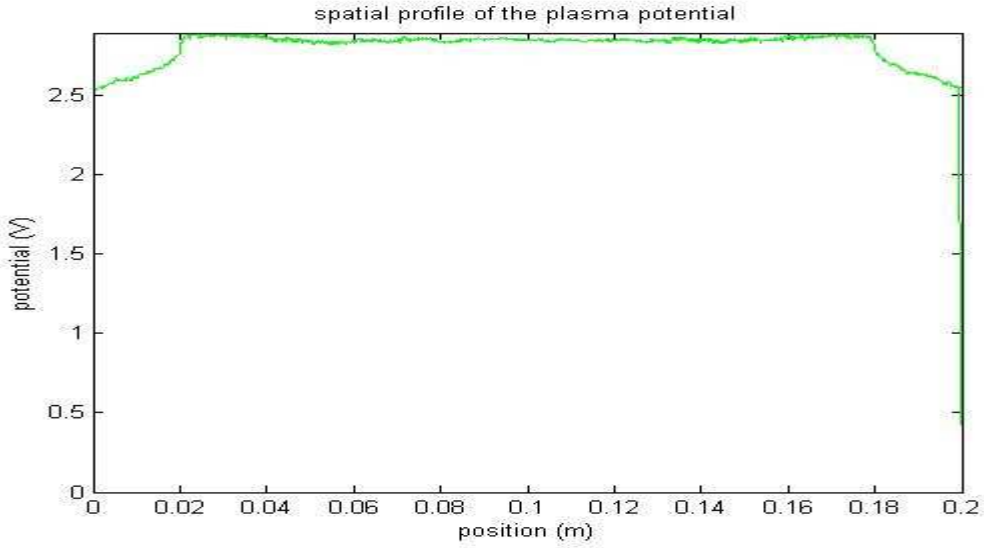

Figure 98: Spatial profiles of the plasma potentials for hydrogen beam powers; (a) 2.16 MW, (b) 6.00 MW, (c) 8.04 MW.

(a)

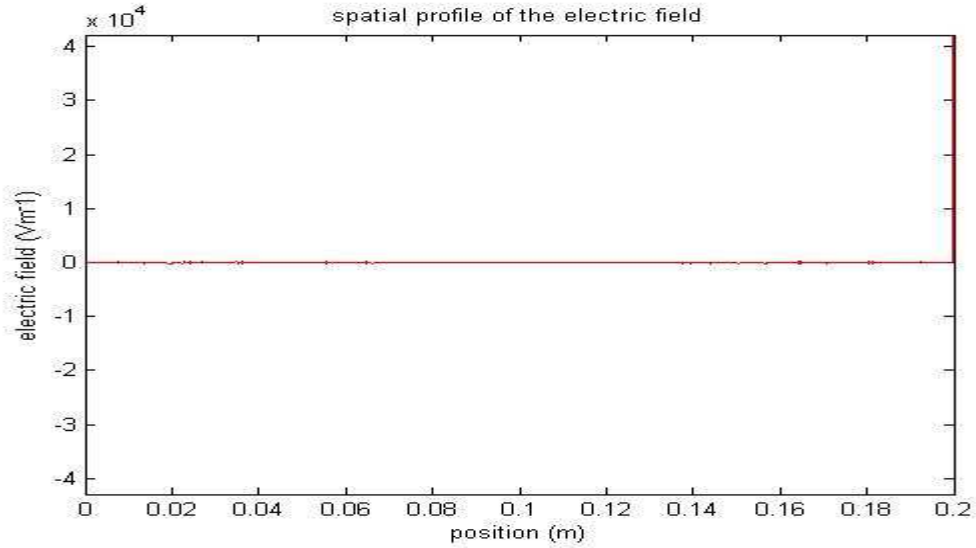

(b)

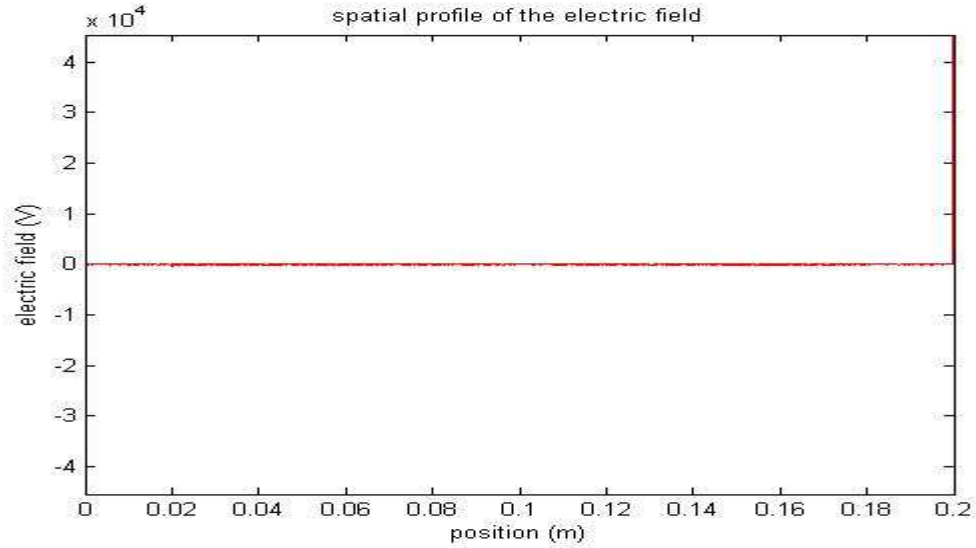

(c)

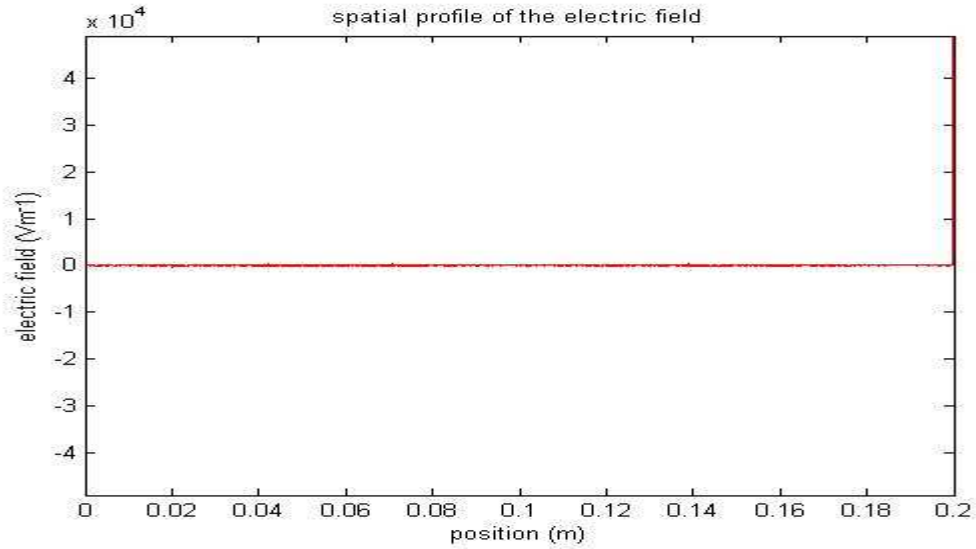

Figure 99: Spatial profiles of the electric fields for hydrogen beam powers; (a) 2.16 MW, (b) 6.00 MW, (c) 8.04 MW.

(a)

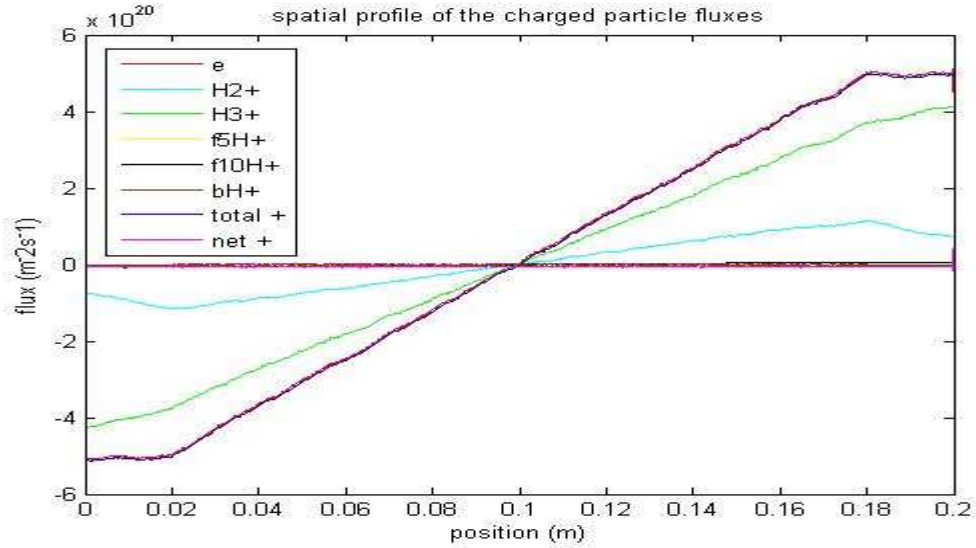

(b)

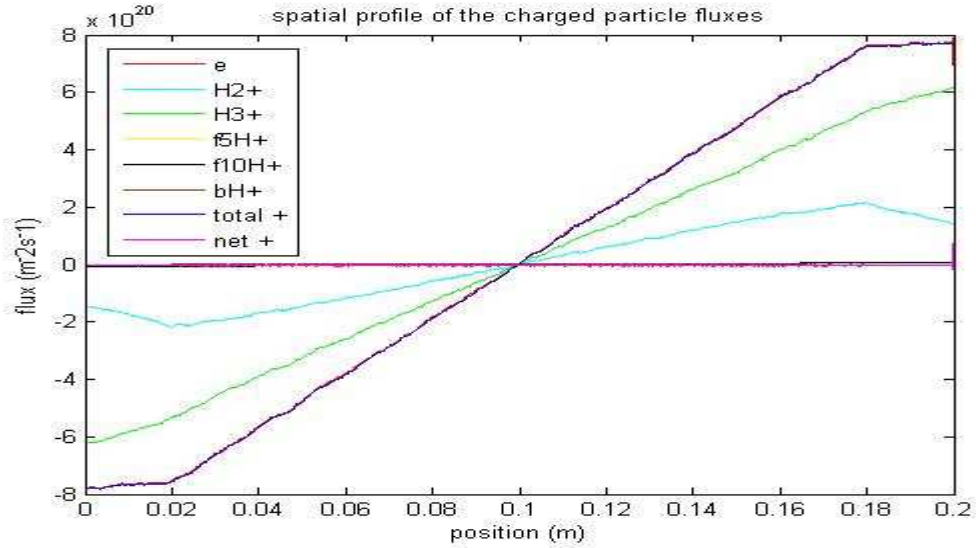

(c)

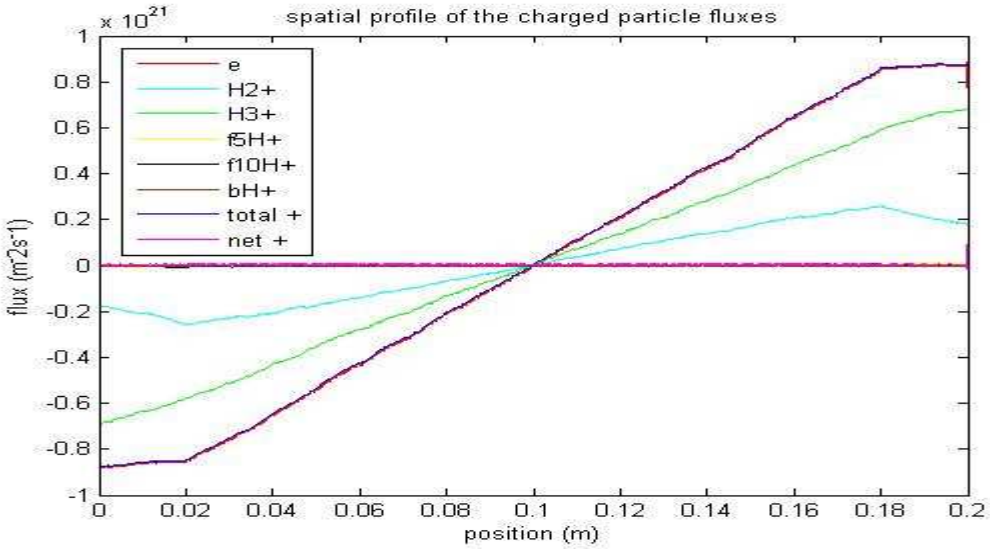

Figure 100: Spatial profiles of the charged particle fluxes for hydrogen beam powers; (a) 2.16 MW, (b) 6.00 MW, (c) 8.04 MW.

(a)

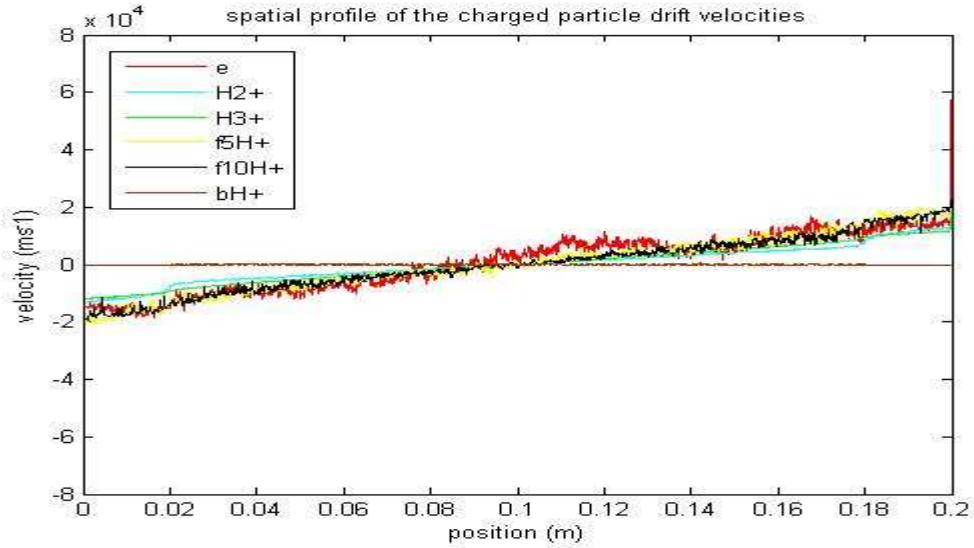

(b)

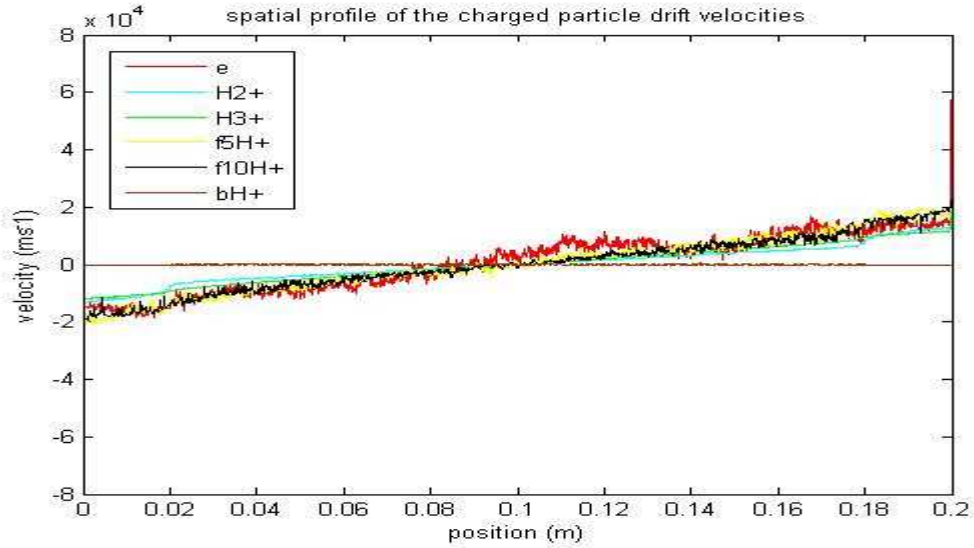

(c)

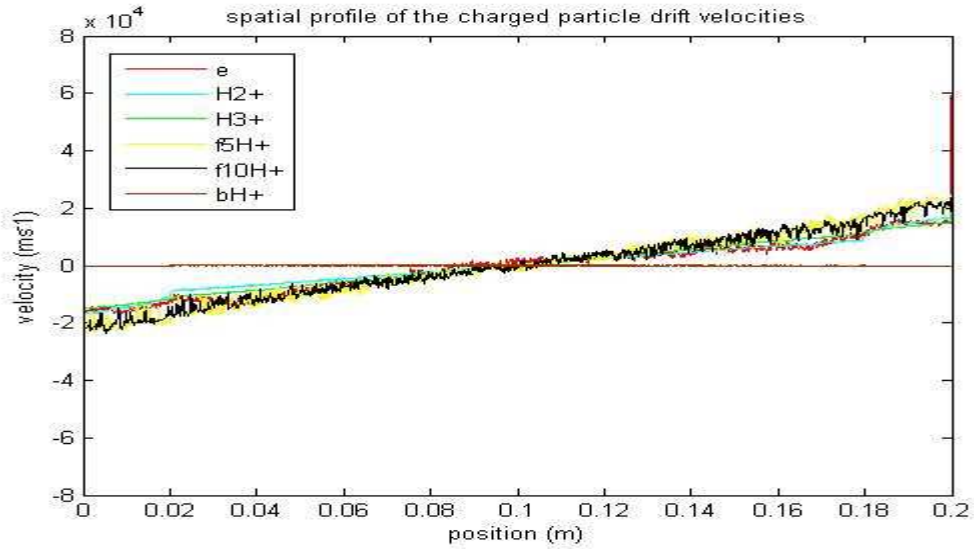

Figure 101: Spatial profiles of the charged particle velocities for hydrogen beam powers; (a) 2.16 MW, (b) 6.00 MW, (c) 8.04 MW.

(a)

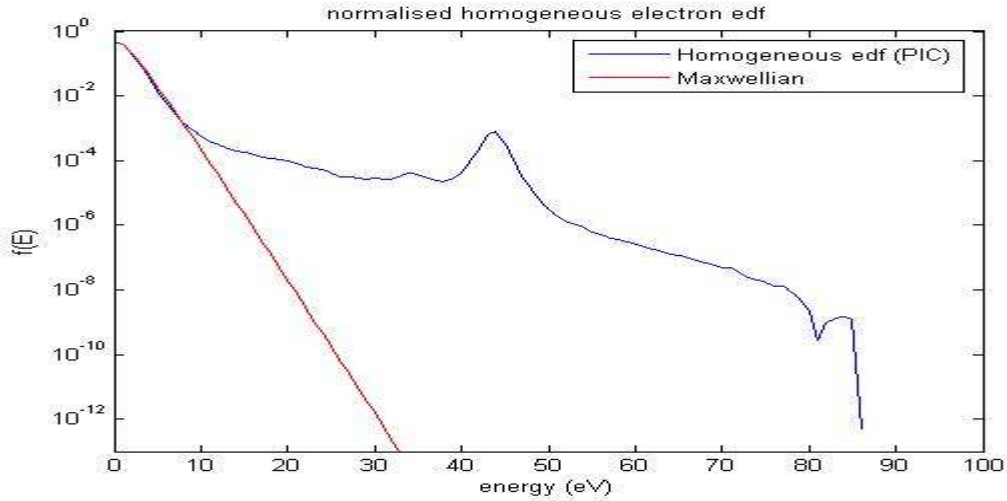

(b)

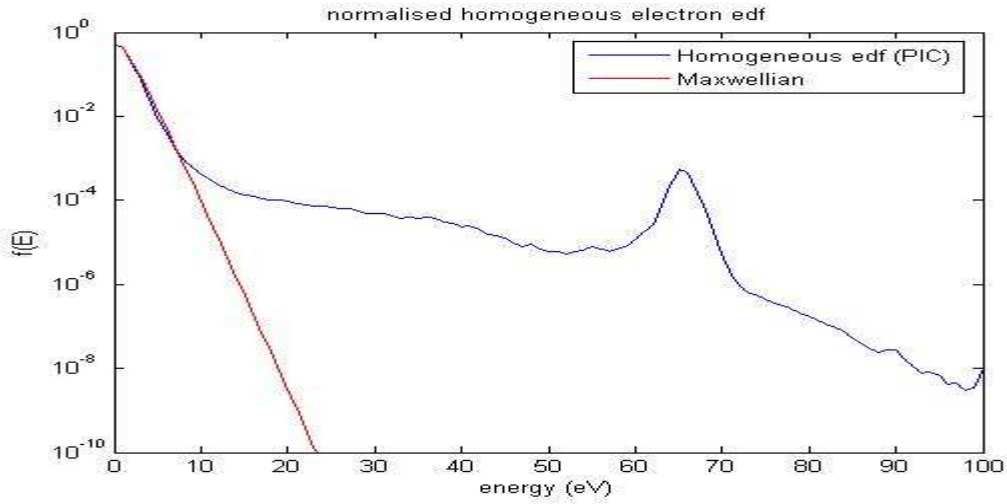

(c)

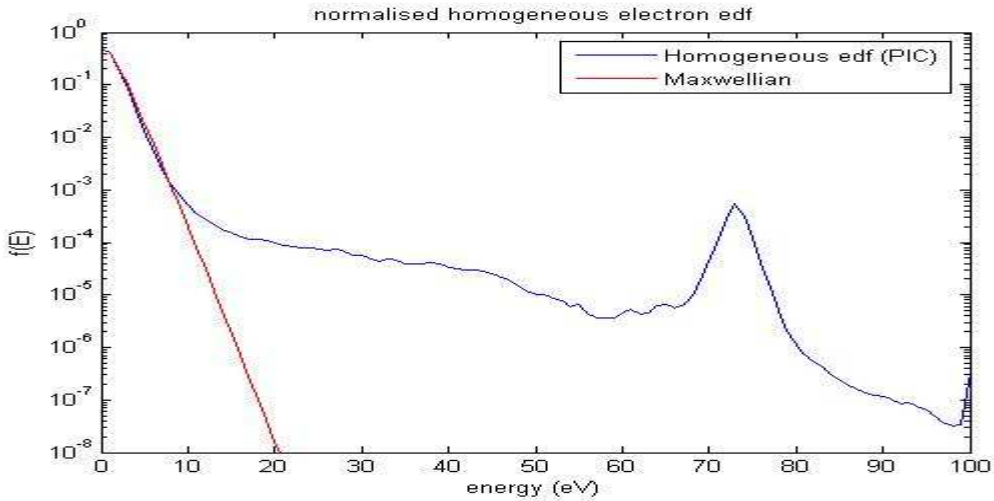

Figure 102: Normalised electron energy distribution functions for hydrogen beam powers; (a) 2.16 MW, (b) 6.00 MW, (c) 8.04 MW.

As in *Figure 90*, the peaks @ ~ 44/65/73 eV are due to stripped electrons.

(a)

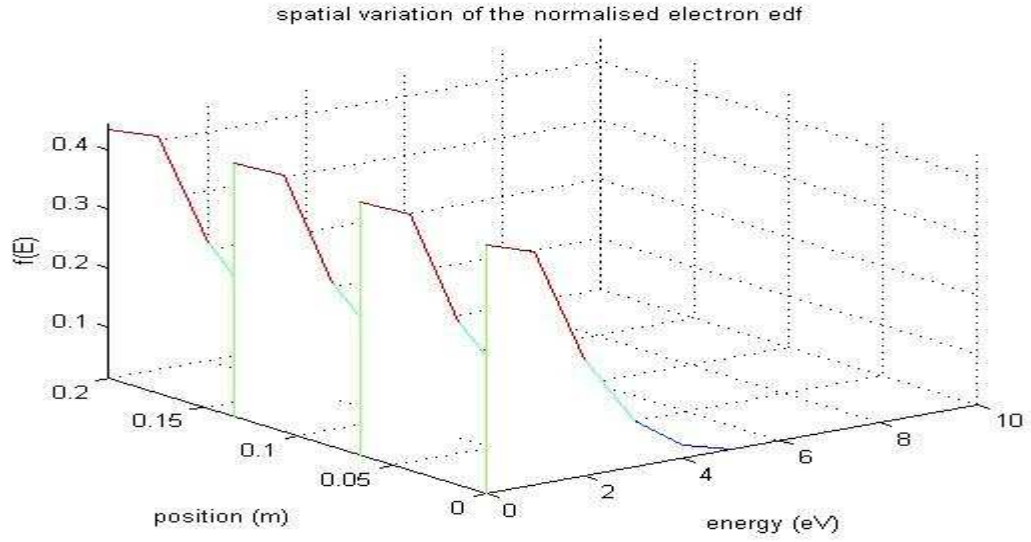

(b)

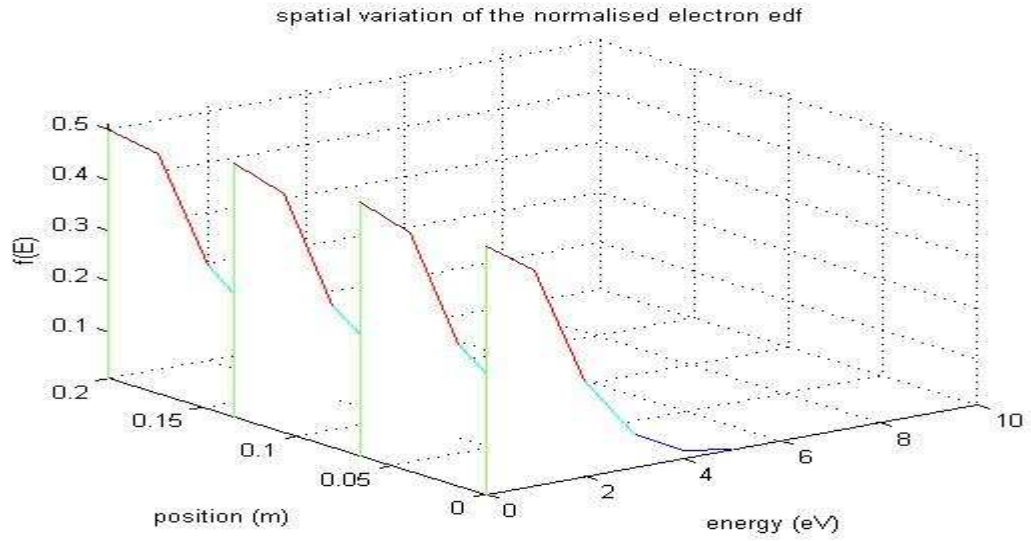

(c)

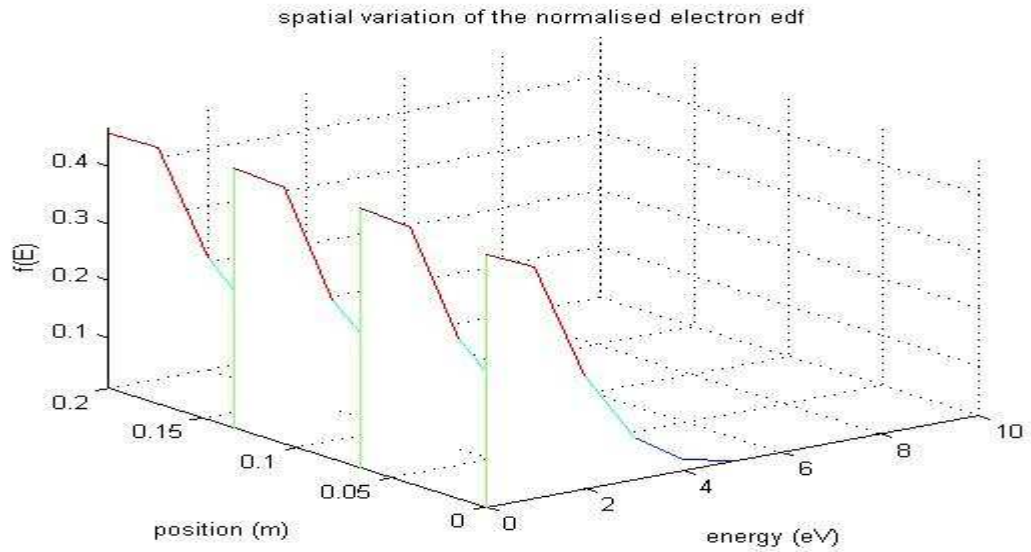

Figure 103: Spatial variation of the normalised electron energy distribution functions for hydrogen beam powers; (a) 2.16 MW, (b) 6.00 MW, (c) 8.04 MW.

(a)

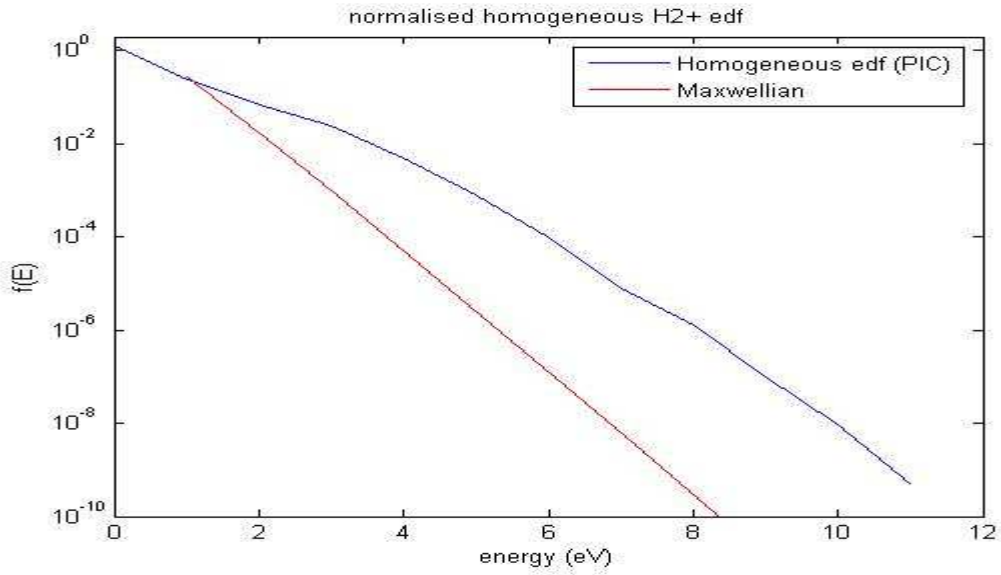

(b)

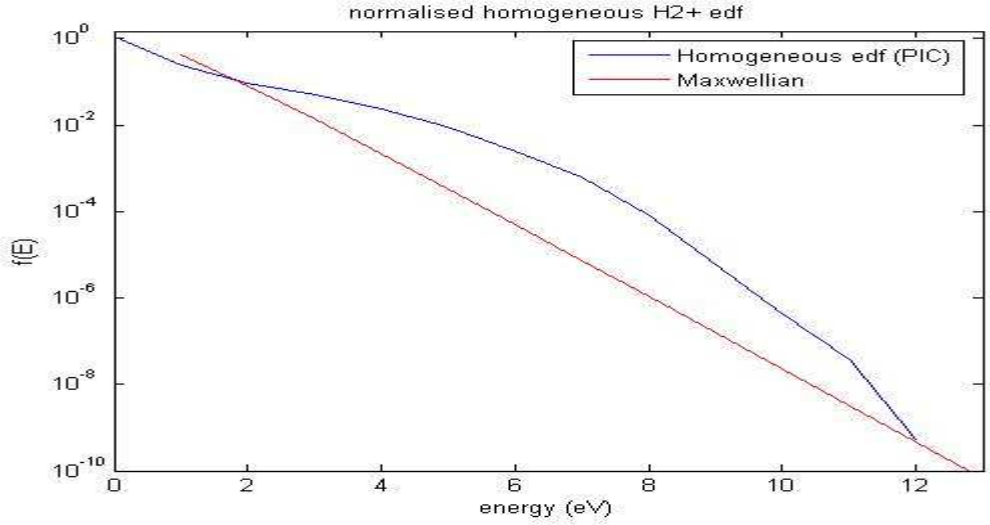

(c)

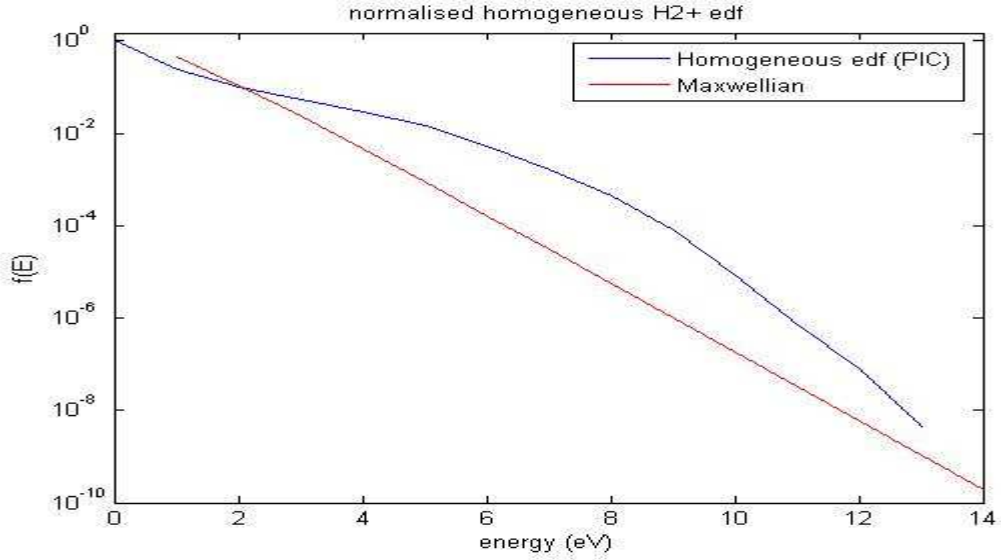

Figure 104: Normalised H_2^+ energy distribution functions for hydrogen beam powers; (a) 2.16 MW, (b) 6.00 MW, (c) 8.04 MW.

(a)

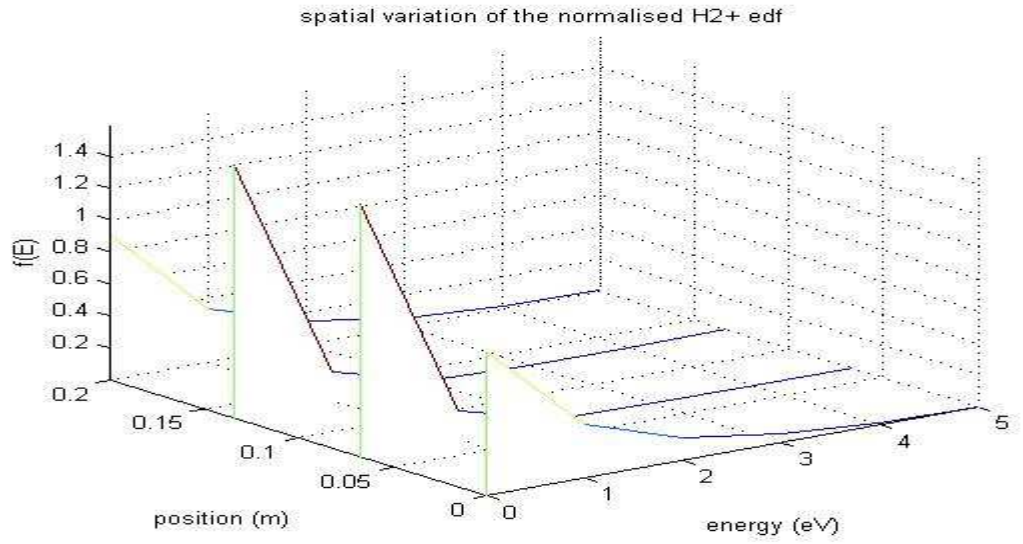

(b)

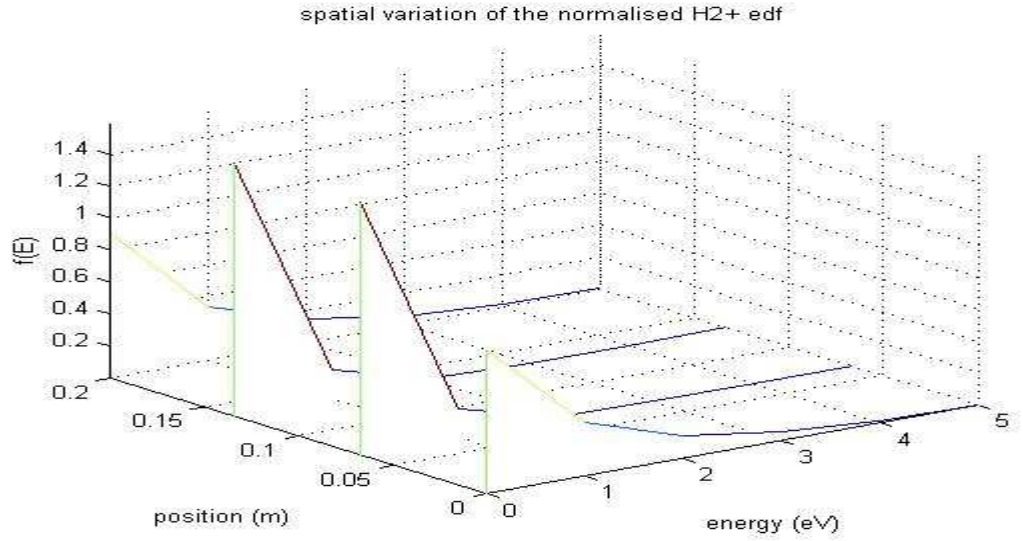

(c)

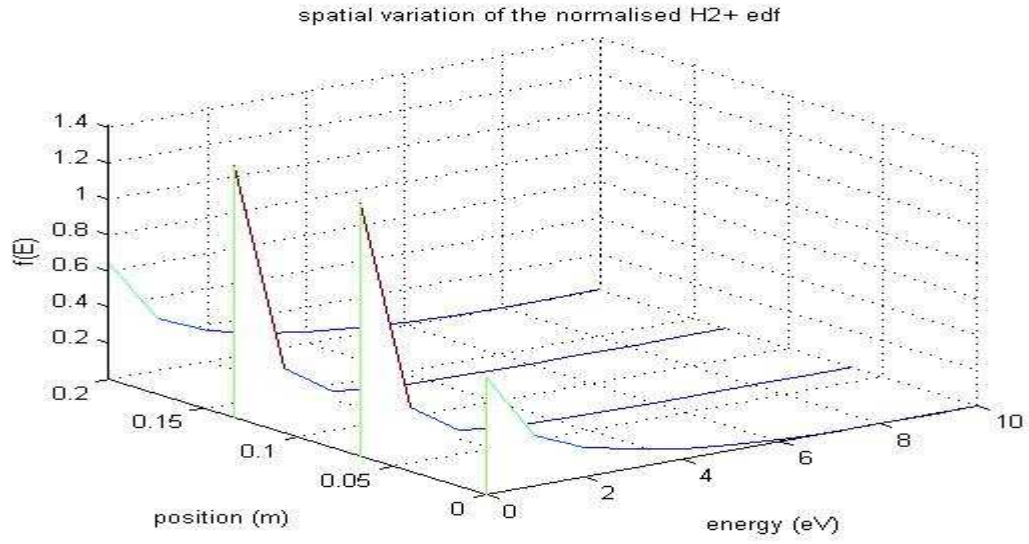

Figure 105: Spatial variation of the normalised H_2^+ energy distribution functions for hydrogen beam powers; (a) 2.16 MW, (b) 6.00 MW, (c) 8.04 MW.

(a)

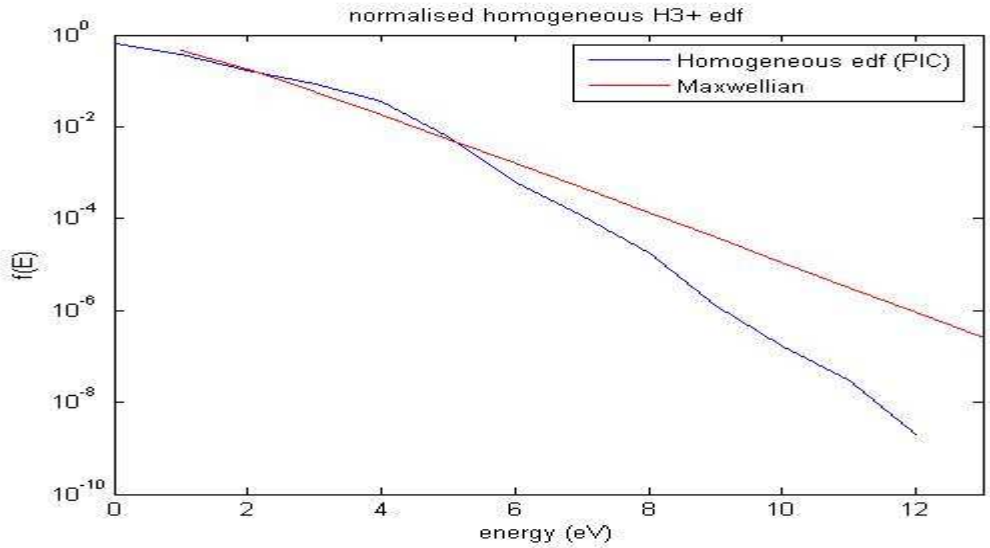

(b)

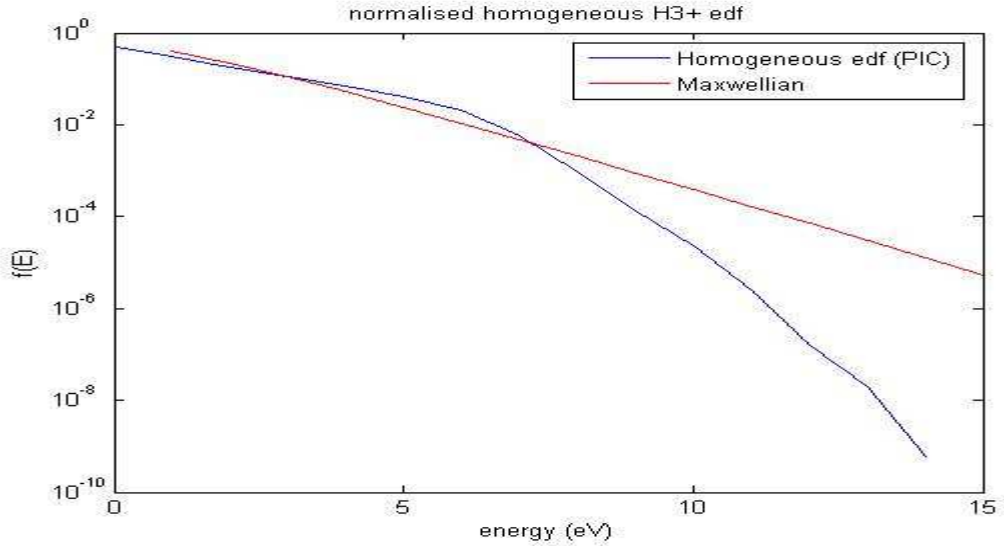

(c)

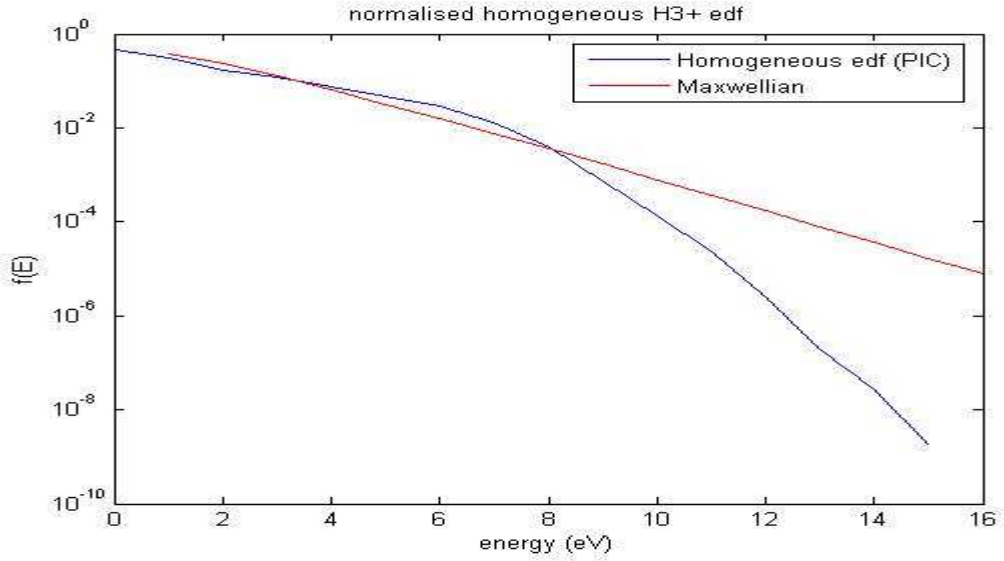

Figure 106: Normalised H_3^+ energy distribution functions for hydrogen beam powers; (a) 2.16 MW, (b) 6.00 MW, (c) 8.04 MW.

(a)

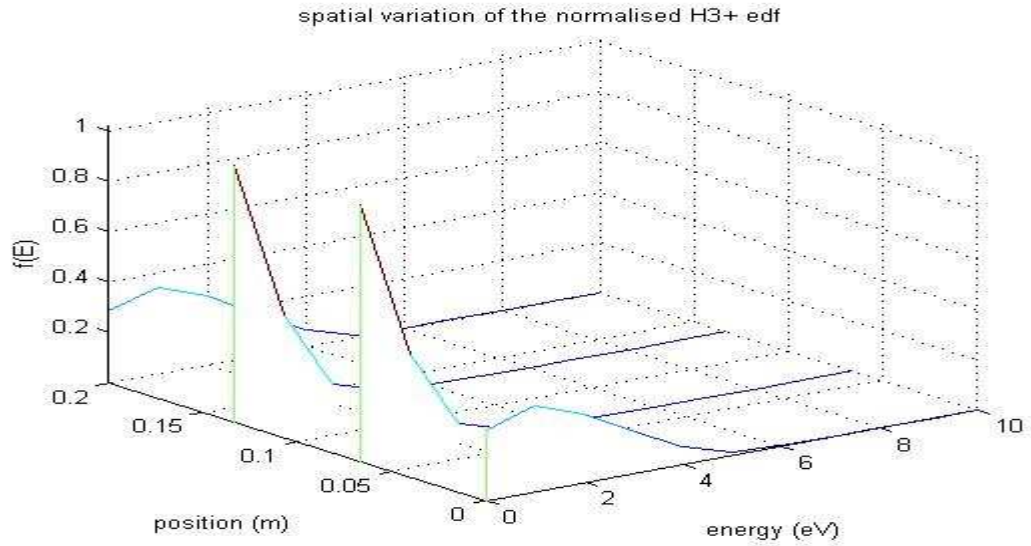

(b)

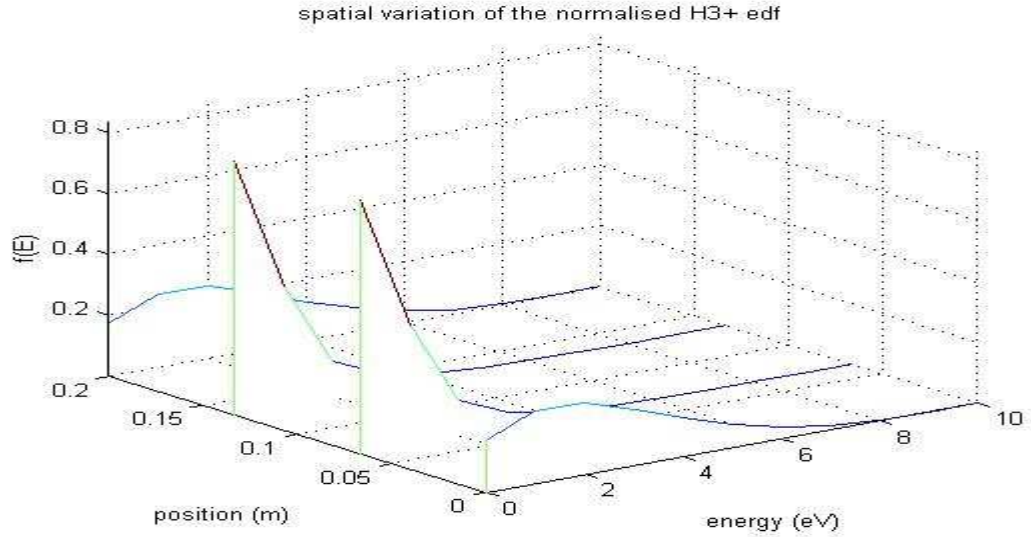

(c)

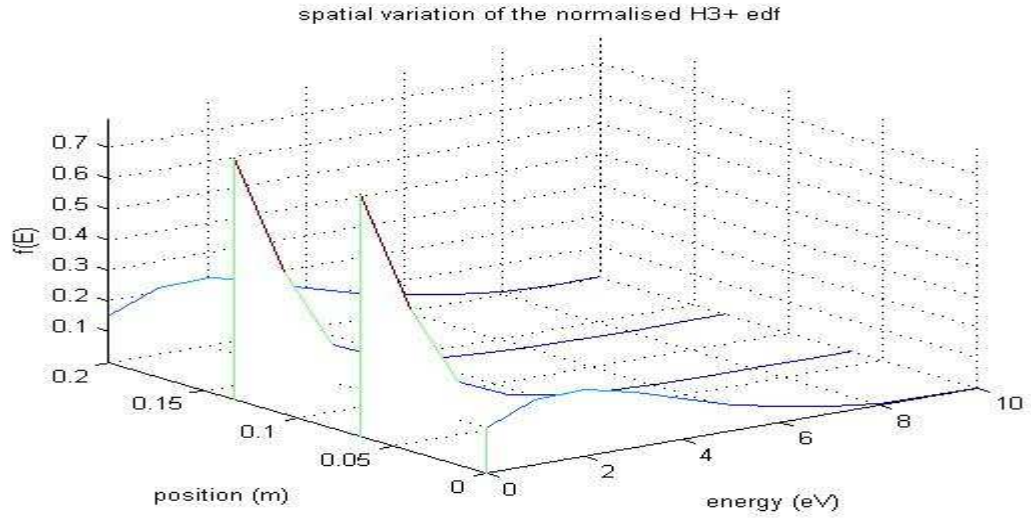

Figure 107: Spatial variation of the normalised H_3^+ energy distribution functions for hydrogen beam powers; (a) 2.16 MW, (b) 6.00 MW, (c) 8.04 MW.

Appendix D Paméla's gas heating model

Paméla's analytic gas heating model [31, 34] (cf. [36]) accounts for three categories of gas heating sources, namely (1) molecular dissociation by beam ions, (2) molecular dissociation by plasma electrons (both forming fast H/H^+ particles capable of heating the neutraliser gas) and (3) reflected neutralised H_2^+ ions (directly capable of heating the neutraliser gas). This model was based on a steady-state neutraliser gas assumption i.e. power losses at the walls = power gained indirectly from the beam:

$$(\tfrac{nv}{4})S_w \alpha k \frac{T-T_w}{\gamma-1} = s(I_{B,}E_B, n, n_e, T_e, V_p, L, x, y) \qquad \text{(D.1)}$$

$$s(I_{B,}E_B, n, n_e, T_e, V_p, L, x, y) =$$

$$\left(\sum_{j=1}^{4}\sigma_j(E_B)E_{dj}P(E_{dj})\right)\frac{nLI_B}{e} + \quad \text{: molecular dissociation by beam ions (}\textit{Table 13}\text{)}$$

$$n_e n\langle\sigma_{de}v_e\rangle V E_{de}P(E_{de}) + \quad \text{: molecular dissociation by plasma electrons}$$

$$n_e S_w R V_p \frac{eT_e^{\frac{1}{2}}}{\sqrt{M^+}}(1-\exp(-\sigma_0 xn)) \quad \text{: reflected neutralised plasma ions}$$

j	*Reaction*	*Process*	E_{dj} *(eV)*	$\sigma(E_B)$ $(10^{-21}m^2)$
1	$\underline{H}^+ + H_2 \rightarrow \underline{H} + H + H^+$	Dissociative Charge Exchange	5	$\exp\{2.6(1-E_B)/100\}$
2	$\underline{H}^+ + H_2 \rightarrow \underline{H}^+ + H + H^+ + e$	Dissociative Ionisation	5	$0.7+(E_B-40)/100$
3	$\underline{H}^+ + H_2 \rightarrow \underline{H}^+(\underline{H}) + H^+ + H^+ + e + (e)$	Double Ionisation	10	$\exp\{0.79(1-E_B/121)\}$
4	$\underline{H}^+ + H_2 \rightarrow \underline{H}^+ + H + H$	Simple Dissociation	2	$\frac{9.7\exp\{-3.4(1-64.4/E_B)^2\}}{1+10^5(E_B/39)^6}$

Table 13: List of beam dissociation collisions leading to the formation of fast particles (initial energy in eV) and formulae for computing the cross sections [36].

To compute the gas density distribution along the neutraliser, the power balance equation (D.1) is used together with an equation describing the density gradient (D.2):

$$\frac{dn(z)}{dz} = \frac{F}{LCK(x/\lambda(z))\sqrt{T(z)}/T_C} \qquad \text{(D.2)}$$

$n(z - \Delta z)$ & $T(z - \Delta z)$ being known; the power balance equation (F.1) is used to calculate $T(z)$ from $n(z - \Delta z)$, and $T(z)$ is then used to calculate $n(z) = n(z - \Delta z) + \Delta z dn(z)/dz$ (Taylor expansion). This method applies to a thin neutraliser transverse gas slice (z, $z + \Delta z$). Since the energy exchange (ΔE) between neighbouring gas slices of the same width is a 2nd order expression, this approach is only strictly valid for 1st order in Δz:

$$\Delta E = \frac{1}{4}\Delta z^2 k \frac{dT}{dz}\left(n\frac{dv}{dz} + v\frac{dn}{dz}\right) + O(\Delta z^3) \qquad \text{(D.3)}$$

L = neutraliser length (z dimension)
x = neutraliser width
y = neutraliser height
V = neutraliser volume
n = neutraliser gas density
v = neutraliser gas mean thermal velocity
S_w = neutraliser wall surface area
T_w = neutraliser wall temperature
T = neutraliser gas temperature
γ= specific heat of the neutraliser gas (dimensionless variable)
α = accommodation coefficient of the neutraliser wall (assumed to be 0.5 for H_2)
I_B = beam current
E_B = beam energy (keV)
v_e = electron mean velocity
n_e = electron density *
T_e = electron temperature (eV) *
V_p = plasma potential *
M^+ = mass of plasma ion
R = reflection coefficient
k = Boltzmann constant
σ_{dj} = beam ion dissociation cross section (j=1-4)
σ_{de} = electron dissociation cross section
σ_0 = energy loss cross section for elastic collisions between reflected neutralised plasma ions and neutraliser gas molecules
E_{dj} = energy transferred to dissociation products from beam ions
E_{de} = energy transferred to dissociation products from electrons
$P(E)$ = probability for energy loss of the dissociation products in elastic collisions with neutraliser gas molecules
C = neutraliser conductance
T_C = Temperature of gas when taking conductance measurement
F = injected gas flow (molecules per second) = Q/kT_i
Q = gas flow (Torr litres per second)
T_i = gas injection temperature
$K(x/\lambda(z))$ = factor by which the conductance is increased (pressure dependent) [34]

*: The three empirical parameters (cf. [36]) can be reduced to just one, namely T_e [31].

Appendix E DNB & HNB initial beam 'plasma' evolution

DNB initial beam 'plasma' evolution

100keV/15A Hydrogen beam injection into a H_2 gas of density $1.45x10^{19}m^{-3}$:

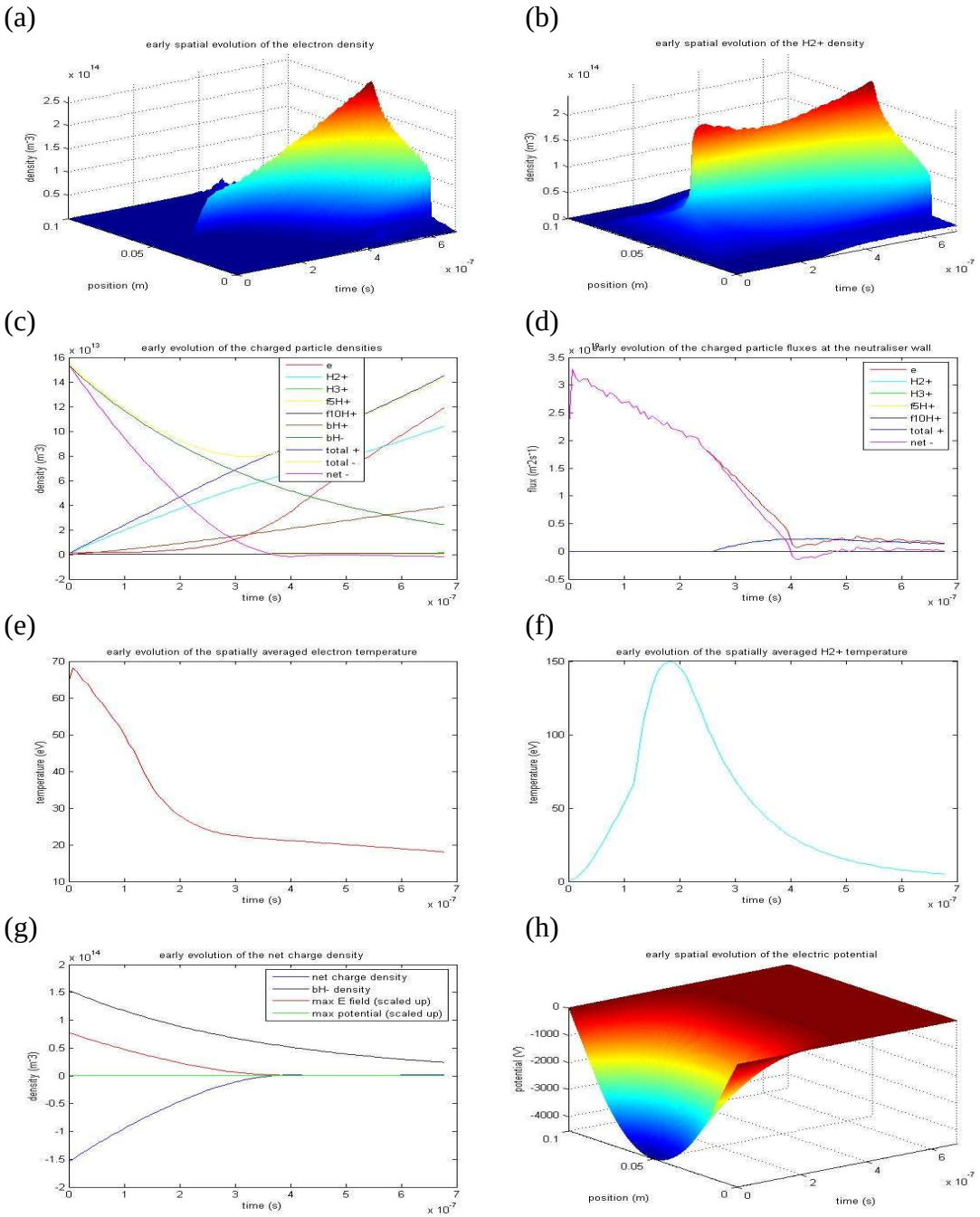

Figure 108: (a) electron density, (b) H_2^+ density, (c) charged particles densities, (d) charged particle fluxes at neutraliser wall, (e) electron temperature, (f) H_2^+ temperature, (g) net charge density ..., (h) electric potential. {beam transit time, 684ns}

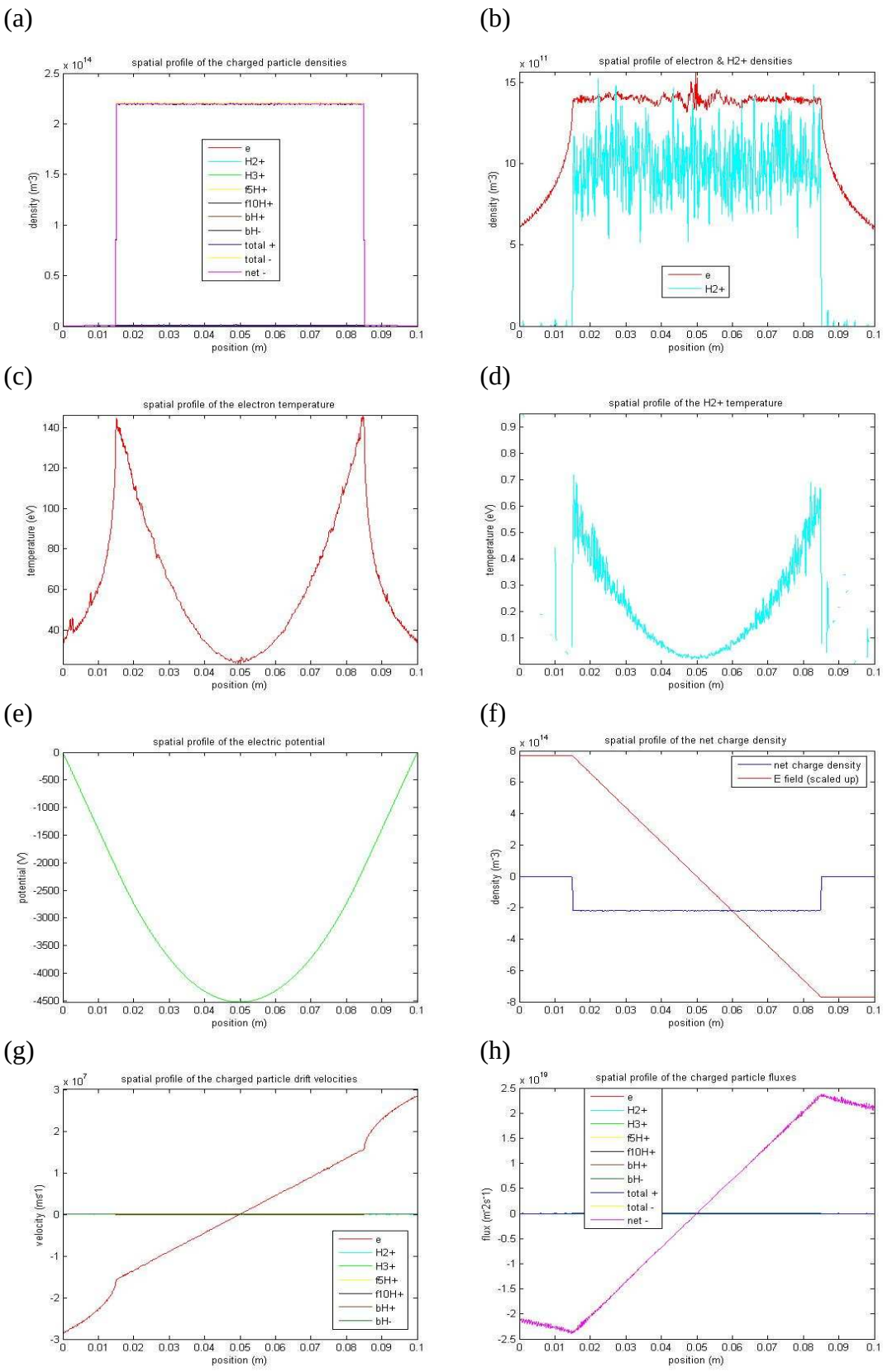

Figure 109: Spatial profiles @ t = 6ns; (a) charged species densities (b) electron & H_2^+ density, (c) electron temperature, (d) H_2^+ temperature, (e) electric potential, (f) net charge density & electric field, charged particle (g) drift velocities and (h) fluxes.

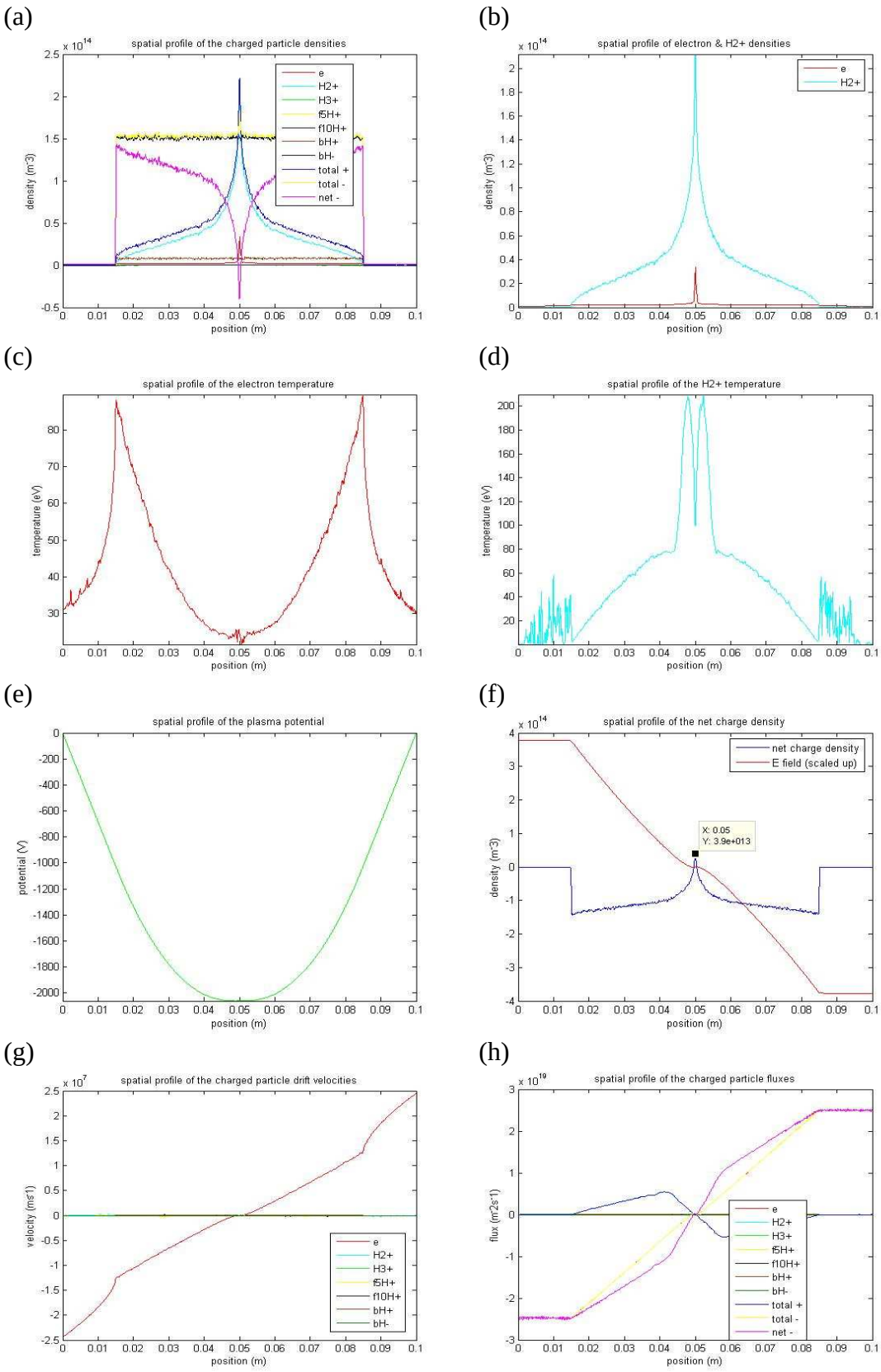

Figure 110: Spatial profiles @ t = 136ns; (a) charged species densities (b) electron & H_2^+ density, (c) electron temperature, (d) H_2^+ temperature, (e) electric potential, (f) net charge density & electric field, charged particle (g) drift velocities and (h) fluxes.

(a) (b)

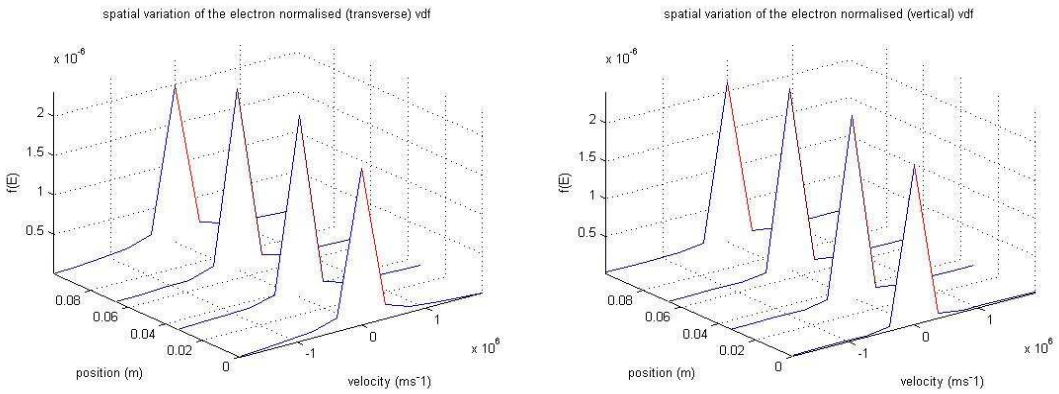

(c) (d)

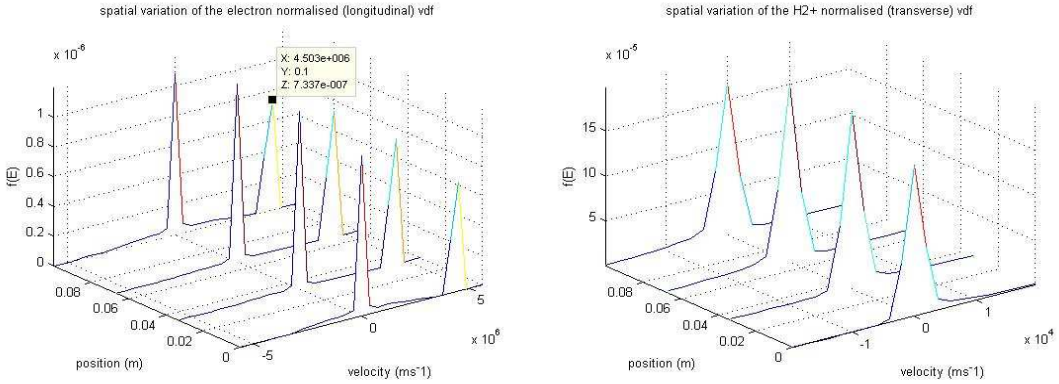

(e) (f)

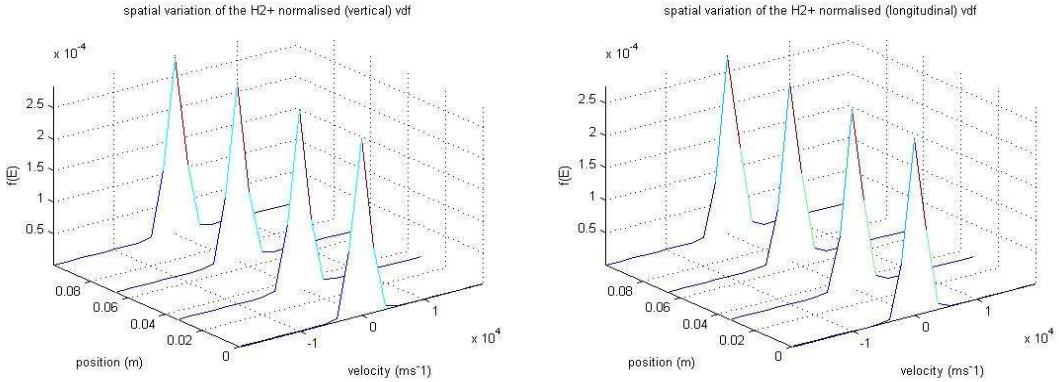

Figure 111: Electron (a) transverse, (b) vertical and (c) longitudinal velocity distribution functions. H_2^+ (d) transverse, (e) vertical and (f) longitudinal velocity distribution functions. All plots @ t = 136ns {title misprint: f(E) is not normalised}.

Note the presence of beam stripped electrons i.e. with velocity equal to the beam velocity, in the longitudinal beam direction (*Figure 111 (c)*). The differences in the electron & H_2^+ velocity distribution functions at the neutraliser walls (*Figure 111 (a) & (d)*) are due to the plasma sheath, where for example the H_2^+ ions have a preferential direction towards the walls (opposite direction for electrons), hence the difference in their mean and thermal energies (*Figure 112 (b)*).

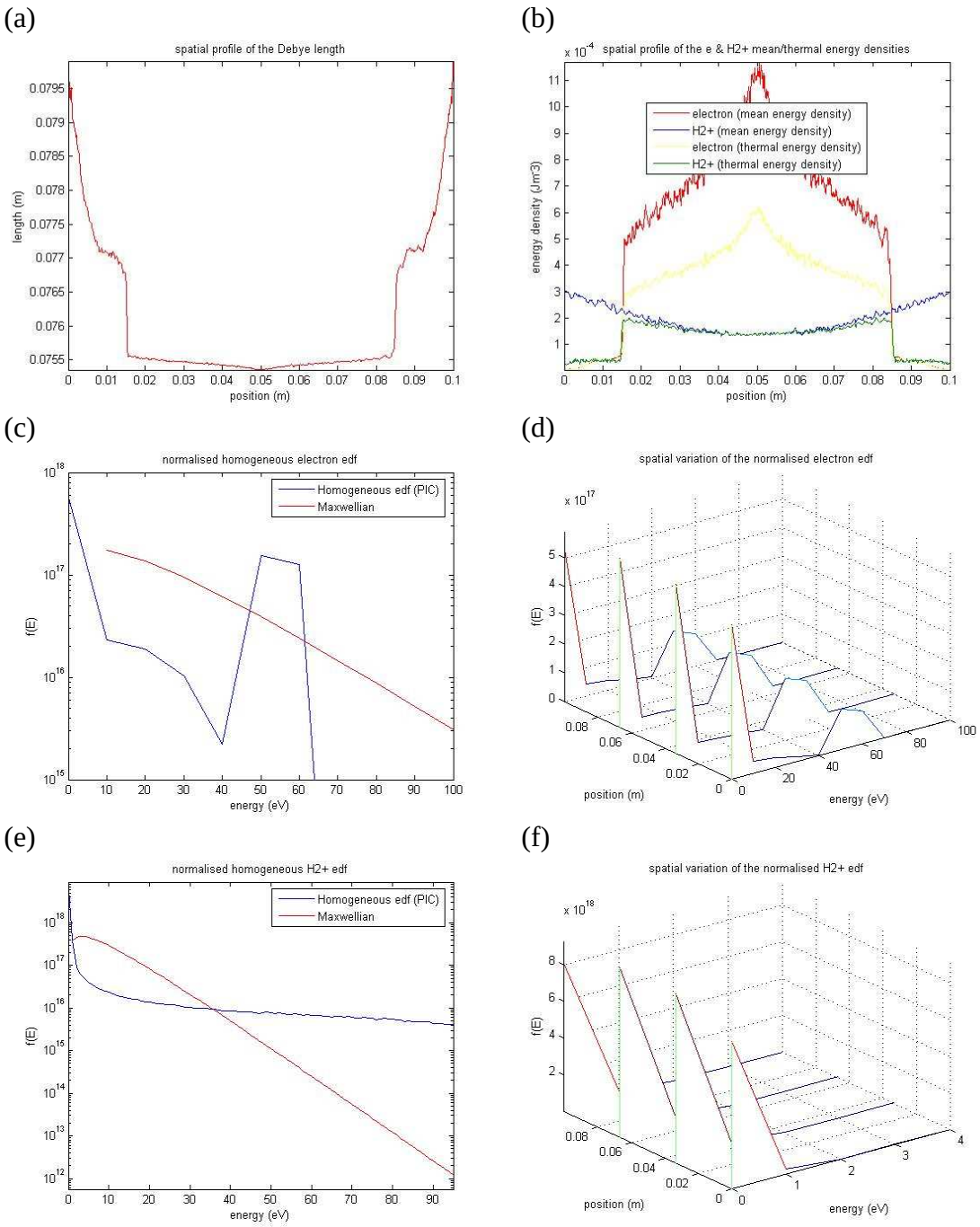

Figure 112: (a) Debye length. (b) Electron & H_2^+ mean/thermal energies. (c) Electron & (e) H_2^+ energy distribution functions. Spatial variation of the (d) electron & (f) H_2^+ edfs. All plots @ t = 136ns {title misprint: f(E) is not normalised}.

The prominent peak (almost identical @ 6ns) in the electron edf @ ~ 55eV (*Figure 112 (c)*), evidences the presence of beam stripped electrons, since their initial velocity of 4.503×10^6 ms^{-1} (*Figure 111 (c)*) corresponds to an energy of ~ 55eV.

HNB initial beam 'plasma' evolution

1MeV/10A Deuterium beam injection into a D_2 gas of density $4.67 \times 10^{19} m^{-3}$:

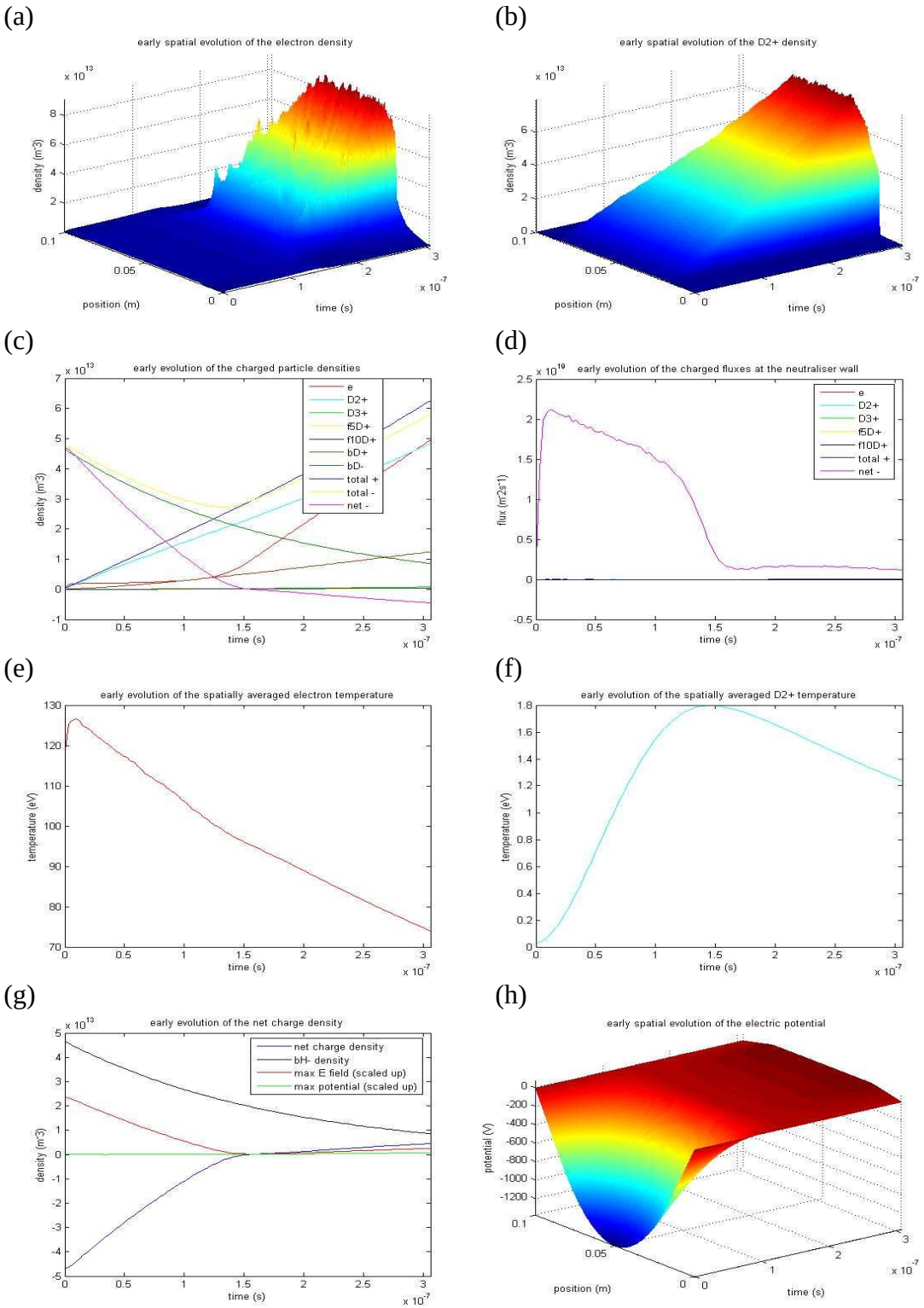

Figure 113: (a) electron density, (b) D_2^+ density, (c) charged particles densities, (d) charged particle fluxes at neutraliser wall, (e) electron temperature, (f) D_2^+ temperature, (g) net charge density ..., (h) electric potential. {beam transit time, 306ns}

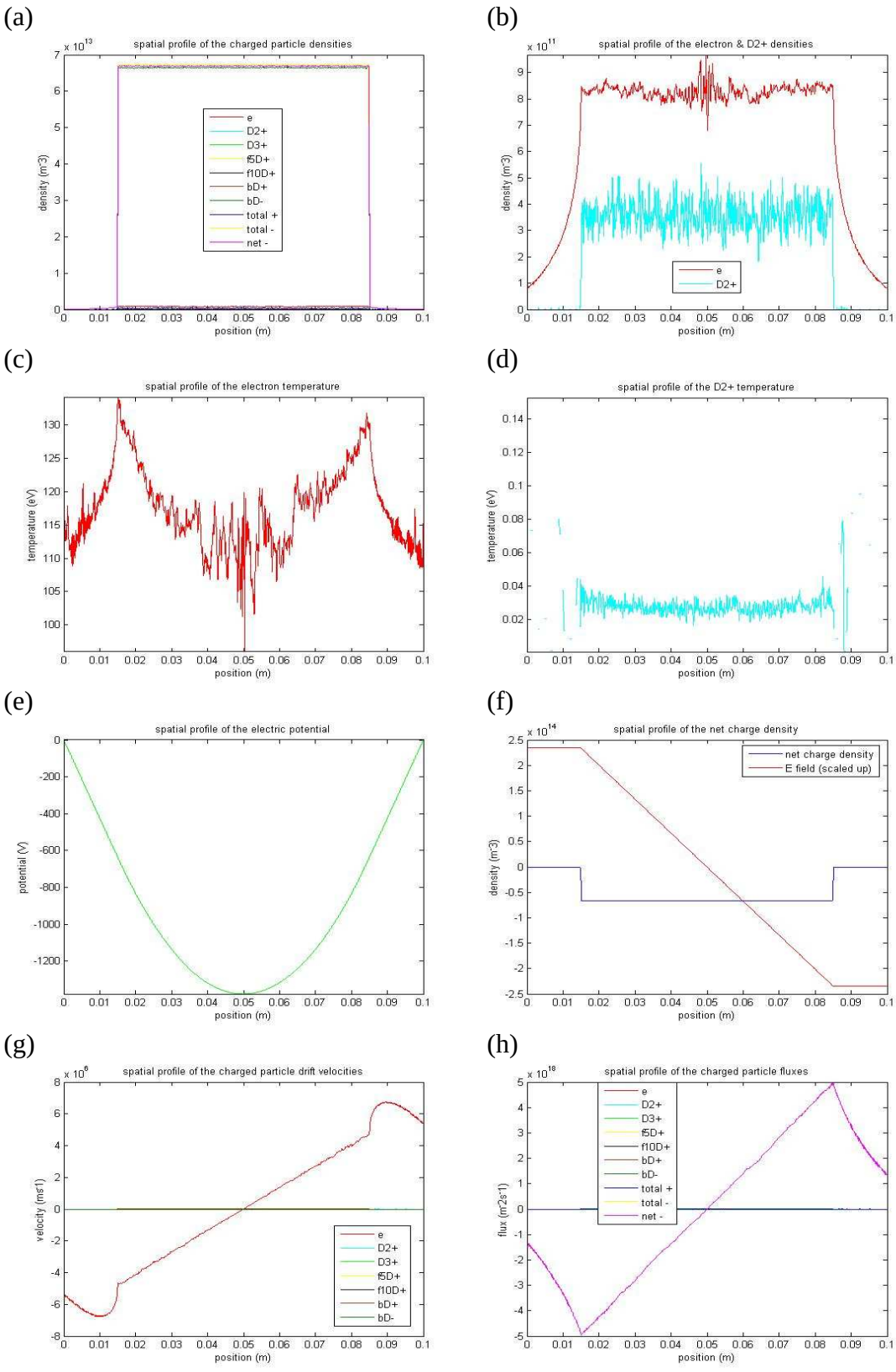

Figure 114: Spatial profiles @ t = 3.06ns; (a) charged species densities (b) electron & D_2^+ density, (c) electron temperature, (d) D_2^+ temperature, (e) electric potential, (f) net charge density & electric field, charged particle (g) drift velocities and (h) fluxes.

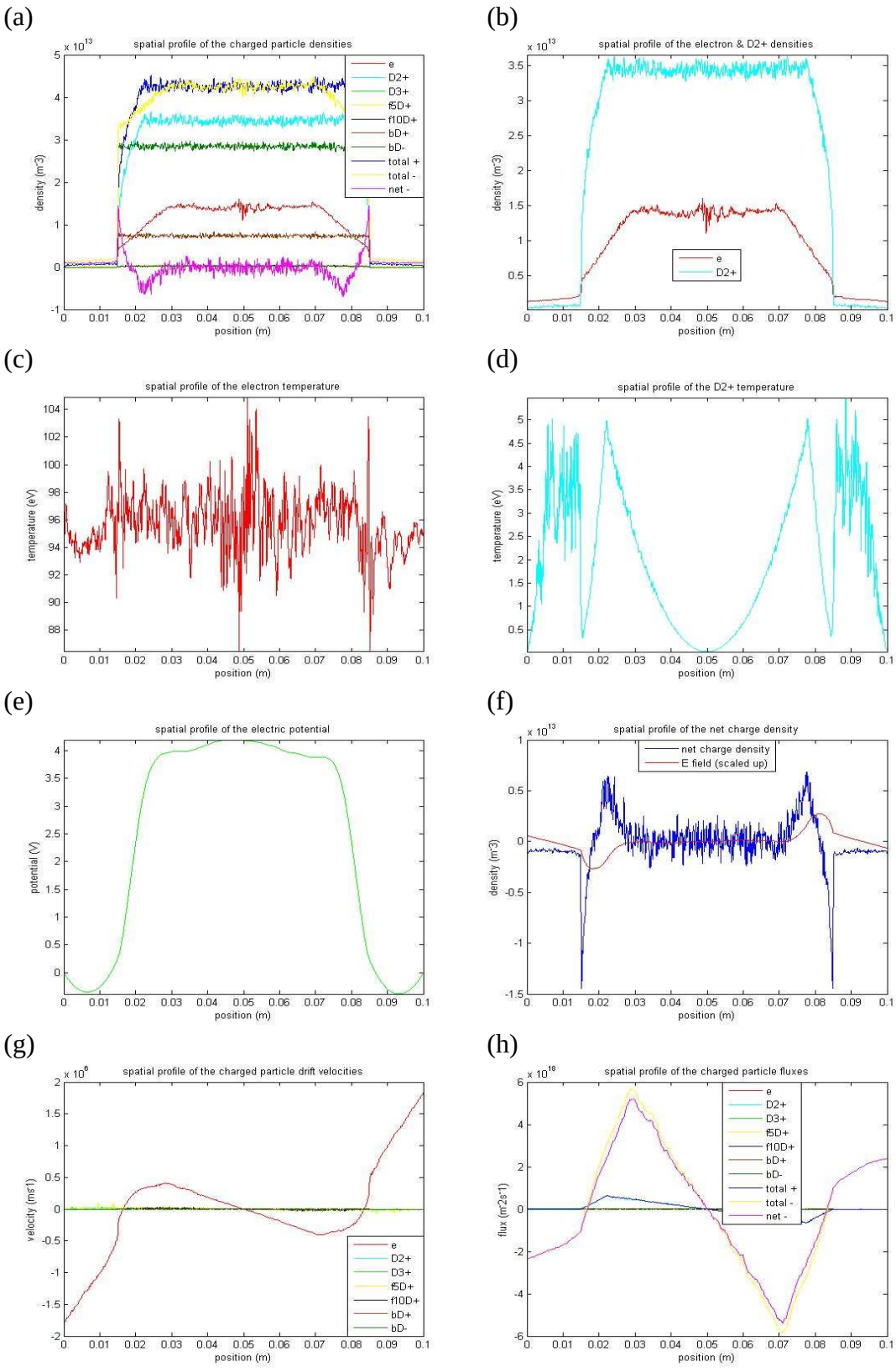

Figure 115: Spatial profiles @ t = 153ns; (a) charged species densities (b) electron & D_2^+ density, (c) electron temperature, (d) D_2^+ temperature, (e) electric potential, (f) net charge density & electric field, charged particle (g) drift velocities and (h) fluxes.

Clear evidence of (fleeting) double layers at each side of the beam (*Figure 115 (f)*).

(a) (b)

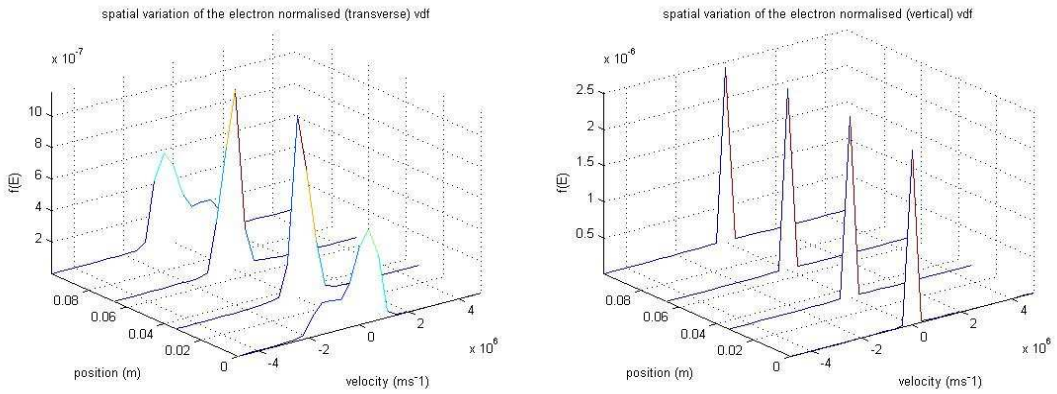

(c) (d)

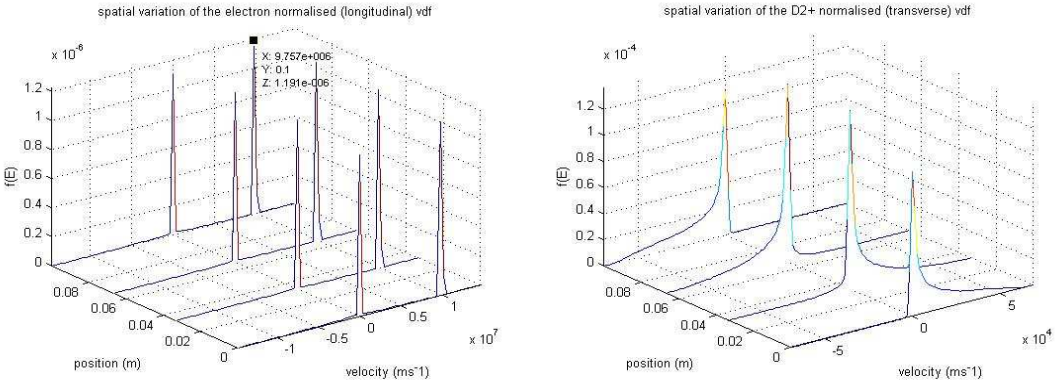

(e) (f)

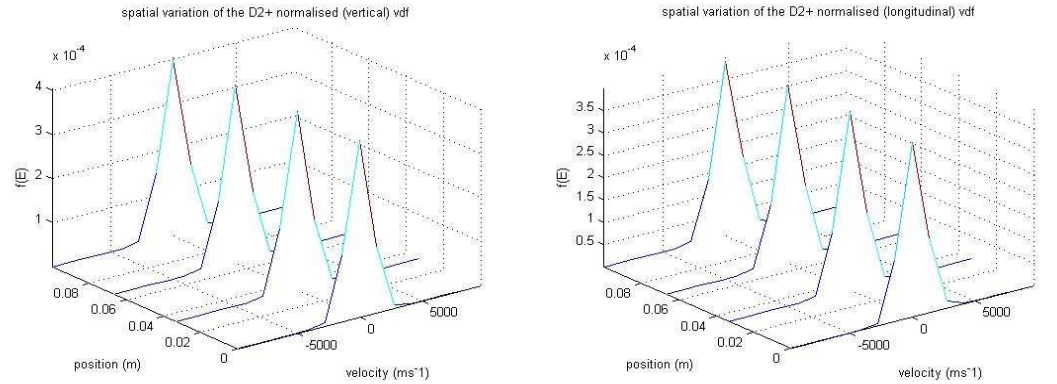

Figure 116: Electron (a) transverse, (b) vertical and (c) longitudinal velocity distribution functions. D_2^+ (d) transverse, (e) vertical and (f) longitudinal velocity distribution functions. All plots @ t = 153ns {title misprint: f(E) is not normalised}.

Again, note the presence of beam stripped electrons (with velocity equal to the beam velocity) in the longitudinal beam direction (*Figure 116 (c)*). The differences in the electron & D_2^+ velocity distribution functions at the neutraliser walls (*Figure 116 (a)* & *(d)*) are due to the plasma sheath, where for example the D_2^+ ions have a preferential direction towards the walls (opposite direction for electrons), hence the difference in their mean and thermal energies (*Figure 117 (b)*).

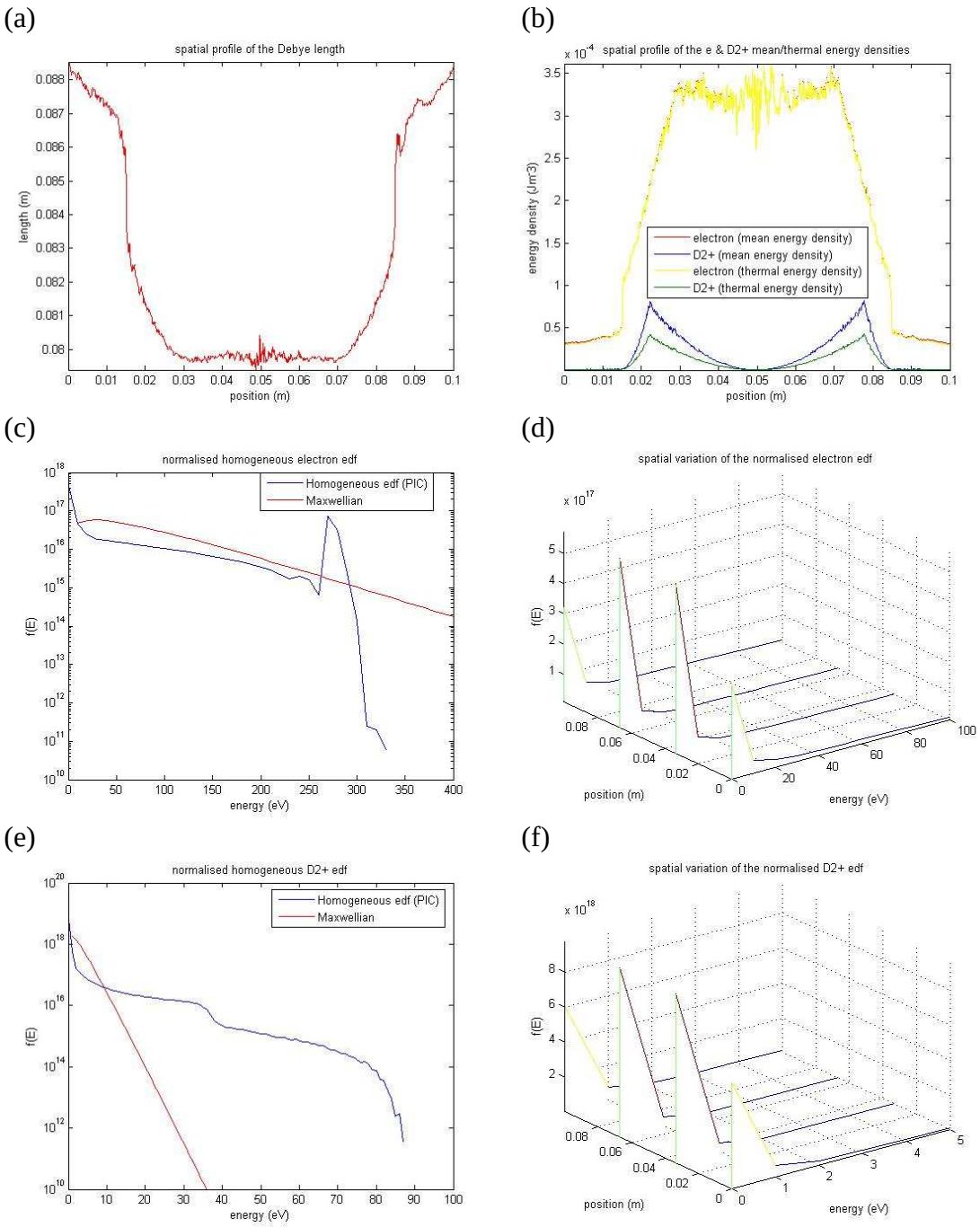

Figure 117: (a) Debye length. (b) Electron & D_2^+ mean/thermal energies. (c) Electron & (e) H_2^+ energy distribution functions. Spatial variation of the (d) electron & (f) H_2^+ edfs. All plots @ t = 153ns {title misprint: f(E) is not normalised}.

The prominent peak (almost identical @ 6ns) in the electron edf @ ~ 270eV (*Figure 117 (c)*), evidences the presence of beam stripped electrons, since their initial velocity of 9.757×10^6 ms^{-1} (*Figure 116 (c)*) corresponds to an energy of ~ 270eV.

Bibliography

[1] A. Einstein, 'Ist die Trägheit eines Körpers von seinem Energieinhalt abhängig? {Does the inertia of a body depend upon its energy-content?}', Annalen der Physik 18, 639-643, September 27, 1905.

[2] A. Einstein, 'Zur Elektrodynamik bewegter Körper {On the Electrodynamics of Moving Bodies}', Annalen der Physik 17:891, June 30, 1905.

[3] F.W. Aston, 'A positive ray spectrograph', Phil. Mag. 38, 707-714, 1919.

[4] H.A. Bethe, 'Energy Production in Stars', Physical Review 55 (5) 434-456, 1939.

[5] B.B. Kadomtsev, 'Evolution of the tokamak', Plasma Physics and Controlled Fusion, volume 30, number 14, 2031-2049, 1988.

[6] JET website: http://www.jet.efda.org.

[7] ITER website: http://www.iter.org.

[8] IPCC, 2007: Summary for Policymakers. In: Climate Change 2007: The Physical Science Basis. Contribution of Working Group I to the Fourth Assessment Report of the Intergovernmental Panel on Climate Change [S. Solomon, D. Qin, M. Manning, Z. Chen, M. Marquis, K.B. Averyt, M. Tignor and H.L. Miller (eds.)]. Cambridge University Press, Cambridge, United Kingdom and New York, NY, USA.

[9] D.L. Royer, R.A. Berner, J. Park, 'Climate sensitivity constrained by CO_2 concentrations over the past 420 million years', Nature 446 (7135): 530-532.

[10] K.S. Krane, 'Introductory Nuclear Physics', John Wiley & Sons, Inc. 1988.

[11] C. Llewellyn Smith, 'The Path to Fusion Power', Institue of Physics in Ireland, 2007 Spring Weekend Meeting, Birr, Co. Offaly.

[12] Wikipedia website: http://www.wikipedia.org/wiki/Nuclear_power.

[13] T. Hamacher & A.M. Bradshaw, 'Fusion as a future power source: recent achievements and prospects', World Energy Council (18th Congress), October 2001.

[14] P.K. Kuroda, 'Nuclear fission in the early history of the earth', Nature 187, 36-38, 2 July 1960.

[15] F. Gauthier-Lafaye, P. Holliger and P-L. Blanc, 'Natural fission reactors in the Franceville Basin, Gabon: a review of the conditions and results of a "critical event" in a geologic system', Geochim. Cosmochim. Acta, 60 (1996) 4831-4852.

[16] A.S. Eddington, 'The Internal Constitution of the Stars', Cambridge Sci. Classics.

[17] E.M. Burbidge, G.R. Burbidge, W.A. Fowler and F. Hoyle, 'Synthesis of the Elements in Stars', Reviews of Modern Physics, 29 (1957) 547.

[18] European Commision, 'ITER – Uniting science today global energy tomorrow', 2007, ISBN 978-92-79-05548-5.

[19] E. Surrey, C.D. Challis, D. Ciric, S.J. Cox, B. Crowley, I. Jenkins, T.T.C Jones, D. Keeling, 'Measurement of the depletion of neutraliser target due to gas heating in the JET neutral beam injection system', Fusion Eng. and Design 73 (2005) 141-153.

[20] D. Ćirić et al.,'Overview of the JET neutral beam enhancement project', Fusion Engineering and Design 82 (2007) 610-618.

[21] T.S. Green & A.J.T. Holmes, 'Measurements of the neutralisation efficiency of a 50-keV He^+ beam in a He gas cell', Rev. Sci. Instrum., 53(6), 816-818, June 1982.

[22] E. Surrey, 'Calculation of Beam Plasma Parameters in the Neutraliser' UKAEA internal report, CD/HFD/DN(01)004, included in the 'Improved NB Neutraliser' JET Enhancement Project (JWO-EH-2.2) [DCU & UKAEA], December 2001.

[23] D. Ćirić, 'PINI Alignment & Beam Simulation Program Installation', NB Test Bed Group, UKAEA Fusion – JET Facility.

[24] H. Tawara & A. Russek, ‘Charge Changing Processes in Hydrogen Beams’, Reviews of modern physics, volume 45, number 2, April 1973.

[25] Max-Planck-Institut fur Plasmaphysik (IPP) website: http://www.ipp.mpg.de.

[26] R.S. Hemsworth, ‘Calculation of the gas target in the neutraliser in the absence of the beam’, JET-DN-C(87)41.

[27] H.D. Falter et al., ’60 KV Hydrogen Neutralisation Scan’, JET-R(98)10, Dec 1998.

[28] H.D. Falter, ‘Conductance of the JET Neutralisers’, JET internal report.

[29] A. Roth, ‘Vacuum Technology’, North-Holland Publishing Company, 1976.

[30] E. Surrey & B. Crowley, ‘Spectroscopic measurements of the gas temperature in the neutraliser of the JET neutral beam injection line’, Plasma Phys. Control. Fusion 45 (2003) 1209-1226.

[31] J. Paméla, ‘Gas Heating Effects in the Neutralisers of Neutral Beam Injection Lines’ Rev. Sci. Inst. 57 (6), page 1066–1086, June 1986.

[32] P. Bayetti, F. Bottiglioni, G. Martin and J. Pamela, ‘Charged fusion product analysis as diagnostics in high-energy deuterium beam’, Rev. Sci. Inst., vol. 57, no. 1, January 1986.

[33] H.D. Falter, G.H. Deschamps, R.S. Hemsworth and P. Massmann, ‘Implantation and re-emission of Hydrogen and Helium in the beam-stopping panels of a 10 MW ion beam line’, Journal of Nuclear Materials, 176 & 177, (1990) 678-682.

[34] J. Paméla, ‘Gas heating effects in the neutralisers of neutral beam injection lines’ Report EUR-CEA-FC-1279, CEN Fontenay-aux-roses, October 1985.

[35] ‘Improved NB Neutraliser JET Enhancement Project’ (JWO-EH-2.2) [DCU & UKAEA], December 2001.

[36] B. Crowley, E. Surrey, S.J. Cox, D. Ciric and A.R. Ellingboe, 'Experimental Studies of the JET NBI Neutraliser Plasma' J Fus Eng and Design, 66-68, (2003) 591.

[37] D.A. Dunn & S.A. Self, 'Static Theory of Density and Potential Distribution in a Beam-Generated Plasma', Journal of Applied Physics, volume 35(1), Jan. 1964.

[38] A.J.T. Holmes, 'Theoretical and experimental study of space charge in intense ion beams' Physical Review A, volume 19, number 1, January 1979.

[39] M. de Graaf, 'A new hydrogen particle source', Thesis, T.U.E, 1994.

[40] E. Surrey, 'Gas heating in the neutralizer of the ITER neutral beam injection systems', Institute of Physics Publishing, Nuc. Fusion 46 (2006) S360-S368.

[41] 'Improved Neutralisation' (Proposal for further work), part of the 'Improved NB Neutraliser' JET Enhancement Project (JWO-EH-2.2) [DCU & UKAEA], Dec. 2001.

[42] PRL-DCU website: http://prl.dcu.ie.

[43] M.A. Lieberman & A.J. Lichtenberg, 'Principles of Plasma Discharges and Materials Processing', John Wiley & Sons Inc., New York, 1994.

[44] F.F. Chen, 'Introduction to Plasma Physics and Controlled Fusion – Volume 1: Plasma Physics', Springer, second edition, 1984.

[45] R. Dendy, 'Plasma Physics: An Introductory Course', Cambridge Uni. Press, 1993.

[46] V. Vahedi, C.K. Birdsall, M. A. Lieberman, G. diPeso and T.D. Rognlien, 'Capacitive RF discharges modelled by particle-in-cell Monte Carlo simulation II: comparison with laboratory measurements of electron energy distribution functions', Plasma Sources Sci. Technol. 2(1993), 273-278. Printed in the UK.

[47] C.K. Birdsall & A.B. Langdon, 'Plasma Physics via Computer Simulation', Institute of Physics, 1991.

[48] T. Takizuka & H. Abe, J. Comp. Phys. 25, 205 (1977).

[49] R.W. Hockney & J.W. Eastwood, ‘Computer Simulation Using Particles’, Institute of Physcis Publishing, 1988.

[50] M.M. Turner, ‘Kinetic properties of particle-in-cell simulations compromised by Monte Carlo collisions’, Physics of Plasmas, vol. 13, 033506, 2006.

[51] M. Surendra, ‘Radiofrequency discharge benchmark model comparison’, Plasma Souces Sci. Technol., vol. 4, page 56-73, 1995.

[52] S.J. Buckman & A.V. Phelps, ‘JILA Information Center Report 27’, 1985.

[53] International Atomic Energy Agency Atomic and Molecular Data Unit, Vienna, Austria, website: http://www-amdis.iaea.org/ALADDIN/.

[54] C.F. Barnett, ‘Atomic Data for Fusion’, volume 1, (ORNL-6086/V1), July 1990. {Published and edited by H.T. Hunter, M.I. Kirkpatrick, I. Alvarez, C.Cisneros, University of Mexico, and R.A. Phaneuf, Controlled Fusion Atomic Data Center}.

[55] A.B. Wittkower, P.H. Rose, R.P. Bastide, and N.B. Brooks, ‘Small-Angle Scattering Observed in the Formation of Neutral Atoms from 10- to 55-keV Positive Ion Beams’, Physical Review, volume 136, number 5A, 30 November 1964.

[56] C.E. Kuyatt & T. Jorgensen Jr., ‘Energy and Angular Dependence of the Differential Cross Section for the Production of Electrons by 50-100 keV Protons in Hydrogen Gas’, Physical Review, volume 130, number 4, 15 May 1963.

[57] M.E. Rudd & T. Jorgensen Jr., ‘Energy and angular distribution of electrons from hydrogen and helium Gas by protons’, Phys. Rev., vol. 131, no. 2, July 1963.

[58] W. Eckstein & H. Verbeck, ‘Data on Light Ion Reflection’, Max-Planck Inst. Plasma Phys. Rep. IPP 9/32 (1979).

[59] G.M. McCracken & P.E. Scott, ‘Plasma-surface interactions in Tokamaks’, Nucl. Fusion, vol.19, no. 7, July 1979, p 889-981.

[60] J. Kim & H.H. Haselton, ‘Analysis of particle species evolution in neutral-beam injection lines’, J. Appl. Phys. 50 (6), June 1979.

[61] R.B. Miller, ‘An Introduction to the Physics of Intense Charged Particle Beams’, Plenum Press, New York.

[62] V.N. Gorshkov, A.M. Zavalov, I.A. Soloshenko, ‘Process of Compensation of the Space Charge of a Negative Ion Beam in a Gas’, Plasma Physics Reports, 33(12), 2007.

[63] M.D. Gabovich, L.P. Katsubo, and I.A. Soloshenko, ‘Charge separation in a stable, quasineutral ion beam due to Coulomb collisions’, Sov. J. Plasma Phys. 1(2), 1975.

[64] C. Burrell, W.S. Cooper, R.R. Smith, W.F. Steele, Rev. Sci. Instrum, 1451, 1980.

[65] B. Crowley (unpublished).

[66] Stephen Cox, ‘Neutralisation Efficiency Measurements at JET (Including the upgraded triode PINIs)’, Coordinating Committee on Neutral Beams, December 2002.

[67] Tae-Seong Kim et al., ‘Neutralizer experiment of KSTAR NBTS system’, Vacuum (Article in Press – available online 23 June 2009).

[68] J.D. Cockcroft & E.T.S Walton, ‘Disintegration of Lithium by Swift Protons’, Nature 129, 242, 1932.

[69] S.K. Allison, J. Cuevas, and M. Garcia-Munoz, ‘Partial Atomic Stopping Power of Gaseous hydrogen for Hydrogen Beams. I’, Phys. Rev., 127(3), 1962.

[70] M.N. Huberman, ‘Partial Ionic Stopping Power and Energy Expended in electron Capture and Loss Collisions of Protons in Hydrogen Gas. II’, Phys. Rev., 127(1), 1962.

[71] A.C. Bajpai, L.R. Mustoe, D. Walker, ‘Engineering Mathematics’, Wiley, 1980.

[72] R. Hemsworth et al. ‘Status of the ITER heating neutral beam system’, Nucl. Fusion 49, 2009, 045006.

[73] JT60 website: http://www-jt60.naka.jaea.go.jp.

[74] L.R. Grisham, ‘The operational phase of negative ion beam systems on JT-60U and LHD’, IEEE Transactions on plasma science, volume 33, number 6, December 2005.

[75] M. Hanada et al., ‘Long pulse production of high current D^- ion beams in the JT-60 negative ion source’, Review of Scientific Instruments, volume 79, issue 2, 2008.

[76] DIII-D website: http://fusion.gat.com.

[77] LHD website: http://www.lhd.nifs.ac.jp/en.

[78] Y.M. Fogel, A.G. Koval, Y.Z. Levchenko, A.F. Khodyachikh, ‘Composition of Slow Ions Produced During the Ionization of Gases by Negative Ions’, SOVIET PHYSICS JETP-USSR, 12 (3): 384-389 1961.

[79] Y.M. Fogel, A.G. Koval, Y.Z. Levchenko, Y.M FOGEL, ‘Ionization of Gases by Negative Ions’, SOVIET PHYSICS JETP-USSR, 11 (4): 760-765 1960.

[80] A. Krylov & T. Inoue, ‘Compact Beamline and Design against Radiation’, J. Plasma Fusion Res., vol. 81, no. 10, 779-784, 2005.

[81] A. Krylov & R.S. Hemsworth, ‘Cyropumping in the ITER injectors and the Neutral Beam Test Facility (NBTF) with vertical access’, NBTF meeting, Garching, 2004.

[82] V.V. Serikov, S. Kawamoto, K. Nanbu, ‘Particle-in-Cell Plus Direct Simulation Monte Carlo (PIC-DSMC) Approach for Self-Consistent Plasma-Gas Simulations’, IEEE transactions on Plasma Science, volume 27, number 5, October 1999.

[83] A. Krylov and R.S. Hemsworth, ‘Gas flow and related beam losses in the ITER neutral beam injector’, Fusion engineering and design, vol. 81, pp. 2239-2248, 2006.